SYSTEMATIC APPROACHES TO DESIGN CHITOSAN FUNCTIONALISED 3D - PRINTED MONOLITH WITH AI TECHNOLOGY FOR COLOUR REMOVAL IN WASTEWATER TREATMENT

NURUL HUSNA BINTI MOHD YUSOFF, MEng

Under supervision of

IR DR CHONG CHIEN HWA, PhD

IR DR WAN YOKE KIN, PhD

Thesis submitted to the University of Nottingham

for the degree of Doctor of Philosophy

ABSTRACT

Access to clean water is a fundamental problem that has been emphasised by the United Nations and World Health Organization. Water is one of the vital necessities for humans to stay alive and prevent disease. However, due to the increasing world population and climate change, it is predicted water resources will be stressed and limited due to poor quality. Various water treatment processes have been developed based on the presence of contaminants in water to solve the urgent issue. To date, 3D printing has been utilised over the conventional method in water treatment due to its capability to manufacture geometrically complex structures and cost-effectiveness with minimum wastage of materials. The latest approaches of synergising additive manufacturing (AM) and surface functionalisation have drawn tremendous attention in recent years due to their outstanding performance to achieve the requirements of commercial applications. In this work, a critical review on 3D printable functional materials in water application was prepared. The robust approach of applying surface functionalisation strategies for additively manufactured material have been discussed along with emerging application water application. This project taking the approach of treating the textile wastewater through experimental work with enhancement strategy and modelling using artificial intelligence. The first experimental data that focusing on the development of novel design on chitosan – grafted 3D -printed monolith were established. A set of 81 experimental data were run to evaluate the adsorption performance of the chitosan-grafted monolith with series of

characterisation analysis was studied. It was reported the removal efficiency (R%) of methyl orange (MO) dye ranged from 20.8 to 90.4% and the equilibrium uptake capacity (K) was ranged from 1 to 12.62 (mg/g) after 2 h. The percent reduction for BOD and COD are 62.4% and 2 - 3.9%, respectively when using real textile wastewater. The recyclability of the chitosan - grafted PEGDA monolith was verified by evaluating its adsorption for four consecutive cycles and retained at 78%. The combined methodology of integrating 3D printing technique with surface grafting techniques has effectively led to the creation of an innovative environmental-friendly wastewater treatment technology. This approach embodies principles of sustainability and zero waste by eliminating the necessity for replacing adsorbents and removing sludge. This approach also is a cost-effective solution as it can reduce the cost of spending on the chemicals and maintenance. Moreover, structural design of body centred cubic (BDD) has the best adsorption performance with high surface area and permeability which further enhance contact point between the adsorbent with the adsorbate. Additionally, the resin formulation of PEGDA and addition of 3wt.% of HDDA has shown to be the best candidate to be developed as green water technology, whereas silane - grafted with GLYMO on the 3D-printed monolithic structure has achieved a good hydrophobicity, reduction in moisture absorption content, good mechanical as well as chemical stability. This approach has extended the functionality of the 3D-printed monolith for utilisation in aquatic settings in contrast to conventional polymeric materials that exhibit a propensity for water absorption. Further to this, the results of

the convective hot air drying have better performance while retaining the surface morphology and removed adequate moisture content within 6% for better storage and lifespan of the functional groups of the chitosan to be used as an adsorbent. Meanwhile, the electron beam treatment with 200cGy has successfully increased the adsorption performance to 96.6% within 80 min. The integration of four stages of the enhancement strategy is anticipated to facilitate the development of a 3D-printed enhanced adsorbent that exhibits excellent adsorption efficacy, robust mechanical and chemical durability, and shorter adsorption time for the treatment of textile wastewater. Lastly, the prediction of water analysis using convolutional neural network and AlexNet was performed to predict the colour of textile wastewater based on real-time images. It was found that both networks demonstrated excellent results in terms of its ability to accurately classify data, as well as its efficient training and testing time. For large data sets, CNN has the highest training accuracy with 94.2%, while AlexNet has better performance in handling small date sets with 89.8%. The conclusions and future works are included in the end of this thesis.

ACKNOWLEDGEMENT

First and foremost, I would like to take this opportunity to express my sincere gratitude to my supervisor, Ir. Ts. Dr. Chong Chien Hwa for his continuous support, mentoring, encouragement and patience that enabled me to not only develop understanding but also the passion to complete this research. This dissertation would not have been feasible without his careful, perceptive, and enthusiastic supervision. Besides, I would like to thank all my co-supervisors, Ir. Dr. Wan Yoke Kin, Dr. Wong Voon Loong and Dr. Cheah Kean How, for their support and guidance that was given to me throughout my PhD study. Under their supervision, I have gained a lot of experience through exchanging research ideas with this research group. I was frequently urged to approach problem-solving with a critical and analytical mindset. Working with them has altered both my working style and how I approached challenging problems. I would like to thank Dr Chew Wei Jen for her guidance in developing the image processing model for water quality predictions. A special shoutout to Prof. Dominic C. Y. Foo for his kind advice and encouragement. Prof. Dominic particularly guided me to develop P-graph research for unit synthesis and arranging research attachment overseas. I would like to thank my friends and colleagues from University of Nottingham Malaysia namely, Shannen Marcus Ng, Nadiah Syafiqah, Tee Wan Ting, Wong Hock Yee, Adriel Tan and Newton Well Lo for the wonderful memories, discussions, involvement of research ideas and selfless sharing of knowledge.

Additionally, I would like to thank my research attachment hosts and collaborators for their insightful advice and passionate support during my PhD studies. I would like to thank Mr. Lim from Eco Solution Sdn. Bhd. for his insight and knowledge on the wastewater treatment process as well as providing data and water samples for my PhD project. I would like to express my gratitude to Prof. Ference Friedler, Jean Pimentel, Dr. Akos Orosz, Dr. Richard Teng and other researchers from P-graph research group for providing me valuable exposure during my research attachment at Gyor University, Hungary. Further to this, I would also like to thank Dr. Antoni Szumny, Prof. Adam Fiegel and the rest of the research group at Wrocław University of Environmental and Life, Poland for hosting me and providing some unique ideas and sharing knowledge that are valuable for my work.

My deepest appreciation to Dr. Chan Yi Jing for her time in reviewing my annual reports and providing insightful advice to improve my work. My sincere thanks and gratitude are extended to the technical staffs of the Faculty of Engineering of University of Nottingham Malaysia (Mr. Ahmad Fareez, Mr. Asyraf, Mr. Shahril Aidil, Mr. Shahbudin, Mr. Halim, Ms. Filzah, Ms. Husna, Ms. Khairani and Ms. Siti) for their counsel on using analytical tools and their help in resolving any technical issues I encountered while conducting my research. Furthermore, I would like to express my gratitude to The University of Nottingham Malaysia Campus for providing financial support under Science and Engineering PhD Research Scholarship (SEPRS).

I am grateful for the affection I have received from my parents, siblings and friends, who have supported, prayed for, and encouraged me during my postgraduate studies. Their unwavering encouragement has helped me to go through during this challenging period and restored my confidence to finish my studies. To mummy Jemilah and daddy Yusoff, thank you for your wisdom words, prayers and checking on me day and night to ensure I am not burning out throughout this marathon. To all my brothers and sisters, thank you for your understanding, constant support and encouragement in completion of this research particularly my second brother, Dr. Mohd Azlan whom I shared a lot the bottlenecks and challenges that I faced during my PhD journey. A special mention to my extended family members, colleagues and friends specifically from The Kalsom Movement, Biosekitar Enterprise, RC coaching, Axiata Foundation and Dritech Chemicals for their enthusiasm and motivation to complete my PhD. Lastly, I would also like to thank everyone who had contributed directly or indirectly in completion of my thesis and research.

LIST OF PUBLICATIONS

Some parts of the thesis version work were submitted and accepted as scientific journal articles. The accepted and under review scientific journal articles are listed as follows:

1. **Nurul Husna Mohd Yusoff**, Lui-Ruen Irene Teo, Sue Jiun Phang, Voon-Loong Wong, Kean How Cheah, Siew-Shee Lim, 2022, Recent Advances in Polymer-based 3D Printing for Wastewater Treatment Application: An Overview, Chemical Engineering Journal, Volume 429, 132311 [*Accepted 31 August 2021; IF 16.744*].
2. **Nurul Husna Mohd Yusoff**, Chien-Hwa Chong, Voon-Loong Wong, Kean How Cheah, Yoke Kin Wan, 2022, 3D - printed PEGDA monolith with robust silane - grafted chitosan for enhanced textile wastewater treatment, Journal of Environmental Chemical Engineering. [*Accepted 8 September; IF 7.968*].
3. **Nurul Husna Mohd Yusoff**, Chien-Hwa Chong, Yoke Kin Wan, Voon-Loong Wong, Kean How Cheah, 2022, Optimization Strategies and Emerging Application of Functionalised 3D-Printable Materials in Water Treatment: A Review, Journal of Water Process Engineering. [*Accepted 2 December 2022; IF 7.34*].
4. **Nurul Husna Mohd Yusoff**, Chien Hwa Chong, Voon - Loong Wong, Kean How Cheah, Yoke Kin Wan, 2022, The Influence of Structural Topology of Additively Manufactured PEGDA Monolith on Removal Performance of Textile Wastewater Treatment, Asia-

Pacific Journal of Chemical Engineering. [*Accepted 24 July 2023; IF 1.777*]

5. **Nurul Husna Mohd Yusoff**, Chien Hwa Chong, Kean How Cheah, Yoke Kin Wan, Voon-Loong Wong, 2023, Enhancing multifunctional properties of a biocompatible PEGDA-based 3D printed monolith structure for water applications. [*Under Review*]
6. **Nurul Husna Mohd Yusoff**, Chien Hwa Chong, Voon-Loong Wong, Kean How Cheah, Yoke Kin Wan, 2023, Comparison of different drying techniques on silane - grafted chitosan of 3D-printed PEGDA monolithic structure and its effect on adsorption performance for anionic dye removal. [*Under Review*]
7. **Nurul Husna Mohd Yusoff**, Li Miin Loh, Chien Hwa Chong, Voon-Loong Wong, Kean How Cheah, Yoke Kin Wan,2023, Influence of electron beam irradiation on nanoscale structured of grafted chitosan monolith to enhance colour removal of textile wastewater. [*Under Review*]
8. **Nurul Husna Mohd Yusoff**, Wei Jen Chew, Chien Hwa Chong, Yoke Kin Wan, Identification and classification of colour parameter predictions of textile wastewater using convolutional neural network and AlexNet with transfer learning. [*Under Review*]

LIST OF CONFERENCE PAPER

1. Yong, J.J.I., Wong, VL., Yeap, S.P., Lim, S.S., **Yusoff, N.H.M**. (2023). Direct and Indirect Ultrasonic-Assisted Preparation of Calcium Alginate Monolithic Pellets for the Removal of Methylene Blue from Aqueous Solution. In: Jeon, HY. (eds) Sustainable Development of Water and Environment. ICSDWE 2023. Environmental Science and Engineering. Springer, Cham.

CONFERENCE PRESENTATION

1. **Nurul Husna Mohd Yusoff**, Chien Hwa Chong, Voon - Loong Wong, Kean How Cheah, Yoke Kin Wan, 2022. 3D-Printed PEGDA Monolith with Robust Silane-Grafted Chitosan for Enhanced Textile Wastewater Treatment: Response Surface Methodological Approach in 19th Asia Pacific Confederation of Chemical Engineering (APCChE) Congress, 9 - 12 August 2022, Kuala Lumpur Convention Centre (KLCC), Kuala Lumpur, Malaysia, Paper no. 1170.
2. **Nurul Husna Mohd Yusoff**, Chien Hwa Chong, Voon - Loong Wong, Kean How Cheah, Yoke Kin Wan, 2022. Robust Surface Functionalised 3D-Printed PEGDA Monolith for Enhanced Textile Wastewater Treatment in 1st International Conference on Water and Environment for Sustainability (ICWES 2022), 7 – 9 December 2022, Kuala Lumpur Convention Centre (KLCC), Kuala Lumpur, Malaysia, Paper no. 81.
3. **Nurul Husna Mohd Yusoff,** Chien Hwa Chong, Kean How Cheah, Yoke Kin Wan, Voon-Loong Wong, 2023. Formulation of

a Biocompatible Silane Functionalised Polyethylene Glycol Diacrylate (PEGDA) - Based 3D Printed Monolith Structure of Enhanced Multifunctional Properties for Water Application in 24th Polish Conference of Chemical and Process Engineering, 13 – 16 June 2023, Hotel Radisson Blu, Szczecin, Poland.

4. **Nurul Husna Mohd Yusoff**, Chien Hwa Chong, Voon - Loong Wong, Kean How Cheah, Yoke Kin Wan, 2023. Comparison of different drying techniques on silane - grafted chitosan of 3D-printed PEGDA monolithic structure in 20th Asia Pacific Confederation of Chemical Engineering (APCChE) Congress, 4 – 9 September 2023, SMX Convention Center Manila, Pasay City, Philippines, Paper no. 395.

LIST OF AWARDS

1. Vice-Chancellor's Medal (Research Team) University of Nottingham 2023.
2. Best Presenter Award, 24th Polish Conference of Chemical and Process Engineering 2023.
3. Best Paper Award, International Conference on Sustainable Development of Water and Environment 2023.
4. Gold Medal, International Virtual Expo of Innovation Product and System Design 2023.
5. Gold Medal, Malaysia Invention and Innovation Expo (MIIX) 2023.
6. Gold Medal Award and Best Video Winner (Category: Higher Institution - Science, Engineering & Technology), International Invention & Innovative Competition (INIIC) 2022 Award.

7. Gold Medal Award, International Conference and Exposition on Inventions by Institutions of Higher Learning (PECIPTA) 2022.
8. Diamond and Gold awards, 3rd Virtual Innovation Competition 2022 (VIC22).
9. Gold Medal Award, ASIA International Innovation Exhibition 2022.

TABLE OF CONTENTS

ABSTRACT i

LIST OF PUBLICATIONS vii

LIST OF CONFERENCE PAPER ix

CONFERENCE PRESENTATION ix

LIST OF AWARDS x

TABLE OF CONTENTS xii

LIST OF FIGURES xxiii

LIST OF TABLES xxx

LIST OF ABBREVIATIONS xxxiv

CHAPTER 1: INTRODUCTION 1

1.1 Research Background 1

1.2 Problem Statement 3

1.3 Research Questions 5

1.4 Research Objectives 6

1.5 Research Scope 6

1.6 Research Hypothesis 9

1.7 Risk Assessment 10

1.8 Outline of thesis 12

CHAPTER 2: LITERATURE REVIEW 15

2.1 Presence of dye in textile wastewater 15

2.2 Current technology for treating dye effluent 16

2.3 Introduction to 3D-printed adsorbent 17

2.4 Performance optimisation strategies and recent advances of dye removal using 3D-printed enhanced adsorbent 19
2.4.1 3D Printing route consideration 19
2.4.2 Material consideration 25
2.4.2.1 Polymer 26
2.4.2.2 Bio-based materials 28
2.4.3 Application of surface functionalisation in 3D-printed enhanced adsorbent 36
2.4.3.1 Surface grafting 43
2.4.3.2 Electron beam treatment 45
2.5 Recent advances of scientific and innovative functionalised 3D-printed enhanced adsorbent for dye removal 52
2.6 Current challenges of the application of functionalised 3D-printed enhanced adsorbent for dye removal 63
2.7 Deep learning for colour prediction of textile wastewater using real-time images 66
CHAPTER 3: 3D - PRINTED PEGDA MONOLITH WITH ROBUST SILANE - GRAFTED CHITOSAN FOR ENHANCED TEXTILE WASTEWATER TREATMENT 69
ABSTRACT 70
3.1 Introduction 71
3.2 Materials and methods 75
3.2.1 Materials 75
3.2.2 Fabrication of 3D-printed monolith 75

3.2.3 Synthesis of silane - grafted chitosan of 3D-printed monolith adsorbent 77
3.2.4 Characterisation study 79
3.2.4.1 FESEM – EDX 79
3.2.4.2 FTIR Analysis 80
3.2.4.3 XPS 80
3.2.4.4 XRD 80
3.2.5 Mechanical properties 81
3.2.6 Adsorption and desorption studies 81
3.2.7 Degradation study 83
3.2.8 Experimental design and response analysis 83
3.2.9 BOD and COD analysis 86
3.2.10 Adsorption Isotherm Modelling 87
3.2.10.1 Langmuir Isotherm 88
3.2.10.2 Freundlich Isotherm 88
3.2.10.3 Temkin Isotherm 89
3.2.10.4 Dubinin - Radushkevich (D - R) Isotherm 89
3.2.10.5 Harkins - Jura (H - J) Isotherm 90
3.2.10.6 Redlich - Peterson (R - P) Isotherm 90
3.2.11 Adsorption Kinetics 90
3.2.12 Thermodynamic modelling 92
3.3 Results And Discussion 92
3.3.1 Characterisation of samples 92

3.3.1.1 FESEM and EDX Analysis 92
3.3.1.2 XPS 96
3.3.1.3 FTIR 98
3.3.1.4 XRD 99
3.3.2 Mechanical properties 101
3.3.3 Optimisation Analysis of Batch Adsorption Studies 102
3.3.3.1 Effects of concentration, dipping time, pH and temperature on removal efficiency (R%) and uptake capacity, K(mg/g) 102
3.3.4 Analysis of Variance (ANOVA) Results 109
3.3.5 Confirmation of Experiment 110
3.3.6 Influence of initial MO dye concentration on adsorption efficiency 113
3.3.7 Degradation Study 114
3.3.8 Adsorption Isotherm Modelling 115
3.3.9 Adsorption Kinetics Studies 118
3.3.10 Thermodynamics studies 121
3.3.11 BOD and COD analysis 123
3.3.12 Desorption and Recyclability 124
3.3.13 Adsorption Mechanism of MO dye 125
3.3.14 Comparison with other chitosan-based adsorption system 126
3.4 Conclusion 130
CHAPTER 4: THE INFLUENCE OF STRUCTURAL TOPOLOGY OF ADDITIVELY MANUFACTURED PEGDA MONOLITH ON ADSORPTION PERFORMANCE FOR TEXTILE WASTEWATER TREATMENT 132

ABSTRACT 133

4.1 Introduction 134

4.2 Experimental 140

4.2.1 Materials 140

4.2.2 Design of structural architecture and manufacturing 141

4.2.2.1 3D printing formulations and printer settings 141

4.2.2.2 Details of different structural configuration of monolithic structures 142

4.2.3 Preparation of silane-chitosan grafted monolith 144

4.2.4 Characterisation methods 145

4.2.4.1 FESEM Analysis 145

4.2.4.2 FTIR spectroscopy 146

4.2.4.3 Mechanical properties study 146

4.2.4.4 Permeability analysis 146

4.2.4.5 Batch adsorption performance evaluation 147

4.2.4.6 Colour and COD removal analysis 148

4.2.4.7 Mechanical stability study 149

4.3 Results and discussion 150

4.3.1 Characterisation samples 150

4.3.1.1 FESEM and EDX analysis 150

4.3.1.2 FTIR analysis 152

4.3.2 Mechanical properties 157

4.3.3 Removal efficiency of MO dye via adsorption 159

4.3.3.1 Specific surface area of monolithic structure..... 160

4.3.3.2 Permeability of monolithic structure 161

4.3.4 COD and colour removal efficiency using textile wastewater..... 163

4.3.5 Mechanical stability 165

4.3.6 Comparison with other chitosan - based monolithic system 166

4.4 Conclusion 167

CHAPTER 5: COMPARISON OF DIFFERENT DRYING TECHNIQUES ON SILANE - GRAFTED CHITOSAN OF 3D-PRINTED PEGDA MONOLITHIC STRUCTURE AND ITS EFFECT ON ADSORPTION PERFORMANCE FOR ANIONIC DYE REMOVAL 170

ABSTRACT 171

5.1 Introduction 172

5.2 Materials and methods 177

5.2.1 Materials 177

5.2.2 Sample preparation of silane-grafted chitosan of 3D-printed monolith 178

5.2.2.1 Preparation of resin formulations and 3D printer settings..... 178

5.2.2.2 Surface functionalisation with silane-grafted chitosan on 3D-printed monolith via epoxide amine reaction and the use of different drying methods 179

5.2.3 Characterisation studies..... 181

5.2.3.1 Field emission scanning electron microscopy (FESEM) analysis 181

5.2.3.2 Fourier transform infrared (FTIR) spectroscopy. 181

5.2.3.3 X-ray diffraction (XRD) analysis 181
5.2.4 Energy consumption in all drying methods 182
5.2.5 Moisture content analysis 182
5.2.6 Batch adsorption - desorption studies 183
5.3 Results and discussion 184
5.3.1 Characterisation study 184
5.3.2 Energy consumption and moisture content analysis 191
5.3.3 Adsorption and desorption studies 192
5.4 Conclusion 197
CHAPTER 6: ENHANCING MULTIFUNCTIONAL PROPERTIES OF A BIOCOMPATIBLE PEGDA-BASED 3D PRINTED MONOLITH STRUCTURE FOR WATER APPLICATIONS 199
ABSTRACT 200
6.1 Introduction 201
6.2 Materials and methods 207
6.2.1 Materials 207
6.2.2 Formulation and preparation of photocurable resin 207
6.2.3 3D printing of monolith structure 209
6.2.4 Surface functionalisation via silane coupling agent. 210
6.2.4.1 Surface grafting with (3-Glycidyloxypropyl) trimethoxy silane 210
6.2.4.2 Surface grafting with hybrid silanization strategy 210
6.2.5 Characterisation study 211
6.2.5.1 FESEM analysis 211

6.2.5.2 X-ray photoelectron spectroscopy (XPS) 212

6.2.5.3 X-ray diffraction analysis (XRD) 212

6.2.5.4 Thermogravimetric and differential scanning calorimetric analysis (TGA – DSC) 212

6.2.5.5 Texture Analyser 213

6.2.5.6 Dynamic Mechanical Thermal analysis (DMTA) 213

6.2.6 Moisture absorption analysis in distilled water and dried state .. 213

6.2.7 Surface contact angle analysis 215

6.2.8 Mechanical and chemical stability of the grafted surface 216

6.3 Results and discussion 216

6.3.1 Photopolymerisation reaction in the formulated PEGDA-based resins 216

6.3.2 Surface functionalised 3D-printed monolith structure 218

6.3.3 Improvement in thermo-mechanical properties 223

6.3.3.1 Thermal properties 223

6.3.4 Mechanical properties 227

From the experimental results, it can be concluded that the addition of 3wt.% of HDDA has enhanced the mechanical properties significantly as compared to other resin formulations. Thus, 3D-printed monolith using PEGDA/HDDA3 formulation was surface functionalised, and its mechanical properties was evaluated again. As shown in 229

6.3.5 Viscoelastic analysis 230

The viscoelastic properties and morphologies of all samples can be obtained from the dynamic mechanical thermal analysis as presented in 230

6.3.6 Enhancement in surface properties 231

6.3.6.1 Resistance to moisture absorption 231

6.3.6.2 Surface wettability and its stability 236

6.3.7 Comparison with other studies 238

6.4 Conclusion 240

CHAPTER 7: EFFECT OF ELECTRON BEAM IRRADIATION ON SILANE - GRAFTED NANOCHITOSAN OF 3D - PRINTED MONOLITH ADSORBENT FOR COLOUR REMOVAL IN TEXTILE WASTEWATER TREATMENT 243

ABSTRACT 244

7.1 Introduction 245

7.2 Experimental 250

7.2.1 Materials 250

7.2.2 3D-printed monolithic structure fabrication 251

7.2.3 Synthesis of nanochitosan 251

7.2.4 Surface functionalisation of silane - grafted nanochitosan and irradiation process 252

7.2.5 Characterisation analysis 253

7.2.6 Batch adsorption studies 254

7.2.7 Mechanical properties and stability 255

7.3 Result and discussion 256

7.3.1 Characterisation 256

7.3.2 Adsorption studies 264

7.3.3 Mechanical strength and stability 267

7.4 Conclusion 270

CHAPTER 8: IDENTIFICATION AND CLASSIFICATION OF COLOUR PREDICTIONS OF TEXTILE WASTEWATER USING CONVOLUTIONAL NEURAL NETWORK AND ALEXNET 272

ABSTRACT 273

8.1 Introduction 274

8.2 Methodology 278

8.2.1 Fabrication of silane – grafted nanchitosan of 3D-printed monolith 278

8.2.2 Sample collection and treatment 278

8.2.3 Operating parameter analysis 278

8.2.4 Data acquisition 279

8.2.5 Image Normalisation 280

8.2.6 Image labelling 280

8.2.7 Network architecture 281

8.2.7.1 Convolutional Neural Network (CNN) 281

8.2.7.2 AlexNet 285

8.3 Result and Discussion 287

8.3.1 Performance of the trained network 287

8.3.2 Application of trained network 290

8.4 Conclusion 292

CHAPTER 9: CONCLUSION AND FUTURE WORK 293

9.1 Conclusion 293

9.2 Future work 301

REFERENCES 303

APPENDICES 365

Supplementary information- Section 3.2.8 RSM DOE Approach 365

Supplementary Information – Section 3.3.1.1 FESEM and EDX Analysis ... 365

Supplementary Information – Section 3.3.3 Response Optimiser Plots for removal efficiency (R%) and uptake capacity, K (mg/g) 366

Supplementary Information – Section 3.3.4 ANOVA Results 367

Supplementary Information – Section 3.3.5 Confirmation of experiment 368

Supplementary Information – Section 3.3.10 Thermodynamic parameters for MO dye removal at different temperatures 369

Supplementary information- Section 6.3.2.1 DSC Analysis 370

Supplementary information- Section 6.3.2.2 TGA Analysis 371

LIST OF FIGURES

Figure 1.1.1: Common process for textile wastewater treatment plant(Pang and Abdullah, 2013). 2

Figure 1.8.1: Outline of thesis. 14

Figure 2.3.1: Publication trends in 2011 – 2022, (a) Water treatment and 3D printing (Web of Science, 2022a); (b) Water treatment, 3D printing and surface functionalisation (Web of Science, 2022b). 18

Figure 2.4.1: Schematic diagram of AM technologies, (a) Powder bed fusion(Tan *et al.*, 2016b); (b) Binder jetting (Zhang *et al.*, 2021b); (c) Directed energy deposition (Hu *et al.*, 2018); (d) Material jetting (Liu, Song and Huang, 2020); (e) Material extrusion (Srinivasan *et al.*, 2020); (f) Sheet lamination (Ahn *et al.*, 2012); and (g) Vat photopolymerisation (Cai *et al.*, 2020)..... 25

Figure 2.4.2: Versatile strategy in functionalised 3D printing (Jiang *et al.*, 2020). 36

Figure 2.4.3: Techniques in surface functionalisation on 3D printing. (a) Dip-coating (Jin *et al.*, 2021); (b) Atomic layer deposition (Grillo *et al.*, 2018); (c) Spin-coating (Huang *et al.*, 2019); (d) Thermal coating (Kumru *et al.*, 2019); (e) Plasma etching (Rosso *et al.*, 2011); (f) Electronic beam etching (Riveiro *et al.*, 2018); (g) Wet chemical etching (Zhang *et al.*, 2020); (h) Silane treatment (Tan *et al.*, 2016a); (i) Hydrogel coating (Gao *et al.*, 2016); (j) Plasma etching (Rosso *et al.*, 2011); (k) Electronic beam etching (Riveiro *et al.*, 2018); and (l) Wet chemical etching (Zhang *et al.*, 2020). 42

Figure 2.5.1: Schematic of 3D printing method selection and post 3D printing treatment for different type of materials..... 53

Figure 2.5.2: Schematic of 3D printing method for functional materials..... 54

Figure 2.5.3: Application of various 3D-printed device for dye removal. (a) SEM images of various numbers of layers of MOFs coating; (b) Plot of removal

efficiency of MG from water; (c) SEM images of regeneration of PLA skeleton; and (d) Plot of regeneration efficiency after 5 cycles. 56
Figure 2.6.1: Future look of surface functionalised 3D printing technology for wastewater treatment applications. 63
Figure 3.2.1: Illustration presentation of new grafted - chitosan monolith adsorbent. 78
Figure 3.2.2: PEG200DA cross-linking reaction with Irgacure 819 under UV exposure..... 79
Figure 3.2.3: Surface grafting mechanism of grafted - chitosan PEGDA monolith. 79
Figure 3.3.1: SEM image of 3D-printed monolith;(a)(i) view of square -shaped 3D-printed monolithic structure, (a)(ii) enlarged segment of monolith struts before surface grafting process, (b) surface morphology of 3D-printed monolith after grafting; (i)view from 600 magnification and (ii) view from 3000 magnification with wrinkled layers. 93
Figure 3.3.2: SEM - EDX Analysis; (a) pure PEGDA monolith, (b) grafted - chitosan PEGDA monolith; (i) before adsorption, (ii) after adsorption. 95
Figure 3.3.3: (a) - (b) Wide-scan XPS spectra of grafted - chitosan PEGDA monolith structure. (c) High resolution of spectra of original 3D-printed PEGDA monolith of C 1s core-level for C-C/C-H; (d) High resolution spectra of grafted - chitosan on the monolith of O 1s core-level. Representative of high - resolution spectra of GPTMS structure produced by silane - cross-linked chitosan; (e) Si 2p core-level and (f) C 1s Core level for Si-C. 96
Figure 3.3.4: FTIR spectra of PEGDA monolithic structure with and without silane cross-linked chitosan. 98
Figure 3.3.5: XRD pattern for; (a) pure chitosan and PEGDA monolith;(b) with grafted chitosan and (c) without grafted chitosan. 100

Figure 3.3.6: Main effects plot for; (a) removal efficiency (R%) and (b) Uptake capacity, K (mg/g)..... 103

Figure 3.3.7: (a) Plot of removal efficiency (R%) and (b) Uptake capacity, K (mg/g) at optimal condition (C_o= 2 wt.%, dipping time = 45 min, pH = 6.3, temperature = 60℃) agitated in incubator shaker at 150 rpm for 2 h..... 113

Figure 3.3.8: Plot of Initial concentration of MO dye (ppm) in; (a) Removal efficiency (R%) and (b) Uptake capacity, K (mg/g) at optimal condition (Co= 2 wt.%, dipping time = 45 min, pH = 6.3, temperature = 60℃) agitated in incubator shaker at 150 rpm for 2 h..... 114

Figure 3.3.9: Adsorption isotherm model plots for adsorption of MO dye by grafted chitosan monolith; (a) Langmuir Isotherm, (b) Freundlich Isotherm, (c) Temkin Isotherm, (d) Dubinin - Radushkevich Isotherm, (e) Harkins-Jura Isotherm and (f) Redlich- Peterson Isotherm..... 117

Figure 3.3.10: Plot of adsorption kinetic studies; (a) Pseudo-first order; (b) Pseudo-second order; (c) Intra-particle diffusion model; (d) Bangham kinetic model; and (e) Elovich kinetic model. 121

Figure 3.3.11: BOD and COD analysis; (a) Reduction in mg/L and (b) Percentage of reduction (%). 124

Figure 3.3.12: (a) Desorption capacity of NaOH with respect to MO dye solution. (b) Reusability profile of the grafted - chitosan monolith after 4 consecutive cycles. (Inset: Visual outlook of grafted - chitosan monolith;(i) after MO dye adsorption and (ii) after recyclability test). 125

Figure 3.3.13: Adsorption mechanism of MO dye onto chitosan grafted PEGDA monolith..... 126

Figure 4.2.1: Synthesis of grafted 3D-printed PEGDA monolith with silane-crosslinked chitosan. 142

Figure 4.2.2: 3D-printed monolithic structure of different structural configuration. (a) Gyroid; (b) Fischer; (c) Kagome and (d) Body centred cubic lattice. 144

Figure 4.2.3: Silane-chitosan grafted monolithic structure of different structural configuration. (a) Gyroid; (b) Fischer; (c) Kagome and (d) Body centred cubic lattice. 145
Figure 4.3.1: FESEM images of grafted – chitosan PEGDA monolith of different structural topologies of monolith from front, top and cross-section view at different magnifications. (a) Gyroid structure; (b) Fischer Koch S structure; (c) Flat Kagome structure; and (d) Body centred cubic structure. 151
Figure 4.3.2: (a) FTIR spectra of pure 3D-printed PEGDA before grafting and grafted 3D-printed PEGDA of different monolithic structural designs before adsorption and (b) FTIR spectra of grafted 3D-printed PEGDA monolith after adsorption for body centred cubic design. 156
Figure 4.3.3: Schematic illustration of adsorption mechanism of MO dye with grafted 3D-printed PEGDA monolith. (a) Electrostatic attractions, (b) Yoshida H-bonding, (c) n-π interactions and (d) Dipole-dipole hydrogen bonding. 157
Figure 4.3.4: (a) Plot of removal efficiency of MO dye (%) and (b) Maximum uptake capacity of MO dye (mg/g) at optimum conditions (pH = 6.3, Temperature = 60℃) agitated for 2 h in incubator shaker at 150 rpm. 159
Figure 4.3.5: Percentage removal of (a) colour and (b) COD of real textile wastewater at optimum condition. 165
Figure 5.2.1: Schematic diagram of sample preparation of silane-grafted chitosan on 3D-printed monolith with different drying techniques. 180
Figure 5.3.1: SEM images of (a) Blank PEGDA monolith with enlarged segment of monolith struts; (b) ODC silane-grafted monolith;(c) VDC silane-grafted monolith and (d) FDC silane-grafted monolith. 187
Figure 5.3.2: (a) FTIR spectra for different drying methods; (b) FTIR spectra of photocured PEGDA resin, ODC silane-grafted monolith before and after adsorption; and (c) XRD spectra of (i) pure chitosan; (ii) ODC silane-grafted

monolith, (iii) VDC silane-grafted monolith and (iv) FDC silane-grafted monolith. 190

Figure 5.3.3: Plot of (a) Removal efficiency (%) and (b) Uptake capacity, K (mg/g) of different drying methods at optimal conditions (pH = 6.3, temperature = 60 ℃) agitated in incubator shaker at 150 rpm for 2 h and (c) Recyclability efficiency of different drying methods for 5 cycles. 196

Figure 5.3.4: Possible adsorption mechanism between chitosan and methyl orange (MO) dye. 197

Figure 6.2.1: Schematic diagram of; (a) Preparation of resin formulations; (b) 3D printing process and (c) Final printing part of the 3D-printed monolith. .. 209

Figure 6.2.2: Schematic of the surface functionalisation process via surface-grafted silanization. The structures of the silane agent used are known..... 211

Figure 6.3.1: Illustration of photopolymerisation of PEGDA200 with Irgacure 819 and comonomer under UV exposure. 217

Figure 6.3.2**:** (a) FESEM images and (b) FTIR analysis of pure PEGDA and silane - grafted 3D-printed monolith. 218

Figure 6.3.3: (a) XPS spectra wide scan of 3D-printed PEGDA monolith before and after silane grafting; High resolution spectra of;(b) C1s of 3D-printed PEGDA monolith; (c) O1s of 3D-printed PEGDA monolith; and (d) Si2p of silane grafted monolith. 222

Figure 6.3.4: XRD pattern for (a) different resin formulation for 3D-printed monolith and (b) 3D-printed PEGDA monolith with and without grafted silane. 223

Figure 6.3.5**:** (a) DSC and (b) TGA results of pure 3D-printed PEGDA monolith, surface grafting with GLYMO and hybrid silane (GLYMO-APTMS). 224

Figure 6.3.6**:** Stress-strain curve of PEGDA with and without silane grafted. 228

Figure 6.3.7**:** Experimental moisture absorption-desorption data of the samples before and after surface grafted with different silane coupling agents. Moisture absorption rate curve of all samples and fitted curve of moisture absorption rate curve of; (b) 3D-printed PEGDA, (c) Silane functionalised with GLYMO and (d) Silane functionalised with GLYMO-APTMS..... 233

Figure 6.3.8: Water contact angle measurements; (a) 3D-printed PEGDA monolith before surface grafting; (b) Grafted with GLYMO and (c) Grafted with hybrid silane agent GLYMO – APTMS. Water contact angle (WCA) measurements of; (a) Ultrasonication time and (b) after 24 h immersion in three different solvents. 237

Figure 7.2.1: Schematic diagram preparation of electron beam assisted silane – grafted nanochitosan of 3D-printed monolith..... 253

Figure 7.3.1: FESEM of the grafted-nanochitosan 3D-printed PEGDA monolith;(a) before EB treatment; after EB treatment at (b) 50cGy; (c) 100cGy and (d) 200cGy. 257

Figure 7.3.2: AFM images in 2D and 3D view of; (a,f) 3D-printed PEGDA, (b,g) silane-grafted nanochitosan before EB treatment, silane-grafted nanochitosan at (c,h) 50cGy, (d,i) 100 cGy and (e,j) 200 cGy. 259

Figure 7.3.3: (a) FTIR spectra of photocured PEGDA resin, grafted-nanochitosan before and after EB treatment, and grafted-nanochitosan after adsorption. (b) XRD spectra of nanochitosan..... 261

Figure 7.3.4: (a - b) High-resolution XPS spectra peak for C1s in PEGDA monolith, (c - d) Si-C and Si2p high-resolution spectra peaks for GLYMO after surface grafting and (d - e) High resolution spectra for O1s and N1s produced by nanochitosan coated substrate. 263

Figure 7.3.5: (a) Removal efficiency rate and (b) Adsorption capacity of silane - grafted nanochitosan for different dosage of electron beam treatment..... 265

Figure 8.2.1: Schematic diagram of: (a) Synthesis of silane - grafted nanochitosan of 3D-printed monolith, (b) Adsorption performance of 3D printed monolith and (c) Data collection of water samples. 280
Figure 8.2.2: Schematic diagram of CNN architecture. 282
Figure 8.2.3: Transfer learning architecture of AlexNet. 287
Figure 8.3.1: Training and validation accuracy plots of Case I for (a) CNN and (b) AlexNet. 289
Figure 8.3.2: Original images of textile wastewater. 291
Figure 9.1.1:Summary of the design of silane -grafted chitosan of 3D-printed monolith. 299

LIST OF TABLES

Table 1.7.1: Risk Assessment of research work. 10

Table 2.3.1: Publication extraction based on relevant keywords (Web of Science, 2022)..... 18

Table 2.4.1: Printing parameters for common printing techniques for 3D printing technologies.(Stwora and Skrabalak, 2013; Kitsakis *et al.*, 2015; Tan *et al.*, 2016b; Ferreira *et al.*, 2017). 31

Table 2.4.2: Material parameters and impacts towards additive manufacturing process (Tan, Zhu and Zhou, 2020)..... 35

Table 2.4.3: Advantages and disadvantages of different strategy in functionalised 3D printing..... 41

Table 2.4.4: Overview of various surface functionalisation method in 3D printing for wastewater application. 48

Table 2.5.1: Summary of recent advancements in 3D printing for water treatment. 57

Table 3.2.1: 3D printing process parameters. 77

Table 3.2.2: Level of four different factors. 85

Table 3.2.3: 3-level Box-Behnken design (BBD) with 4 factors and comparison of experimental and predicted results for each set of experiment..... 85

Table 3.3.1: Mechanical properties of 3D printed PEGDA monolith before and after grafting with silane-crosslinked chitosan. 101

Table 3.3.2: Comparison data of experimental and predicted results. 111

Table 3.3.3: Retention weight of grafted chitosan monolith before and after MO dye adsorption. 115

Table 3.3.4: Different Isotherm linear forms and parameters for MO dye solution adsorption..... 118

Table 3.3.5: Different kinetic modelling and parameters for MO dye solution adsorption. 120
Table 3.3.6: Thermodynamic parameters of adsorption of MO dye on 3D-printed chitosan-grafted monolith at different temperature. 123
Table 3.3.7: Comparison of the adsorption properties for MO dye adsorption onto different chitosan-based adsorbents. 128
Table 3.3.8: Comparison of the adsorption properties for COD and BOD removal onto different chitosan-based adsorbents. 129
Table 4.2.1: Parameters of 3D printing. 142
Table 4.2.2: Details of detailed design. 143
Table 4.2.3: Mass of different structural topologies before and after grafting procedure. 145
Table 4.2.4: Characteristics of textile wastewater sample collected from the industry. 149
Table 4.3.1: EDX analysis of elemental weight composition of pure PEGDA monolith and silane-crosslinked chitosan samples before and after adsorption. 152
Table 4.3.2: Mechanical properties of 3D printed PEGDA monolithic structured with different structural topologies. 158
Table 4.3.3: Permeability measurement of different structural topologies ... 163
Table 4.3.4: Weight of all structural design before and after MO dye adsorption. 166
Table 4.3.5: Comparison of the adsorption properties for MO dye adsorption onto different chitosan-based monolithic system. 167
Table 5.3.1: Energy consumption, and moisture content of silane-grafted chitosan monolith of different drying methods. 192
Table 6.2.1: Composition of the different chemicals used in the formulation of resins. 208

Table 6.3.1**:** EDX analysis of pure PEGDA monolithic structure before and after silane grafted. 218

Table 6.3.2**:** DSC and TGA data for pure 3D-printed PEGDA monolith, surface grafting with GLYMO and hybrid silane (GLYMO-APTMS). 224

Table 6.3.3**:** Mechanical properties of different resin formulations and surface grafted with GLYMO and hybrid silane coupling agent GLYMO-APTMS for 3D-printed monolithic structure. 228

Table 6.3.4: Dynamic mechanical thermal analysis data of different resin formulations and surface grafted with GLYMO and hybrid silane coupling agent GLYMO-APTMS. 230

Table 6.3.5: Values of initial slope of the water absorption curve and diffusion coefficient for each of the samples..... 236

Table 6.3.6**:** Comparison of the mechanical properties of the materials for 3D printing and conventional method in water application. 239

Table 7.2.1: 3D printing specifications for the monolithic structure design. . 251

Table 7.3.1: Elemental weight composition of 3D-printed PEGDA monolith before and after adsorption from EDX analysis. 258

Table 7.3.2: Root mean squared roughness and arithmetic roughness of 3D printed samples. 259

Table 7.3.3: Degree of deacetylation of different dosages electron beam irradiation..... 266

Table 7.3.4: Mechanical properties of silane-grafted nanochitosan before and after EB treatment..... 269

Table 7.3.5: The retention weight of grafted-nanochitosan monoliths before and after MO dye adsorption for different EB dose. 269

Table 8.2.1:The architecture of CNN. 282

Table 8.2.2: The architecture of AlexNet. 286

Table 8.3.1: Classification accuracy and cross-entropy loss for each epoch of training and validation for all cases. 289

Table 8.3.2: Percentage of classification accuracy for each image. 291

Table A0.1: Results of ANOVA for removal efficiency (R%). 367

Table A0.2: Results of ANOVA for uptake capacity, K (mg/g). 367

Table A0.1: Experimental setup with different conditions. 368

LIST OF ABBREVIATIONS

Abbreviations

AM	Additive manufacturing
3D	Three dimensional
PBF	Powder Bed Fusion
SLM	Selective laser melting
SLS	Selective laser sintering
EBM	Electron Beam Melting
DMLS	Direct Metal Laser Sintering
BJ	Binder Jetting
MIM	Metal Injection Mold
DED	Directed Energy Deposition
MJ	Material Jetting
ME	Material Extrusion
FDM	Fused Deposition Modelling
SL	Sheet Lamination
LOM	Laminated Object Manufacture
UAM	Ultrasonic Additive Manufacturing
UC	Ultrasonic Consolidation
PSL	Plastic Sheet Lamination
VP	Vat Photopolymerisation
DLP	Digital Light Processing
LCD	Liquid Crystal Display
SLA	Stereolithography
PJM	PolyJet Matrix

UV	Ultraviolet
PC	polycarbonate
ABS	Acrylonitrile butadiene styrene
PEEK	Poly ether ester ketone
PVDF	Polyvinylidene fluoride
PLA	Polylactic acid
PU	Polyurethane
TMC	Polytriethylene carbonate
PF	Polypropylene fumarate
CS	Chitosan
$-NH_2$	Amine
-OH	Hydroxide
Cu	Copper
IPA	Isopropyl alcohol
HCl	Hydrochloric acid
NaOH	Sodium hydroxide
PEGDA	Poly (ethylene glycol) diacrylate
GLYMO/GPTMS	Glycidyloxypropyl trimethoxysilane
APTMS	(3-aminopropyl) trimethoxysilane
COD	Chemical Oxygen Demand
BOD	Biochemical Oxygen Demand
MO	Methyl orange
HDDA	1,6-Hexanediol diacrylate
BDDA	1,4-Butanediol diacrylate
FESEM	Field Emission Scanning Electron Microscopy

EDX	Energy Dispersive X-Ray
FTIR	Fourier-Transform Infrared Spectroscopy
XPS	X-Ray Photoelectron Spectroscopy
XRD	X-Ray Diffraction Analysis
AFM	Atomic Force Microscopy
TGA	Thermogravimetric Analysis
DSC	Differential Scanning Calorimetry
DMA	Dynamic Mechanical Analysis
UV-Vis	Ultraviolet-visible
TX-XT	Texture analyser
ASTM	American Society for Testing and Materials
ANN	Artificial Neural Network
RSM	Response Surface Methodology
DOE	Design Of Experimental
BBD	Box-Behnken Design
CCD	Composite Central Design
ANOVA	Analysis of Variance
CNN	Convolutional Neural Network
RBF-ANN	Radial Basis Function Neural networks
ANFIS	Adaptive Neural-Fuzzy Inference System
MLP-ANN	Multi-Layer Perceptron Neural Networks
IoT	Internet of Things

Parameters

$R\%$	Percentage of dye removal
K	Equilibrium of uptake capacity by silane - grafted chitosan monolith (mg/g)
C_o	The initial concentration of dye solution (mg/L)
C_t	Concentration of dye solution at t time (mg/L)
V	Volume of dye solution (L)
m	Mass of silane - grafted chitosan PEGDA monolith (g)
E'	Storage modulus
C_2	Concentration of MO dye in NaOH solution(mg/L)
C_1	Final concentration of MO dye (mg/L)
V_2	volume of NaOH solution (L)
τ	Desorption ratio
W_i	Initial weights (g) of sample after adsorption-desorption procedure
W_d	Dried weights (g) of sample after adsorption-desorption procedure
Co	Concentration of chitosan
q_e	Equilibrium amount of adsorbed dye on the adsorbent
C_e	Equilibrium concentration of dye in the solution
q_m	Maximum adsorption capacity (mg/g)
K_L	Langmuir Isotherm constant

K_f	Freundlich constant
$\frac{1}{n}$	Adsorption intensity
R	Gas constant (0.008314 kj/molk)
T	Absolute temperature (K)
$\frac{1}{b_T}$	Temkin constant (heat of sorption (kJ/mol) indicating the potential of adsorption (intensity)
K_t	Temkin constant for adsorption capacity (L/g)
q_{DR}	theoretical saturation capacity (mol/g)
K_{DR}	D - R constant related to the adsorption mean free energy (mol^2J^{-2})
ε	Dimensionless constant (polyani potential)
β	Exponent between 0 to 1
k_1	Rate constant of pseudo-first order
k_2	Pseudo-second order
k_{id}	Rate constant of intra-particle diffusion model
K_0	Bangham kinetic model
K_c	Equilibrium adsorption constant
$\Delta H°$	Standard enthalpy (kj mol^{-1})
$\Delta S°$	Standard entropy (kj mol^{-1})
$\Delta G°$	Standard free energy change (kj mol^{-1}).
v	Inlet velocity
μ	Fluid viscosity which in this case is water ($1.0016\ mPa.s$)

L	Size of unit cell of the monolith
ΔP	Pressure drop under same boundary conditions
P_o	Initial colour value of raw wastewater (Pt Co)
P_t	Colour value of treated wastewater (Pt Co)
D_i	Initial dissolved O_2 concentration (mg/L)
D_f	Final dissolved O_2 concentration (mg/L)
P	Dilution factor of wastewater
A_i	Initial COD concentration (mg/L)
A_f	COD concentration after the adsorption process (mg/L)
E_t	Total energy consumption for each dryer (kW)
E_S	Specific energy consumption for each dryer (kW)
M_w	Initial weight of wet sample (g)
M_d	Weight of dry sample (g)
M_s	Weight sample (g)
$m(t)$	Mass of the total mass of resin with moisture
m_{dried}	Mass of the resin after drying
m_h	Mass of the humidified sample
G'	Storage modulus
tan δ	Tangent delta
T_g	Glass transition temperature
θ	Contact angle
k_w	Width of convolution kernel

k_h	Height of convolution kernel
k_n	Number of convolution kernel
Ch_s	Number of input data of channels

CHAPTER 1: INTRODUCTION

1.1 Research Background

Textile factories generate enormous amounts of highly coloured wastewater carrying a varied spectrum of persistent pollutants. The wastewater, which contains dye, poses a significant threat to the environment, as it not only adversely affects the well-being of humans but also serves as a major pollutant. Every year, over 7×10^7 tons of synthetic dyes are manufactured worldwide, with over 10,000 tons of such dyes used by the textile industry (Chandanshive *et al.*, 2020). The presence of colouring chemicals can impede the transmission of light in water, thereby hindering the ability of aquatic plants to carry out photosynthesis successfully. The current physico-chemical techniques such as flocculation, oxidation process, adsorption, coagulation, membrane processes, ozonation, reverse osmosis, and chemical oxidation, have demonstrated effectiveness in treating the colour. The incorporation of a colour treatment unit operation is an essential aspect of the design for a textile wastewater treatment facility. This colour treatment stage serves as a final polishing step as shown in Figure 1.1.1 are employed to meet the global regulations and laws to mitigate environmental consequences as well as to comply with certain standards for the water to be reused. At this polishing step, one of the treatments that is effective to treat the dye is adsorption process.

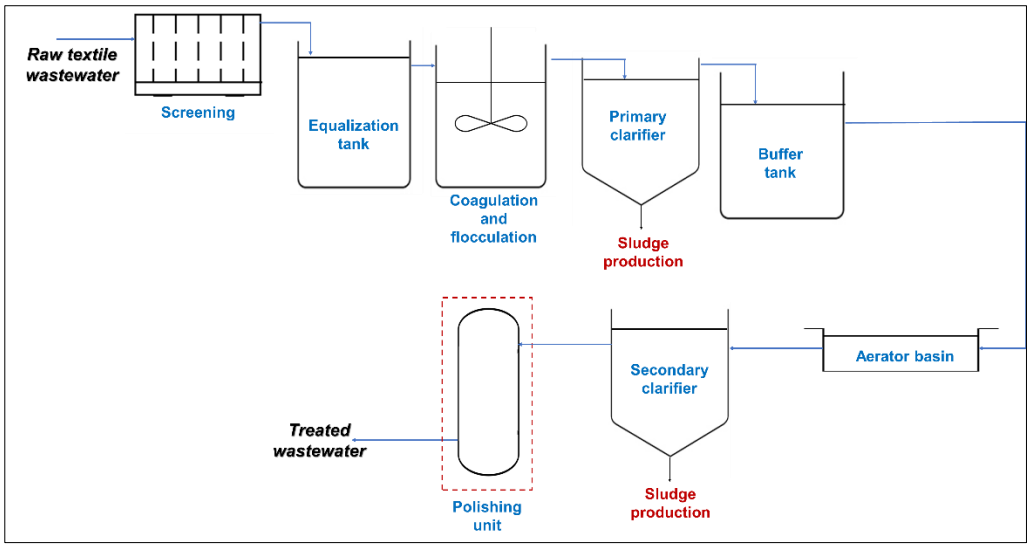


Figure 1.1.1: Common process for textile wastewater treatment plant(Pang and Abdullah, 2013).

Adsorption process is attractive methodology in textile wastewater treatment specifically due to the low cost and absence of a preliminary treatment stage for the adsorbent prior to implementation, as well as the simplicity of its regeneration. The method is also a straightforward approach that is relatively unaffected by the issue of producing undesired byproducts and achieves a satisfactory level of dye removal. The effectiveness of the adsorption process is mostly dependent on the physical and chemical properties of the adsorbents such as pore size, fast kinetics, mechanical stability and compatibility and ease of regeneration. Despite the challenges linked to the disposal of adsorbents and the occurrence of post-contamination when employing them, the challenges can be overcome by modifying the ordinary form of the adsorbent that is commonly in the form of flakes, beads and spherical pellets into adsorbent film.

Adsorbent film is a revolutionary method in the field of adsorption. This method entails restructuring and converting typical adsorbent materials

into a liquid form, which is then graft as a layer onto a substrate. The adsorbent film simplifies the synthesis process and enables for variable application in a variety of settings by changing the standard concept of adsorption. This novel approach seeks to improve dye removal efficiency while also lowering energy consumption, operational cost, save time and solve the issue of by-product generation which is more sustainable. When combined with a substrate, the adsorbent needs to have a remarkable level of mechanical properties and stability without compromising its adsorption properties such as specific surface area and porosity. In comparison to the traditional subtractive manufacturing approach, additive manufacturing (AM) technology, often known as 3D printing, have emerged as one of the most advanced options for constructing complex geometric structures which can be tailored specific requirements. Therefore, the integration of 3D printing and adsorbent film was explored as a 3D-printed enhanced adsorbent for dye removal.

1.2 Problem Statement

Direct utilisation of adsorbents in the form of fine powders or flakes form may lead to the process of leaching or rapid depletion of the adsorbent. Following the treatment, an extra separation procedure is always required, specifically to recover the powdered, beads type or flakes adsorbents from the treated water. This cause high maintenance effort and cost in order to clean the water. It is crucial to acknowledge that the presence of these adsorbents in the wastewater can hinder the efficacy of the treatment process, rendering it ineffective in its primary objective to treat the wastewater. Furthermore, the subsequent separation step

between the saturated adsorbent and the treated water, whether through sedimentation or filtration, can pose significant challenges in terms of its complexity, time consumption, and financial resources. These obstacles must be addressed to ensure the successful implementation of the treatment procedure. One of the ways to overcome the above challenges are by integration of 3D printing and surface functionalisation to develop 3D-printed adsorbent.

There are several areas that necessitate careful consideration with a suitable evaluation in relation to the grafted 3D-printed adsorbents in order to enhance the performance of adsorption. When the adsorbent material is grafted to a substrate, it is plausible for the adsorption capacity to decrease as a result of limited accessibility of the adsorbate to the surface or internal sites of the adsorbent. Furthermore, there exist potential scenarios where the active sites of the adsorbents may be obstructed by the crosslinker. In order to ensure that the entire grafted 3D-printed adsorbent functions effectively, it becomes imperative to enhance the surface grafting technique and overall formulation of the adsorbent. Hence, the grafted 3D-printed adsorbent coating will be able to fulfil its role as an efficient adsorbent in addressing the aforementioned issues.

The role of 3D printing structure, surface functionalisation and modification will also play an important role in improving the adsorption performance. Hence, the selection of adsorbent materials and functional crosslinkers is the primary objective to improve the performance and enhance the behaviour of the grafted 3D-printed adsorbent.

The grafted 3D-printed adsorbent necessitates a meticulously optimised chemical and physical stability in order to form a strong bond with the designated 3D-printed enhanced adsorbent. This is to prevent leaching during the adsorption process. This research work discussed on the latest approach in wastewater application by combining polymer-based additive manufacturing and surface functionalisation that has gauged tremendous attention in recent years due to its remarkable performance to meet the criteria of practical applications.

Further to this, the anticipation of the colour of textile wastewater holds significant importance for various reasons, primarily related to concerns about the environment and regulations. It is necessary to always test the colour index regularly as it is one of the most obvious visual pollutants. However, testing the colour index requires specific equipment such as colorimeter or spectrometer which is expensive and time consuming. To speed up the process, artificial intelligence can be employed as a tool to do the colour prediction based on the images. This technique can be early indications for water quality monitoring and efficiently treated textile dyes from industrial wastewater.

1.3 Research Questions

1. How does silane-grafted chitosan of 3D-printed monolith can remove the dye colour of textile wastewater?
2. How does structural topology and drying method affect the adsorption performance of the silane-grafted chitosan of 3D-printed monolith?
3. What are the optimum parameters for the silane-grafted chitosan of 3D-printed monolith to achieve optimal adsorption performance?

4. What is the effect of surface modification technique on the adsorption performance of silane-grafted chitosan of 3D-printed monolith?
5. How to predict the colour of textile wastewater using real-time images?

1.4 Research Objectives

This research work was aimed to remove the colour of the discharged textile wastewater using a functionalised 3D-printed monolith. The objectives of this study are:

1. To design silane-grafted chitosan of 3D-printed monolith and its optimal performance in wastewater application.
2. To improve and compare the performance of multifunctional materials for 3D-printed monolith using different resin formulations that consider the material compatibility, mechanical strength, as well as mechanical and chemical stability.
3. To improve the performance of grafted-nanostructured chitosan of 3D-printed monolith and modify the surface morphology using electron beam irradiation treatment.
4. To design a systematic approach for colour prediction of water using machine learning image processing.

1.5 Research Scope

Based on the identified research objectives, this research work is divided into five main scopes.

1. Synthesis of silane - grafted chitosan of 3D-printed monolith using a novel surface grafting method and its optimisation performance in wastewater application.

   In this scope, a synergistic approach of combining 3D printing and surface grafting method was applied to fabricate silane- grafted of 3D-printed monolith. The adsorption performance was evaluated using synthetic dye with various parameters such as pH (3 to 12), temperature (30 to 60 ℃), concentration of chitosan (1 to 3 wt.%) and dipping time (30 to 45 min) during grafting procedure. Optimisation of the performance of dye removal and uptake capacity was carried out using Box-Behnken design in Response Surface Methodology (RSM). Further to this, adsorption performance was carried out using real textile wastewater to remove colour. The enhancement of the adsorption performance was carried out by identifying the influence of monolithic structural designs (Kagome, gyroid, Fischer, and body centred cubic) and different drying methods (hot-air drying, freeze drying and vacuum drying) on the removal efficiency.

2. Synthesis of hydrophobic 3D-printed monolith using different resin formulations with addition of comonomer and surface grafting with silane coupling agent for wastewater application that consider thermomechanical properties, mechanical strength, as well as mechanical and chemical stability.

   This scope covered the formulation different resin using biopolymer with commercial resin and addition of different concentration of comonomer (1 to 3 wt.%), consists of 1,6-Hexanediol diacrylate

(HDDA) and 1,4-Butanediol diacrylate (BDDA) to fabricate 3D-printed monolith. The mechanical properties such as Young's modulus, storage modulus, ultimate tensile strength and elongation at break were evaluated. The effect on the thermal, mechanical and chemical stability of the monolith as well as hydrophobic behaviour and moisture absorption content were also reported under this scope.

3. Development of modified synthesis method of silane – grafted nanochitosan of 3D-printed monolith with good mechanical strength using electron beam irradiation treatment and its effect on the adsorption performance.

   In this scope, electron beam irradiation treatment was applied to reduce contact time of the silane – grafted nanochitosan of 3D-printed monolith to achieve equilibrium of colour removal. Different dosages of irradiation election beam between 50 to 200cGy and its effect on the surface morphology based on the characterisation study, adsorption performance and mechanical strength were reported in this scope.

4. Conceptual design of colour prediction tool using deep learning image processing.

   Convolutional neural network (CNN) and AlexNet model using MATLAB were utilised to design a machine learning system to predict the colour of the textile wastewater based on real-time image. The quantitative data of colour and images of textile wastewater were integrated into model to obtain the final machine learning system for colour prediction based on classification and identification of

acceptable (0 to 199) and not acceptable range (above 200) for 800 images.

1.6 Research Hypothesis

The following research hypothesis were tested in this study.

1. The proposed surface grafting technique using silane coupling agent can successfully grafted chitosan onto the 3D-printed monolith.
2. The 3D-printed adsorbent will enhance the removal the dye colour of textile wastewater.
3. Different structural topologies and drying method will enhance the adsorption performance of the silane-grafted chitosan of 3D-printed monolith.
4. The adsorption performance of the silane-grafted chitosan of 3D-printed monolith will be optimised based on optimum parameters in Response Surface Methodology.
5. The application of surface modification technique will enhance the adsorption performance of silane-grafted chitosan of 3D-printed monolith.
6. The image of the textile wastewater can be used to predict the colour index using deep learning tools.

1.7 Risk Assessment

The potential risk that might arise when carrying out the research work were identified and discussed as shown in Table 1.7.1.

Table 1.7.1: Risk Assessment of research work.

Type of risk	Description	Level			Justification
		Low	Medium	High	
Technical	Failing in printing 3D - printed monolith	x			The student is well-trained to handle 3D printing samples and has prior experience before joining PhD programme.
	Malfunctions of 3D printer	x			
	Failing to graft chitosan onto the 3D – printed monolith		x		The proposed technique is still new and require trial and error process.
	Lack of skills and expertise	x			The project was supervised by 4 different supervisors that are expert and knowledgeable in their own field.
	Unable to get textile wastewater samples	x			The project is supported by industry collaborator and the student

				frequently go for site visit to collect water samples.
	Research outcomes are not effectively promoted to meet industry need	x		The proposed technique is validated with industry player and are expected to be scaled up in future work.
Timing	Failure to meet the research outcomes according to the timeline	x		The student actively seeks for advice and update the progress every week.
Managerial	Insufficient financial resources		x	The inflation rate of consumables and external analysis cost due to malfunction of in-house facilities.
Infrastructure	Lack of suitable facilities to conduct research	x		Most of the required facilities are available on campus except for certain high-end analysis that can be outsource.
	Cease of operation of research analysis due to breakdown/malfunction	x		Outsource to other research facilities for testing.

1.8 Outline of thesis

The overall flow chart of the research work in this thesis from Chapter 1 to Chapter 9 were presented in Figure 1.8.1. Chapter 1 covered the introduction of research study including identifying problem statement, research questions, research objectives and research scope, and followed by literature review was conducted in Chapter 2. The literature review covered the trends of the 3D-printed monolith used in wastewater treatment plant and the optimisation strategies to improve the performance of the 3D-printed monolith by taking into consideration of the material strength and compatibility, printing parameters and strategies of surface functionalisation initiated by surface grafting and surface modification through electron beam irradiation treatment. Further to this, the current trend of implementing image processing and Artificial Intelligence intersect with Industrial Revolution 4.0 using in water quality prediction and control were reviewed. Finally, the outline of thesis was presented.

Following to this, Chapter 3 depicted the development of reusable chitosan-grafted 3D-printed polymer monolith for wastewater treatment. A functionalisation strategy of surface grafting and optimisation of operating parameters for adsorption performance using Response Surface Methodology were proposed.

The enhancement strategy to improve the adsorption performance and reducing the reaction time was carried out by varying the structural topology of the silane-grafted chitosan of 3D-printed monolith which was

covered in Chapter 4. Further to this enhancement strategy, Chapter 5 explored the application of different drying methods to change the surface properties of the silane-grafted chitosan. Chapter 6 depicted the strategy to develop multifunctional materials to fabricate 3D-printed monolith with excellent mechanical strength and stability, chemical resistance and creating hydrophobic surface to increase the lifespan in the water environment. The material was developed by formulating different resin using biopolymer with commercial resin and addition of different concentration of comonomers, and subsequently grafted with single and hybrid silane agent.

With the intention to integrate the surface grafting method and formulated multifunctional material described in Chapter 3 and Chapter 6, Chapter 7 reported the modified synthesis method of silane - grafted nanochitosan of 3D-printed monolith. A surface modification technique using electron beam irradiation treatment was applied to further enhance the adsorption efficiency and reduce the reaction time to 1 h, meeting the industrial requirements.

Lastly, Chapter 8 covered the conceptual design of water prediction analysis system using machine learning image processing. Finally, in the final chapter of this thesis (Chapter 9), conclusions and future works were presented.

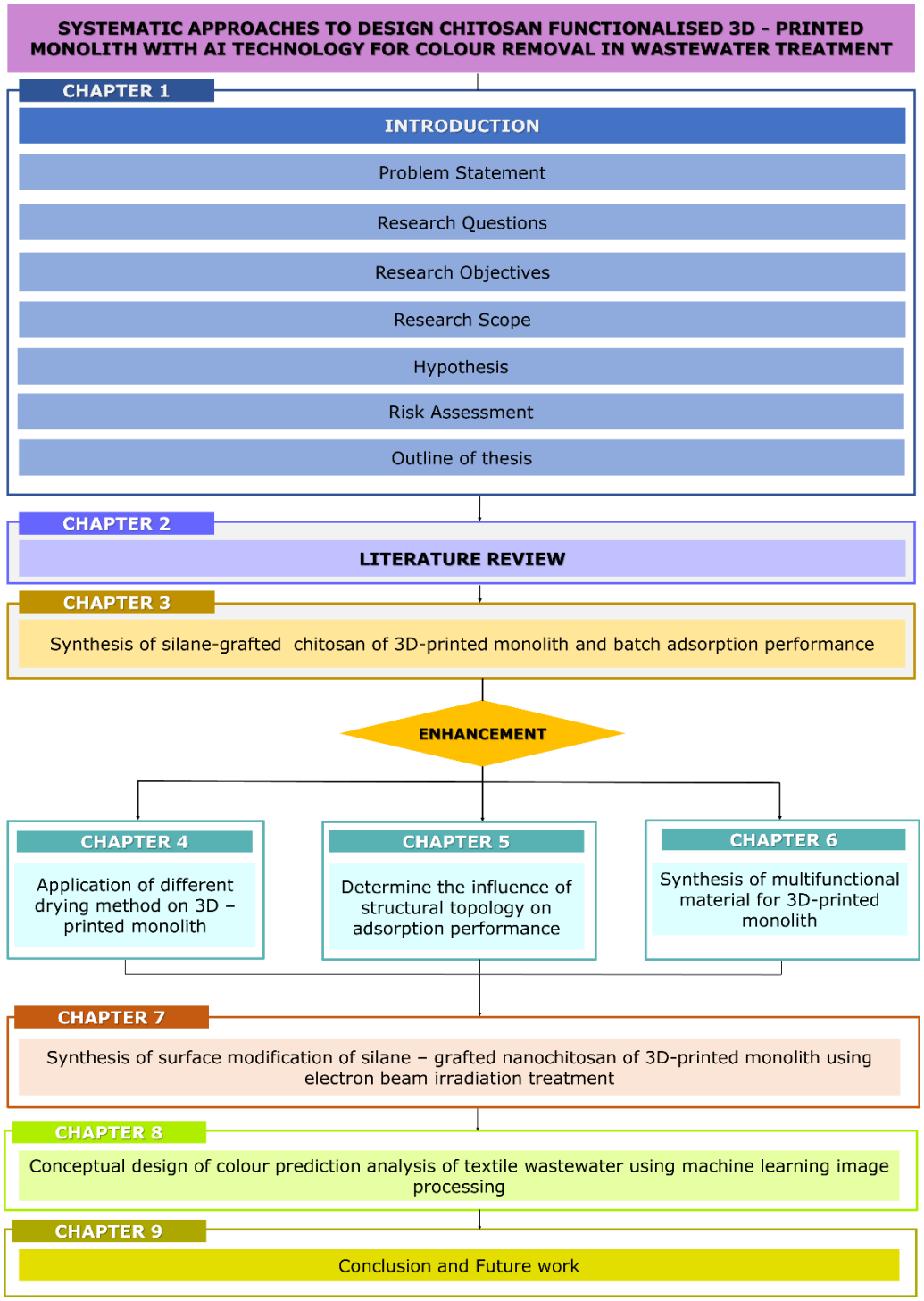


Figure 1.8.1: Outline of thesis.

CHAPTER 2: LITERATURE REVIEW

The literature review encompasses the examination of dyes removal treatment, with a particular focus on the process of adsorption. The detailed discussion on a new approach of functionalised 3D-printed adsorbent for colour removal in textile wastewater was presented. The review covered different 3D printing techniques, materials options, adsorption efficiency, mechanical strength, chemical and mechanical of the functionalised 3D-printed enhanced adsorbent.

2.1 Presence of dye in textile wastewater

Dyes are categorised in accordance with their intended usage and chemical composition. They can be classified into various groups based on their chromophoric entities, including nitro dyes, azo dyes and nitroso dyes(Morsi and Elsalamony, 2019). Furthermore, dyes can also be categorised based on their ionic properties as either anionic, cationic, or non-ionic dyes. Azo dyes, which are commonly produced through the process of diazotization of aromatic primary amine followed by coupling with electron-rich nucleophiles like amino acids and hydroxy acids, constitute the most extensive category of synthetic dyes. It is arduous to eliminate these dyes through conventional techniques due to their elevated solubility in water. Most dyes are mutagenic, toxic, and carcinogenic, which caused major environmental concern (Khatri *et al.*, 2018). Dyes in wastewater kill aquatic life and have a chemical and biological effect on the dissolved oxygen concentration of the stream. This process also hinders the penetration of sunlight, thereby impeding the activity of photosynthesis. Therefore, it is imperative to o eliminate

environmental contaminants within an acceptable threshold from industrial waste containing dyes before it is discharged into the environment.

2.2 Current technology for treating dye effluent

Various physical treatment such as ion exchange, adsorption and membrane filtration have been reported as effective process for treating dye wastewater (Gadekar and Ahammed, 2020). Each treatment process has advantages and disadvantages, and its limitations are determined by the unique circumstances of the effluent. The ion exchange treatment method is efficient in treating soluble dyes (i.e., anions and cations dye) and can retrieve the adsorbent. However, the main disadvantage of using the ion exchange technology is that it cannot treat non-ionic dyes and the ion resin must be regenerated before reuse. Membrane filtration offers the most effective and quick process for treating all types of dye. However, membrane system is expensive, has the limitation in removing dissolved solids and short lifespan due to frequent clogging. Further to this, adsorption process has emerged as the prevailing method for treating wastewater due to its uncomplicated and direct nature, and its efficacy in treating the contaminants from water. Although the adsorption process produces waste sludge which poses disposal issues, it has the least restrictions comparing to other methods which have been further examined. The effective enhancement of adsorption process requires the use of adsorbent with a substantial surface area, high pore volume, and suitable functionalities. In this context, the notion of 3D printing as an innovative technological

advancement, presents the potentiality of constructing design that possess complex structures with tailored to specific surface area and porosity. Moreover, the application of 3D printing can overcome the challenges faced using conventional adsorbent as 3D printing can be integrated with the adsorbent via surface functionalisation technique. This synergistic approach is more economical and environmentally viable as it can reduce the material used during the synthesis process as well as solve the sludge generation. A detailed discussion on functionalised 3D-printed adsorbent can be found in the following section.

2.3 Introduction to 3D-printed adsorbent

Recently, there has been a significant advancement in 3D-printed enhanced adsorbent for wastewater treatment as shown in Figure 2.3.1a due to its inherent advantages of rapid fabrication process with good control in pore structure and porosity, better energy efficiency, and excellent mechanical properties for regeneration and reusability of the device. Additionally, the use of surface functionalisation, by chemical or physical means, to enhance the surface properties of 3D-printed parts has also recently garnered much attention. The combination of 3D printing and surface functionalisation has been used on a large scale for industrial applicability to produce structures and components with unique physical and chemical properties. One of the promising applications is in the area of environmental and water treatment research. These new innovative solutions aimed at simultaneous increase of performances in terms of dyes removal and decrease of the energetic footprint by bringing to cost minimization in operation and time saving. Surface functionalised

of 3D-printed adsorbent also can reduce the amount of solid adsorbent required with exact formulation prepared. In addition to that, using substrate as support can prolong the lifetimes of used adsorbent. Other advantages of coating also indirectly can protect the underlying substrate materials from a harmful environment. Currently, the number of publications associated to this area is relatively limited, but its trend currently rising, as shown Figure 2.3.1(b). Thus, the combination of 3D printing and surface functionalisation will not only improve the performance of the technologies but also take a robust approach towards a sustainable environment and better water quality. Number of reviewed publications based on the keywords have been summarised in Table 2.3.1.

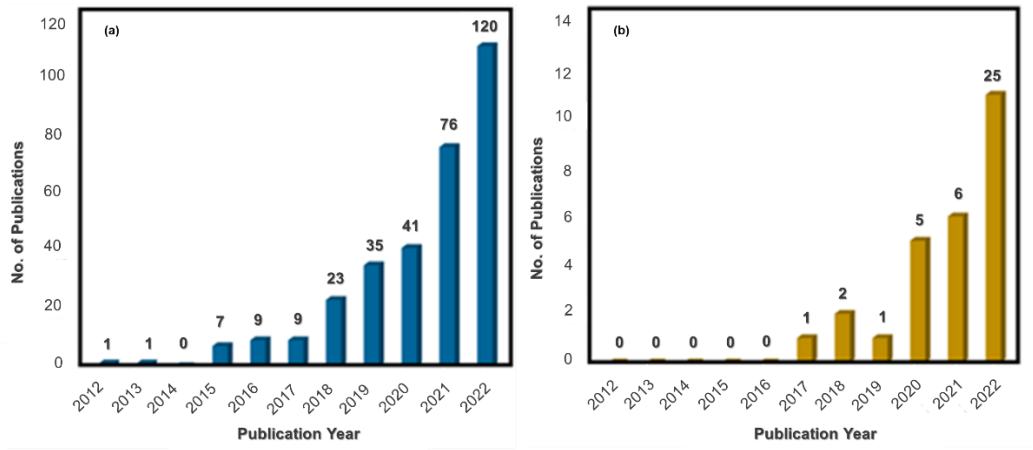


Figure 2.3.1: Publication trends in 2011 – 2022, (a) Water treatment and 3D printing (Web of Science, 2022a); (b) Water treatment, 3D printing and surface functionalisation (Web of Science, 2022b).

Table 2.3.1: Publication extraction based on relevant keywords (Web of Science, 2022).

Keywords	No. of paper
"Water treatment", "3D printing"	120
"Water treatment", "3D printing" and “surface functionalisation”	25
"Water treatment", "3D printing" and “surface functionalisation”, and “review”	1

2.4 Performance optimisation strategies and recent advances of dye removal using 3D-printed enhanced adsorbent

The promising potential of 3D printing is demonstrated by its ability to construct structures with integration of greater parts and desired geometry. The performance and mechanical properties of 3D-printed monolith will vary depending on the printing method and material chosen, which will be the fundamental optimisation techniques for a variety of applications. The performance measurements of 3D-printed functional materials as well as optimisation techniques are provided and addressed in this section.

2.4.1 3D Printing route consideration

In water treatment, it is important to select the suitable material with the right printing technique to produce a structure that can withstand aggressive environmental conditions while maintaining its function. There are several controlling parameters that must be met for 3D printing to be effective and produce the desired quality of printed parts. These controlling parameters can be divided into two categories which are printing, and material parameters. Below is a brief description of each 3D

printing technique with its advantages, limitations, and its potential to be explored.

- Powder Bed Fusion (PBF)

  Powder bed fusion technology uses sintering and melting as a binding mechanism. Sintering is a process of partial melting, while melting is a complete process. Selective laser melting (SLM), selective laser sintering (SLS), electron beam melting (EBM), and direct metal laser sintering (DMLS) are all common PBF techniques. SLS uses powdered plastics, metals, ceramics, and glass, whereas SLM only uses metals such as alloys and stainless steel for this printing technique. It has been found that both plastics and polymers offer PBF great design freedom with complex geometries, as they do not require supporting material, have very high strength and stiffness, and excellent mechanical properties comparable to those of bulk materials. The main limitations of PBF are shrinkage and distortion due to internal and surface porosity, which make post-processing challenging in handling and disposal of the powder (Casini, 2022). In addition, the PBF printing process requires large amount of powder to ensure appropriate powder flow and uniformity during printing.

- Binder Jetting (BJ)

  Binder jetting is a process in which powder particles are bonded together by selectively depositing a liquid binder, and subsequently produced 3D-printed object. Typical materials used in this method are metals, sand, and ceramics. The main advantages of this technique are the ease of operation, no requirement of support is needed, and

low cost (Mostafaei *et al.*, 2021). The main disadvantages of binding jetting are the multi-step post-processing of the print (i.e., curing and densification), the high surface roughness and lower resolution of the printed parts, and the fact that post-processing strategies still need to be developed for most materials. The inability to predict the large amount of distortion that occurs when individual alloys are sintered to full density to achieve the desired final geometry is one of the main drawbacks that limiting the potential of this process. It also reduces the overall accuracy of the process when producing parts from a single alloy that are much larger than the size of the metal injection mold (MIM). Binding jetting is one of the oldest AM processes that is useful for metal materials which currently used in the fabrication of injection moulding using stainless steel powder for industrial application.

- Directed Energy Deposition (DED)

  Direct energy deposition focuses the energy of a high-powered laser on a small area to heat the substrate and melt the printing materials. The amount of powders that are melted and the energy source (e.g., laser > electron beam > arc due to heat input) both affect the print resolution of the DED process while the deposition rate is affected by the production speed. The advantages of the DED process are the ability to fabricate of complex geometries and deposit functional materials and reduction of material waste. The disadvantages of the DED process are distortion, porosity and inhomogeneities, low quality

and accuracy of parts, and the need for expensive materials and longer production time.

- Material Jetting (MJ)

  Material jetting or utilised the light-curable resin, and its printing principle is similar to common paper printing. To create the desired design, the photopolymer resin is dropped on various substrates layer by layer (Badalov, Oren and Arnusch, 2015). This process is categorized into three types: (1) Nanoparticle jetting, (2) Polyjet, and (3) drop-on demand. MJ technique able to fabricate complex shapes with very fast manufacturing process, high accuracy (>14 microns), produce smooth surface and ability to combined different materials as ink formulation. The only limitation is high manufacturing cost, heat resistance for certain materials is limited and unable to produce functional prototypes.

- Material Extrusion (ME)

  Material extrusion uses continual pressure to drive the material out of the print head and onto the printing platform. Once the material has been extruded and solidified, the procedure is repeated until the desired output is obtained. Fused deposition modelling (FDM) uses this principle of material extrusion. This technique is cost effective, mechanically resistant, and capable of producing durable components. The disadvantages are low to moderate manufacturing accuracy, the production of grooves, slow manufacturing process and the need for support structures. Another significant limitation is that the addition of fibers or fillers to improve mechanical properties leads

to clogging in the nozzle. It has been reported that the extrusion nozzle can affect print resolution due to thermal radiation effect, as it is the component of the printing system that comes into contact with the filament before it is extruded into the print bed (Quero *et al.*, 2021).

- Sheet Lamination (SL)

  Laminated object manufacture (LOM), ultrasonic additive manufacturing (UAM), ultrasonic consolidation (UC), and plastic sheet lamination are the techniques utilised in the sheet lamination process (PSL). The most often used manufacturing processes are ultrasonic additive manufacturing (UAM) and ultrasonic consolidation (UC) (Hehr *et al.*, 2019). In this process, the raw materials are cut through the use of digital guided user and the sheets are stacked layer by layer through bonding via diffusion to form the final product (Balogun *et al.*, 2019). Various materials such as ceramics, papers, polymers, and metals can be used in this process. This process is integrated as a hybrid manufacturing system which does not require the support structures, low operation cost and easy to handle. However, sheet lamination process causes a lot of wastage compared to other methods, poor surface finish before post-processing, low dimensional accuracy, poor bonding between the stacked layers and difficult to fabricate complex geometries (Rouf *et al.*, 2022).

- Vat Photopolymerisation (VP)

  In the VP process, photopolymerisation of materials such as acrylate resin with high reactivity is used to produce solid parts. The mixed photopolymer, usually consisting of a polymer and photoinitiator, is placed in the vat and sintered with a laser. Laser is used in stereolithography (SLA) while light mask projector is used in digital light processing (DLP) for sintering. The laser was exposed over the mixed resin, which undergoes a photochemical process that bonds like a chain to cure and form solid material (Westbeek *et al.*, 2020). This process produces high resolution and accuracy, precise and capable of printing complex geometries and surface quality. The printing process is relatively fast and can print large components. The only limitation of this process is that the 3D printer is expensive, material selection is limited, and the post-processing time is longer. Recent studies have shown that photopolymerisation has found its place in the production of 3D nanoprinting, tomographic printing and 4D printing (Pagac *et al.*, 2021). This is because there is an increasing industrial demand for smart composites and materials that enable better capabilities and safe human interaction in various fields such as robotics, healthcare, and wastewater application.

The common 3D printing techniques under AM technologies are illustrated in Figure 2.4.1. There are various controlling parameters that also play an important role to ensure the effectiveness of 3D printing and desired quality of printed parts. These controlling parameters can be

divided into two categories which are printing parameters and material parameters as summarised in Table 2.4.1 and Table 2.4.2.

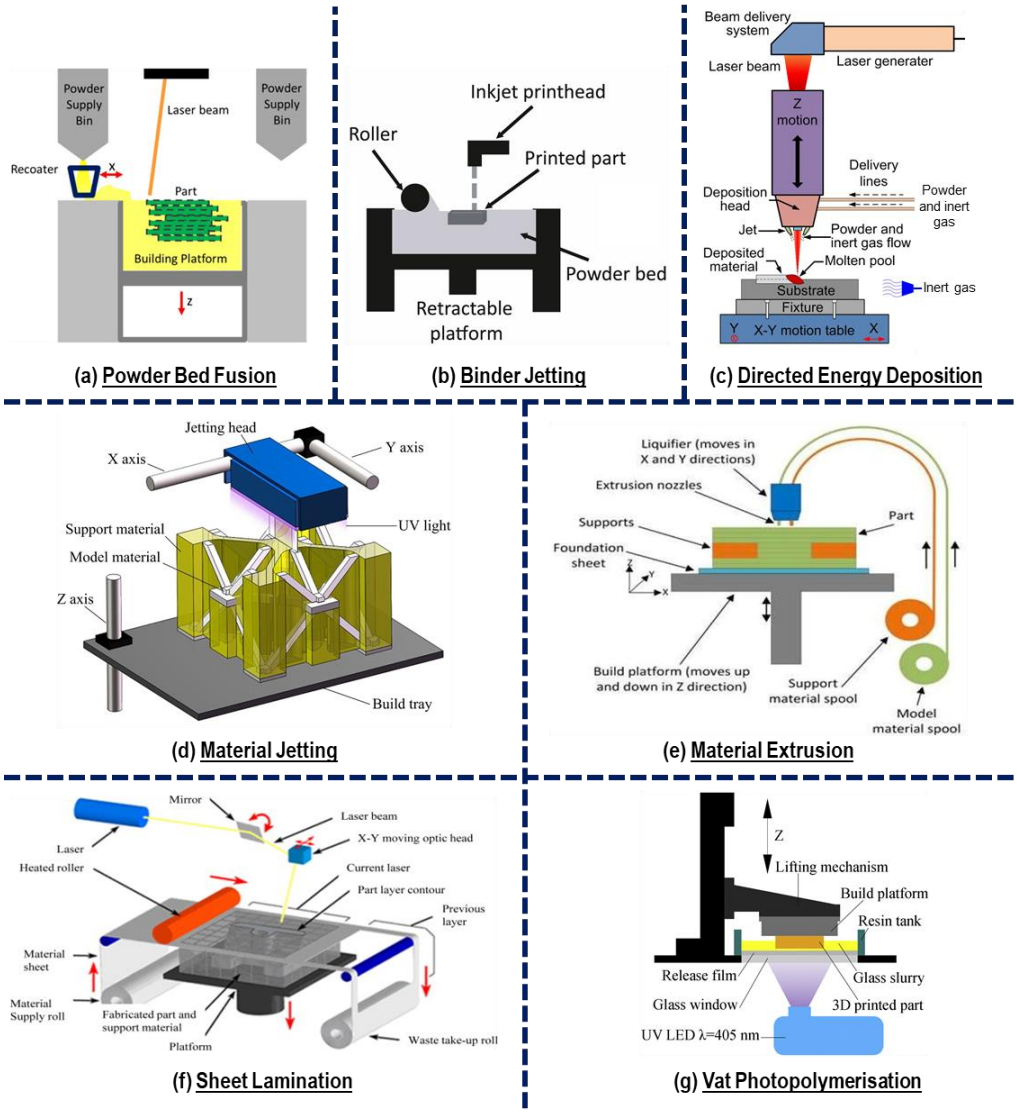


Figure 2.4.1: Schematic diagram of AM technologies, (a) Powder bed fusion(Tan *et al.*, 2016b); (b) Binder jetting (Zhang *et al.*, 2021b); (c) Directed energy deposition (Hu *et al.*, 2018); (d) Material jetting (Liu, Song and Huang, 2020); (e) Material extrusion (Srinivasan *et al.*, 2020); (f) Sheet lamination (Ahn *et al.*, 2012); and (g) Vat photopolymerisation (Cai *et al.*, 2020).

2.4.2 Material consideration

The two primary design factors during the 3D printing process are the preparation of functional materials and the printing process to obtain the desired output and 3D architectures. Similarly, for wastewater treatment

application, the selection of material for ink formulation based on the two essential factors: (1) mechanical stiffness and strength and (2) viscoelastic properties.

The surface wettability and tension are extremely important surface properties for water treatment because they determine how the surface of printed materials interacts with the environment. Sufficient mechanical stiffness and strength of the ink is required to support the entire structure during the solidification process after printing and ink deposition. As reported by Pagac *et al.* (2021), the common mechanical strength for photocurable resins are (i) ultimate tensile strength (23 MPa - 65 MPa), (ii) tensile modulus (0.9 GPa - 2.8 GPa) and (iii) elongation failure (7% - 17%), while the mechanical performance of hydrogel can reach the elastic modulus (~0.1 - 1.0 MPa), tensile stress (~1 - 10 MPa), tensile elongation (~10 - 20 times), toughness (~0.1 - 10 kJ/m^2) and work of elongation (~1 - 100 MJ/m^3) (Wei *et al.*, 2015). Recently, functional materials made of bio-based materials and polymers have been intensively explored by researchers to develop robust materials for wastewater application which will be discussed in the following section.

2.4.2.1 Polymer

In AM process, two common polymers are thermoplastic and thermoset plastic. Thermoplastics (also known as melt-processable plastics) can be warmed and remoulded without undergoing any chemical changes. Photopolymer is an alternative form of polymeric material that is employed in additive manufacturing (AM) procedures. This material possesses the ability to absorb ultraviolet (UV) light and subsequently

solidify. Notably, VP (specifically SLA and DLP) are the relevant AM technologies that utilise this specific polymer. The photopolymers used in the methods of VP consistently demonstrate superior resolution and dimensional accuracy in the production of 3D printed parts compared to other AM techniques. The common polymers used in these AM techniques are polycarbonate (PC), acrylonitrile butadiene styrene (ABS), and poly ether ester ketone (PEEK), whereas some biodegradable polymers used are polylactic acid (PLA), polyurethane (PU), poly (ethylene glycol) diacrylate (PEGDA) polytriethylene carbonate (TMC), and polypropylene fumarate. Out of these polymers, ABS is the most common materials used in 3D printing due to its high mechanical properties and wear resistance, however, it caused the warping and produce toxic fumes during printing. Further to this, the issue with other biodegradable resins are they exhibit a high level of viscosity, necessitating the use of a diluent to modulate this viscosity.

PEGDA, on the other hand, outperformed other polymers due to its low cost, good processability, biodegradability, and non-toxicity. It has been authorized by the Food and Drug Administration (FDA) for the fabrication of a variety of medical devices and ecological applications. PEGDA is an acrylate crosslinker repeating polymer crosslinker. Moreover, the surface wetting properties of PEGDA depend on the molecular weight. Nam *et al.* (2018) reported that PEGDA250 is insoluble in water and hydrocarbon oil, which exhibits both hydrophilic and hydrophobic properties. The primary benefits associated with PEGDA are its ability to be modified with specific surface functions, and the capability to adjust its mechanical

properties according to its molecular weight which make it suitable to be used for hydrogel, microfluidic device, and encapsulation fabrication. PEGDA has been further investigated in this study for its potential use as a green 3D-printed enhanced adsorbent for the treatment of wastewater, considering the aforementioned benefits.

2.4.2.2 Bio-based materials

3D-printed bio-based materials such as chitosan, alginate-based materials, konjac glucomannan, and cellulose acetate have gained popularity due to their potential application in the wastewater treatment. All of these materials have been shown to be highly reusable and provide tailored adsorbents for the removal of common water contaminants like dyes.

Chitosan is a polymer bio-adsorbent with polycationic properties, derived through the process of deacetylating a crucial constituent of shellfish exoskeleton called chitin. Chitosan has received interest in a variety of applications due to its adsorption effectiveness, biocompatibility, ease of chemical modifications, and biodegradable properties. Chitosan is regarded as an excellent adsorbent. The -NH_2 and -OH groups on the polymeric backbone can operate as chelating and reaction sites.

Chitosan is commonly found as a powder or flakes as the final product of the production process. Its crystalline state is the result of strong inter- and intramolecular hydrogen bonding within its structure, which results in poor acid resistance and has limitation is adsorption performance. Moreover, currently the utilisation of chitosan-adsorbent is impeded by a constraint that restricts its broader application: the absence of effective

method for the restoration of the adsorbent material. The disposal or storage of exhausted adsorbents without proper regeneration may result in the release of contaminants into the surrounding environment. One of the ways to mitigate this issue is by applying graft-polymerization via surface grafting. This approach is a popular method for increasing adsorption capacity and improving chelation or complexation capabilities as well as improve the regeneration of the adsorbent. This technique can be done on the inert substrate. By taking the advantages of 3D printing, a customise design can be done to further enhance the performance and functionality of the adsorbent. For example, Zhang *et al.* (2019a) fabricated a highly reusable and porous chitosan monolith that can adsorb Cu (II) ions. This method took advantage of 3D printing for the optimal design of the porous structure combined with surface functionalisation techniques for immobilized functional chitosan layers on the surface, resulting in a fast response with high specific sorption capacity and excellent diffusion resistance. 3D printing and bio-based materials manufacturing is a relatively new approach in the wastewater application especially for dye removal, which has open door for more researchers to venture and explore.

In short, it can be concluded biopolymers and polymer-based additive manufacturing are two main materials of interest for water applications due to their remarkable flexibility in design novel, geometrically complex, and lattice structures. The printing parameters and control parameters of 3D-printed bio-based and polymeric functional materials and their implications for AM techniques are summarised in Table 2.4.1 and Table

2.4.2, respectively. As shown in Table 2.4.2, the critical material requirements for AM techniques. They can be divided into chemical, optical, rheological, thermal, extrinsic, and mechanical properties. The surface properties of water or moisture absorption was considered. Water absorption indicates the ability of the polymer to absorb moisture/water from its environment. High absorption has reversible effects on mechanical strength by reducing glass transition temperature and moduli and enlarge fracture strain and impact strength. Since 3D-printed polymeric functional materials will be exposed to water, it is critical to consider the water peak and its absorption range, which indicates the material stability in water. This information is also crucial to see if further modification is required to change the surface property from hydrophilic to hydrophobic.

Table 2.4.1: Printing parameters for common printing techniques for 3D printing technologies.(Stwora and Skrabalak, 2013; Kitsakis *et al.*, 2015; Tan *et al.*, 2016b; Ferreira *et al.*, 2017).

AM Process	Printing parameters											Materials		Advantages/ Drawbacks
	Layer thickness	Minimum wall thickness	Typical build size	Dimensional accuracy	Temperature	Nozzle diameter	Infill density	Printing Speed	Exposure time	UV intensity	Laser power	Polymer	Bio-based	
Powder Bed Fusion														
• **SLS**	100-120 microns	0.7 mm (Recommended: 1 mm)	300 x 300 x 300 mm (Max: 750 x 550 x 550 mm)	± 0.3% (lower limit of ± 0.3 mm)	✓	-	-	✓	✓	-	✓	Nylon (PA), TPU	-	+ Good mechanical strength + Excellent resolution + No support needed. + Able to print complex structures. - Require high processing temperature. - Time-consuming and slow printing process
Material Jetting														
• **MJM** • **PJM**	16-32 microns	1 mm	380 x 250 x 200 mm (Max: 1000 x 800 x 500 mm)	± 0.1% (lower limit of ± 0.05 mm)	✓	-	-	✓	-	✓	-	Polymer, Waxes	Alginate, chitosan, cellulose acetate, and PLA	+ Good accuracy + Excellent surface finish + No support material is needed. - Limited wax-like material - Slow printing process

Table 2.4.1: (Continued)

AM Process	Printing parameters											Materials		Advantages/ Drawbacks
	Typical layer thickness	Minimum wall thickness	Typical build size	Dimensional accuracy	Temperature	Nozzle diameter	Infill density	Printing Speed	Exposure time	UV intensity	Laser power	Polymer	Bio-based	
Material Extrusion														
Desktop FDM	50-400 microns (Recommended: 200 microns)	0.8-1 mm	200 x 200 x 200 mm	± 0.5% (lower limit ± 0.5 mm)	✓	✓	✓	✓	-	-	-	PLA, ABS, PETG, Nylon, PEI (ULTEM), ASA, TPU	PLA, Alginate	+ Good strength + Good mechanical anisotropy + Low cytotoxicity + Relatively inexpensive + Minimal maintenance - Limited materials - Require support structure for complex geometry. - Low resolution Poor surface finish
Industrial FDM	50-400 microns (Recommended: 200 microns)	1 mm	1000 x 1000 x 1000 mm	± 0.15% (lower limit ± 0.2 mm)	✓	✓	✓	✓	-	-	-	ABS, PC, PEI	-	+ High accuracy + Better production capabilities + Eliminate in post-processing. + Smooth surface + Easy to print complex parts. + Expensive

Table 2.4.1: (Continued)

AM Process	Printing parameters											Materials		Advantages/ Drawbacks
	Typical layer thickness	Minimum wall thickness	Typical build size	Dimensional accuracy	Temperature	Nozzle diameter	Infill density	Printing Speed	Exposure time	UV intensity	Laser power	Polymer	Bio-based	
Vat Photopolymerisation														
• **Desktop SLA Bottom-up**	25-100 microns (Recommended: 100 microns)	0.5 mm	145 x 145 x 175 mm	± 0.5% (lower limit: ± 0.010 - 0.250 mm)	✓	-	-	✓	✓	✓	✓	Tough resin (ABS), Standard resin, Durable resin (PP-like), Clear resin, Dental resin	Chitosan	+ High surface quality + Excellent resolution + High complexity + Limited to a certain type of polymers - Expensive - Moderate mechanical strength - Susceptible to heat and sunlight
• **Industrial SLA Top-down**	25-150 microns	0.1-0.3 mm	2100 x 700 x 800 mm	± 0.15% (lower limit ± 0.010 - 0.030 mm)	✓	-	-	✓	✓	✓	✓	Clear, castable, dental, flexible, wax-like, ABS-like	-	+ Very large build size + Faster build times - Expensive - Require specialist operator - Involve in emptying the whole tank for material changes
• **Desktop DLP**	5-150 microns	0.1 mm	58 x 32 x 127 mm	Standard accuracy: 0.030 - 0.140 mm	✓	-	-	✓	✓	✓	✓	Clear, castable, dental	Chitosan	+ High precision + High complexity – complex shapes and sizes - Limited product thickness - Limited range of materials

Table 2.4.1: (Continued)

AM Process	Printing parameters											Materials		Advantages/ Drawbacks
	Typical layer thickness	Minimum wall thickness	Typical build size	Dimensional accuracy	Temperature	Nozzle diameter	Infill density	Printing Speed	Exposure time	UV intensity	Laser power	Polymer	Bio-based	
Vat Photopolymerisation														
Industrial DLP	25-150 microns	0.1 mm	48 x 28 x 100 mm (Max: 192 x 120 x 230 mm)	Standard accuracy: 0.010 - 1.100 mm	✓	-	-	✓	✓	✓	✓	Clear, castable, dental, flexible, wax-like, ABS-like	-	+ Stable output + Large Build Size + Fast Printing Speed + Excellent Light Uniformity Require a lot of resin
Binder Jetting														+
BJ	100 microns	2mm	400 x 250 x 250 mm (up to 1800 x 1000 x 700 mm)	± 0.2 mm (± 0.3 mm for sand printing)	✓	✓	-	✓	✓	-	-	Sand, ceramics, stainless steel (bronze-filled or sintered)	-	+ No required support material is needed. + Low cost - Brittle - Require extensive post-production manual handling. - Poor surfaces furnish

* Note: Most data are obtained from the manufacturers' websites – 3D Hubs (Hubs, 2022). The symbol "✓" indicates the influencing printing parameters for the particular 3D printing technique.

Table 2.4.2: Material parameters and impacts towards additive manufacturing process (Tan, Zhu and Zhou, 2020).

AM Technologies	**VP/MJ**	**SLS**	**FDM**
Chemical properties			
Functional group	✓	/	/
Degree of functionality	✓	/	/
Molecular weight	✓	/	/
Polymerization pathway	✓	/	/
Active centre stability	✓	/	/
Impact	*Curing kinetics*		
Optical properties			
Absorption	✓	✓	/
Scattering	✓	/	/
Reflection	✓	✓	/
Refraction		✓	/
Transmission	✓	✓	/
Impact	*Cure depth*	*Energy absorption*	
Rheological properties			
Viscosity	✓	✓	✓
Surface tension	✓	✓	✓
Relaxation behaviour	/	✓	✓
Impact	*Droplet formation stability*	*Particle coalescence*	*Adhesion and filament extrusion*
Thermal properties			
Melting temperature	/	✓	/
Crystallization temperature	/	✓	/
Melting range	/	✓	/
Crystallization kinetics	/	✓	✓
Heat capacity	/	✓	✓
Melting enthalpy	/	✓	/
Coefficient of thermal expansion	/	✓	✓
Conductivity	/	/	✓
Impact		*Shrinkage and warpage*	*shrinkage and warpage*
Extrinsic properties			
Particle shape	/	✓	/
Particle size	/	✓	/
Particle size Distribution	/	✓	/
Impact		*Powder flow behaviour*	
Mechanical properties			
Elastic modulus	/	/	✓
Strain at yield	/	/	✓
Impact			*Filament extrusion*

2.4.3 Application of surface functionalisation in 3D-printed enhanced adsorbent

Several functionalisation strategies have been developed to extend the capabilities of 3D-printed material for practical applications. There are three main strategies, as shown in Figure 2.4.2, consisting of developing functional materials, bioinspired materials, and surface functionalisation.

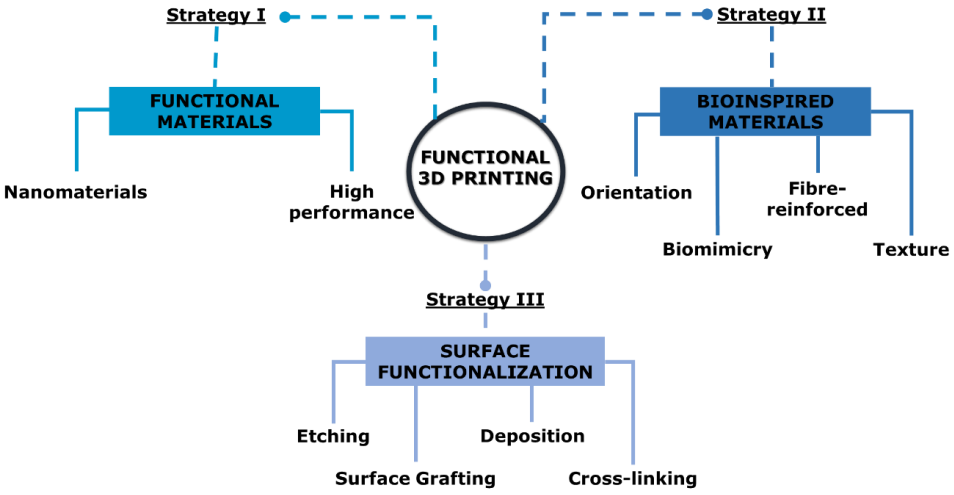


Figure 2.4.2: Versatile strategy in functionalised 3D printing (Jiang *et al.*, 2020).

Strategy I focus on the identification and use of suitable high-performance materials and nanomaterials to print 3D structures and components. There have been many discussions in the literature about the development of additively manufactured functional materials made of ceramics, polymers, nanocomposites, and metals for various applications. Various researchers have developed various 3D-printed monolith related to heavy metal removal, oil/water separation, fouling reduction, water splitting, desalination, and organic matter removal in environmental and water applications. Currently, the development of advanced functional materials for 3D printing is quite straightforward, but it is tailored to a specific system and requires a time-consuming and

costly process of trial and error. The number of trials can be reduced by using a computational modelling optimisation approach in the development phase. However, process modelling has high computational cost and may require high performance computing.

Furthermore, although the process of preparing the feedstock for printing ink is quite simple, it must be adapted to the intended AM technology, which requires knowledge of the surface properties, especially in terms of surface wettability and chemistry. Surface properties plays an important role in the adhesion of particles in the structure through binding or fusion. Another factor that must be considered in the development of the ink materials is the property that they must have strong and sufficient compaction and cohesion for the AM product. This is because minor changes in the ink materials have a large impact on the performance of the final printed product. To date, specific cost considerations for AM technology have not been reported. However, cost has been identified as one of the major factors holding the industry back from adopting AM technology. Machine costs are estimated to be between 50% and 75% of total production costs, 20% to 40% of material costs, and 5% to 30% of labour costs (Hopkinson, Hague and Dickens, 2006). Nevertheless, metrology can play an important role in optimising the AM system at low cost by minimizing the use of feedstock materials, reducing part scrap and post-processing requirements, and increasing production yield and energy efficiency. Thus, overall costs are reduced due to the flexibility offered by AM technology.

Strategy II produces bioinspired materials, which are (1) Lightweight structural materials of high mechanical toughness and strength, (2) Topological structures, which focus on designing bioactivity, super wettability, and stimuli responsiveness (Wang, Naleway and Wang, 2020). Wang et al. have reviewed bioinspired materials in terms of functional and structural categories from a wide range of fascinating biological materials. Detailed representative functions of paradigmatic biological and bioinspired were illustrated. The fundamentals for the specific property, followed by a discussion of insights into structure-property mechanisms from biological materials and their corresponding bioinspired materials that exhibit special functions/properties for relevant applications, were discussed. On the other hand, Yan *et al.* (2021) focused on reviewing recent development in biomimetic 3D printing materials with improved properties, mainly on single material-bioinspired reinforced structures inspired by creatures and multi-materials inspired by the balsa wood structures, Bioligand structure, nacre structures, and shape-changing structures. Based on the literature, it was also noted that geometrically structured materials based on the number of species found in nature exhibit high performance with excellent mechanical properties such as toughness, high stiffness, strength, and fatigue resistance. In contrast, functional structures exhibit exciting properties such as super wettability, liquid repellence, shape-changed, and memory. Although 3D printing can be used to design bioinspired materials and structures, this approach has numerous challenges and limitations. These include anticipating different interfacial materials to

fabricate bioinspired structures with multi-materials with different properties and functions. Another challenge is the fabrication of macroscale nanomaterials, which has yet to be reported because of the trade-off between high resolution, fabrication speed, and low cost. Future advancements in multi-material fabrication with high efficiency and low cost are expected, as well as a guide for fabricating 3D printing technology from nanoscale to macroscale.

Strategy III is an approach that combines the 3D printing process and post-processing methods to develop surface functionalisation for the desired application. Typically, there are two main strategies: Top-down and bottom-up. The top-down strategy mainly focuses on changing the surface microstructures without altering the chemical compositions. Polishing and physical etching are the typical methods under this strategy. On the other hand, the bottom-up strategy aims to form a layer of material with specific chemical compositions on the printed surface (Kumar, Bhushan and Bhattacharya, 2018). Example methods under this strategy are physical and chemical deposition (i.e., atomic layer deposition, vapor phase deposition), coating, surface grafting, self-assembly, and sol-gel technique. Surface functionalisation or post-treatment was preferred due to its advantages in achieving favourable surface properties and desired material performance, which is more practical in industry practice than the fabrication of bulk functional materials or pure structural materials. Based on the research results published in the literature, tailored surface functionalisation can achieve unique properties such as surface wetting and morphology, roughness,

biocompatibility, catalytic properties, and various mechanical properties like hardness, wear, friction, residual stress, and fatigue behaviour. To date, only one review paper done by Jiang *et al.* (2020) discussed surface-functionalised 3D printing, including robust methodologies, outstanding properties, and its potential application in different fields.

Based on the advantages and disadvantages of different strategies listed in Table 2.4.3, of the three strategies, surface functionalisation highlighted in Strategy III such as surface grafting and electron beam irradiation treatment has been not widely applied in wastewater treatment, particularly for post-treatment. Considering the gap, the following selection will be further discussed on Strategy III, as the methods of surface functionalisation on 3D-printed monolith are summarised in Figure 2.4.2, and the surface enhancement properties in Table 2.4.4 followed by a discussion of its application in the subsequent sections.

Table 2.4.3: Advantages and disadvantages of different strategy in functionalised 3D printing

	Advantages	Disadvantages	Ref.
Strategy I	- Easy and straightforward fabrication process - Offers light weight fabrication. - Waste minimisation - Reduce material cost and complexity on fabrication process	- Fabrication process tailor to specific system - Time consuming - Not cost effective as require trial and error procedure. - Not sustainable (one time usage) - Difficult to clarify the synthesis mechanism of different materials	(Ghosal *et al.*, 2021; Berber, 2020; Saidulu, Srivastava and Gupta, 2022; Mohd Yusoff *et al.*, 2022)
Strategy II	+ Excellent performance and mechanical properties + Offers unique design with arbitrary geometry. + Offers high complexity and feature resolution	- Difficult to align the reinforcement phase in the matrix during fabrication process. - Hard to achieve precise printing (interlocking bond between each layer) - Difficult to anticipate the effects of using different interface materials. - Require high cost of manufacturing. - Lower manufacturing speed	(Wang, Chen and Chen, 2020; Yan *et al.*, 2020; Yan *et al.*, 2021)
Strategy III	+ Time - saving + Waste minimization and cost - effective + Highly desirable approach for 3D printing in meeting variety of demand + Capable to fabricate robust functional layer on 3D-printed materials	- Require optimisation on stability and durability of the resultant structure - Difficult to achieve desired interfacial adhesion between the acquired surface functional layer and the 3D-printed substrate	(Jiang *et al.*, 2020; Mohd Yusoff *et al.*, 2022)

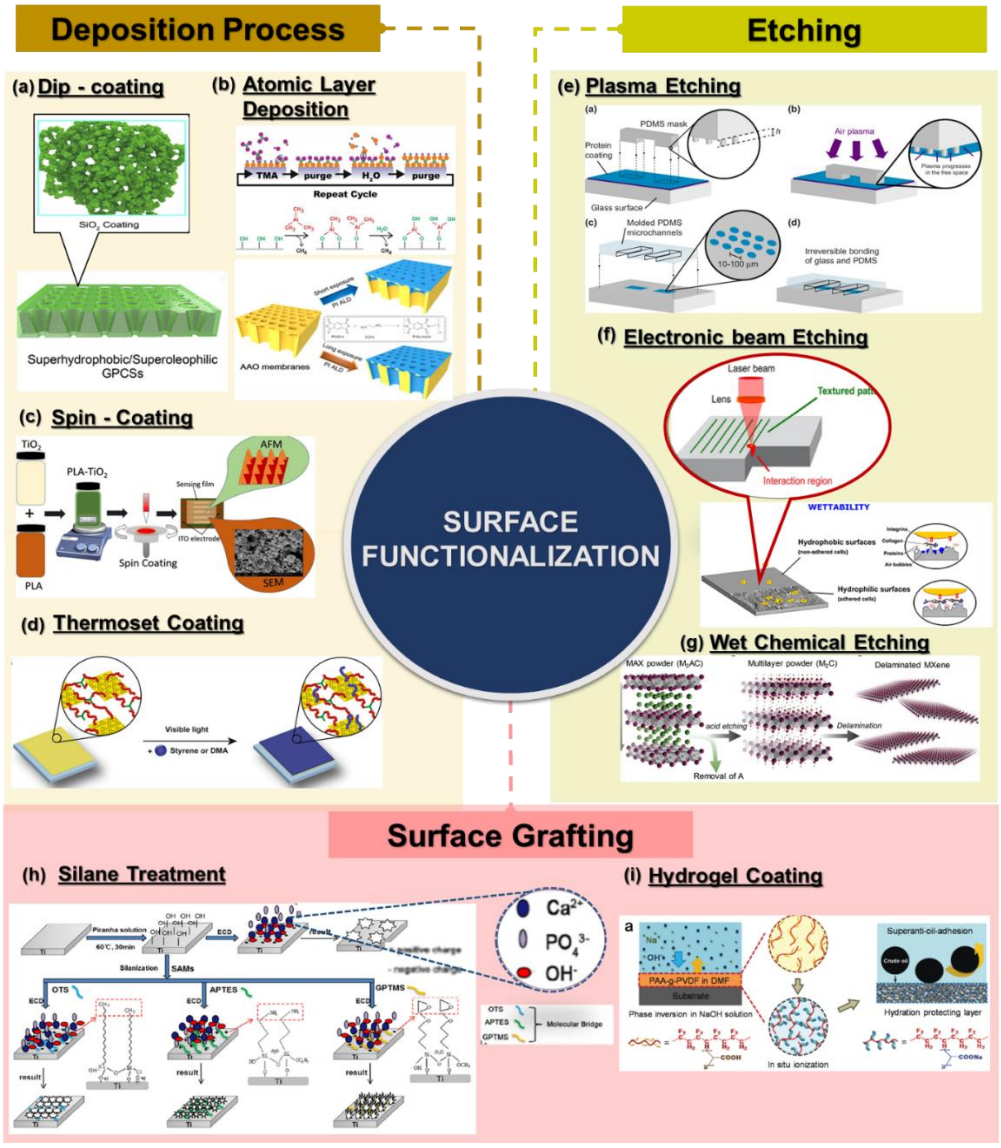


Figure 2.4.3: Techniques in surface functionalisation on 3D printing. (a) Dip-coating (Jin *et al.*, 2021); (b) Atomic layer deposition (Grillo *et al.*, 2018); (c) Spin-coating (Huang *et al.*, 2019); (d) Thermal coating (Kumru *et al.*, 2019); (e) Plasma etching (Rosso *et al.*, 2011); (f) Electronic beam etching (Riveiro *et al.*, 2018); (g) Wet chemical etching (Zhang *et al.*, 2020); (h) Silane treatment (Tan *et al.*, 2016a); (i) Hydrogel coating (Gao *et al.*, 2016); (j) Plasma etching (Rosso *et al.*, 2011); (k) Electronic beam etching (Riveiro *et al.*, 2018); and (l) Wet chemical etching (Zhang *et al.*, 2020).

2.4.3.1 Surface grafting

Surface grafting, as a bottom-up approach has been used to perform interfacial modification by either adding onto or growing the polymer chain from the material surface to achieve a desired surface property, such as anti-fouling, chemical stability, super wetting, biocompatibility, and antibacterial property, which find its applications in membrane technology, environmental remediation, adsorption, and oil separation.

Silane treatment is a liquid or vapor phase chemical reaction for surface grafting. The technique has been widely used in surface functionalisation due to its simplicity and cost-effectiveness. A broad range of chemical functionalities could be formed on the surface using different types of silane coupling agents (different functional groups) to enhance the mechanical properties, cross-linked density, thermal stability, improve wettability and dispersion stability. The surface activation through hydrolysis of the alkoxy group is crucial to have the good formation of silane treatment. Piranha solution is commonly hydroxylation method utilised to remove unbound and adsorbed surface contamination before surface activation and after silane treatment. Moreover, silane coupling agent also can act as surface modifier to improve hydrophobic property of the materials, which is favourable characteristics in water treatment. Zhang *et al.* (2019b) used a hybrid silane solution which is (3-Glycidyloxypropyl) trimethoxysilane (GPTMS) and (3-aminopropyl) trimethoxy silane (APTMS) as coupling agents. The silane coupling is to graft chitosan on the flat skew-hexagonal monolithic structure for heavy metal adsorption application. The deposited of the grafted chitosan were

confirmed via characterisation studies of fourier-transform infrared spectroscopy (FTIR), scanning electron microscopy (SEM), X-ray diffraction (XRD), and X-ray photoelectron spectroscopy (XPS). Zhang *et al.* (2019b) successfully fabricated an optimal design of a 3D porous structure with polymer chelation properties that exhibits high specific sorption capacity with fast reaction and superior diffusion resistance. However, the mechanical properties of the modified 3D-printed monolithic structure were not reported in this research.

In another study, Figuerola *et al.* (2022) utilised the surface grafting method to immobilize polyvinylidene fluoride (PVDF) derived carbons that act as a binder on the 3D-printed ceramic support and subsequent calcination. The PVDF/C-coated 3D printed ceramic device has good thermal stability as it can withstand temperatures above 1273 K with no apparent weight loss. Based on the UV–vis spectrophotometer reading, the intensity of the signal is always zero, indicating it is chemically stable and can be used in extraction applications. This study demonstrates that surface grafting can be used on ceramic supports under optimal grafting conditions. This method can overcome the limitation of functional porous solids becoming embedded in the binder, which limits overall performance.

In conclusion, surface grafting can be further utilised to achieve functional surfaces with tailored unique features. The drawback of this strategy is that it required compatible active materials such as modifier or crosslinker to graft with the 3D-printed monolith without compromising

the intrinsic properties of 3D-printed structure, impacting the 3D printing process and resolution.

2.4.3.2 Electron beam treatment

Electron beam etching methods have been widely used to improve the biological properties and quality of the printed parts by; (a) creating surface topography on the microstructures, (b) reducing surface roughness and grain size (Grillo *et al.*, 2018), and (c) producing antifouling, biocompatible (Jin *et al.*, 2021) and corrosion resistant surface (Huang *et al.*, 2019). This is primarily owing to the ability to accurately regulate the input energy and the remarkably short duration required for the process. The electron beams irradiation for polymers is widely adopted due to their variety of treatment conditions available and can efficiently modify the functional characteristics of the polymer surface while keeping the material's intrinsic qualities.

Shahbazi *et al.* (2020) used electron beam irradiation to crosslink acrylic acid graft copolymers into the structure of a high-performance 3D network nanohydrogel. The printed alginate/clay-g-poly (acrylic acid) nanocomposite ink was irradiated at different doses in a static mode of the conveyor belt using a Rhodotron-type electron accelerator machine at room temperature. The irradiated ink has shown improvement in structural strength due to the high extent of crosslinking density of the chains. From the result, the high density of the cross-linked network at 45 kGy was reported to have great water resistance and low water solubility, indicating the structure is stiff and capable to withstand mechanical deformation during printing including improvement in thermal

stability and crystalline properties after printing. This can conclude that the irradiation treatment significantly improves the quality of the printed superabsorbent hydrogel with a promising strategy to be applied in removing heavy metals in a short period.

Surface functionalisation, aided by etching, offers great postprocessing techniques as its low cost requires a simple process with high feature resolution. The problem with these approaches is the difficulty of efficiently and evenly etching complex 3D structures, particularly hierarchical porous structures. Additionally, it is hard to control the etching rate as it can affecting the mechanical properties of the printed parts and cause low feature resolution. Nevertheless, the electron beam irradiation treatment is worth investigating because it can create surface roughness and change the size of the particles, which will influence performance, particularly in the adsorption process in wastewater treatment.

In summary, surface functionalised 3D printing postprocessing methods using surface grafting and surface modification via electron beam irradiation have been extensively used to produce a variety of structural materials with distinctive properties. Some of the techniques were used as first-level modification techniques to preferentially change surface morphologies and physicochemical characteristics for ensuing functional postprocessing, while others were used as second level postprocessing techniques to produce other flexible features. Furthermore, in terms of surface properties, different approaches have distinct functionalisation capacities. It is worth noting that combining surface functionalisation

methods can lead to synergistic mechanisms that improve the overall performance of devices and components. As a result, this effective approach will be a powerful route to further improve and meet industrial demand.

Table 2.4.4: Overview of various surface functionalisation method in 3D printing for wastewater application.

Surface functionalisation techniques	Important steps	Surface enhancement property						Ref.
		Anti-fouling	Mechanical stability	Chemical stability	Hydrophilicity	Superoleophobicity	Hydrophobicity	
Atomic layer deposition	Partial hydrolysis basic solution followed by deposition of functional polyoxometalate anions	-	-	-	δ	-	-	(Ji *et al.*, 2018)
Atomic layer deposition	Deposition of TiO_2 layers with precursors ($TiCl_4$ and H_2O) and nitrogen as carrier gas.	-	-	ε	-	-	-	(Browne *et al.*, 2019)
Spin coating	Ink coating on the substrate layer-by-layer, with dip time of 10s followed by spin coating 1 min at 4000rpm	β	-	-	-	-	-	(Lyu *et al.*, 2020)
Dip coating	Hydrolysis using acidic solution followed by iron-oxide coating	-	-	-	δ	-	-	(Kim *et al.*, 2020a)
Dip coating	Mixture of polyamide-12 powder with the candle soot/hexane solution and left for evaporation	-	γ	ε	-	η	α	(Yuan *et al.*, 2020)
Dip coating	Immersion of 3D-printed PSU membrane in 0.1wt% mixture of candle soot/hexane solution	-	γ	ε		η	α	(Yuan *et al.*, 2017)
Dip coating	3D-printed device coated with MOF/polyvinylidene fluoride ink, followed by silver-functionalised UiO-66-SO_3H	-	γ	-	-	-	-	(del Rio *et al.*, 2021)
Electroless deposition	Surface activation steps: Immersing for 5 min in a Pd based commercial activator and subsequent immersion for 30 s in a reducing bath composed of $NaBH_4$. Deposition of copper using an alkaline electroless bath at 45 °C and pH 12 for 15 min	-	γ	-	-	-	α	(Bernasconi *et al.*, 2019)

Table 2.4.4: (Continued)

Surface functionalisation techniques	Important steps	Surface enhancement property						Ref.
		Anti-fouling	Mechanical stability	Chemical stability	Hydrophilicity	Superoleophobicity	Hydrophobicity	
Dip coating	Immersion of ABS polymer skeleton in cyclic steps in copper-benzene tricarboxylic acid solution for 8 cycles							(Wang *et al.*, 2014)
Electron beam etching	Electron beam irradiation treatment of nanocomposite hydrogel-forming ink via grafting copolymers	-	γ	-	-	-	-	(Shahbazi *et al.*, 2020)
Silane Treatment	Using hybrid silane coupling agent to graft chitosan brushes	-	γ	-	-	-	-	(Zhang *et al.*, 2019b)
Hydrogel coating	Immersion into acrylic acid (AA) & acrylamide (AM) solution followed by in the saturated salt solution	-	-	-	δ	η	-	(Yan *et al.*, 2019)
Hydrogel coating	Incorporating a zwitterionic hydrogel coating onto mechanically rigid membrane via in situ photopolymerisation	β	γ	-	δ	η	-	(Song *et al.*, 2020)
Wet chemical etching	Chemical etching in acetone followed by submerging in mixture of dopamine solution followed and polystyrene (PS) nanospheres	-	γ	ε	-	-	α	(Xing *et al.*, 2018)
Biofilm functionalisation	Forming initial film of BSA on catalytic static mixer (CSM), followed by dipped into the ZIF-8 precursor solution for 1 min and dried under a flow of N_2 gas	-	γ	ε	-	-	α	(Singh *et al.*, 2020)

Table 2.4.4: (Continued)

Surface functionalisation techniques	Important steps	Surface enhancement property						Ref.
		Anti-fouling	Mechanical stability	Chemical stability	Hydrophilicity	Superoleophobicity	Hydrophobicity	
Thermoset coating	Immobilized layer of graphitic carbon nitride homojunction (g-C_3N_4) homojunction-based thermoset coating via synthesis of gCN with ethylene glycol (EG), followed by photo grafting of hydroxyethyl methacrylate (HEMA) and crosslinked using citric acid	-	-	-	δ	-	-	(Phang *et al.*, 2021)
In situ chemical cross - linking	Soaking in high-concentration of $CaCl_2$ solution to increase its structural stability, followed by further treated in low concentration $CaCl_2$ solution for cross -linking.	-	γ	ε	-	-	-	(Fuxiang *et al.*, 2022)
Chemical cross - linking	Immersion into a 4wt% $CaCl_2$ aqueous solution	-	γ	-	-	-	α	(Pei *et al.*, 2020)
Plasma treatment	Using O_2 plasma treatment to fabricate nanopillars on the fiber surface	β	-	-	δ	-	-	(Ko *et al.*, 2021)
Biofilm growth	Inoculated for a period of 19 days in tilapia wastewater for microbial assemblages	-	-	-	-	-	-	(Proano-Pena, Carrano and Blersch, 2020)
Biofilm growth	Aerated in inoculated sludge for 30 days in a bioreactor for biofilm growth	-	-	-	-	-	-	(Tang *et al.*, 2017)

Table 2.4.4: (Continued)

Surface functionalisation techniques	Important steps	Surface enhancement property						Ref.
		Anti-fouling	Mechanical stability	Chemical stability	Hydrophilicity	Superoleophobicity	Hydrophobicity	
In-situ growth coating	Synthesized ZnO nanosheets on the surface of 3D scaffold followed by immersion in the solution. 30 mg/mL of NaOH/ethanol solution	-	-	-	-	-	α	(Kumbhakar *et al.*, 2021)
In-situ growth coating	Immersed in a 10 wt% solution of 2-methylimidazole in methanol and subsequent drying in a vacuum oven at 40 °C	-	γ	-	-	-	α	(Waheed *et al.*, 2021)
Plasma etching	Using radio frequency plasma-enhanced chemical vapor deposition for mesh fabrication, followed by coating with hexamethyldisiloxane (HMDSO)	-	-	-	-	-	α	(W. Jo, 2014)
Surface grafting	Dipped in a solution of PVDF in DMF, and calcined under N2 atmosphere in a tubular furnace at 1273 K	-	γ	ε	-	-	α	(Figuerola *et al.*, 2022)
Surface grafting	Dipped into silane-crosslinked chitosan solution for 45 minutes	-	γ	ε	-	-	-	(Husna *et al.*, 2022)

**Note: α: Increase in hydrophobicity; β: Enhance antifouling ability; γ: Improve mechanical stability; ε: Improve chemical stability; δ; Increase in hydrophilicity; ζ: Increase in hydrophobicity; and η: Increase in superoleophobicity.*

2.5 Recent advances of scientific and innovative functionalised 3D-printed enhanced adsorbent for dye removal

The recent advancements that take the approach of combining 3D printing and pre/post-treatment for performance enhancement in wastewater treatment for dye removal are summarised in Table 2.5.1, alongside the pros and cons of the application based on the proposed system and the performance efficiency including its reusability and recyclability. From Figure 2.5.2, it can be concluded that SLA, FDM, and SLS are the most preferred printing techniques to be utilised for fabrication and the chemical modification method is widely utilised for the post-treatment as shown in Figure 2.5.2. Various industries have shown an interest in serial production aided with FDM, compared to other printing techniques, although it has been proven that SLA is most preferred due to its precision and better quality of printing. As shown in Figure 2.5.2 and Figure 2.5.2, a detailed guideline was given from material selection, recommended printing technique, and lastly further post-treatment to be applied based on 3 different routes: chemical, physical, or biological functionalisation. From this guideline, the researchers can further develop based on their research of interest and opportunities in utilising additive manufacturing and surface functionalisation for various applications specifically in wastewater treatment.

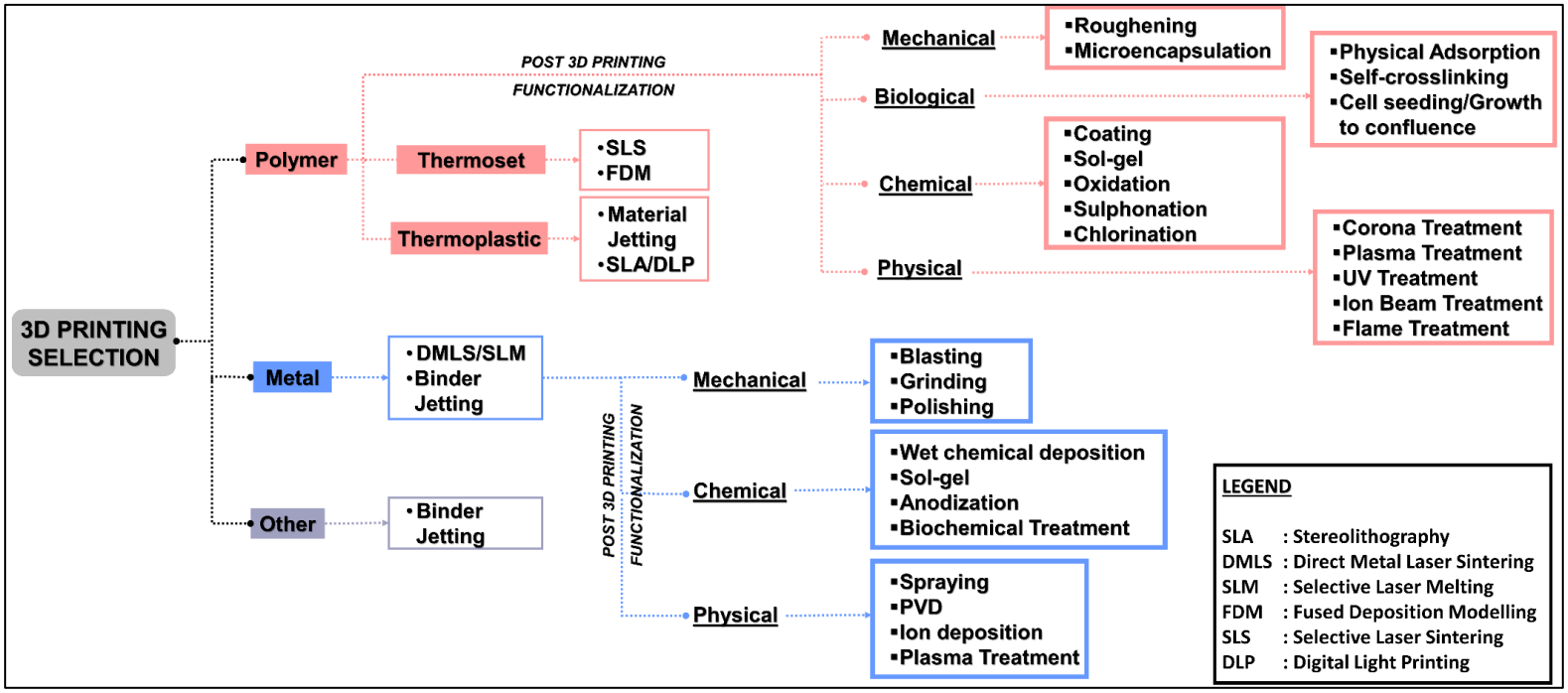


Figure 2.5.1: Schematic of 3D printing method selection and post 3D printing treatment for different type of materials.

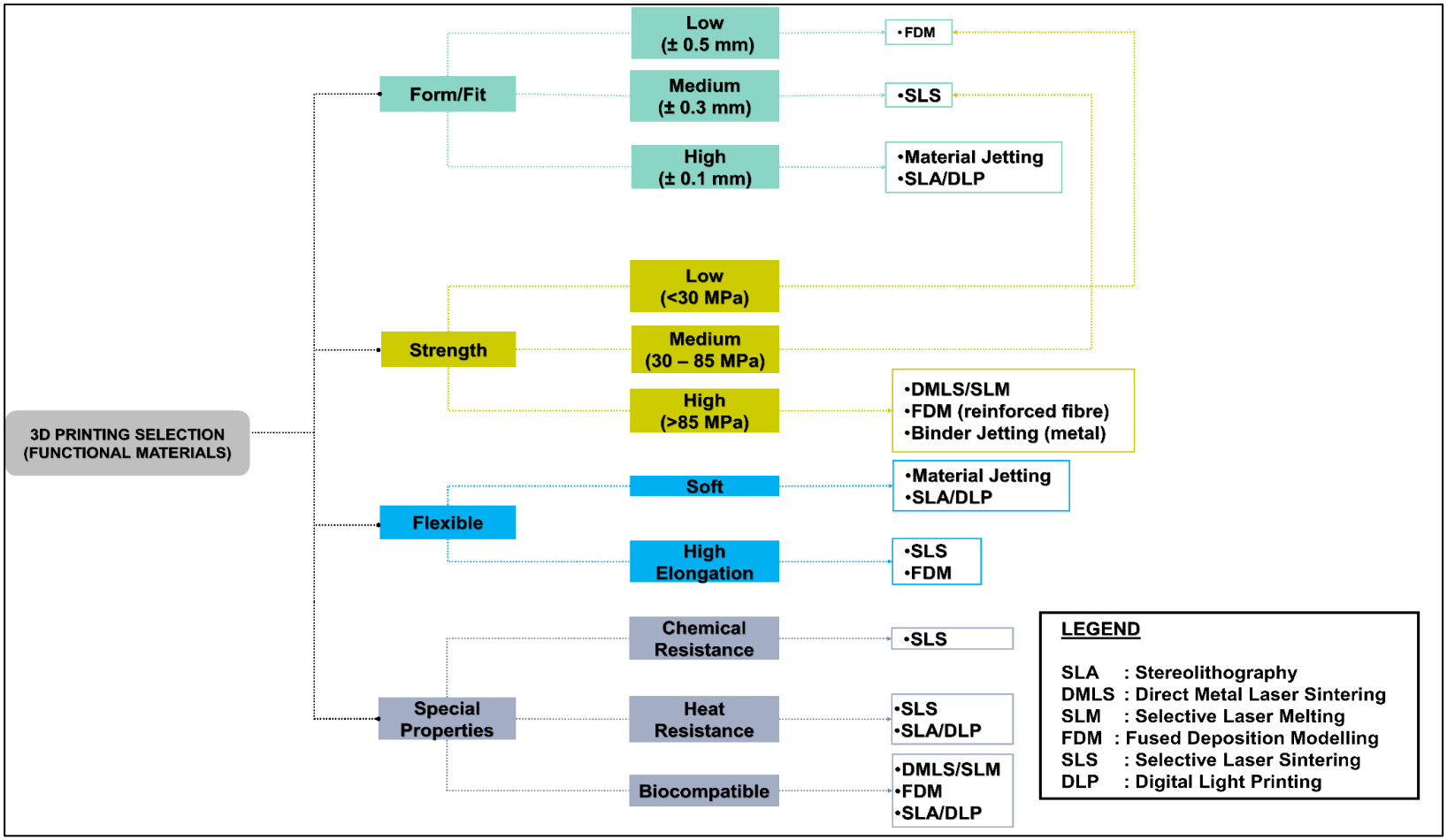


Figure 2.5.2: Schematic of 3D printing method for functional materials.

A lot of extensive works done by researchers to synthesise 3D-printed enhanced adsorbent to offer the purpose in dye removal especially in textile industry. For example, Wang *et al.* (2014) developed simple and complex coated 3D-printed acrylonitrile butadiene styrene (ABS) frameworks. The printed skewer was then coated with Cu-BTC via in situ stepwise coating. After that, the Cu-BTC/ABS was used as an absorbent to remove methylene blue from an aqueous solution. Wang et al. found that the removal efficiency of MB solutions was high, reaching 98.3% and 93.3% for the 5 and 10 mg/L concentrations, respectively, within 10 minutes. This work uses ABS extensively in synthesising the Cu-BTC/ABS composites. Hence, the ability of the ABS polymer to be recycled is critical for its practical applications. The MB removal efficiency remained over 58% (10 mg/L) and 68% (5 mg/L) after 5 cycles. Although the results for reusability and recyclability did not show a good value, the adsorbent can be easily separated without requiring centrifugation, filtration, or magnetic separation. This study demonstrates that the Cu-BTC/ABS composite may be an effective adsorbent for environmental cleanup and that 3D printing may be a quick and environmentally friendly way to create new functional composites for uses other than adsorption. In another study, Shi *et al.* (2017) developed similar approach by fabricating 3D-printed metal-organic-frameworks (MOF) with polylactic acid (PLA), where Cu-MOFs are coated on the surface via in situ step-by-step growth to remove malachite green (MG) from water. In this study, the printed PLA skeleton was coated with different layers of MOF. Figure 2.5.3a illustrated the SEM images of Cu-MOFs crystals after in situ

stepwise coating. It can clearly be seen that there are octahedral crystals on the PLA surface indicating the Cu-MOFs can growth efficiently on the PLA surface after multilayer of coatings via in situ process. The removal effectiveness of MG was determined to be greater than 90% within 10 minutes (Figure 2.5.3b). The coated PLA sheet with Cu-MOFs has high removal efficiency with spontaneous adsorption. It was discovered that the colour of the PLA skeleton changed to pure white during recyclability test using HCl solution, and SEM imaging revealed a smooth surface, as shown in Figure 2.5.3c. The film can also be washed in acetone and can be reused up to five times (. Figure 2.5.3d). Although it has excellent capability of removal within short period of time, however, it needs to recoat again for regeneration process and the removal efficiency decrease from one cycle to another cycle or repetition.

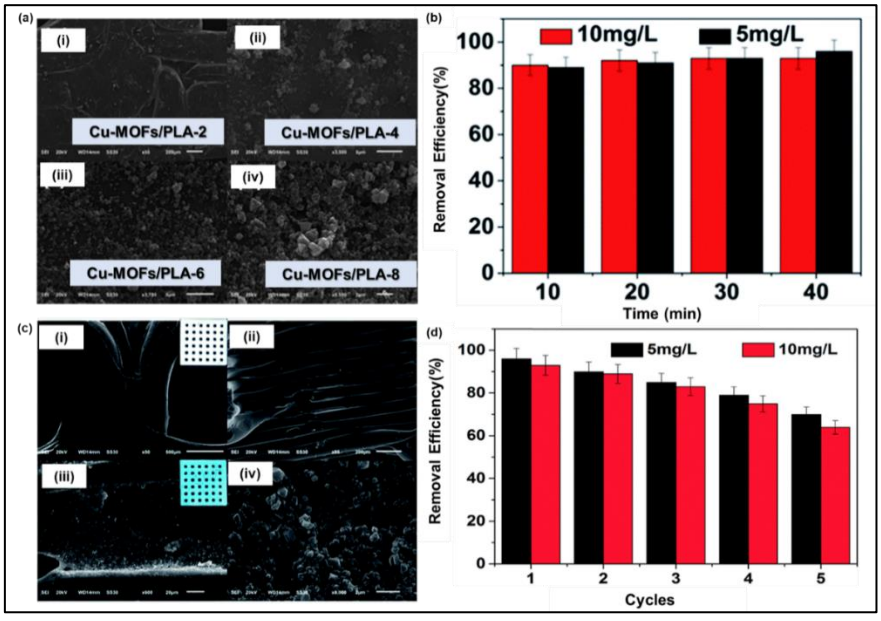


Figure 2.5.3: Application of various 3D-printed device for dye removal. (a) SEM images of various numbers of layers of MOFs coating; (b) Plot of removal efficiency of MG from water; (c) SEM images of regeneration of PLA skeleton; and (d) Plot of regeneration efficiency after 5 cycles.

Table 2.5.1: Summary of recent advancements in 3D printing for water treatment.

AM part fabrication	AM technique	Material	Surface functionalisation	Pollutant removal	Mechanical properties	Mechanism	Efficiency		Pros and cons	Ref.
							Performance capacity	**Reusability and recyclability**		
<u>Monolithic Structure</u>	SLA	Acrylate based UV curable resin (Asiga)	Surface grafting	Cu (II)	-	Adsorption	• Maximum adsorption capacity: 13.7 mg/g with skewed hexagonal holes	• Adsorption – desorption cycles: 13.7 mg/g – 11 mg/g after 4 repetitions • Desorption efficiency ~ 91%	+ Great advantages of simplified manufacturing, customized design, large yield, and fast treatment + High efficiency of bio-absorption – desorption + Easy to scale up for industry application - Need further study on competitive adsorption of multiple metal ions - Further lowering the processing solution viscosity and surface tension.	(Zhang *et al.*, 2019b)
	FDM	PLA	Dip-coating	Arsenic	-	Adsorption	• Removal rate of 96.2% for the 1st adsorption	• Adsorption capacities more than 77% after 3rd repeated recycling processes	+ Filter with larger internal surface areas offer better purification performance + Not required external pumping - Serve as a small-scale water-purification	(Kim *et al.*, 2020a)
	DLP	PEGDA and plant-based commercial resin	Surface grafting and dip coating	• Methyl orange (MO) dye • COD • BOD	• Storage Modulus: 427.73 MPa • Ultimate Tensile Strength: 1.34 MPa	Adsorption	• MO dye: 90.4% • COD: 2.0% • BOD: 62.4%	• Adsorption – desorption cycles retained at 78% after 4 cycles	+ New material design for lattice structure monolith with formulated biopolymer ink + High adsorption efficiency with great mechanical stability + Easy to scale up and maintain after performance degradation - Require adsorption enhancement for COD removal - Further optimisation is required for material stability for real application	(Husna *et al.*, 2022)
<u>Scaffold</u>	FDM	ABS	Atomic deposition process	Heavy metal	-	Adsorption	• Removal efficiency ✓ Cu^{2+} : 67.1% ✓ Ni^{2+} : 44.2% ✓ Co^{2+} : 40.5%	-	+ New material designed for porous polymer/polyoxometalate (POM) composites + No leaching of the POM + Stable deposition of the POMs - Longer adsorption time (> 12 hours) - Lower removal efficiency	(Ji *et al.*, 2018)
	SLA	Clear photoactive resin	Coating	Radioactive iodine	-	Adsorption	Extraction: • 50 Bq: 100% extraction • 1000 Bq: 86%	Recovery rate after 3 consecutive cycles remain with hospital waste: (90 ± 5%) and sewage waste (98 ± 4%)	+ Excellent extraction capacity + Able to be used in real water samples with recovery rate of 90% + No significant Ag leaching detected + Longer extraction time (~24 hrs)	(del Rio *et al.*, 2021)

Table 2.5.1: (Continued)

AM part fabrication	AM technique	Material	Surface functionalisation	Pollutant removal	Mechanical properties	Mechanism	Efficiency		Pros and cons	Ref.
							Performance capacity	**Reusability and recyclability**		
	DIW	Sodium alginate	In-situ chemical cross-linking	Uranium (VI)	-	Adsorption	• Adsorption from 53.84% to 98.08% with different concentrations within 15 h	• Adsorption percentage only dropped by approximately 18% after 6 cycles	+ Able to print macroscopic structure and layered microstructure. + Excellent U(VI) recovery and enrichment from strong acidic aqueous solutions + Good acidic stability without compromising the structure and performance - Longer reaction time (within 15 h) - Lower adsorption (24%) in co-exist synthetic radioactive wastewater	(Fuxiang *et al.*, 2022)
	DIW	Sodium alginate/gelatin/Cu-BTC nanoparticle	Chemical cross-linking	• Methylene blue (MB) dye • Methyl violet (MV) dye • Malachite green (MG) dye • Rhodamine B (RhB) • Auramine O (AO)	• Tensile strength: 0.4MPa • Ultimate elongation: 56.7% • Compressive strength: 1.79 - 2.62 MPa	Adsorption	• MB dye: 99% • MV dye: 98% • MG dye: 83% • RhB dye: 79% • AO dye: 38%	• Removal efficiency still retains 82% after repeated use for 10 times	+ Excellent recyclable, and scalable adsorbent with required mechanical strength for practical usage + Printed adsorbents can be fully regenerated + Fast reaction time (20 min)	(Pei *et al.*, 2020)
	GP	Na-alginate/clay nanocomposite	Etching	• Lead (II)	• Elastic moduli of irradiated inks > non-irradiated up to 45 kGy	Adsorption	Adsorption Capacity: - • With irradiation - 241 mg/g at 45 kGy • Without irradiation - 308 mg/g	-	+ No post-print crosslinking is needed + Faster adsorption kinetics (< 10 mins) + High-capacity and fast-responsive - Decrease in adsorption ability with the interference of other metal ions - Remaining adsorbent sites difficult to occupy - Weak structure with poor water resistance	(Shahbazi *et al.*, 2020)

Table 2.5.1: (Continued)

AM part fabrication	AM technique	Material	Surface functionalisation	Pollutant removal	Mechanical properties	Mechanism	Efficiency		Pros and cons	Ref.
							Performance capacity	**Reusability and recyclability**		
	FDM	ABS	In-situ growth	Malachite green (MG) dye		Extraction	Malachite green removal at 93.3% with extraction time of 300 min	Extraction efficiency remains at 90% and can be reused atleast 4 times	+ New fabrication method of using functional materials of reactive zinc oxide nanoparticle (NP) / thermoplastic composite filament + Superior performance for the dye extraction - Require recoating of functional materials after 4th cycles - Longer extraction time +	(Waheed *et al.*, 2021)
	SLA	Commercial ceramic resin (Form abs)	Coating	• Pharmaceutical pollutants • Methylene blue (MB) dye • Malachite green (MG) dye	-	Adsorption	• With well water sample: - Pharmaceutical pollutants: 98.9 ± 1.1 % - MB dye: 99.0 ± 1.3 % - MG dye: 99.2 ± 0.9 % • With real wastewater sample - Pharmaceutical pollutants: 98.7 ± 2.2 % - MB dye: 99.1 ± 1.1 - MG dye: 98.7 ± 1.9	- Adsorption capacity remained above 90% after 10 cycles	+ Long-term stability and durability + High specific area and porosity + Exhibits high performance with excellent reusability for practical application + Fast reaction of pollutant extraction within 2 h	(Figuerola *et al.*, 2022)
Mesh	FDM	PLA	Hydrogel coating	• Oil/Water separation	-	Demulsification & filtration	• Separation efficiency of up to 85%	- Separation efficiency remained at ~90% after 15 cycles	+ Excellent underwater repelling and easy flowing away of the oil + Good superhydrophilicity and underwater superoleophobicity	(Yan *et al.*, 2019)

Table 2.5.1: (Continued)

AM part fabrication	AM technique	Material	Surface functionalisation	Pollutant removal	Mechanical properties	Mechanism	Efficiency		Pros and cons	Ref.
							Performance capacity	**Reusability and recyclability**		
Mesh	ME	PVA	Oxygen plasma treatment	Oil/Water separation	-	Filtration	Oil recovery of 95% of the spilled oil	Reusability with > 95% after 5 cycles	+ Excellent efficiency of viscous oil recovery with 180 times higher than conventional oil sorbent + Evaluated filtered water has low oil content (<10%) + Can be utilised for the recovery of floating hazardous substance such as hexane Good water-absorbing, and retaining ability oil recovery device	(Ko *et al.*, 2021)
	CJP	Cyanoacrylate	Oxygen plasma etching technique and coating	Oil/Water separation	-	Filtration	• High separation efficiency **Not stated*	-	+ Exhibited sufficient superhydrophobic and superoleophilic properties + Able to construct micro or nanoscale hierarchical structured using a plasma etching method + The behavior of oil/water separation depending on the different pore sizes although at the same surface condition	(W. Jo, 2014)
	FDM	PLA	Coating	Malachite green (MG)	-	Adsorption	• Adsorption more than 90% with different concentrations • With real water: - Tap water: 93% - Lake: 90% • River: 91%	-	+ Rapid, high-efficiency, economic and convenient adsorption + Fast adsorption time (10 min) + Require recoating procedure for 2nd reusability	(Shi *et al.*, 2017)
	FDM	ABS	Coating	Methylene blue (MB) dye		Adsorption	• Adsorption efficiency: - 10mg/L: 93.3% • 5 mg/L: 98.3%	Removal efficiency retained over 58% (10 mg/L) and 68% (5 mg/L)	+ Offer flexible control of 3D structure with good adsorption performance + Does not require centrifugation, filtration or magnetic separation for desorption + Can be reused and recovered + Require further mechanical stability validation	(Wang *et al.*, 2014)
Membrane	SLS	Polyamide-12	Dip – coating	Oil/Water separation	Tensile strength: ~ 4.7Mpa	Filtration	• Separation efficiency over 99%	-	+ Has very good chemical and mechanical stability even in polar and nonpolar solvents + Can be applied for separation of immiscible organic liquid mixtures + Exhibits hydrophobic, superoleophilic, and underwater superoleophobic	(Yuan *et al.*, 2020)

Table 2.5.1: (Continued)

AM part fabrication	AM technique	Material	Surface functionalisation	Pollutant removal	Mechanical properties	Mechanism	Efficiency		Pros and cons	Ref.
							Performance capacity	Reusability and recyclability		
	SLA	Clear resin (Form labs)	Hydrogel coating	Oil/Water separation	• Tensile modulus 1.1 GPa	Filtration	~100% efficiency	Achieved superior flux for at least ~31 repeating cycles	+ Prominent for reducing oil fouling + Able to support gravity-driven oil-water separation – does not require any external energy + Exhibits hydrophilic/oleophobic properties	(Song *et al.*, 2020)
	DLP	(UV) curable resin	Chemical vapor deposition	Oil/Water separation	• -	Filtration	More than 90% separation efficiency	Steady oil collection efficiency after 10 test cycles ~ 90%	+ Highly efficient floating oil removal + Good durability and oil keeping stability- store oil directly + Exhibit hydrophobic properties + Require scale up and real application validation	(Yan *et al.*, 2016)
	FDM	Alumina ceramic	Dip – coating and spin coating	Wastewater treatment	• -	Filtration	-	-	+ Easy to design any complex architecture and fast fabrication process + Advanced ceramic membrane for wastewater treatment + Has good gradient porous structure + Require optimisation for anti-fouling properties	(Lyu *et al.*, 2020)
	SLS	PSU	Dip – coating	Oil/Water separation	• Tensile strength: • 17.3Mpa	Filtration	• Separation efficiency over 99% with the gravity-driven flux of around 19 000 L (m^2 h)$^{-1}$	• High separation stability ~ higher than 99% after 10 cycles	+ Has good chemical and mechanical stability in acid and alkaline solutions + Exhibit super-hydrophobic surface that could switch to a super-oleophobic state	(Yuan *et al.*, 2017)
Photocatalyst	DLP	HDT resin and Eco UV clear resin	Thermoset coating	• Rhodamine B (RhB) dye Total organic carbon (TOC)	• -	Photodegradation	• RhB dye: 95.62% of dye degradation (with k value of 2.1×10^{-3} min^{-1}) • TOC:78.56% removal under the irradiation	• Retained 98.5% its original photocatalytic efficiency after 5 cycles	+ Eliminate the additional centrifugation step for recovery and photocatalysis + Achieve excellent degradation performance and reusability - Longer degradation time ~ 24 h + Require optimisation on design, material selection, method of coating and operational parameter	(Phang *et al.*, 2021)

Table 2.5.1: (Continued)

AM part fabrication	AM technique	Material	Surface functionalisation	Pollutant removal	Mechanical properties	Mechanism	Efficiency		Pros and cons	Ref.
							Performance capacity	Reusability and recyclability		
	FDM	PLA	In-situ growth coating	• Methyl orange (MO) dye • Rhodamine B (RhB) dye Methylene blue (MB) dye	-	Photodegradation	• Maximum performance removal efficiency with Weissmuller structure • Mixed dye: ~91% • RhB dye: ~88% • MB dye: ~81% MO dye: ~54%	• Retained about 90% its photodegradation efficiency up to 5 cycles with Weissmuller structure	+ User-friendly and low-cost process photocatalytic activity + Quantitative investigation of water cleaning using smartphone-based analysis + Good surface porosity + Superior photodegradation efficiency within shorter time (10 min)	(Kumbhakar *et al.*, 2021)
Biocarrier	MJ	Acrylate resin	Bacterial deposition	Ammonia	•	Nitrification	• Higher of 1.620 ppm per day compared to the commercial carrier of 0.710 ppm.	-	- Novel complex media designs with great microbial assemblages - Can withstand typical operating conditions of MBBR - Result obtained is not statistically significant - Lengthy printing process and requires higher fabrication cost - Still at preliminary work that requires further optimisation and validation	(Elliott *et al.*, 2017)
	SLA	Isocyanate and polyhydric alcoho	Biofilm deposition	+ COD + Total nitrogen (TN)	-	Nitrification	+ COD: 99% + Total nitrogen (TN): 90%	-	- Novel design of semi-suspended bio-carrier with a spindle shape - Fast growing of biofilm (early formation at 6 days) - Complete growing cycles from attachment to maturity stage of biofilm takes about 30 days	(Tang *et al.*, 2017)
Mixer	DLP	ABS	In-situ coating and encapsulation	• Methyl parathion (MP) • Cu^{2+} ion	-	Biodegradation	+ MP: ~ 90% conversion + Cu^{2+} ion: 42%	-	+ Precise integrated catalytic enzyme onto 3D-printed polymer + Simple production process and easy to be scaled up - Lower removal capacity of heavy metal	(Singh *et al.*, 2020)
Microrobot	SLA	Urethane acrylate-based resin	Wet metallization (nanocoating)	• Rhodamine B (RhB) Bacteria *(Staphilococcus Aureus)*	-	Photodegradation	• Bacteria degradation - 89%	•	+ Fast fabrication time (30 min) + Cost-effective fabrication with excellent integrity - Require support material during printing process - Limited resolution (only for microscale)	(Bernasconi *et al.*, 2019)

*Note: The symbol “+” and “- “represent the advantages and disadvantages of the functionalised AM fabrication parts used in water treatment

2.6 Current challenges of the application of functionalised 3D-printed enhanced adsorbent for dye removal

The adoption of additive manufacturing for wastewater treatment applications has shown significant growth in the industry, including surface functionalisation of 3D-printed monolith using physical and chemical modifications. Many current studies have investigated and demonstrated the potential of surface functionalised 3D-printed monolith as emerging and innovative wastewater treatment methods of industrial standard. Despite the rapid development, challenges such as materials selection, additive manufacturing procedure, and resolution require continuous improvements. An important diagram representing the development of surface functionalised 3D-printed monolith for wastewater application is shown in Figure 2.6.1.

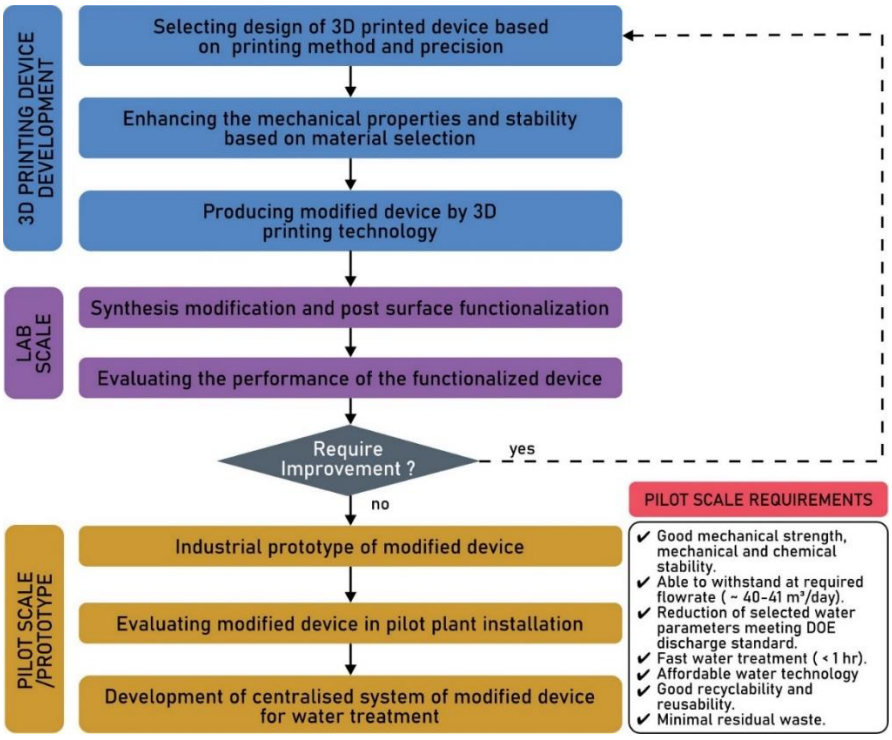


Figure 2.6.1: Future look of surface functionalised 3D printing technology for wastewater treatment applications.

Firstly, the mechanical strength and stability of 3D-printed monolith continue to be critical issues in creating robust and functional layers that promote interfacial adhesion between 3D structures. Assessing the mechanical properties of 3D-printed monolith is critical not only to their design, but also for studying their failure mechanisms, including the surface damage, mechanical and chemical ageing, delamination, and loss of dimensional stability. Further research is necessary to elucidate the mechanism in enhancing interfacial bonding when a surface functionalised strategy is used. Previous studies have revealed the effective interfacial bonding for polymeric materials is via the chemical approach. For example, the adhesive mechanism in low-surface-energy polymeric materials is not adequately understood, which could limit the wider applications of the material.

Secondly, stability of the 3D-printed monolith in extreme conditions, such as strong acidic and alkaline media, is crucial as the substrates produced by 3D printing play a significant role in defining the functional and structural features of the wastewater treatment device. Moreover, it is also important to avoid leaching into the environment. There is evidence that certain polymer materials used in 3D printing form leachates and affect the environment and aquatic life when they come into contact with water. To date, there is no clear information on the limits of chlorine/chemical resistance, which leads to degradation and eventual reduction of performance, especially in wastewater treatment. Due to this limitation, it was suggested that the chemical stability of 3D-printed

monolith need to be improved while maintaining efficiency through chemical modification and surface functionalisation.

Lastly, hydrophobic or superhydrophobic is the key surface property as it affects the overall achievable adsorption efficiency. The degree of surface wetting was highly dependent on the interfacial tension between the phases in contact. Surface wettability is influenced by nanofeatures or dual-microfeatures, as well as the surface's chemical composition. Although the utilisation of 3D printing could assist in the creation of superhydrophobic surfaces by decrease the quantity of steps in the printing process, the need for subsequent coatings remains a key problem to address. Currently, surface functionalisation is a desirable technique to control the wetting properties of 3D printing structures.

The development of multifunctional 3D-printed enhanced adsorbent and components that utilise functional-induced biomaterials combined with desirable surface-modified functionality could be a promising approach. A substantial effort in synthesis modification and post-synthetic functionalisation involving the attachment or incorporation of adsorbent has potential to be utilised for dye colour removal. In addition, the surface grafting method can form a chelating and strong bond to both polar and non-polar surface character of the pollutants. Therefore, surface functionalisation with the integration of 3D printing has shown an avenue that has promising direction in this field. The surface functionalisation method of post 3D printing is limited and tailored to certain types of materials (i.e., polymer, metallic surface), which require further exploration. Therefore, this thesis is mainly evaluating the surface

functionalisation technique to fabricate high-performance emerging grafted 3D-printed monolith that can be used for dye colour removal. The ultimate goal of this research is to design an innovative adsorbent with centralised system of functional technology for wastewater treatment applications.

2.7 Deep learning for colour prediction of textile wastewater using real-time images

Artificial intelligence (AI) has emerged as a possible method for monitoring the colour index. In textile wastewater, colour is one of the most noticeable visual contaminants in textile effluent (Liu, Lo and Kan, 2022). Coloured pollutants have also been shown to be harmful and carcinogenic and caused complaint among the public. Moreover, as pollution restrictions tighten, the textile sector is under pressure to release higher-quality effluents. Colour is one of the pollution control parameters that affect textile dyeing processes which can be monitored by visual comparison and spectrophotometric methods (Suwanboriboon, Meesiri and Wongkokua, 2018). The transparency approach involves a subjective visual comparison analysis. As a result, it is unsuited for regulating coloured industrial effluents (Kao *et al.*, 2001). On the other hand, the American Dye Manufactures Institute (ADMI) units' method has been used for measuring the sample's true colour, regardless of hue which is more suitable for textile effluents (Yu *et al.*, 2006; Suwanboriboon, Meesiri and Wongkokua, 2018). This is because the colour attributes of industrial wastewater are governed by the type of wastewater and dye pigment used in the process, which has a significant

colour index variability. However, the application of adopted analytical method using ADMI is remained a challenge as not all spectrophotometers available in the market has the ADMI method and standards. The common colour characteristics measured in spectrophotometer is in platinum-cobalt (Pt-Co) standards, which only has the ability to measure similar in hue concentration to the standards (Kao *et al.*, 2001). Therefore, as alternative method, the textile manufacturers have to opted to outsource the sample to analyse the colour of wastewater at relevant laboratory which is time consuming and expensive.

Due to this constraint, the practice of image analysis has emerged as a prominent analytical tool to speed up the process and give real-time colour index. They are useful for classifying patterns in data with minimal assumptions, where great prediction accuracy can be achieved by fine-tuning the algorithm. Recent improvements have shown that image processing algorithms have been successfully utilised for predicting the colour of the lakes or wastewater. The utilisation of deep learning methodologies, specifically convolutional neural networks (CNN) and AlexNet have demonstrated their remarkable performance in the realms of image processing analysis and classification. CNN has been introducing a proficient group of models to enhance comprehension of the elements depicted in an image, thus leading to improved image identification, division, detection, and recovery. The advantage of employing CNNs lies in their capability that enables the model to acquire knowledge of both position and scale within the data of the images, even

in the presence of diverse structures, which is particularly crucial in the context of image processing. Moreover, its effectiveness primarily hinges on the architectural design of the convolutional layers and the volume of data employed for training the network. However, when confronted with a small training dataset, achieving high accuracy poses a daunting challenge due to the phenomenon of overfitting. AlexNet, which has previously been trained on a big picture dataset, can produce good results when dealing with small datasets. Vijay Anand *et al.* (2023) has first proposed a conceptual design utilising CNN to predict the quality of the lake water based on the colour. This model proves advantageous for the initial stage of testing with the aim of ascertaining the suitability of water for prospective application. The prediction accuracy level for the collected water samples stands at 85%. Although it produced a good accuracy percentage, it is easy to predict the colour of the lake water as the colour ranges from pale to dark green. However, the application of the model for textile wastewater, it is remained a challenge due to the variation of colour produced in a daily basis of the production at the wastewater treatment plant. Nevertheless, the utilisation of an image processing tool significantly improves the effectiveness to predict the colour of textile wastewater. Furthermore, it can serve as a straightforward and expeditious approach and open a door for its application to assess the colour of different type of wastewaters.

CHAPTER 3: 3D - PRINTED PEGDA MONOLITH WITH ROBUST SILANE - GRAFTED CHITOSAN FOR ENHANCED TEXTILE WASTEWATER TREATMENT

This chapter covers the novel design of chitosan - grafted PEGDA monolith using DLP printing technology and post-treated with surface grafting process. The adsorption performance was evaluated using response surface methodology (RSM). The optimised condition was used for BOD and COD reduction using real textile wastewater, alongside recyclability and reusability of the technology were studied for practicality in the industry. This chapter consists of thesis-version of work submitted in the *Journal of Environmental Chemical Engineering.*

ABSTRACT

A novel and newly developed 3D-printed poly (ethylene glycol) monolith grafted with chitosan was fabricated by adopting a robust approach, combining 3D printing technology and surface grafting to improve the adsorption capacity. In present work, response surface methodology (RSM) approach was used to investigate the controlling factors of dipping time, chitosan concentration, pH and temperature. All factors have significant effect on adsorption performance, except for dipping time. The removal efficiency (R%) of methyl orange (MO) dye ranged from 20.8% to 90.4% and the equilibrium uptake capacity (K) ranged from 1 to 12.7 (mg/g) after 2 h. Six isotherm models, adsorption kinetics, followed by thermodynamic studies were performed. BOD and COD tests were analysed to investigate the feasibility of its use in wastewater treatment. The recyclability of the grafted - chitosan PEGDA monolith was verified by evaluating its adsorption for four cycles and retained at 78%, indicating it is stable and reusable. It also has good mechanical properties and stability, which is practical to be applied in real application. The synergistic effect of 3D-printed monolith and tuneable chemical properties of the monolith surface enhances the adsorption performance, while implementing a statistical tool to determine the optimal conditions and influenceable process parameters with good predictability.

Keywords: 3D printing; chitosan; silane; adsorption; optimisation; wastewater treatment

3.1 Introduction

The textile industry plays an important role in the economy of several countries around the world. However, the undesirable dye wastewater containing various impurities is a significant problem in textile wastewater and has become a major environmental problem (Yaseen and Scholz, 2019). Due to their hydrolysing property in water, reactive textile dye wastewater pollutes the environment in comparison to other textile dye wastewater. Generally, nearly 10 - 50% of all used reactive dyes remain in wastewater after the dyeing stage (Sadeghi-Kiakhani, Arami and Gharanjig, 2013). Therefore, the reactive dyes removal from wastewater is crucial to prevent the release of hazardous dyes into the environment. Apart from this, wastewater also contains high chemical oxygen demand (COD), biochemical oxygen demand (BOD), suspended solids and other pollutants. Therefore, the standard concentration as set in industrial effluent discharge regulations must be complied with before the treated wastewater being discharged to the environment. There are three main categories (physical, chemical, and biological) for dye removal treatment.

There are three main categories (physical, chemical, and biological) for dye removal treatment. Among these methods, physical or physicochemical treatment with adsorption is the most effective dye remediation method. This is because of the large number of adsorbents available, ease of operation, high efficiency, and economic feasibility of all dye removal treatment processes (Das and Debnath, 2021). Commonly, adsorbents are derived from natural resources such as clays,

ores, zeolites, charcoal and other waste materials including fly ash, palm kernel and saw dust. Chitosan (CS), a kind of bio-adsorbent, has attracted attention in various applications due to its adsorption performance, biocompatibility and non-degradable properties (Bakshi *et al.*, 2020). A typical application for the use of chitosan as an adsorbent is the dissolution of chitosan powder or flakes in an acidic solution (Szyguła *et al.*, 2008). Thus, this process was intended for a single function and the recycling process is complex (Zhang *et al.*, 2019a). Moreover, according to Li *et al.* (2019), the application of using chitosan flakes is not favourable due to its low surface area, exhibits hydrophilicity, non – porous and has low adsorption capability.

Thus, blended/functionalised chitosan have become the focus of recent research due to their excellent biosorption properties such as macromolecular and cationic structure with high adsorption rate. To overcome the above limitations of the current technology, a newly developed strategy was introduced to improve the applications in terms of adsorption efficiency, reusability, and recyclability. Physical functionalisation of chitosan by grafting/brushing onto the adsorbent is an alternative technique to overcome the shortcomings where this method does not compromise the biocompatibility and biodegradability of chitosan (Qamar *et al.*, 2020).The functional derivative can be attached to the chitosan backbone via hydroxyl groups or free amino groups. Silane coupling agents are among the bioactive functional derivative used to functionalise hydrophilic materials and bonded with epoxy and methoxysilane groups of organic materials. Silane coupling

agents show bioactive properties to structures and increase mechanical properties, free volume, interaction energy as well as hydrogen bonds on thermodynamic properties (Wang *et al.*, 2019). Due to the aforementioned properties, silane coupling agent is widely used in tissue engineering application and polymers processing, but very less in water treatment (Aziz *et al.*, 2021). Silane coupling agent is a way of taking an eco-sustainable approach with excellent mechanical, swelling and dynamic viscoelastic properties of materials that potentially to be used in water applications.

Monolithic structured adsorbents are advantageous in recent studies because the structures can be mass-produced, have high stability with a controllable pore structure, and are efficient (Prevot and Tokudome, 2017; Zhang *et al.*, 2011b). Moreover, by incorporating the structure and materials used in monoliths, a package of integrated functional adsorption and photocatalysis could be provided. For example, Zhang *et al.* (2019a) fabricated a highly reusable and porous chitosan monolith that can adsorb Cu (II) ions. This method took advantage of 3D printing for the optimal design of the porous structure combined with surface functionalisation techniques for immobilized functional chitosan layers on the surface, resulting in a fast response with high specific sorption capacity and excellent diffusion resistance. Newly developed 3D-printed monolithic scaffold has become a hot research topic in recent years, but its application is still limited to certain fields such as gas separation, chemical reactors as a monolithic adsorbent, and metal ion removal, based on various studies conducted (Mohd Yusoff *et al.*, 2022). As far as

we know, the integration of 3D-printed monolith with silane crosslinked chitosan for dye removal and COD and BOD reduction has not yet been described in any experimental work and literature.

Therefore, in this work, a newly developed grafted - chitosan 3D-printed monolith is fabricated using Digital Light Processing (DLP) 3D printing technology and grafted with a layer of silane cross-linked chitosan. This silane cross-linked chitosan layer will be used as a filter for water treatment. A batch process has been studied in this work to investigate the adsorption performance of the grafted – chitosan 3D - printed monolithic adsorbent with methyl orange dye (MO) and real textile wastewater samples. In addition, the Response Surface Methodology (RSM) approach developed in Minitab 19 software has been used as a tool to define the design of experimental (DOE). The DOE is used to determine the optimal conditions for the selected process parameters that contribute significantly to the adsorptive performance and to reduce the number of experiments. This research demonstrates a robust and novel way to combine 3D printing technology with surface grafting as a sustainable strategy for various wastewater applications. In the next part of the paper, Section 3.2 will describe materials used and methods applied in this experiment, followed by results and discussion Section 3.3 in and lastly the conclusion for the experimental work.

3.2 Materials and methods

3.2.1 Materials

Chitosan (CS) white powder (AR grade; degree of deacetylation of 99%, MW: average of 890,000 g/mol) was purchased from Fulltime Asia Sdn. Bhd. Isopropyl alcohol (IPA) (≥90%, MW: 60.1 g/mol), hydrochloric acid (HCl) (37%, MW:36.46 g/mol) and sodium hydroxide (NaOH) (99%, MW: 40 g/mol) were purchased from Giti Eco Sdn. Bhd, Malaysia. Poly (ethylene glycol) diacrylate (PEG200DA) and liquid resin (≥ 99.9%, MW: 308 g/mol, viscosity: 10 – 30 cP at 25°C) were purchased from Ryoji, China. Photoinitiator (Irgacure 819); Phenylbis(2,4,6-trimethylbenzoyl) phosphine oxide (MW: 418.5 g/mol) and methyl orange dye (MO) ACS reagent (85%, MW: 327.34 g/mol, pKa = 3.4) were purchased from Chemmart Asia Sdn Bhd. COD digestion vials [high range (20 - 1500mg/L)], and nutrient buffer solution pillows were purchased from HACH Malaysia Sdn Bhd. Glycidyloxypropyl trimethoxysilane (GPTMS) (≥98%, MW: 236.34 g/mol) and (3-aminopropyl) trimethoxysilane (APTMS) (97%, MW: 179.29 g/mol, density: 1.027 g/mL at 25°C) were purchased from Macleans, Shanghai respectively. Distilled water was used in all experiments.

3.2.2 Fabrication of 3D-printed monolith

A 3D printer was used to fabricate the 3D-printed monolith, using the Digital Light Process (DLP) method via photo-polymerization of the photo curable resin with a cross-linker. This printing technique is preferred due to its excellent printing accuracy and speed (Zhang *et al.*, 2019c). The photo curable polymer liquid resin was formulated using a polymer matrix

of polyethylene (glycol diacrylate) (PEG200DA), a plant-based photopolymer resin, and 1 wt.% photoinitiator (PI), as shown in the schematic diagram in Figure 3.2.1a**.** PEG200DA was preferred as the base because the 3D structure is easy to fabricate and allows precise surface functionalisation (Khandaker *et al.*, 2016). The liquid resin was then mixed well for 30 min using a magnetic stirrer (Thermo Fisher Scientific, United Kingdom). Computer-aided design software (CAD) was used to design the monolith structure with dimensions (0.5 cm × 2 cm ×1 cm). The 3D monolith was printed layer by layer using a Phrozen Sonic Mini UV Photocuring LCD resin 3D printer. During this procedure as shown in Figure 3.2.2, Irgacure 819 absorbed the UV light and produces free radicals. These free radicals then combined and reacted with monomer molecules, which is PEGDA by opening the carbon-carbon bond. Reactive monomers then combine to form large molecules, which continue to grow until two chains combine and the reaction is terminated (Yang *et al.*, 2015). The finished product was then rinsed with isopropanol to remove all resin and surface residue before being irradiated with UV light for 10 min. The printer processing parameters are presented in Table 3.2.1.

Table 3.2.1: 3D printing process parameters.

Printing Parameter	Value
Exposure Time (s)	4
Bottom exposure time (s)	40
Light-off delay (s)	7
Bottom light-off delay (s)	7
Lift distance (mm)	5
Bottom lift distance (mm)	6
Lift speed (mm/min)	100
Bottom lift speed (mm/min)	100
Retract speed (mm/min)	200
Layer height (mm)	0.05

3.2.3 Synthesis of silane - grafted chitosan of 3D-printed monolith adsorbent

The newly silane - grafted chitosan of 3D-printed monolith was prepared by grafting, according to the procedure of Zhang *et al.* (2019a) with some modifications, as shown in the schematic diagram in Figure 3.2.1a-c. GPTMS and APTMS was used as a hybrid coupling agent and as a crosslinker to crosslink chitosan onto the acrylate substrate, in this case PEGDA. First, a formulation of the coupling agent was prepared by dissolving 3 ml of GPTMS in 1 ml of APTMS, 6 ml of IPA, and 1 ml of DI water. Then, the solution was mixed with 2 wt.% chitosan solution (pH ~ 5) at a ratio of 1:10 and stirred for 10 min. Then, the chitosan growth procedure was performed by immersing the sample in the mixture, as depicted in Figure 3.2.1b and leaving it at 60℃ for 4 h in the oven as presented in Figure 3.2.1c. The sample was then rinsed with DI water to remove all impurities and the polymer on the surface. The surface area

of the chitosan grafted PEGDA monolith was determined using ImageJ software. The calculated surface area is 0.532 m^2/g.

The surface grafting mechanism started with epoxide-amide reaction where the O-Si-O from GPTMS will covalently bonded to the H-N-H of chitosan. Then, the surface grafting procedure will take place and a layer of chitosan deposited onto the surface of PEGDA monolith. The C-H bond from GPTMS bonded with acrylate substrate, in this case PEGDA monolith and firmly anchor the silane-crosslinked chitosan. Figure 3.2.3 showed the surface grafting mechanism grafted - chitosan PEGDA monolith.

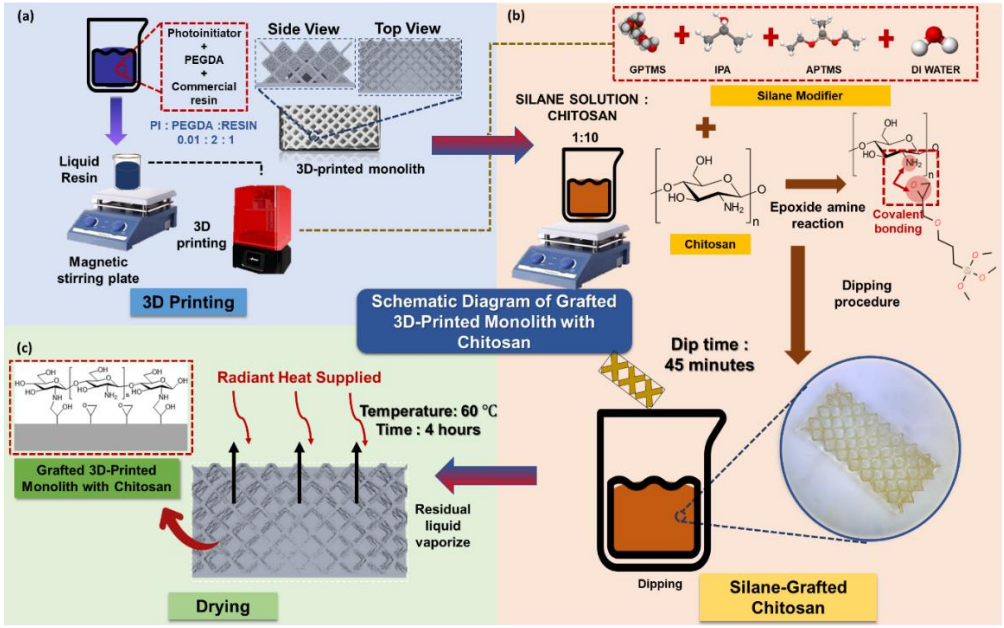


Figure 3.2.1: Illustration presentation of new grafted - chitosan monolith adsorbent.

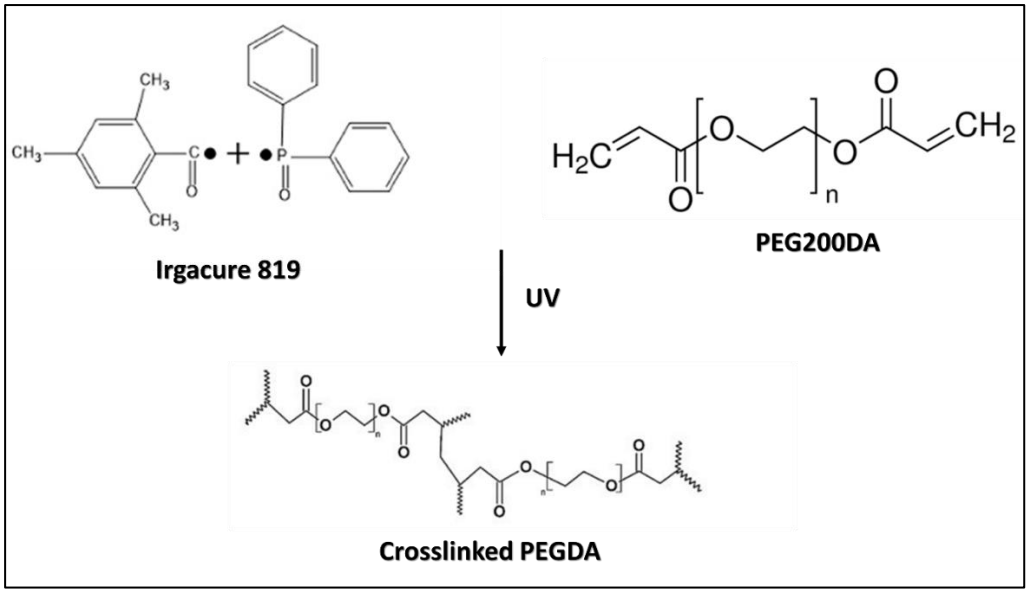


Figure 3.2.2: PEG200DA cross-linking reaction with Irgacure 819 under UV exposure.

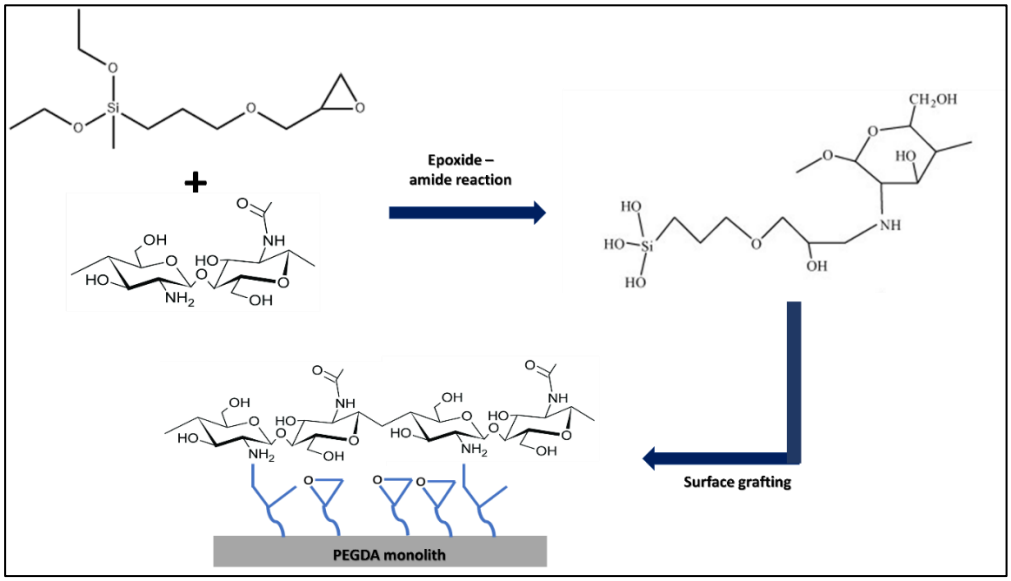


Figure 3.2.3: Surface grafting mechanism of grafted - chitosan PEGDA monolith.

3.2.4 Characterisation study

3.2.4.1 FESEM – EDX

The surface morphology and microstructure of the grafted - chitosan monolith was observed using field emission scanning electron microscopy (FESEM, FEI Quanta 400 F, USA). In addition, the presence of grafting medium was detected using energy dispersive X-rays (EDX). Since the sample is of non-conductive materials, it was coated with

platinum in rotary pumped coater (Quorum, 150 A S plus, UK) with deposition current of 20 mA and deposition rate of 6 nm/min. The prepared samples were placed in a vacuum chamber and electron beams were sputtered on them. The images were examined at different magnifications (90–3000x) and scale (1 mm – 40 nm).

3.2.4.2 FTIR Analysis

Fourier transform infrared spectra (ATR-FTIR, Perkin Elmer Frontier FT Mid-IR/Far-IR, USA) was used to identify functional groups involved in the adsorption and to verify the grafting of the chitosan on the monolith. The spectral analysis was performed within the range of 400 – 4000 cm^{-1} with triplicates at 3 different locations.

3.2.4.3 XPS

X-ray photoelectron spectroscopy (XPS) was conducted (Scienta Omicron XPS system, Germany) to determine the chemical composition, the binding energy of the compound and the type of bond on the grafted - chitosan monolith. The samples were analysed under ultra-high vacuum (UHV) conditions and exposed to X-rays of Al Ka with photon energies of 1486 eV and 1256 eV, respectively.

3.2.4.4 XRD

Panalytical powder diffractometer XRD system (X'Pert Pro, Netherlands) was used to determine the composition, stoichiometry, crystalline structure, and lattice parameter of the generated grafting. The XRD diffractometer is irradiated with Cu K α X-rays. The diffraction patterns are collected at 45 kV generator voltage and 40 mA currents with a

wavelength of 0.154nm. The scan is carried out with 2θ ranging from 7° to 80° each with a step of 0.2° and 0.5 ° second/per step.

3.2.5 Mechanical properties

The mechanical properties of the grafted chitosan were measured with Texture analyser, TX-XT Plus (Stable Micro Systems, USA) using a crosshead speed of 1mm/min with a maximum load of 30N load cell. The monolith was subjected to a load cell of 50 $\pm$ N according to American Standards for Testing Methods (ASTM) D1708. Compressive modulus was determined from the initial elastic slope of the stress-strain curve. On top of that, storage modulus E' of grafted chitosan monolith was performed using Perkin Elmer dynamic mechanical thermal analyzer (PE-DMTA, USA). The experiments were carried out under single cantilever mode in the temperature range of 20℃ to 80℃ at a heating rate of 10℃/min and frequency of 1 Hz.

3.2.6 Adsorption and desorption studies

The adsorption studies were performed based on the control factors set using RSM and are shown in Table 3.2.2. There was a total of 27 experiments with 3 replications (a total of 81 runs) and each experiment was done in 40 ml of an aqueous solution containing 50 ppm MO dye at different pH (3 - 11) and temperature (30 - 60℃), with the samples stirred in an incubator shaker at 150 rpm (N). The initial pH of the MO dye solution was adjusted by adding 0.5M of sodium hydroxide (NaOH) or 0.5M of hydrochloric acid (HCl) while measuring the pH of the solution with a pH meter (METTLER TOLEDO, Japan). The samples were collected in a cuvette at 1 h intervals for 5 h. The obtained MO dye

solution was analyzed using a UV-Vis spectrophotometer (Perkin Elmer Lambda 35, United States) and the maximum wavelength scan (λ_{max}) was determined at 464 nm (Nandini and Vishalakshi, 2012). The adsorption equilibrium was determined based on the removal efficiency $R\%$ and the uptake capacity of the MO dye, $K\ (mg/g)$ at different time intervals using Eqs. (1) and (2).

$$R\% = \frac{C_o - C_t}{C_o} \times 100\% \quad (1)$$

$$K = \frac{(C_0 - C_t)V}{m} \quad (2)$$

where R is the percentage of dye removal (%), K is the equilibrium of uptake capacity by grafted - chitosan monolith (mg/g), C_o is the initial concentration of dye solution (mg/L), C_t is the concentration of dye solution at t time (mg/L), V is the volume of dye solution (L) and m is the mass of grafted - chitosan PEGDA monolith (g).

For the desorption process, 0.01M NaOH solution was used as the eluent to desorb dye molecules from the monolith. This was also suggested by Szygula *et al.* (2008); that anionic dyes can be desorbed using an alkaline medium. The concentration of NaOH solution containing the desorbed MO dye was determined once desorption equilibrium was reached. The measurement was performed as previously described for the adsorption studies.

Subsequently, the grafted - chitosan PEGDA monoliths were thoroughly washed with distilled water until the pH of the wash solution was neutral (pH ~ 7), and then oven-dried at 60℃ for an hour. This adsorption-

desorption process was repeated four times with the same chitosan-grafted filter to verify its reusability. The desorption ratio, τ was calculated using Eq (3).

$$\tau = \frac{C_2 V_2}{(C_0 - C_1)V} \quad (3)$$

where C_2 denotes the concentration of MO dye in NaOH solution(mg/L), C_1 is the final concentration of MO dye (mg/L) and V_2 is the volume of NaOH solution (L).

3.2.7 Degradation study

To further analyse the mechanical stability of grafted - chitosan PEGDA monolith, degradation study based on weight lost measurement was carried out before and after adsorption for each cycle during recyclability test. Each measurement was repeated three times, and the mean value $\pm$ error of the mean was reported. The weight of the samples were taken using the equation stated in Eq. (4).

$$Weightloss(\%) = \frac{W_i - W_d}{W_i} \times 100\% \quad (4)$$

where, W_i and W_d correspond to the initial and dried weights (g) of sample after adsorption-desorption procedure respectively. The mean value of three samples were calculated and reported.

3.2.8 Experimental design and response analysis

In this work, the design of experimental (DOE) based on Response Surface Methodology (RSM) in Minitab Software 19 was used to perform optimisation studies of experimental factors to estimate the influence of operating parameters on dye adsorption. 3-level Box-Behnken design

(BBD) with continuous 4 factors (34-1) in the RSM was chosen to build the quadratic models in this experiment (Table 3.2.2). The model of regression equation for removal efficiency (%R) and uptake capacity, K (mg/g) were tabulated in Tables S1 and S2 (see Supplementary information – Section 3.2.8). This design was preferred over the central composite design (CCD) to reduce the number of trials required, and to provide maximum efficiency for RSM problems that have more than three factors (Elmoubarki *et al.*, 2017). The experiments designed by BBD have a total of 27 experiments each as shown in Table 3.2.3. The controlling factors in this study are the concentration of chitosan, dipping time during preparation, pH, and process temperature. The experimental data for the responses can be fitted into a second-order polynomial model represented by Eq. (5).

$$\boldsymbol{Y = Q_e(MO) = a_0 + a_1X_1 + a_2X_2 + a_3X_3 + a_{12}X_1X_2 +} \quad (5)$$
$$\boldsymbol{a_{13}X_1X_3 + a_{23}X_2X_3 + a_{11}X_1^2 + a_{22}X_2^2 + a_{33}X_3^2}$$

where *i, j* is the number of independent variables, Y is the response, a_0 is the constant, a_i is the linear coefficient, $a_{ii}$is the quadratic coefficient, b_{ij} is the interaction coefficient and X_i is coded variable level.

Hence, the BBD strategy aims to reduce the number of experiments carried out to reduce the amount of chemical wastage, while remaining an efficient and economic approach (Lim *et al.*, 2021).

Table 3.2.2: Level of four different factors.

Controlling factors	**Unit**	**Ranges and levels**		
		-1	0	+1
Co (wt.%)	wt%	1	2	3
Dipping time	min	30	45	60
pH	-	3	7	11
Temperature	℃	30	45	60

Co is concentration of chitosan.

Table 3.2.3: 3-level Box-Behnken design (BBD) with 4 factors and comparison of experimental and predicted results for each set of experiment.

Set	Controlling Factors				Removal Efficiency			Uptake capacity		
	Co (wt.%)	Dipping time (min)	pH	Temperature ℃	Exp. %	Pred. %	Dev. %	Exp. mg/g	Pred. mg/g	Dev. %
1	1	30	7	45	45.7	43.4	5.03	6.10	5.63	7.64
2	3	30	7	45	69.6	67.0	3.74	10.8	9.81	8.70
3	1	60	7	45	55.4	51.9	6.32	8.62	7.89	8.45
4	3	60	7	45	89.1	81.3	8.75	12.4	10.7	14.2
5	2	45	3	30	70.3	63.2	10.1	7.84	7.53	3.90
6	2	45	11	30	42.7	41.1	3.75	6.85	6.12	10.7
7	2	45	3	60	89.7	88.1	1.78	12.8	12.6	1.66
8	2	45	11	60	45.5	41.1	9.67	5.78	5.17	10.6
9	2	45	7	45	87.9	83.0	5.57	11.7	11.6	1.10
10	1	45	7	30	49.8	47.1	5.42	6.28	5.71	9.08
11	3	45	7	30	85.0	83.9	1.29	11.8	11.7	1.40
12	1	45	7	60	74.7	67.30	9.91	10.2	9.60	5.67
13	3	45	7	60	89.9	88.6	1.45	12.1	11.8	1.82
14	2	30	3	45	65.4	63.1	3.53	9.35	8.93	4.51
15	2	60	3	45	77.0	70.8	8.05	10.5	9.77	7.28
16	2	30	11	45	20.8	20.60	0.96	2.91	2.81	3.33

17	2	60	11	45	38.1	35.9	5.75	5.57	5.08	8.82
18	2	45	7	45	88.3	83.00	6.00	11.9	11.6	2.50
19	1	45	3	45	54.4	53.20	2.21	8.01	7.66	4.40
20	3	45	3	45	86.4	85.7	0.81	12.6	12.6	1.08
21	1	45	11	45	27.8	25.2	9.35	4.09	3.68	10.1
22	3	45	11	45	39.0	35.1	10.0	6.04	5.72	5.23
23	2	30	7	30	62.4	57.1	8.49	8.21	7.53	8.27
24	2	60	7	30	70.4	64.20	8.81	9.56	8.32	13.0
25	2	30	7	60	73.2	66.3	9.43	9.12	8.99	1.37
26	2	60	7	60	87.2	79.9	8.37	11.0	10.9	0.67
27	2	45	7	45	90.4	83.0	8.19	12.7	11.6	9.05

3.2.9 BOD and COD analysis

BOD and COD analysis were conducted with real textile wastewater samples supplied by Eco Solution Services Sdn. Bhd. located in Batu Pahat, Johor, Malaysia. The textile wastewater was filtered first to remove the solid particles as suggested by Sela *et al.* (2020). Then, the pH of the wastewater was adjusted to optimum condition (pH ~ 6.3) by adding 0.1M of hydrochloric acid. The treatment was performed using a grafted - chitosan PEGDA monolith before conducting the analysis. For BOD analysis, BOD_3 was chosen to reduce the incubation time that can be compensated by increasing the temperature to normal ambient temperature 27 $\pm$ 3 ℃ (Anusha and Jayatunga, 2017). The analysis was performed where the treated wastewater samples were incubated for 3 days at 30°C. The measurement of dissolved oxygen (DO) was collected on Day 1 and Day 3 and the final BOD was calculated using Eq. (6).

$$BOD = \frac{D_i - D_f}{P} \quad (6)$$

where BOD is Biochemical Oxygen Demand (mg/L), D_i is the initial dissolved O_2 concentration (mg/L), D_f is the final dissolved O_2 concentration (mg/L) and P is the dilution factor of wastewater.

COD test was carried out according to the procedure described by HACH Company. 2ml of treated samples were pipetted into the COD vials and digested for 2 h at 150°℃ using HACH COD reactor (DRB200, United States). Then, the vials were cooled down to room temperature before taking the COD measurement using HACH Spectrometer (DR3900, United States). COD reduction was calculated using Eq. (7).

$$COD = \frac{A_i - A_f}{A_i} \times 100\% \quad (7)$$

where COD is the Chemical Oxygen Demand (%), A_i is the initial COD concentration (mg/L), A_f is COD concentration after the adsorption process (mg/L).

3.2.10 Adsorption Isotherm Modelling

The optimum isotherm model was described using experimental data from the equilibrium amount of adsorbed dye (q_e) on the adsorbent, and the concentration of dye in the solution (C_e) at a constant temperature and pH. The equilibrium data were analysed using the linear forms of the Langmuir, Freundlich, Temkin, Dubinin - Radushkevich, Harkins–Jura and Redlich – Peterson equations as described briefly below. The correlation coefficients (R^2) were used to compare the applicability of this isotherm modelling.

3.2.10.1 Langmuir Isotherm

Langmuir isotherm is used to determine the adsorption capacity of aqueous compounds onto the adsorbent (Elmorsi, 2011). This isotherm assumes that adsorption and desorption rates are equal at equilibrium, as the surface coverage of the adsorbent is governed by the equilibrium constant. This model described a single layer, or monolayer is formed when adsorbate particles adhere to specific locations on the surface, resulting in a horizontal asymptote at a unit load (Hammond and Conner, 2013). The Langmuir equation is expressed as in Eq. (8).

$$\frac{C_e}{q_e} = \frac{1}{(q_m K_l)} \times \frac{1}{C_e} + (\frac{1}{q_m}) \quad (8)$$

where C_e is the concentration of dye after adsorption process at equilibrium (mg/L), q_e is the equilibrium adsorption capacity (mg/g) and q_m is maximum adsorption capacity (mg/g). $K_L$is the isotherm constant that is related to the affinity of the binding sites (L/mg).

3.2.10.2 Freundlich Isotherm

Freundlich isotherm model is for multilayer adsorption and is applied to determine the adsorption process on a heterogeneous surface (Pollard *et al.*, 1992). The linear equation of the isotherm is shown in Eq. (9).

$$lnq_e = ln\, K_f + \frac{1}{n} lnC_e \quad (9)$$

where K_f is the Freundlich constant that is associated with the uptake capacity (mg/g) and $\frac{1}{n}$ is adsorption intensity.

3.2.10.3 Temkin Isotherm

Temkin isotherm model studied the effects of indirect adsorbate - adsorbate interactions upon the adsorption process (Cao *et al.*, 2021). Based on assumption, the heat of the adsorption of all molecules decreases linearly as the layer coverage increases (Ayawei, Ebelegi and Wankasi, 2017). The linear equation of the isotherm is stated in Eq.(10).

$$q_e = \frac{RT}{b_T}(lnK_t + lnC_e) \quad (10)$$

where R is the common gas constant (0.008314 kJ/molK), T is the absolute temperature (K), $\frac{1}{b_T}$is the Temkin constant (heat of sorption (kJ/mol) indicating the potential of adsorption (intensity) of the adsorbent and K_t (L/g) is Temkin constant for adsorption capacity.

3.2.10.4 Dubinin - Radushkevich (D - R) Isotherm

Referring to Theivarasu et. al (Theivarasu and Mylsamy, 2011), D – R isotherm is used to study the porosity characteristics of the adsorbent and apparent adsorption free energy onto a heterogeneous surface. The linear equation of D – R isotherm is represented as in Eq. (11).

$$lnq_e = lnq_m - K_{DR}\varepsilon^2) \quad (11)$$

$$\varepsilon = RTln(1 + \frac{1}{C_e})$$

where $q_m$is the theoretical saturation capacity (mol/g),K_{DR} is the D - R constant related to the adsorption mean free energy (mol^2J^{-2}), whereas ε is a dimensionless constant (polyani potential), which is related to the equilibrium constant.

3.2.10.5 Harkins - Jura (H - J) Isotherm

H - J isotherm predicts the possibility of multilayer adsorption on the absorbents with heterogeneous pore distribution. The adsorbent with multilayer adsorption will have more than one layer of active sites where all the surface layer is not in contact with the adsorbed molecules (Ayawei, Ebelegi and Wankasi, 2017). The model can be expressed as shown in Eq.(12).

$$\frac{1}{q_e^2} = \frac{B}{A} - \left(\frac{1}{A}\right) logC_e \tag{12}$$

where A and B are the model constant.

3.2.10.6 Redlich - Peterson (R - P) Isotherm

R - P isotherm is an empirical adsorption model with three parameters that contains elements of both the Langmuir and Freundlich isotherms; the adsorption mechanism is a hybrid rather than an ideal monolayer adsorption (Kumara *et al.*, 2014) and can be shown in Eq. (13).

$$ln\frac{C_e}{q_e} = \beta lnC_e - lnA \tag{13}$$

where β is the exponent between 0 to 1 and A is Redlich-Peterson isotherm constants that can be obtained from the slope and intercept of the plot.

3.2.11 Adsorption Kinetics

The adsorption kinetics of amount of dye adsorbed at optimum condition was investigated to determine adsorption rate and its underlying mechanism based on the kinetic equations of 5 models. The kinetic models are pseudo-first order, pseudo-second order, intra-particle

diffusion model, Bangham kinetic model and Elovich kinetic model as shown in Eqs.(14), (15),(16),(17) and (18) respectively.

$$q_t = q_e(1 - e^{-k_1 t}) \tag{14}$$

$$\frac{t}{q_t} = \frac{1}{k_2 q_e^2} + \frac{1}{q_e} t \tag{15}$$

$$q_t = k_{id} t^{\frac{1}{2}} + c \tag{16}$$

$$log(log \frac{C_0}{C_0 - q_t m}) = log\left(\frac{K_0 m}{2.303V}\right) + \alpha \, log \, T \tag{17}$$

$$q_t = \frac{1}{\beta} ln(\alpha\beta) + \frac{1}{\beta} ln \, t \tag{18}$$

where $k_1$and $k_2$are the rate constant of pseudo-first order and pseudo-second order. The rate constant k_{id} and K_0 the rate constant of intra-particle diffusion model and Bangham kinetic model. In the case of Elovich kinetic model, α and β are the rate constant of the model. For pseudo-first order, a linear plot of ln $(q_e - q_t)$ vs t was plotted to obtain ln q_e and slope k_1 whereas for pseudo-second order, a linear plot of $\frac{t}{q_t}$ vs t was plotted to obtain $\frac{1}{k_2 q_e^2}$ as y-intercept and $\frac{1}{q_e}$ as slope. For intra-particle diffusion, a linear plot of q_t vs $t^{\frac{1}{2}}$ was plotted to obtain c as y-intercept and slope k_{id}. A plot of $log(log \frac{C_0}{C_0 - q_t m})$ vs $log \, T$ was used to obtain slope α and y-intercept $log\left(\frac{K_0 m}{2.303V}\right)$ for Bangham model whereas for Elovich model, a linear plot of q_t vs $ln \, t$ was plotted to obtain slope $\frac{1}{\beta}$ and y-intercept $\frac{1}{\beta} ln(\alpha\beta)$.

3.2.12 Thermodynamic modelling

The thermodynamics of the adsorption process at different temperatures was evaluated to determine whether the process is physical or chemical, spontaneous or non-spontaneous, and exothermic or endothermic, based on the thermodynamic parameters - activation energy (E_a), change in standard free energy ($\Delta G°$), enthalpy ($\Delta H°$) and entropy ($\Delta S°$) - based on the equations stated in Eqs.(19), (20) and (21).

$$K_c = \frac{q_e}{C_e} \tag{19}$$

$$ln\, K_c = \frac{\Delta S°}{R} - \frac{\Delta H°}{RT} \tag{20}$$

$$\Delta G° = -RT ln K_c \tag{21}$$

where K_c is the equilibrium adsorption constant, R is the universal gas constant (8.314 J mol^{-1} K^{-1}), T is the absolute temperature (K), $\Delta H°$ is the standard enthalpy (kJ mol^{-1}), $\Delta S°$ is the standard entropy (kJ mol^{-1}), and $\Delta G°$ is the standard free energy change (kJ mol^{-1}). The values of $\Delta H°$ and $\Delta S°$ were obtained from the slope and intercept of a linear plot of $ln\, Kc$ and $\frac{1}{T}$.

3.3 Results And Discussion

3.3.1 Characterisation of samples

3.3.1.1 FESEM and EDX Analysis

FESEM-EDX was used to demonstrate the morphological changes due to surface functionalisation with grafted - chitosan PEGDA monolith as shown in Figure 3.3.1 and Figure 3.3.2. Figure 3.3.1a(i) showed the overview of a square shaped 3D-printed PEGDA monolithic structure

with an enlarged segment of the monolith struts before the surface grafting process (Figure 3.3.1a(ii)**).** The original printed monolith showed a smooth surface as shown in Figure 3.3.1a(ii) while wrinkled layers of deposition of chitosan can be spotted Figure 3.3.1b at different magnification. This indication further confirmed the monolith was successfully grafted with the layer of chitosan.

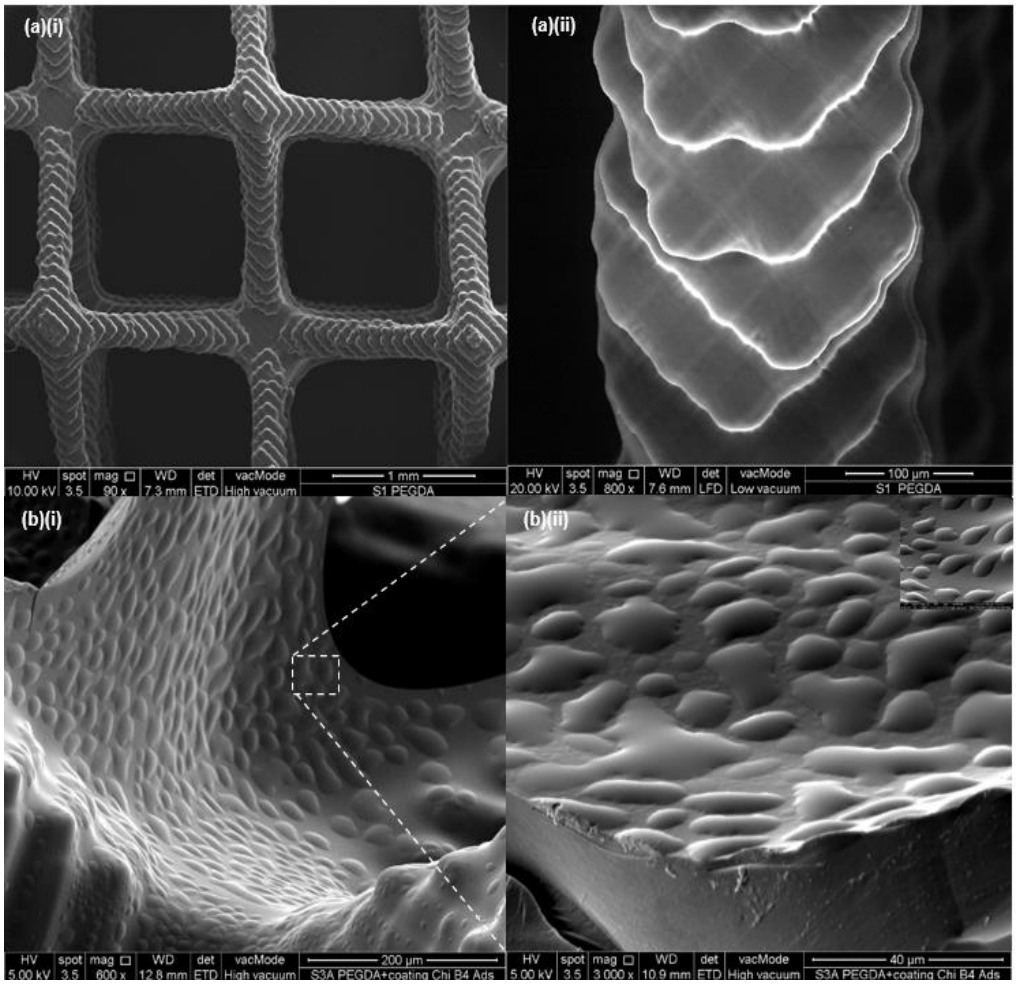


Figure 3.3.1: SEM image of 3D-printed monolith;(a)(i) view of square -shaped 3D-printed monolithic structure, (a)(ii) enlarged segment of monolith struts before surface grafting process, (b) surface morphology of 3D-printed monolith after grafting; (i)view from 600 magnification and (ii) view from 3000 magnification with wrinkled layers.

As shown in Figure 3.3.2a**,** the EDX spectrum of 3D-printed PEGDA monolith indicated the presence of C and O only, whereas the

characteristic signal of Si and N elements on the surface can be seen in Figure 3.3.2b(i) after grafted with silane cross-linked chitosan at 1.739 keV and 0.392 keV respectively. This confirmed the binding of Si ions and protonation of chitosan onto the surface of the monolith after the grafting process. After the MO dye adsorption (Figure 3.3.2b(ii))**,** the characteristic signal of the Si ion has significantly reduced for the grafted - chitosan PEGDA monolith. This reduction happened due to the formation of dye ion pairs and ion pair associations between protonated chitosan layer and the SO_3^- group in anionic dyes. Hence, the intensity spectra of the Si element are reduced when it exhibits electrostatic interaction with the dye ions. The successful adsorption of MO dye was further verified as the S element appeared in the EDX spectrum, which is belongs to chemical structure of MO dye.

Furthermore, the element Cl was also identified through the EDX analysis. Based on the EDX spectrum of pure chitosan as depicted in Fig A1 (see Supplementary in Section 3.3.1.1), Cl element had already existed as the process of producing chitosan requires the usage of hydrochloric acid during the hydrolysis process (Aljbour, Beg and Gimbun, 2019; Bristow and Inc, 2012). However, the percentage of Cl as detected by EDX spectrum is less than 1% which is negligible. Overall, it can be concluded that the layer of chitosan has been successfully grafted on the surface of the 3D-printed monolith.

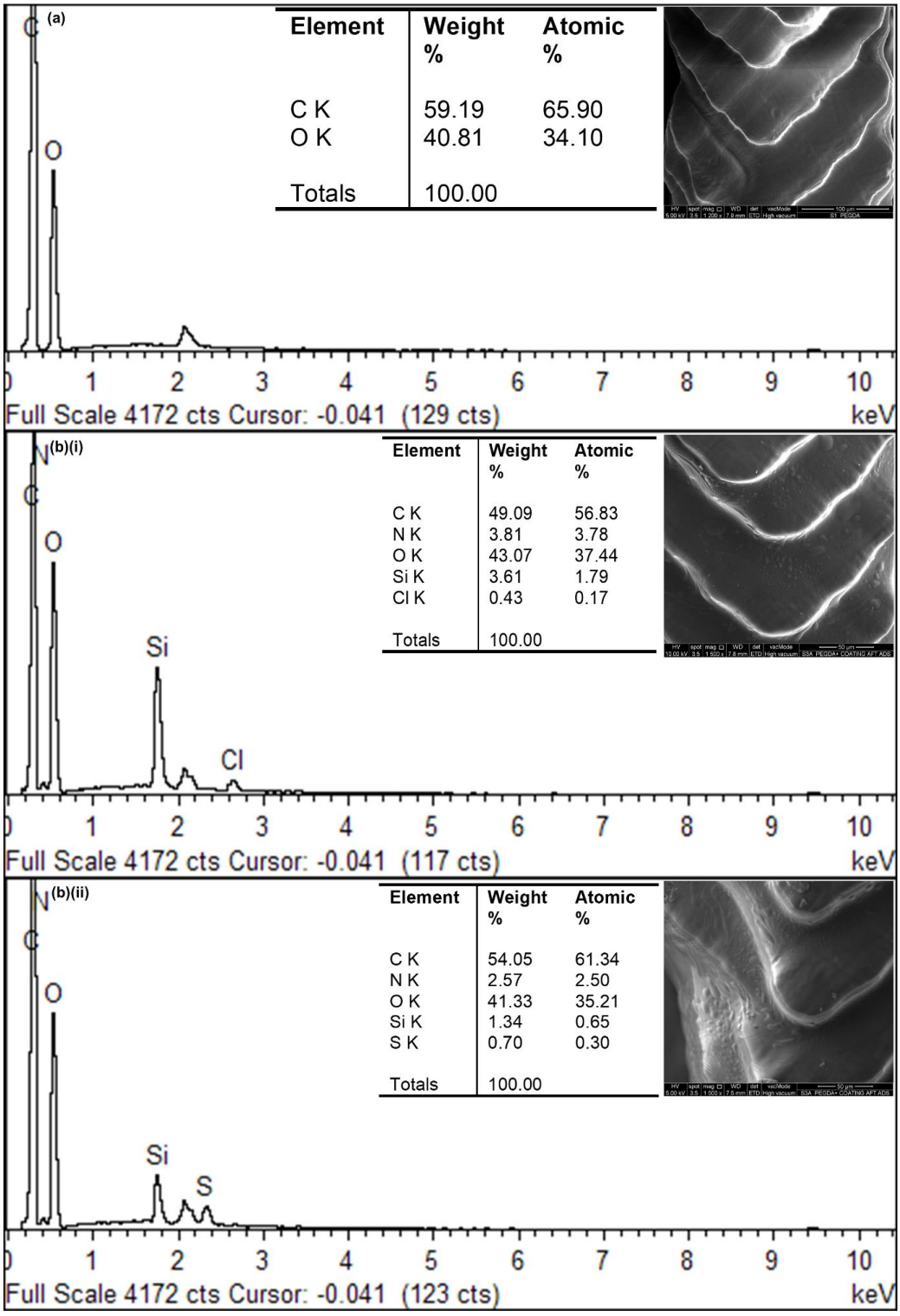


Figure 3.3.2: SEM - EDX Analysis; (a) pure PEGDA monolith, (b) grafted - chitosan PEGDA monolith; (i) before adsorption, (ii) after adsorption.

3.3.1.2 XPS

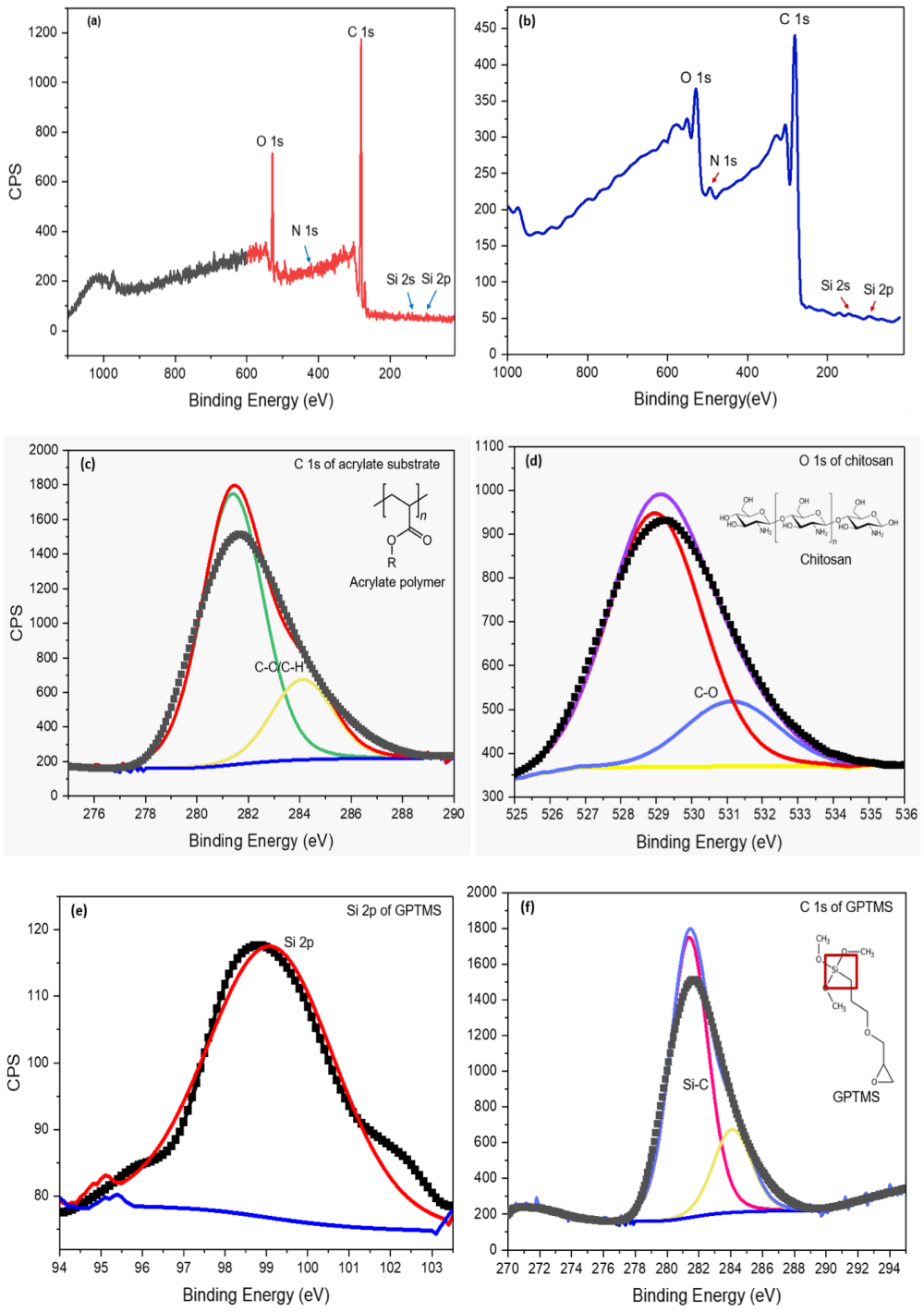


Figure 3.3.3: (a) - (b) Wide-scan XPS spectra of grafted - chitosan PEGDA monolith structure. (c) High resolution of spectra of original 3D-printed PEGDA monolith of C 1s core-level for C-C/C-H; (d) High resolution spectra of grafted - chitosan on the monolith of O 1s core-level. Representative of high - resolution spectra of GPTMS structure produced by silane - cross-linked chitosan; (e) Si 2p core-level and (f) C 1s Core level for Si-C.

XPS studies were conducted to determine the elemental composition and bonding on the surface of the grafted - chitosan PEGDA monolith. As shown in Figure 3.3.3a - b, the wide scan spectra of grafted - chitosan PEGDA monolith contains C, O, N and Si elements. The C 1s core level spectrum presented in Figure 3.3.3c is composed of a peak at 284.10 eV which corresponds to typical binding C-C or C-H bond. This bond could be associated to acrylate substrate of PEGDA. The presence of chitosan can be confirmed from O 1s spectrum as shown in Figure 3.3.3d. The major peak located at 531.13eV corresponds to the C-O bond of oxygen polysaccharide backbone. Intriguingly, N element cannot be detected in grafted - chitosan PEGDA monolith sample, which might be due to the sample preparation or the change in the chemical interaction in the mixing ratio of the silane coupling agent solution with chitosan. Nevertheless, the element was verified in SEM - EDX analysis as discussed earlier (Figure 3.3.3b(i))**.** Besides that, the Si 2p core level spectrum, as shown in Figure 3.3.3d**,** corresponded to Si element which was blended with chitosan before grafted on the monolith. The C 1s core level depicted in Figure 3.3.3f displayed a dominant peak at 281.39eV, which is associated to silicon carbide bond of GPTMS. Si and C atoms (sharing of electron pairs in sp^3 hybrid orbitals) form a very strong tetrahedral covalent bonds (bond energy = 4.6 eV), making it suitable to be used as a cross-linker (Davis, 2017). Overall, all results obtained are evidence confirming that the chitosan layer was successfully grafted onto the surface of the 3D-printed sample.

3.3.1.3 FTIR

FTIR analysis was used to elucidate the chemical composition and molecular structure of PEGDA monolithic structure before and after the grafting process as presented in Figure 3.3.4.

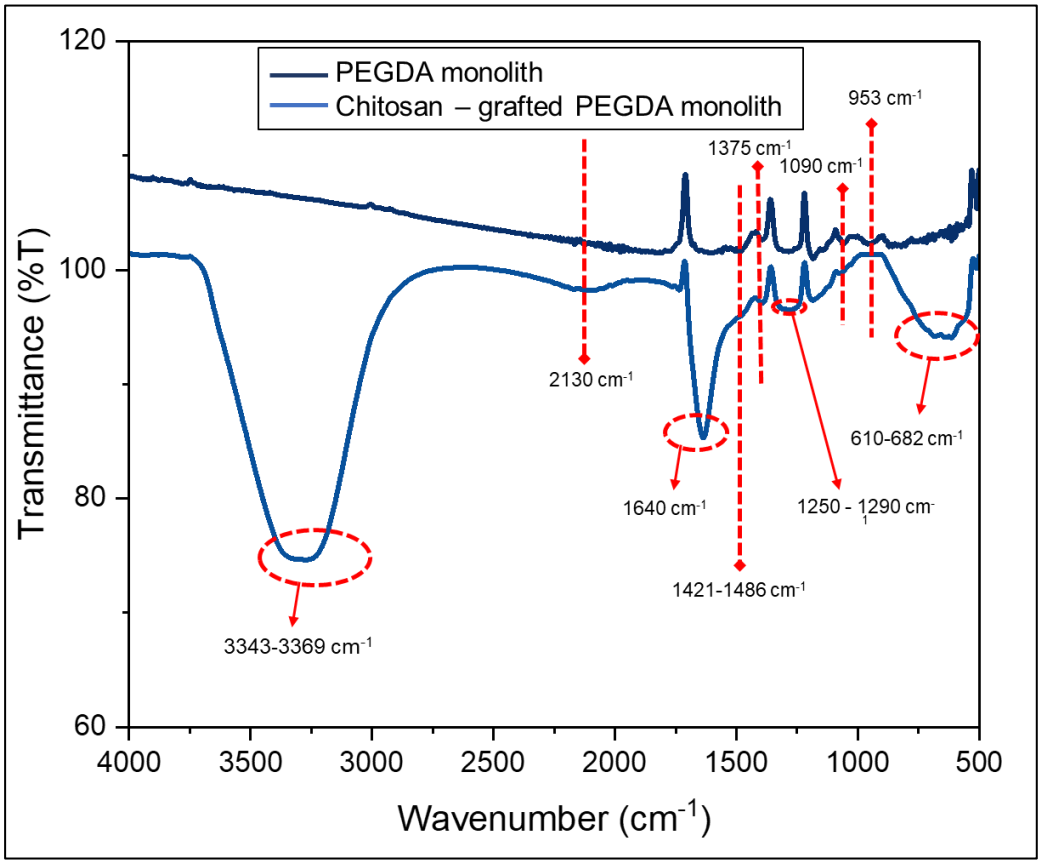


Figure 3.3.4: FTIR spectra of PEGDA monolithic structure with and without silane cross-linked chitosan.

Referring to Figure 3.3.4, FTIR spectra of both components are seen to have a similar pattern, except at three broad peaks. The intense band between $\lambda = 3343 - 3369\ cm^{-1}$ corresponded to the stretching vibration of O–H and/or N–H. This peak is also associated with Si-OH from the hydrolysis of silane coupling agent (GPTMS - APTMS structure). This is because it is expected there is formation of N-C bonding between chitosan and GPTMS during surface grafting procedure. Moreover, the peaks assigned to $1250 - 1290 cm^{-1}$ are due to the overlapping peaks for

Si-CH_2 from GPTMS structure (Ma *et al.*, 2010). There are several peaks that are associated with chitosan. The absorption band at 1640 cm^{-1} is attributed to the ionic interaction between chitosan and the acrylate substrate (Zhang *et al.*, 2019a). However, the stretching of vibration at this absorption band might be due to overlapping of the C=O amide band at 1640 cm^{-1} with Si-OH bond from GPTMS and APTMS. Moreover, a significant peak at 1375 cm^{-1} of chitosan is corresponding to the C–O bond in the primary alcoholic group. Another minor peak between 1421 – 1486 cm^{-1} is assigned to the CH_3 symmetrical deformation mode and corresponds to the C–H side chain bending—CH_2OH (Milosavljević *et al.*, 2011). A small band located at 1090 cm^{-1} showing intensity increase which corresponds to the Si–O–C bonds (Reyes-Peces *et al.*, 2020). This peak is associated to silane-crosslinked chitosan which showed that the silane cross-linked chitosan was successfully grafted on the 3D-printed monolith.

3.3.1.4 XRD

Figure 3.3.5 illustrated the X-RAY diffraction patterns for 3D-printed PEGDA without and with grafted - chitosan PEGDA monolith. The PEGDA was observed to have two major XRD peaks at 2θ of 20.38°, 21.5° and some minor peaks at 36.7°, 39.3°, 42.15°, 46.5° and 75.3°. The strong diffraction peak at around $2\theta = 21°$ showed that PEGDA is amorphous and has a limited crystallinity which was also previously reported in (Piao *et al.*, 2022). According to Bhattacharyya and Ray (2015), the strong peak and crystallinity is associated with the intermolecular hydrogen bonding between the –OH groups of the glycol.

In addition to this, a strong peak was also observed for grafted - chitosan PEGDA monolith. Samuels (1981) reported that there are 2 broad peaks for pure chitosan, which were assigned at 2θ = 10.3° (crystal forms I) and strongest reflection appeared at 2 θ = 20.1° (crystal forms II) as depicted in Figure 3.3.5a. However, it was observed that there was a slight shift for grafted - chitosan PEGDA monolith as shown Figure 3.3.5b**,** with 2θ = 10.1° and 19.9° respectively. This phenomenon could be caused by the chemical grafting procedure, where the long chain hindered the formation of inter- and intra - molecular hydrogen bonds. Another reason could be due to chitosan derivative being amorphous as previously reported in (Li *et al.*, 2009; Zhang, Yang and Nie, 2008).

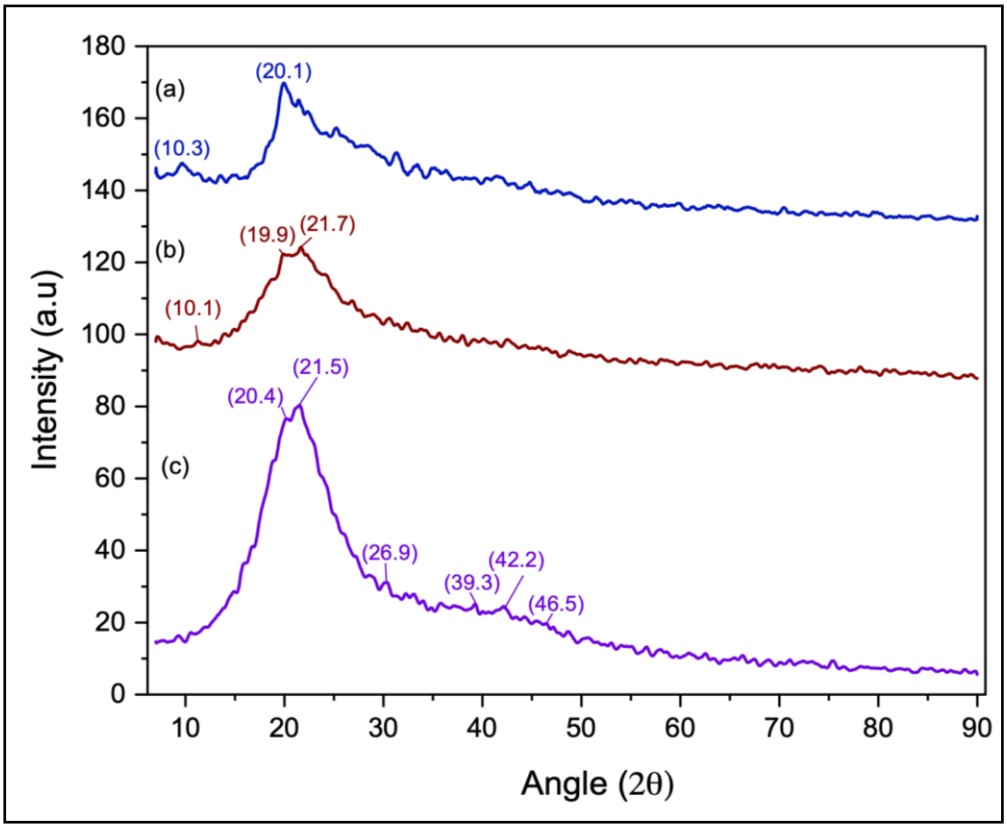


Figure 3.3.5: XRD pattern for; (a) pure chitosan and PEGDA monolith;(b) with grafted chitosan and (c) without grafted chitosan.

3.3.2 Mechanical properties

The results of the tensile strength test of 3D printed PEGDA monolith before and after grafting with silane-crosslinked chitosan are shown in Table 3.3.1. It can clearly be observed that the mechanical properties of the grafted - chitosan 3D-printed monolith improved after the surface grafting procedure using silane coupling agent as the crosslinker. The increased of storage modulus and ultimate tensile strength values insist that the interaction between chitosan and silane coupling solution become stronger and grafted - chitosan 3D-printed monolith have more stiffness. Hydrogen bonding and covalent bond formation also increase interfacial strength in APTMS. This is because APTMS has a primary amine structure that forms hydrogen bonds with hydroxyl and carboxyl end groups and reacts with the carboxyl end groups of PEGDA. Covalent bond formation improves interfacial strength in GPTMS. GPTMS contains an epoxy group that can react with the carboxyl and hydroxyl end groups of chitosan through a nucleophilic substitution reaction (Arslan and Dogan, 2018). Overall, interfacial strength increases in conjunction with the tensile strength of the grafted - chitosan 3D-printed monolith. Similar outcome was also reported by Shirosaki, Okabayashi and Yasutomi (2020), who utilised silane coupling agent to improve the mechanical properties of the chitosan microfiber.

Table 3.3.1: Mechanical properties of 3D printed PEGDA monolith before and after grafting with silane-crosslinked chitosan.

Mechanical Properties	Measurement (MPa)	
	PEGDA monolith	Grafted chitosan PEGDA monolith
Storage Modulus	335.83	427.73
Ultimate Tensile Strength	1.31×10^6	1.34×10^6

3.3.3 Optimisation Analysis of Batch Adsorption Studies

Respond optimiser was analysed to determine the optimal conditions for the batch adsorption study (see Figure A1 in Supplementary Information – Section 4.3.3). The optimal condition for removal efficiency (R%) is at a concentration of 2 wt.% with an dipping time of 45 min at pH of 6.3 and temperature of 60 ℃, while the optimal condition for the uptake capacity, K, is at 2.7 wt.% with a dipping time of 45 min at pH of 4.2 and a temperature of 60℃. A series of confirmatory tests were carried out and are discussed in more detail in Section 3.3.5.

3.3.3.1 Effects of concentration, dipping time, pH and temperature on removal efficiency (R%) and uptake capacity, K(mg/g)

Main effect plots of the experimental process parameters (i.e., concentration, dipping time, pH and temperature) were generated using RSM Minitab 19, giving an overview of the importance of the factors for the reaction system. The factorial plots with the fitted mean values of removal efficiency (R%) and uptake capacity, K (mg/g) were illustrated as shown in Figure 3.3.6a **–** b.

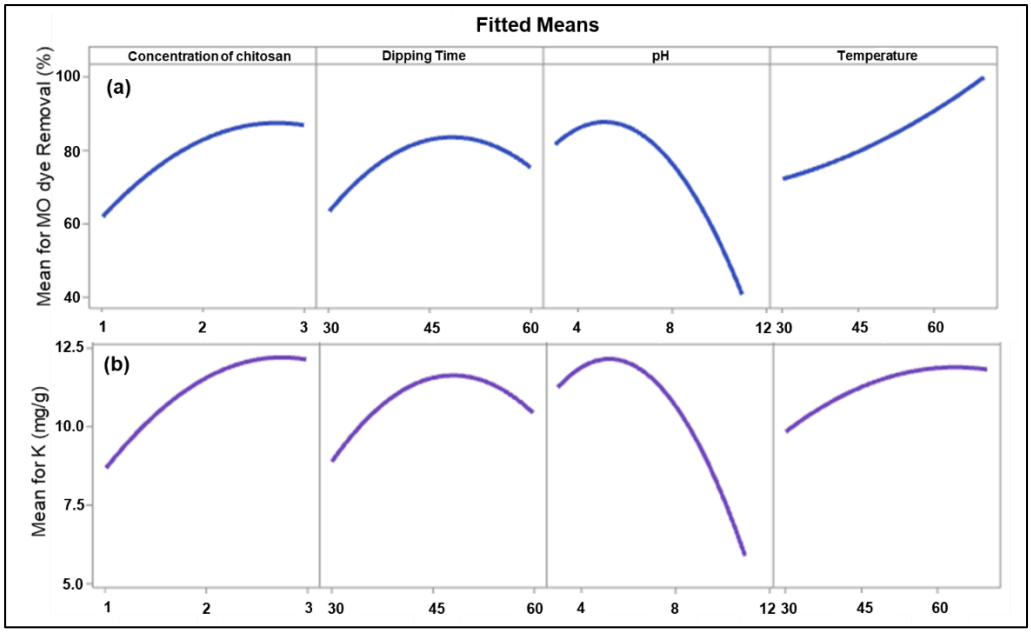


Figure 3.3.6: Main effects plot for; (a) removal efficiency (R%) and (b) Uptake capacity, K (mg/g).

As shown in Figure 3.3.6, as the chitosan concentration (wt.%) increases, the removal efficiency (R%) and the uptake capacity of the MO dye increase. This can explain the significant effect ($p < 0.05$) of chitosan concentration (wt.%). A slight decrease in removal efficiency (R%) and uptake capacity, K (mg/g) value was observed at high concentration of chitosan (>2 wt.%). This could be due to the degree of saturation of the active sites, which do not allow further adsorption at higher concentration because the surface-active sites are saturated on the adsorbent (Zhu *et al.*, 2007). According to Zhou *et al.* (2008), chitosan concentration was considered high when the chitosan was no longer flowable (i.e., 2.5% (w/v). This can be explained by the fact that the viscosity of the chitosan solution is greatly influenced by the molecular weight and concentration. Chitosan is a cationic electrolyte, which is soluble only in weak acid. The acidic condition changes the

charge density of the degree of de-acetylation of chitosan, resulting in an extended conformation of the chain due to the reduced number of tangles. This resulted in the chain becoming stiffer as the number of entanglements increased. Due to the lack of mobility and resistance to the flow of molecules, it could not form new entanglements, resulting in higher viscosity. As a result, the freedom of movement of individual chains was restricted, leading to a notable change in the bonding network and a reduction in the number of available functional groups. Dye molecules that penetrated and passed through the monolith were adsorbed onto functional groups on the outer surface, and the formation of adsorbed dye clusters was hindered, which consequently reduced the accessibility of dyes to available active sites. Wang *et al.* (2022b) reported that the maximum adsorption capacity can be reached at 0.6 wt.%, while the adsorption capacity of Cu (II) ions decreases when the mass fraction of aerogel-impregnated chitosan is greater than 0.6 wt.%. This is because the average pore size of chitosan at molecular scale (typically ~ 50 to 200 μm) decrease with increasing concentration of impregnated chitosan. The pore size is highly dependent on the heat and mass transfer rates (Madihally and Matthew, 1999). In this case, the temperature was kept constant, so the pore size is dominated by the mass transfer rate. Increasing the viscosity of the chitosan solution decreases the mass transfer rate, resulting in smaller pores as it decreases the pore size network (Fang *et al.*, 2014; Ren *et al.*, 2019). It can be concluded that it is crucial to select optimum concentration of chitosan for better adsorption performance. In this work, the optimal

chitosan concentration was ~ 2 wt.%, as predicted by the RSM (see Supplementary Information – Section 3.3.4).

Dipping time in chitosan was studied to see how the cross-linking conditions could allow better grafting on the monolith, leading to proper tuning of the morphology and increasing the adsorption performance. Based on RSM study, dipping time does not have significant effect (p > 0.05) on removal efficiency (R%) and uptake capacity, K (mg/g). Surface grafting of the 3D-printed monolith with chitosan at a dipping time of 45 min resulted in wrinkled chitosan layers on the monolith surface, as shown in Figure 3.3.1b. Thus, dip time of 45 min was sufficient to firmly anchor the chitosan to the monolith surface via a surface grafting process in which a silane coupling agent was used as a cross-linking agent. The presence of amine and hydroxyl groups in the chitosan was confirmed by FTIR and XPS analysis. In this study, it was found that a longer dipping time (> 45 min) could lead to an excess of chitosan being deposited on the monolith, resulting in less binding between the chitosan molecules and the monolith surface because the cross-linker was too weak to support the increase in the mass of deposited chitosan. Increasing dipping time also resulted in non-uniform dispersion on the surface, which prevents further adsorption (Hamzah *et al.*, 2012). Li *et al.* (2021) also reported increasing in dipping time from 10 min to 60 min reduced the water flux of a PES membrane that can be attributed to the clogging of membrane pores after surface functionalisation. Hence, 10 min of dipping time is sufficient to increase the hydrophilicity of unfunctionalised membrane. According to Budianto, Muthoharoh and

Nizardo (2015), increasing the cross-linking time has a significant effect on the swelling behaviour of chitosan and its mechanical properties. As the cross-linking time increases, the swelling behaviour decreases while the mechanical properties increase. Thus, the structure becomes firmer and denser because the degree of cross-linking between the amine group in chitosan and the carbonyl group increases. However, this phenomenon is unfavourable for adsorption application because the swelling properties are the major contributor to the adsorption capacity (Shukla, Rattan and Madras, 2012). Therefore, it can be concluded that the control factor of dipping time or cross-linking time is varied depending on the desired result and application. In this experiment, it was confirmed that increasing the dipping time has no significant effect on adsorption, which is consistent with the results of ANOVA in this study ($p > 0.05$). Therefore, this control factor was not optimised.

The process parameter pH has the greatest influence on the removal efficiency (R%) and the uptake capacity, K(mg/g) of the MO dye ($p < 0.05$) (Jawad *et al.*, 2019a). According to Lewis Theory of Acid–Base reactions, the pH of MO dye solution plays an important role in the whole adsorption system (Mishima *et al.*, 2019). This is because the pH affects the dissociation of the functional groups at the active sites and the surface charge of the adsorbent. The highest MO dye removal and uptake capacity, K, under alkaline conditions (pH = 11) is 41% and 4.56 (mg/g) with respect to Set 22, reflecting the curve shown in Figure 3.3.6. The low adsorption capacity of the dye MO under alkaline conditions can

be explained based on dissociation of anionic dyes in an aqueous solution as shown in Eq. (22).

$$Dye + SO_3Na \rightarrow Dye + SO_3^- + Na^+ \quad (22)$$

Based on the equation, the sulfonate groups (R-SO_3NA) of the dye MO are dissociated and converted into an anionic dye solution. The adsorption occurs due to the electrostatic attraction between the protonation of the amine groups of chitosan and MO anions. At a higher pH (> 7), there are abundant of OH^- ions. The anionic dyes have to compete with excess OH^- ions in the solution, which leads to a decrease in the number of positively charged functional groups on the surface of the adsorbent. In acidic condition (lower pH), there are a large number of positively charged surface sites and fewer negatively charged active sites. This condition favours the adsorption of negatively charged MO^- ion molecules due to the electrostatic repulsion between the anionic dye and positively charged on the adsorbent's surface. Thus, the surface of the adsorbent acquires a stronger negative charge at lower pH, which promotes the uptake of the anionic dye due to the electrostatic attraction. Similar observations were also reported by other researchers who studied on the different adsorbents for anionic dyes removal where the lowest adsorption removal is at high pH (Mirzaie *et al.*, 2017; Shah *et al.*, 2021).

The optimal pH is about pH 3 - 6 when chitosan is used as adsorbent (Huang *et al.*, 2017; Iqbal *et al.*, 2011). In this study, the optimal pH is between 4 and 6.3, which is consistent with the literature. According to Blackburn (2004), the electrostatic interactions between the cationic

centres in the chitosan chains and the anionic dyes, which are in equilibrium with the unprotonated form, have a significant effect at high pH. This is because the equilibrium favours the unprotonated form of the polysaccharide and almost completely excludes the protonated form. Further to this, adsorption of anionic dye on chitosan by the combination of electrostatic forces, Van der Waals interactions and hydrogen bonding are likely to occur at low pH. Thus, this explains the optimum adsorption of chitosan onto anionic dye are observed at neutral pH (da Silva Alves *et al.*, 2021).

Finally, process temperature has significant effect ($p < 0.05$) on removal efficiency (R%) and uptake capacity, K (mg/g). As the process temperature increases, the removal efficiency (R%) and uptake capacity, K (mg/g) also increase (Table 3.3.7). The increase in temperature leads to a faster diffusion rate of the adsorbate molecules from the solution into the grafted chitosan monolith. Based on the collision theory, an increase in temperature will increase the reaction rates, as the frequency of the collisions between particles increases. Hence, by assuming the energy of collisions is adequate, this will lead to a faster rate of reaction due to more collisions. An increase in temperature will increase the mobility of the large dye ions but also the internal structure of the chitosan, resulting in reduction of resistance for adsorption of the dye structure by the chitosan (Wong *et al.*, 2008). Thus, based on this theory, increasing temperature can lead to an increase in adsorption capacity. The effect of temperature from a thermodynamic perspective has been discussed in detail in Section 3.3.10.

In summary, all the process parameters can be optimised using RSM except for dipping time because there were no significant effects ($p > 0.05$) on dipping time. Confirmation of experiments were carried out and discussed in detail in Section 3.3.5.

3.3.4 Analysis of Variance (ANOVA) Results

ANOVA was performed using Minitab 19 software to examine the importance and contribution of the process variables and their interaction in each combination to the response. The results of ANOVA are shown in Table S3 and S4 in Supplementary Information – Section 3.3.4. From the analysis results, the *F*-value indicates the significance level of the designed parameters on the adsorption performance. Higher *F*-value indicates that the dye adsorption performance is significantly affected by the process parameters. Apart from that, *F*-value was compared with the *F*-critical (F_{crit}) value to indicate the significance of the statistic and to reject the null hypothesis. The inverse cumulative distribution function in RSM Minitab 19 can be used to find *F*-critical value or can be calculated using the following Eq. (23).

$$F_{crit} = \frac{No.of\ level\ of\ factors - 1}{Degree\ of\ freedom\ for\ error} \quad (23)$$

The null hypothesis in this experiment is defined as the process parameters that do not have any significant effect to the removal efficiency (R%) and uptake capacity, K (mg/g). The calculated F_{crit} for removal efficiency (R%) and uptake capacity, K (mg/g) is 2.75. All designed parameters contribute a significant role for the removal efficiency (R%) of MO dye (Table S3) and uptake capacity, K (mg/g)

(Table S4) except for any combination terms with dipping time and combination of temperature alone as the *F*-value for these parameters below F_{crit}. However, the combination terms of concentration of chitosan and pH did not affect uptake capacity, K (mg/g) of the grafted - chitosan PEGDA monolith**.** In addition, the *P* value (α = 0.05) was also evaluated for significance of each parameter. Any process parameter with ($p \leq 0.05$) indicates that it is statistically significant to against null hypothesis. The same outcomes were reflected for the *P* value where any combination with dipping time and combination of temperature alone is not statistically important towards the removal efficiency (R%) of MO dye and uptake capacity, K (mg/g). The main contribution factors for each parameter can be seen from the Tables A0.1 and A0.2, where the highest contribution for both parameters is pH.

Lack of fit from the regression model tells that the regression fails to describe the functional relationship between the response variable and experimental factors. Commonly, if the p-value of lack of fit larger than 0.05, the model accurately fits the data. From Table A3 and A4 (in Supplementary Information in Section 3.3.4, the p-value are above 0.05 indicating that the model has decent fitting.

3.3.5 Confirmation of Experiment

The experiments were repeated to demonstrate the accuracy of the regression equation generated with Minitab 19 and to improve the predictability of the results. In addition, the confirmation test improved the effectiveness of the regression model within parameter levels. Table A5 in Supplementary Information – Section 3.3.5 showed the experimental

setup of four sets of confirmation experiments conducted under different settings including at the optimal conditions predicted by RSM.

As shown in Table 3.3.2, the experimental data were closed to the predicted value that were generated using regression model for both removal efficiency (R%) and uptake capacity, K (mg/g). The percentage deviation shown all the values are less than 10%. Thus, it can be concluded that RSM can be utilised as a tool in optimising the adsorption performance. Thus, it can be concluded that RSM can be utilised as a tool in optimising the adsorption performance. It is also supported by Ghorbani and Kamari (2016) that used RSM to optimise methyl orange adsorption using Fe-grafting sugar beet bagasse. As a summary, the experimental determined by response values agree with the theoretical values assumed by the model. This confirmed the accuracy and precision of the reaction surface models developed.

Table 3.3.2: Comparison data of experimental and predicted results.

Set	Mean Removal (R%)			Mean Uptake Capacity (mg/g)		
	Experiment	Predicted*	Percentage deviation (%)	Experiment	Predicted*	Percentage deviation (%)
1	85.8	77.1	10.14	9.64	8.75	9.23
2	87.9	78.8	9.10	10.4	9.59	7.79
3	90.4	83.0	8.19	12.7	11.9	5.74
4	89.3	86.5	3.14	11.9	10.9	7.98

*Predicted results based on the regression equation generated in Minitab for R% and K (mg/g)

As shown in Figure 3.3.7, it was observed that desorption tends to occur after it had reached a certain limit (after 2 h) for removal efficiency (R%) and uptake capacity, K (mg/g). The reason could be contributed by the high equilibrium adsorption density with high affinity degree between MO

dye and the grafted chitosan PEGDA monolith, which lead to a shorter equilibrium time required to achieve maximum performance (El maguana *et al.*, 2020). This explained that equilibrium can be reached before 2 h, which in turn explained the slight decrease in removal efficiency (R%) at high temperatures. Since this is a monolayer adsorption, once the active sites are full, they can no longer adsorb, and some of the adsorbates are released back into the system. However, further studies on chemical kinetics and thermodynamics are needed to understand the mechanism of the adsorption process (Pimraksa *et al.*, 2020), which has been discussed in Section 3.3.9 and 3.3.10.

In summary, it is recommended that the experiment conducted reflects normal and more environmentally relevant conditions in real-world industrial applications. In wastewater treatment, especially in secondary treatment, higher temperature is not common due to the unfavourable conditions for the bacteria, as it can destroy the bacteria and hinder the process of organic matter removal (Marrone, 2020). The optimal condition for the bacteria is between 20 and 35℃. In addition, high operating condition led to an increase in operating costs for the industry (Huang *et al.*, 2017). Moreover, in terms of pH, the global standard pH for wastewater discharge compliance is from pH 6 to 9 (Raheem, 2018). If the pH of effluent is not meeting the standard, hence pH alteration needs to be done before discharging it into the environment. Therefore, all experiments in the following section are conducted at room temperature (30 ℃) and pH 6.3.

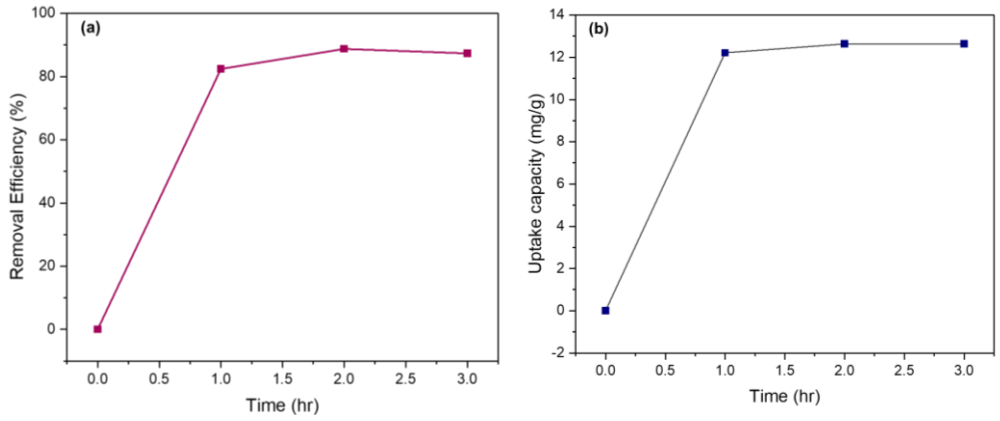


Figure 3.3.7: (a) Plot of removal efficiency (R%) and (b) Uptake capacity, K (mg/g) at optimal condition (C_o= 2 wt.%, dipping time = 45 min, pH = 6.3, temperature = 60℃) agitated in incubator shaker at 150 rpm for 2 h.

3.3.6 Influence of initial MO dye concentration on adsorption efficiency

To further understand the adsorption mechanism of grafted - chitosan PEGDA monolith, experimental work was done to study the influence of initial MO dye concentration on adsorption efficiency. Figure 3.3.8 showed the removal efficiency (R%) and dye uptake capacity, K(mg/g) varied from 25 ppm to 100ppm. The trend for the K(mg/g) gradually increases from 25 ppm to 100 ppm as depicted in Figure 3.3.8, confirming that as the initial dye concentration increases, mass transfer is now more likely to occur due to an increase in dye molecules. On the other hand, the removal efficiency (R%) dropped as the initial concentration of MO dye increases. This is likely to occur as at higher MO dye concentration, adsorption site of adsorbents has reached its saturation equilibrium faster compared to lower concentration. The similar outcome was also reported by other research works (Andrade *et al.*, 2020; Saha, Debnath and Saha, 2022).

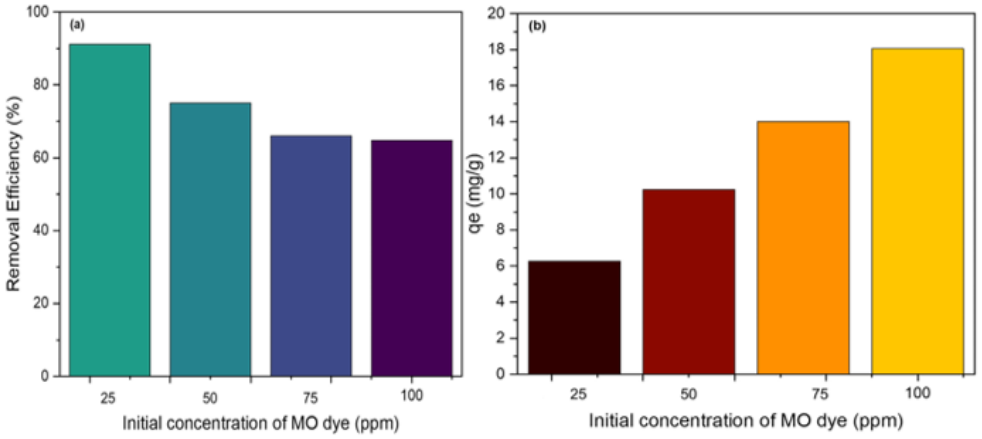


Figure 3.3.8: Plot of Initial concentration of MO dye (ppm) in; (a) Removal efficiency (R%) and (b) Uptake capacity, K (mg/g) at optimal condition (Co= 2 wt.%, dipping time = 45 min, pH = 6.3, temperature = 60℃) agitated in incubator shaker at 150 rpm for 2 h.

3.3.7 Degradation Study

The mechanical stability of the grafted chitosan monolith can be determined by measuring the changes of grafted chitosan monolith weight before and after adsorption at different pH as shown in Table 3.3.3**.** The weight loss (%) shown in the table is less than 1%, indicating that there is no significant weight loss. Hence, it can be concluded that grafted - chitosan PEGDA monolith is stable in the water during the adsorption procedure at any environment (different pH), which also align with the characterisation analysis that the grafted chitosan was firmly anchored on the monolith even after the adsorption.

Table 3.3.3: Retention weight of grafted chitosan monolith before and after MO dye adsorption.

pH	Mass of grafted chitosan monolith (g)								Weight loss (%)
	Before adsorption				After adsorption				
	1st	2nd	3rd	Average	1st	2nd	3rd	Average	
3	0.243	0.243	0.243	0.243	0.243	0.242	0.241	0.242	0.535
7	0.220	0.219	0.220	0.2200	0.219	0.218	0.219	0.219	0.591
11	0.251	0.251	0.250	0.2505	0.250	0.249	0.247	0.248	0.838

3.3.8 Adsorption Isotherm Modelling

The adsorption results were analysed using the Langmuir, Freundlich, Temkin, Harkins-Jura isotherm, Dubinin - Radushkevich isotherm, and Redlich- Peterson isotherm models. This is crucial to study the isotherm to obtain an equation that accurately represent the adsorption result and can be used in the design of experiment.

All the isotherm plots alongside with parameters and coefficient of regression, and R^2 are well presented in Table 3.3.4 and Figure 3.3.9**.** Based on the coefficient of regression, the fit linear line is the highest for Langmuir (0.9954) > D-R (0.9622) > Freundlich (0.9336) > Redlich-Peterson (0.9142) >Temkin (0.827) > H-J (0.5963). The fitting of the experimental data of MO dye adsorption by grafted - chitosan PEGDA monolith indicated that it is a monolayer adsorption. It was assumed that only one molecule can be adsorbed by the identical adsorption site. Hence, once the active site is fully occupied, there is no further adsorption occurring.

Separation factor or equilibrium parameter, which is an important parameter for the Langmuir model, R_L is further analysed to test whether

the adsorption of the adsorbent is favourable or unfavourable (Kalam *et al.*, 2021). The mathematical model can be represented as shown in Eq. (24).

$$R_L = \frac{1}{1 + K_L C_0} \tag{24}$$

where K_L is the Langmuir constant and C_0 is the highest adsorbent initial concentration. Briefly, the value tells that if $R_L < 1$, the adsorption is favourable whereas, if $R_L > 1$, it is corresponding to unfavourable adsorption. $R_L \sim 0$ is irreversible adsorption and if $R_L = 1$, the adsorption is linear. It is calculated that the R_L value for this experiment is 0.69 indicating it is favourable adsorption.

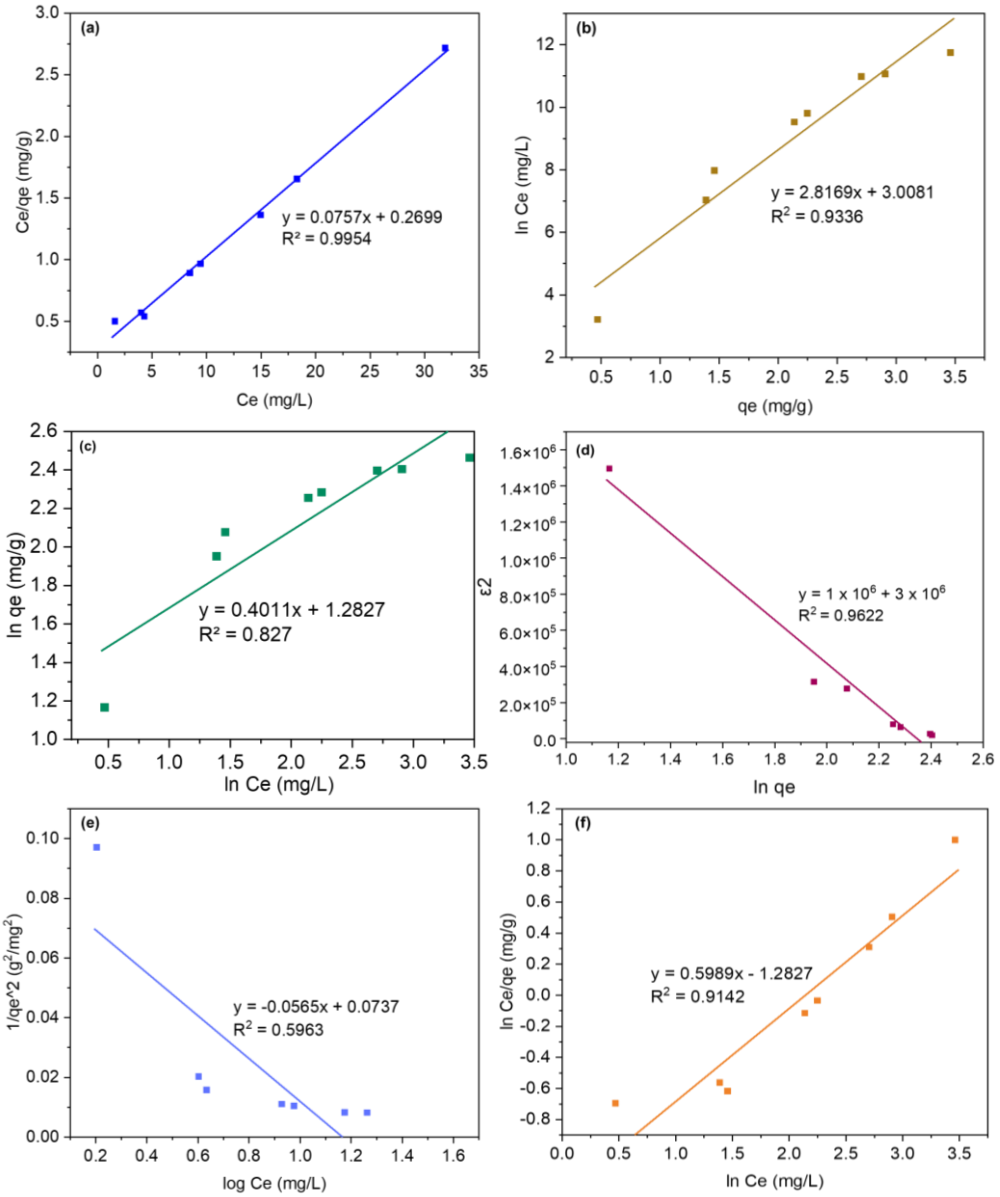


Figure 3.3.9: Adsorption isotherm model plots for adsorption of MO dye by grafted chitosan monolith; (a) Langmuir Isotherm, (b) Freundlich Isotherm, (c) Temkin Isotherm, (d) Dubinin - Radushkevich Isotherm, (e) Harkins-Jura Isotherm and (f) Redlich-Peterson Isotherm.

Table 3.3.4: Different Isotherm linear forms and parameters for MO dye solution adsorption.

Isotherm model	Equation	Parameters	Value	Plot	R^2
Langmuir Isotherm	$\frac{C_e}{q_e} = \frac{1}{(q_m K_l)} \times \frac{1}{C_e} + (\frac{1}{q_m})$	q_m(mg/g) K_L (L/mg)	13.210 0.280	$\frac{C_e}{q_e} vs C_e$	0.995
Freundlich Isotherm	$lnq_e = ln\, K_f + \frac{1}{n} lnC_e$	K_f (mg/g) n	1.283 0.401	$lnq_e vs lnC_e$	0.933
Temkin Isotherm	$q_e = \frac{RT}{b_T}(lnK_t + lnC_e)$	A_t (L/g) b_T	2.909 879.538	$q_e vs lnC_e$	0.827
Dubinin-Radushkevich Isotherm	$lnq_e = lnq_m - K_{DR}\varepsilon^2)$	B_{DR} (mol²/kJ²) q_{max} (mg/g) E (mol/kJ)	-1E+06 27.902 707.107	$lnq_e vs \varepsilon^2$	0.962
Harkins-Jura Isotherm	$\frac{1}{q_e^2} = \frac{B}{A} - \left(\frac{1}{A}\right) log C_e$	A B	17.699 1.304	$\frac{1}{q_e^2} vs log C_e$	0.596
Redlich-Peterson Isotherm	$ln\frac{C_e}{q_e} = \beta lnC_e - lnA$	β A	0.5989 3.606	$ln\frac{C_e}{q_e} vs lnC_{qe}$	0.914

3.3.9 Adsorption Kinetics Studies

All adsorption kinetics model were obtained as shown in Figure 3.3.10. Based on the plot illustrated in Figure 3.3.10b, pseudo-second order fits the linear profile with superior regression coefficient of R^2 = 0.9998. This outcome is in line with the isotherm determined earlier, which is Langmuir isotherm as both plots showed monolayer adsorption. Physisorption occurred in the pseudo-first order reaction. Only physical adsorption occurred between the adsorbate and the adsorbent, which was held together by weak Van der Waals forces (Simonin, 2016). Since the diffusion process was the rate-limiting phase, the concentration of the dye MO had little effect on the results. Multilayer adsorption is illustrated

by the pseudo-first order reaction. In the case of the pseudo-second-order process, chemisorption is assumed to be the predominant mechanism of MO dye adsorption. Monolayer adsorption is demonstrated by the pseudo-second order reaction (Ho and McKay, 1999). Intra-particle diffusion model is related to diffusion-controlled processes - which can be categorized into 3 stages based on the plot of Weber-Morris graph - whereas Elovich model is related to the energy heterogeneity of the surface of the adsorbent. Bangham model is associated with the adsorption process that occurs by means of a pore diffusion mechanism. The plot of the intra-particle diffusion, Elovich and Bangham model for adsorption of MO are represented in Figure 3.3.1c, Figure 3.3.1d and Figure 3.3.1e. For these 3 models, the value of the correlation coefficient, R^2 were lower than the pseudo-second-order model. Hence, it can be concluded that the intra-particle diffusion, Elovich and Bangham model are not a suitable adsorption mechanism for the adsorption of MO onto the grafted - chitosan PEGDA monolith. Table 3.3.5 demonstrated all the kinetic parameters for all models including the experimental value of q_e. It was observed the theoretically calculated value of q_e using the pseudo-second order kinetic modelling approach is significantly closer to the q_e experimental value, showing that the kinetic adsorption curve is accurately represented by this model.

Table 3.3.5: Different kinetic modelling and parameters for MO dye solution adsorption.

Kinetic model	**Parameters**	**Value**	**Plot**	**R^2**
Pseudo-first order	k_1 q_e	-0.3998 12.6200	ln $(q_e - q_t)$ vs t	0.7000
Pseudo-second order	k_2 q_e	1.8303 12.7800	$\frac{t}{q_t}$ vst	0.9998
Intra-particle diffusion	k_{id} c	 12.2571	q_t $vst^{\frac{1}{2}}$	0.6567
Bangham	α K_0	1.1759 60.0172	$log(log\frac{C_0}{C_0 - q_t m})$ vs $log\, T$	0.9714
Elovich	α β	11.4122 3.3681	q_t vs $ln\, t$	0.8343
Experimental value	q_e	12.7000	q_t vs t	-

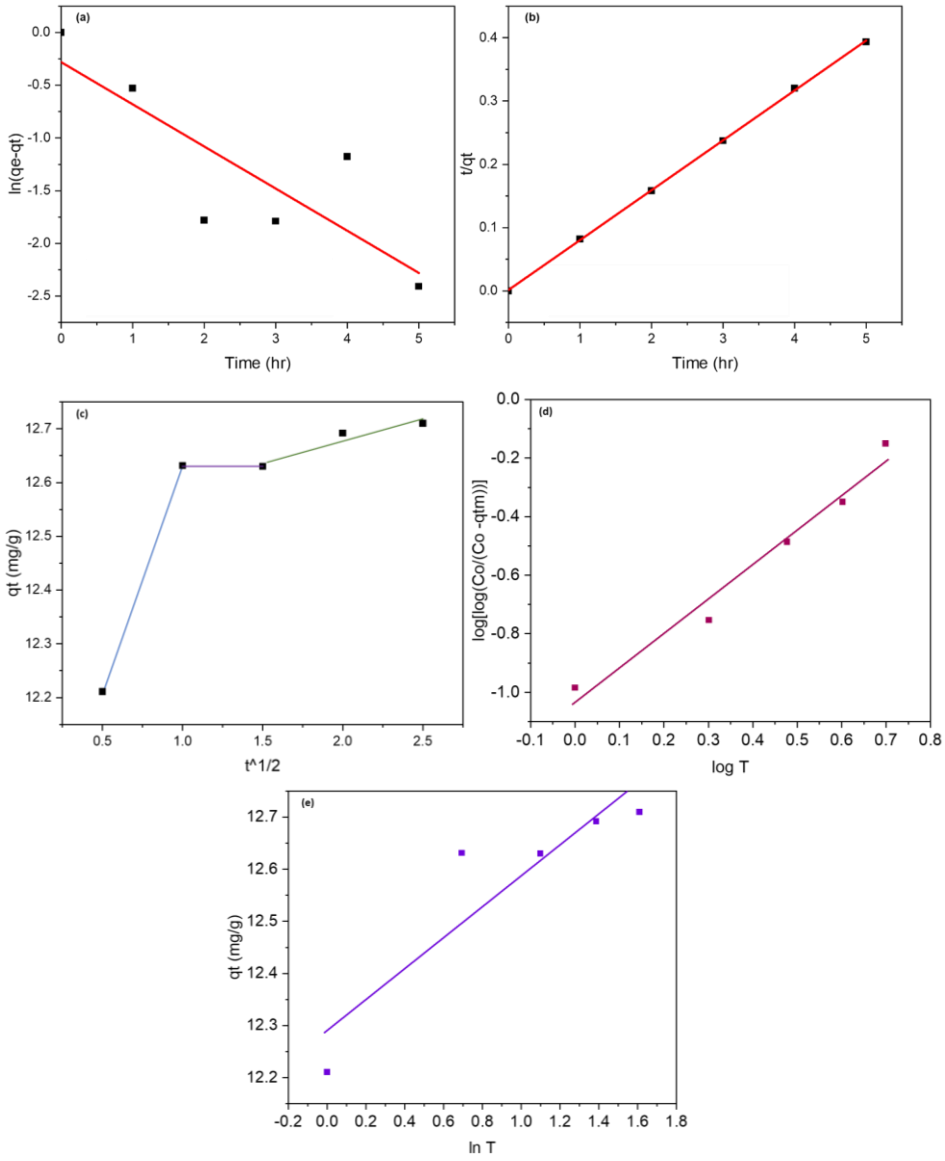


Figure 3.3.10: Plot of adsorption kinetic studies; (a) Pseudo-first order; (b) Pseudo-second order; (c) Intra-particle diffusion model; (d) Bangham kinetic model; and (e) Elovich kinetic model.

3.3.10 Thermodynamics studies

The slope and intercept of the Van't Hoff plot of ln (K_c) versus 1/T were plotted to calculate the values of $\Delta H°$ and $\Delta S°$ as shown in Figure A3 (refer to Supplementary Information-Section 3.3.10) and estimated values for all thermodynamic parameters were tabulated in Table 3.3.6. The negative values of $\Delta G°$ and positive value of $\Delta H°$ indicates that the

adsorption process is spontaneous and endothermic. The adsorption process in a solid-liquid system consists of two steps: (a) desorption of previously adsorbed solvent molecules (water) and (b) adsorption of the adsorbed species. In an endothermic process, the adsorbed species must displace more than one water molecule to adsorb, resulting in the adsorption process becoming endothermic (Saha and Chowdhury, 2011). Besides that, an increase in the negative $\Delta G°$ values with an increase of temperature showed that the adsorption process is less favourable at higher temperature and lower temperature will make the adsorption easier (Saha and Chowdhury, 2011). This could be due to the mobility of the adsorbate, which increases with increasing temperature, allowing the dye molecules to escape from the solid to the liquid phase. As a result, the adsorption capacity of the MO dye decreased as the temperature of the solution increased (Zhou *et al.*, 2014). The positive value of ΔS° suggested that there is an increase in the degree of freedom of the adsorbed species as well as increase in the randomness at the solid-solution interface. It is well known that the heat released during physical adsorption ranges from 2 to 40 kJ mol^{-1} and the heat released during chemical adsorption normally ranges from 80 to 100 kJ mol^{-1} (Potgieter, Pardesi and Pearson, 2021). From Table 3.3.6, it revealed that the magnitude of ΔG° is between 0 to 20 kJ mol^{-1} and $\Delta H°$ is in range of 2.1 to 20.9 kJ mol^{-1}, indicating that the process is physical. As a summary, it can be concluded that the adsorption is physical process, spontaneous and endothermic.

Table 3.3.6: Thermodynamic parameters of adsorption of MO dye on 3D-printed chitosan-grafted monolith at different temperature.

Temperature ($°C$)	$\Delta G°$ (kJ mol^{-1})	$\Delta H°$ (kJ mol^{-1})	$\Delta S°$ (kJ mol^{-1})	R^2
30	-3.192	2.380	18.40	0.9784
45	-3.578			
60	-3.738			

3.3.11 BOD and COD analysis

The grafted - chitosan PEGDA monolith is further analysed for BOD and COD reduction with textile wastewater samples. The experiment was evaluated for 2 h at the optimum condition of the monolith performance which is at T= 30℃ and pH 6.3. As shown in Figure 3.3.11, the 3D-printed grafted chitosan monolith has achieved a 62.4% reduction of BOD, while for COD the reduction is 2% for real wastewater samples and 3.9% for synthetic water samples. The percentage of reduction of BOD was significantly reduced using grafted chitosan monolith, although the reduction of COD was small and does not meet the discharge standard B. This result is consistent with previous publications on the reduction of BOD and COD in the presence of chitosan in the textile industry (Sela *et al.*, 2020), poultry effluent (Bough, Shewfelt and Salter, 1975) and other industries (Okey-Onyesolu *et al.*, 2020). This result highlights the feasibility of using highly robust 3D-printed monoliths with grafted chitosan as a technology to reduce BOD and COD value in a wastewater with good reusability and recyclability (Figure 3.3.12). This approach is more economical and sustainable for industrial applications than the conventional method that tend to be more chemically oriented (e.g.,

ferrous sulphate and alum) as coagulants. In conclusion, the use of grafted - chitosan monoliths integrated with 3D-printing can pave a way as a sustainable solution for BOD and COD reduction, which should be further explored in the treatment of various wastewater samples.

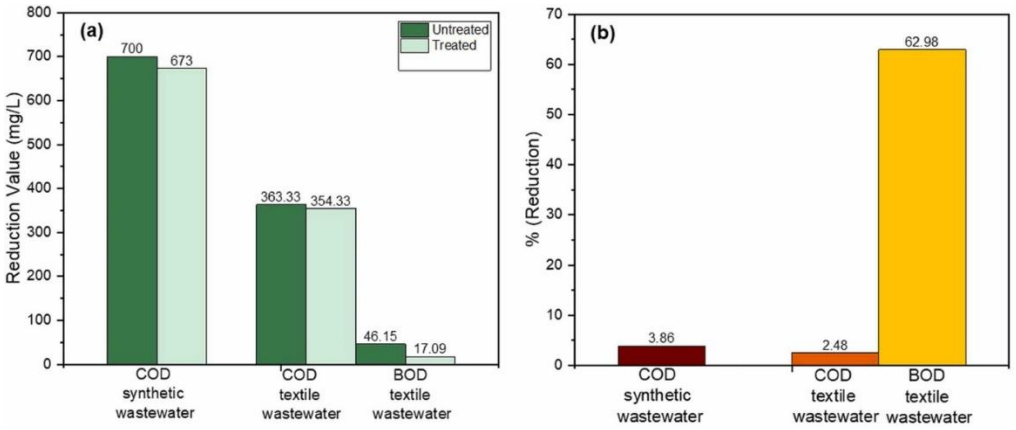


Figure 3.3.11: BOD and COD analysis; (a) Reduction in mg/L and (b) Percentage of reduction (%).

3.3.12 Desorption and Recyclability

Adsorption-desorption studies were performed to investigate the reusability and durability of grafted - chitosan monoliths for industrial applications. To evaluate the reusability of the grafted - chitosan monolith, the sample was evaluated and reused for four consecutive cycles under optimal condition as previously indicated. A new batch of the MO dye was replaced after 2 h of adsorption and absorbance measurements were performed at regular intervals. As shown in Figure 3.3.12a, the NaOH solution can desorb up to 80% of the MO dye solution after 2 h. The result of the reuse test for the grafted chitosan PEGDA monolith is shown in Figure 3.3.12b with the inset outlook of grafted - chitosan monolith after MO dye adsorption and after recyclability. The result showed about 78% of the adsorption performance is retained after

the second cycle and the best adsorption of the grafted - chitosan monolith occurs during the first filtration ~ 90% (Figure 3.3.12b). This result indicates that the saturation of the dye adsorbed on the remaining active sites limits further adsorption, as due to some amounts of MO dye remaining on the monolith after the desorption process. Moreover, it was found that after 4 purification cycles, there is no significant mass loss of the grafted – chitosan monolith. This proved that the grafting is strong and remains on the monolith, resulting in excellent adsorption performance.

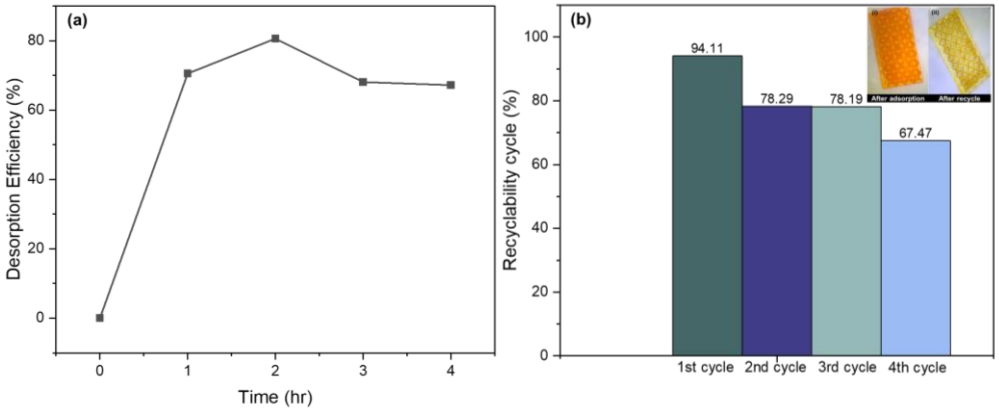


Figure 3.3.12: (a) Desorption capacity of NaOH with respect to MO dye solution. (b) Reusability profile of the grafted - chitosan monolith after 4 consecutive cycles. (Inset: Visual outlook of grafted - chitosan monolith;(i) after MO dye adsorption and (ii) after recyclability test).

3.3.13 Adsorption Mechanism of MO dye

The adsorption MO dye on the grafted - chitosan PEGDA monolith is driven by electrostatic attraction, hydrogen bonding and n–π interaction. MO dye has SO_3^- ions in its structure and it is attracted to the positively charged of $–NH_2$ in chitosan via electrostatic forces. Additionally, the hydrogen bond represents the hydroxyl group on the surface of chitosan, the nitrogen and oxygen in methyl orange. The n- interaction reflects the

O single bond H bonds or oxygen bonds on the surface of chitosan and aromatic ring in methyl orange. Since MO dye can form zwitterion, $–NH_2$ of chitosan will be protonated into $–NH_3^+$ at pH 3, hence cause the repulsion between positive charge in MO and NH_3^+ occurred in acidic condition. The adsorption mechanism is depicted in Figure 3.3.13.

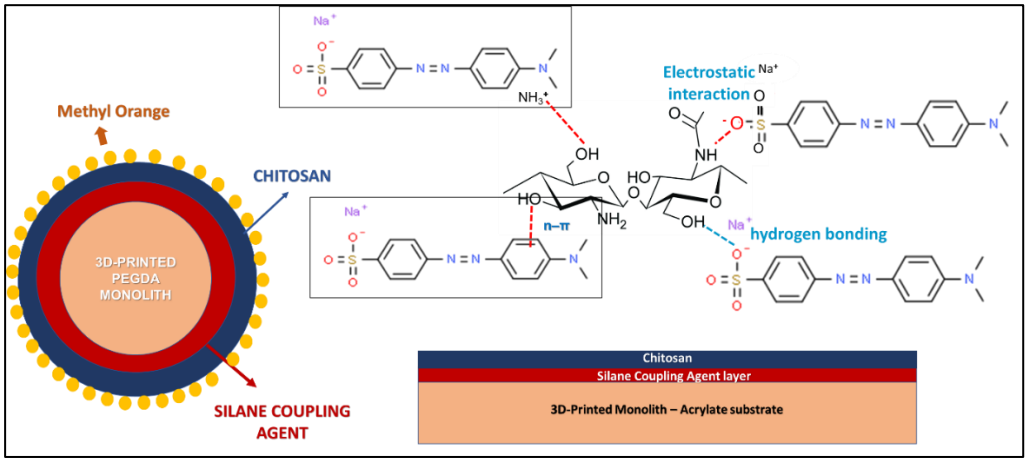


Figure 3.3.13: Adsorption mechanism of MO dye onto chitosan grafted PEGDA monolith.

3.3.14 Comparison with other chitosan-based adsorption system

The comparison of MO dye uptake capacity along with BOD and COD removal were made as shown in Table 3.3.7 and Table 3.3.8. The obtained results were comparable with other works when based on no optimisation studies being conducted under similar conditions. The optimum solution pH range for the majority of the considered adsorption studies was discovered to be acidic which may not be suitable for large scale industrial application (Saha, Debnath and Saha, 2022). In the present study, the pH of the effluent is within neutral range which can be discharged directly to the environment. On top of that, the small uptake capacity of q_e and COD removal is lower is due to small surface area which is 0.532 m2/g and small mass of chitosan attach to the 3D-printed

monolith (0.02g). By comparing reaction time to reach equilibrium, this technology showed it is fast reaction with good recyclability which is more practical for real application as it reduced the production of by-product and the needs to recover the adsorbent compared to other reported works. This demonstrated the feasibility and potential of the current synthesis approach for the fabrication of grafted - chitosan PEGDA monolith with increased uptake capacity.

Table 3.3.7: Comparison of the adsorption properties for MO dye adsorption onto different chitosan-based adsorbents.

Adsorbent	Form	Reaction time (min)	Solution pH	Temperature (K)	q_e (mg/g)	Ref.
γ-Fe_2O_3/SiO_2/ chitosan composite	Nanoparticle	300	2.95	310	34.29	(Zhu *et al.*, 2011)
Magnetic chitosan composite	Particle	1440	5.5	298	149.2	(Cho *et al.*, 2015)
Chitosan/tannin and montmorillonite	Film	80	7.0	298	57.37	(Tahari *et al.*, 2022)
Micro-grooved Chitosan	Bead	3 days	3	298	9.14	(Wong, Wong and Lim, 2021)
Chitosan-glyoxal/TiO_2 nanocomposite	Nanoparticle	180	4.0	313	63.7	(Mohammad, Abdulhameed and Jawad, 2019)
Chitosan/ polyvinyl alcohol/zeolite nanofibrous composite	Membrane	6	N/A	N/A	4.8	(Habiba *et al.*, 2018)
Cs/Kaolin/Fe_3O_4	Film	20	3.21	303	349.7	(Liu *et al.*, 2020)
Grafted - chitosan PEGDA monolith	Monolithic structure	120	6.3	333	12.7	This study

Table 3.3.8: Comparison of the adsorption properties for COD and BOD removal onto different chitosan-based adsorbents.

Adsorbent	Wastewater Industry	Dosage (g)	Reaction time (min)	Solution pH	COD removal	BOD removal	Ref.
TiO_2–chitosan	Petrochemical	2.5	180	7.4	94.5%	-	(Heydari Orojlou, Rastegarzadeh and Zargar, 2022)
Chitosan from prawn waste shell	Textile	0.1	50	4.2	44%	50%	(Sela *et al.*, 2020)
Chitosan coated coconut shell active charcoal	Leather Tanning	5.0	1440	1- 6	99.8%	99.9%	(Lasindrang *et al.*, 2015)
Chitosan -coated bentonite	Thin-film transistor liquid crystal display	0.8	1219.2	4.0	73.34%	-	(Ligaray *et al.*, 2018)
Commercial chitosan flake	Biodiesel	3.5	180	4.0	87.9%	59.3%	(Pitakpoolsil and Hunsom, 2014)
Grafted - chitosan PEGDA monolith	Textile	-	120	6.3	2%	62.4%	This study

3.4 Conclusion

As an overview, the 3D-printed PEGDA monolithic structure of the adsorbent was successfully fabricated using Digital Light Processing (DLP) 3D printing technology, followed by the cross-linked chitosan effectively grafted onto the surface of the 3D-printed monolith. The successful incorporation of the grafted chitosan onto the 3D printed monolith was verified by characterisation tests of FESEM - EDX, XPS, FTIR and XRD. The surface grafting of silane-crosslinked chitosan also improved the mechanical properties and mechanical stability of grafted - chitosan PEGDA monolith. In addition, the application of the grafted - chitosan PEGDA monolith to adsorb MO dye and reduce COD and BOD was further investigated. The response surface method based on the Box-Behnken model was used to optimise the main adsorption control factors. All factors except the dipping time, have a significant effect on the removal efficiency (R%) and the uptake capacity K (mg/g) with ($p < 0.05$). Under optimal conditions, the maximum removal efficiency (R%) and uptake capacity (K) of MO dye are 90.4% and 12.7(mg/g), respectively. The percentage reduction for BOD is 62.4%, while COD is 2% for real wastewater and 3.9% for synthetic water samples. The equilibrium of adsorption was reached in 2 h. The Langmuir isothermal model provided the best fit among six isothermal models with an R^2 of 0.9954. The kinetic studies revealed that the experimental data were best fitted with the pseudo-second order model, confirming that the adsorption is monolayer. It was found that the grafted - chitosan PEGDA monolith exhibits excellent recyclability; by repeating the adsorption-desorption

process for 4 cycles, it was found that the adsorption performance was reduced by 11.3% from its original removal efficiency and maintained at approximately 78% after 2nd cycle. Nevertheless, there are several aspects that still require in depth investigations to enhance its current performance. These include understanding the affinity of grafting chitosan for adsorption of various wastewater treatment, the grafting approach, and material selection for better mechanical properties. In addition, future work is required to analyse the overall mechanical performance in tailoring the final grafted – chitosan PEGDA monolith for practical applications, which is often neglected in the context of 3D printing application. It is anticipated that this research will be deployed as a small-scale pilot test in the industry. This research has demonstrated the potential of exploring a synergistic approach that incorporating 3D printing technique and surface grafting method as a new and sustainable technology for water remediation.

CHAPTER 4: THE INFLUENCE OF STRUCTURAL TOPOLOGY OF ADDITIVELY MANUFACTURED PEGDA MONOLITH ON ADSORPTION PERFORMANCE FOR TEXTILE WASTEWATER TREATMENT

This chapter covers the influence of structural topologies consisting of four different designs of 3D-printed PEGDA monolith. The adsorption performance was evaluated at optimum condition using synthetic dye of methyl orange (MO). The relationship between the surface area and the permeability of the adsorbent was further evaluated. This chapter consists of thesis-version of work submitted in the *Asia Pacific Journal of Chemical Engineering.*

ABSTRACT

The specific surface area and topology of the monolith are one of the most critical parameters that determine the performance and efficiency of the adsorption system. In this work, digital light processing (DLP) was implemented to fabricate four (4) complex monolithic structural designs (Kagome, gyroid, Fischer, and body centred cubic) with specific surface areas varied from 19.4 to 39.84 mm^2. All the monolithic structures with different structural topologies were grafted with chitosan to evaluate their adsorption performance in a batch process. The adsorption studies were operated at an optimal temperature of 60 °C with optimum pH of 6.3 for a reaction time of 2 h using synthetic methyl orange (MO) dye and textile wastewater. Results indicated that the body centred cubic (BCC) design exhibited the highest MO adsorption capacity (12.71 mg/g), with the highest permeability (2.57×10^{-7} m^2) and surface area (39.84 mm^2). Additionally, a direct relationship was found between the surface area and the permeability of the adsorbent as well as adsorption strength. 50% of colour and 2.46% of chemical oxygen demand (COD) removal efficiencies were achieved to verify the adsorbent feasibility in actual application. The present work mainly establishes the feasibility of using different structural topologies to treat the wastewater which can be optimised to enhance the wastewater treatment.

Keywords: Additive manufacturing; Monolithic structures; Permeability; Adsorption; Chitosan; Wastewater

4.1 Introduction

Global water demand is expected to rise by 20-30% to 5,500-6,000 km^3 per year by 2050 (Boretti and Rosa, 2019). However, developing countries are expected to face major water pollution and water scarcity. A substantial portion of this freshwater is converted into industrial effluents, which contain a variety of dyes and chemicals that are contributed by textile industries (Berradi *et al.*, 2019). The pollutants can be distinguished by high levels of biochemical oxygen demand (BOD), chemical oxygen demand (COD), total suspended solids, toxicity, and unpleasant odour, which are typically caused by the presence of nutrients, chlorinated phenolic compounds, and sulphur (Crini and Badot, 2008). Colour of the wastewater is one of the most visible contaminants, and even trace amounts of dye in water can be highly visible and undesirable (Crini and Badot, 2008). Hence, it is necessary to remove at least 90% of pollutants before releasing textile wastewater into the aquatic environment (Mondal, Baksi and Bose, 2016). Therefore, development of advanced monolith is needed to treat the contaminated wastewater to the standard limits (Ghosal *et al.*, 2021; Stefanakis, 2015). There are various contemporary methods have been reported for treating wastewater containing dye. Due to the presence of aromatic rings within the dye, it is hard to biodegrade and posing a significant challenge in terms of its removal in standard biological wastewater treatment. Therefore, the most common and widely used traditional wastewater treatment method in the industry to remove the dye is coagulation-flocculation (Iwuozor, 2019), ion-exchange (Wawrzkiewicz, 2015),

advanced oxidation processes (AOPs) (Bilińska and Gmurek, 2021), and adsorption (Srivastava and Choubey, 2021; Adeyi *et al.*, 2019).The coagulation-flocculation treatment is not effective to remove trace level of pollutants from aqueous solutions. Moreover, this treatment method is only of single usage, thus not able to recycle, and will generate large amount of toxic by-products such as sludge that requires secondary treatment, making the method not sustainable and high cost (Lebogang *et al.*, 2023; Teh *et al.*, 2016). Ion exchange method offers certain benefits, such as the capacity to handle aqueous solutions containing only low concentrations of heavy metals and dye and it is easy to operate. However the drawback of this method is it is too expensive and difficult to elutriate the pollutant from the chelating type (Yasir AlJaberi and Mohammed, 2018). On the other hand, advanced oxidation processes (AOPs) involved the formation of OH radicals and degrade the contaminants efficiently without generating sludge production, but it requires high capital and maintenance cost and the Fenton's reagent caused the formation of iron sludge (Srivatsav *et al.*, 2020). Among of these technology, it is well noted that the most effective dye remediation method is physical or physicochemical treatment with adsorption (Javeed Ganaie, Rafiq and Sharma, 2023). It is regarded as a simple, straightforward, fast, sludge-free process with high efficiency, mechanical stability, and recycling capabilities (Dutta *et al.*, 2021). Nevertheless, the adsorbent has some limitation, such as low surface area, high production cost and difficult to separate the adsorbent from dye during the recovering process (Moosavi *et al.*, 2020). Thus, choosing

a suitable adsorbent is vital in fulfilling the aforementioned requirements to provide a package of adsorbent that can complete the adsorption within a brief period of time and reduce the waste generation.

Various adsorbents, such as activated carbon, bio-adsorbent, polymer-based materials and metal-organic framework (MOF), are frequently employed in dye adsorption from contaminated water (Dutta *et al.*, 2021; Zhou *et al.*, 2019). The use of biopolymer adsorbents has garnered incessant interest among the researchers due to advantageous properties such as biodegradability and cost-effectiveness. The common type of biopolymer adsorbents are chitin, cellulose and chitosan. Chitosan is widely preferred because it is environmentally friendly and biodegradable, as well as able to adsorb significant amounts of dyes and metal ions (Gamage *et al.*, 2023). It is also non-toxic and easy to functionalise to increase the surface area and adsorption performance (Kasiri, 2019). However, the chitosan cannot be used as a stand-alone material for adsorption as it has low porosity and acid resistance (Li *et al.*, 2019). Various methods have been proposed to modify the chitosan through chemical and physical modifications. Recently, graft copolymerisation has piqued the interest of scientific community and evolved into an important technique in polymer chemistry (Dutta *et al.*, 2022). The grafting reaction can improve chemical stability of the polymer in aqueous media with a wide pH range and eventually enhance the sorption performance.

The 3D-printed adsorption system's effective operation and adsorption performance depend not only on the surface area of the structures but also on the interaction of the adsorbent with the adsorbate in the design system that can be measured through mass transport characterisation such as permeability and tortuosity features. The permeability measured the rate of the water movement and how fast or easily the water passes from one point to another (Li *et al.*, 2022b), while tortuosity is the ratio between the point of the straight-line distance in the porous medium to the average length of the routes connecting those sites (Diao, Zhang and Zhao, 2017). Tortuosity can directly impact dynamic specific surface area, fluid permeability and diffusion. The efficient permeability ensures excellent treatment efficiency by giving ample contact time and allowing the adsorbent to function in the most appropriate environment. This can be aided by improving flow mechanics, such as continually agitating in a batch system and selecting porous or high-specific area materials to allow for the greatest contact between adsorbent and adsorbate (Sharma and Kaur, 2011). Li *et al.* (2022b) reported that the porous structures of 3D bio-scaffolds enhanced the permeability of the nutrients for the growth of bacteria, which enhanced the ammonia removal. In another study done by Ma and Liu (2022), the porous structure of the 3D-printed bulking agent improved the microbial activity and oxygen permeability to speed up the breakdown of organic materials. Hence, these show that there is a direct relationship between permeability and surface area that can significantly affect the overall adsorption performance based on the efficiency of fluid flow in the porous media (Prakoso *et al.*, 2023; Song *et*

al., 2024). In addition, the microstructure or porous media with small tortuosity can also produce an outstanding surface-to-volume ratio, which greatly enhances the surface contact. Therefore, it is necessary to consider the parameters described above when designing the 3D-printed adsorbent's system that can be maximised concurrently by rationally designing the adsorbent system. The 3D-printed adsorbent system can be mass-produced, improves operational efficiency and versatile for designing any structural topology of improved resolution, as well as a controllable pore structure. 3D printing has the ability to print complex topologies structures such as triply periodic minimal surfaces (TPMS), shell lattice, strut-based and Voronoi - based structures (Ghannadpour, Mahmoudi and Hossein Nedjad, 2022; Sokollu, Gulcan and Konukseven, 2022). TPMS designs are favourable as it possesses a high degree of control and homogeneity, as demonstrated in studies by (Blanquer *et al.*, 2017; Bohner *et al.*, 2011). The utilisation of TPMS-based porous structures shows promise application in clinical settings (Lv *et al.*, 2022), catalyst (Chen *et al.*, 2024), aerospace field and thermal application (Xu and Lin, 2023), attributed to their notable attributes of high permeability and specific surface area. On the other hand, the consistent arrangement of the lattice unit cell of strut-based design provides a means to manipulate the collective structural behaviour and adjust/refine the lattice configuration in order to produce a functionally graded material tailored for specific design purposes (Bolan, Dean and Bardelcik, 2023; Shin and Chang, 2021). By observing the substantial need for engineering design and conducting a comprehensive analysis of existing literature (Dong

and Zhao, 2021; Yeranee and Rao, 2022; Ramakrishna and Bala Murali, 2022; Isaac and Duddeck, 2022; Egan, 2023), it becomes apparent that this field remains a persistent focus of research, drawing the interest of numerous scholars.

Additionally, the merging of surface functionalisation with additive manufacturing has developed into a new manufacturing paradigm that offers innovative wastewater research which is both promising and convincing in meeting the industrial demand (Mohd Yusoff *et al.*, 2022). The feasibility of grafted chitosan onto the 3D-printed monolith in removing environmental pollutants and parametric optimisation has been demonstrated in our previous study (Husna *et al.*, 2022). This robust approach can minimise the generation of by-product waste without compromising the performance of wastewater remediation.

Currently, this approach is only used in designing 3D-printed biocarrier for biological treatment systems to treat wastewater. To the best of our knowledge, the influence of structural topology of the monolithic structure on the adsorption performance for textile wastewater has not yet been reported in any literature. In this work, four monolithic structures with different structural topologies (Gyroid, Fischer, Kagome and body centred cubic) were fabricated using digital light processing (DLP) technique and grafted with a layer of silane cross-linked chitosan that functions as a filter in the wastewater treatment. Subsequently, this research investigated the influence of the structural topology of the grafted 3D - printed monolith on the adsorption performance with methyl

orange dye (MO) and textile wastewater samples in a batch process. The relationship between specific surface area and permeability was further investigated through water permeability test. On top of that, the mechanical properties of different structural topologies were evaluated. In general, this study is expected to inspire new research ideas in the field of wastewater treatment as it emphasises the flexibility, robustness, and practicality of 3D printing technology. Section 4.2 of the paper will describe the materials and methods used in this experiment, followed by the results and discussion section, and finally the conclusion for the experimental work.

4.2 Experimental

4.2.1 Materials

The acrylate Magma plant-based resin (≥ 99.9 %, MW: 308 g/mol, viscosity: 10 – 30 cP at 25 ℃) was purchased from 3D Gadgets Malaysia. Poly (ethylene glycol) diacrylate (PEG200DA) (MW PEG Block= 200; n=4, viscosity: 25 cP at 25 ℃) was purchased from Ryoji, China. Photoinitiator (Irgacure 819); Phenylbis(2,4,6-trimethylbenzoyl) phosphine oxide (MW: 418.5 g/mol) and methyl orange dye (MO) ACS reagent (85 %, MW: 327.34 g/mol, pKa = 3.4) were purchased from Chemmart Asia Sdn. Bhd. Chitosan (CS) white powder (AR grade; degree of deacetylation of 99 %, MW: average of 890,000 g/mol) was purchased from Fulltime Asia Sdn Bhd. Hydrochloric acid (HCl) (37 %, MW:36.46 g/mol), isopropyl alcohol (IPA) (≥90 %, MW: 60.1 g/mol), and sodium hydroxide (NaOH) (99 %, MW: 40 g/mol) were purchased from Giti Eco Sdn. Bhd., Malaysia. Glycidyloxypropyl trimethoxysilane

(GPTMS) (≥98 %, MW: 236.34 g/mol) and (3-aminopropyl) trimethoxysilane (APTMS) (97 %, MW: 179.29 g/mol, density: 1.027 g/ml at 25 °C) were purchased from Sigma-Aldrich, USA. COD digestion vials [high range (20–1500 mg/L)] was purchased from HACH Malaysia Sdn. Bhd. All chemicals were used as received without any further modification or processing otherwise stated.

4.2.2 Design of structural architecture and manufacturing

4.2.2.1 3D printing formulations and printer settings

A custom photopolymerisable resin with poly (ethylene glycol) diacrylate (MW PEG Block = 200) as the monomer, 1% (w/w) phenylbis(2,4,6-trimethylbenzoyl) phosphine oxide (Irgacure 819) as the photoinitiator, and a plant-based photopolymer resin was formulated as depicted in Figure 4.2.1a. The liquid resin was mixed well for 30 min using a magnetic stirrer (Thermo Fisher Scientific, United) and stored in dark brown bottle to avoid exposure to light as this formulation is sensitive to UV light. Digital light processing (DLP) based additive manufacturing using Phrozen Sonic Mini 3D printer was chosen and used. This fabrication technique offers high-resolution layer-by-layer printing with a minimum size of 50 µm (Husna *et al.*, 2022; Phang *et al.*, 2021). It has a 405 nm LED light source and a projected image plane of 1920 × 1080 pixels. Chitubox slicing tool was used to control and set up all aspects of 3D printing settings, allowing a single print job that includes an arbitrary combination of layer thickness, exposure times, and multiple images for each layer, enabling complete resin control throughout the volume of a 3D-printed part. The printed product was rinsed with isopropanol to

remove all impurities and resin residue before being exposed to UV light for another 10 min. The printing processing parameters are shown in Table 4.2.1.

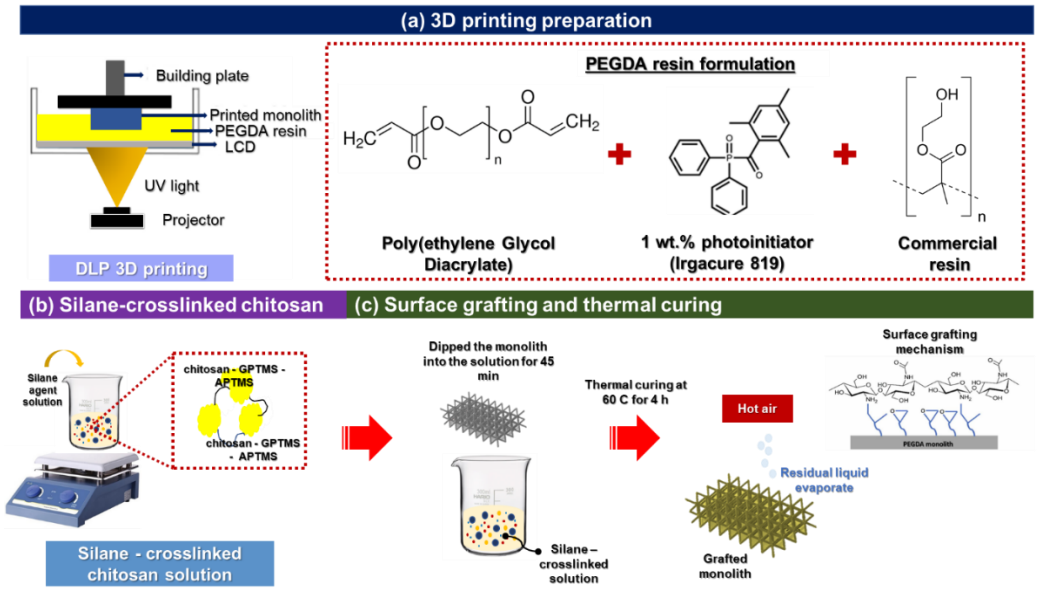


Figure 4.2.1: Synthesis of grafted 3D-printed PEGDA monolith with silane-crosslinked chitosan.

Table 4.2.1: Parameters of 3D printing.

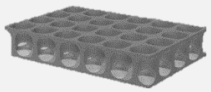
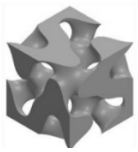
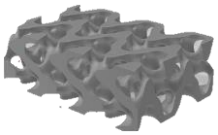
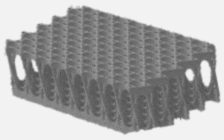
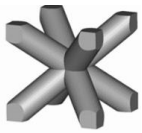
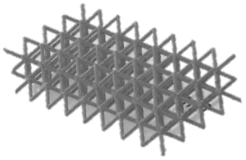
Printer Parameter	Setting
Exposure time (s)	4
Bottom exposure time (s)	30
Lift distance (mm)	5
Lift speed (mm/min)	100
Layer height (mm)	0.05
Retract speed (mm/min)	200

4.2.2.2 Details of different structural configuration of monolithic structures

In this study, triply periodic minimal surface (TPMS) and struts-based designs were considered as both types of lattice design offer high surface

area (Ghannadpour, Mahmoudi and Hossein Nedjad, 2022; Lu *et al.*, 2020). The design was named and labelled as shown in Table 4.2.2. All the monolithic structures with dimensions of 0.5 cm ×2 cm ×1 cm were designed using computer-aided design software (CAD). The printed samples of different structural topologies were illustrated in Figure 4.2.2. The calculated surface area of the model was analysed using Autodesk Fusion360 software.

Table 4.2.2: Details of detailed design.

Name	**Lattice type**	**Unit cell**	**Specific surface area**	**Infill density**	**Monolithic lattice structure**
Gyroid	TPMS		28.81 mm^2	100%	
Fischer Koch	TPMS		38.10 mm^2	100%	
Kagome	Strut-based		19.04mm^2	100%	
Body centred cubic	Strut-based		39.84 mm^2	100%	

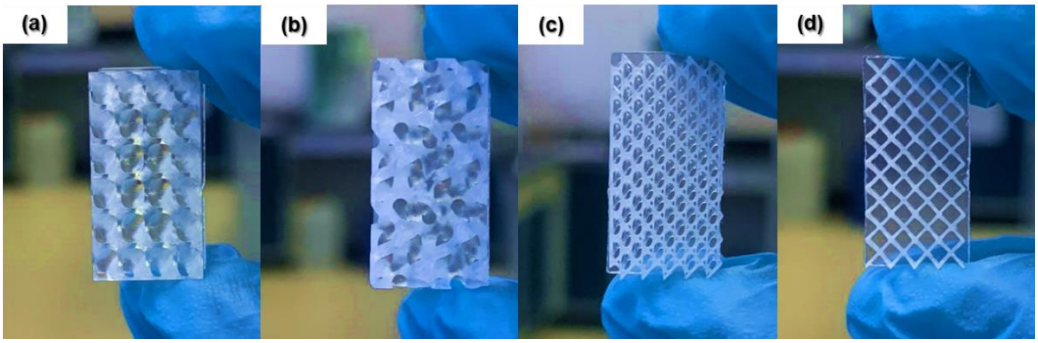


Figure 4.2.2: 3D-printed monolithic structure of different structural configuration. (a) Gyroid; (b) Fischer; (c) Kagome and (d) Body centred cubic lattice.

4.2.3 Preparation of silane-chitosan grafted monolith

The silane-crosslinked and grafted monolith was prepared via epoxide amide reaction with a mixture of chitosan and hybrid alkoxysilanes precursors acting as crosslinker. A hybrid silane agent was selected as it can increase the thermal and mechanical properties of the materials through a siloxane inorganic network and an organic function linked to the same silicon tom, which can interact with or create an organic polymeric network (Lollivier *et al.*, 2021). Briefly, a formulation of silane agent which consist of GPTMS and APTMS was mixed with IPA and DI water at ratio of 3:1:6:1 as described by (Zhang *et al.*, 2019b) for 5 min in a beaker. For the formation of silane-crosslinked chitosan, 1 ml of hybrid silane mixture was added into 10 ml of 2wt% of chitosan (pH ~ 5 – 6) and continuously stir until the mixture became homogenous as shown in Figure 4.2.1b. Subsequently, the 3D-printed monolith was dipped into the solution for 45 min and oven-dried for 4 h at 60℃. During this procedure, the triangle bond of O-Si-O from GPTMS will form a covalent bond with the backbone of H-N-H of chitosan via surface grafting mechanism. The surface grafting procedure will then be

performed, and a layer of chitosan will deposit onto the surface of the PEGDA monolith as depicted in Figure 4.2.1c. Figure 4.2.3 showed the images of monolithic structures of different structural topologies after grafted with silane-chitosan alongside with its mass before and after grafting procedure as illustrated in Table 4.2.3.

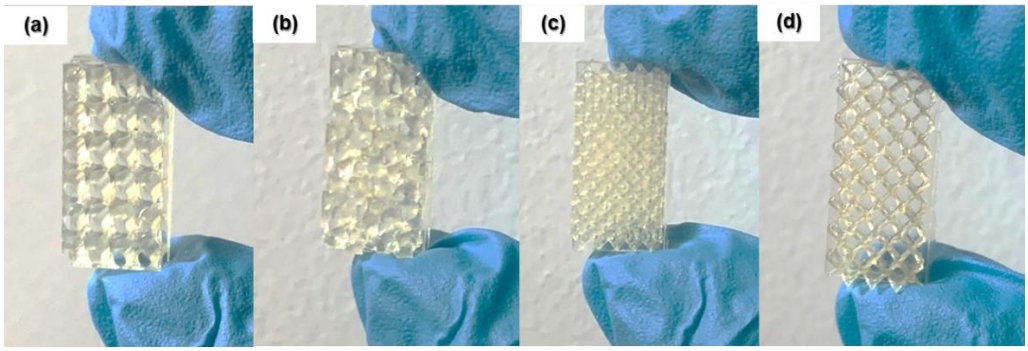


Figure 4.2.3: Silane-chitosan grafted monolithic structure of different structural configuration. (a) Gyroid; (b) Fischer; (c) Kagome and (d) Body centred cubic lattice.

Table 4.2.3: Mass of different structural topologies before and after grafting procedure.

Sample	**Measurement (g)**			
	Gyroid	**Fischer**	**Kagome**	**Body centred cubic**
Mass before grafting	0.582	0.657	0.363	0.204
Mass after grafting	0.594	0.669	0.372	0.234

4.2.4 Characterisation methods

4.2.4.1 FESEM Analysis

Field Emission Scanning Electron Microscope (FESEM) (Quanta 400F, FEI, USA) was used to examine the surface morphology and microstructures at magnifications ranging from x60 to x800. The samples were first coated with a thin layer of platinum in rotary pumped coater

(Quorum, 150 A S plus, UK) at deposition rate of 6 nm/min with deposition current of 20 mA before FESEM observation. The accelerating voltage of FESEM was set to 20 kV in low vacuum for Large Field Detector (LFD) mode and 2 kV in high vacuum for Everhart-Thornley Detector (ETD) mode.

4.2.4.2 FTIR spectroscopy

FTIR spectroscopy (ATR-FTIR, Perkin Elmer Frontier FT Mid-IR/Far-IR, USA) was performed at the range of 400 – 4000 cm^{-1} to verify the uniformity of grafted silane-crosslinked chitosan on the monolithic structure with different structural topologies. It was also used to determine the functional groups involved in the grafting of chitosan on the monolith and to understand the mechanism of its interaction with MO dye before and after adsorption.

4.2.4.3 Mechanical properties study

Texture Analyser, TA.XT plus (Stable Micro Systems, USA) was used to measure the mechanical properties of the different structural configurations at a crosshead speed of 1 mm/min and a maximum load of 30 N load cells based on American Standards for Testing Methods (ASTM) D1708. The initial elastic slope of the stress-strain curve was used to calculate the compressive modulus.

4.2.4.4 Permeability analysis

The morphological properties of the monolith were further studied using water permeability analysis. Briefly, as proposed by Montazerian *et al.* (2019), the monolith was attached to the inlet of a 3D-printed milichamber, where the fluid flows naturally. After that, the volume of the

fluid per unit time at the outlet was measured while the fluid level remained constant. It is important to ensure there is no bubble formation in the monolith prior to the experiment for accurate readings. The fluid flow rate measurement was repeated three times. The longitudinal permeability values (k) were calculated using Darcy's law given by in Eq. (25).

$$k = \frac{v\mu L}{\Delta P} \tag{25}$$

Where v is inlet velocity, μ is fluid viscosity which in this case is water ($1.0016\, mPa.s$), L is the size of unit cell of the monolith and ΔP is the pressure drop under same boundary conditions to exclude the dimensional effects.

4.2.4.5 Batch adsorption performance evaluation

The removal of MO dye by grafted 3D-printed monolith with various structural topologies were investigated. All batch adsorption experiments were conducted with a fixed volume of 40mL of 50 ppm of methyl orange (MO) dye solutions in an incubator shaker at 150 rpm (N) using single unit of monolith. The MO dye samples were collected for analysis at 30-min intervals, and the concentration was determined using a UV-Vis spectrophotometer (Perkin Elmer Lambda 35, United States) at a fixed wavelength of 464 nm. The removal efficiency and uptake capacity of the MO dye were calculated using Eqs. (26) and (27) and, where C_0 and C_t is the initial and the concentration and time t respectively, V is dye solution volume (L) and m is the mass of the grafted monolith.

$$MO\ dye\ removal\ efficiency\ (\%)\ = \frac{C_o - C_t}{C_o} \times 100\% \quad (26)$$

$$Uptake\ capacity\ of\ MO\ dye\ (mg/g) = \frac{(C_o - C_t)V}{m} \quad (27)$$

4.2.4.6 Colour and COD removal analysis

In this study, COD and colour removal analysis were performed on textile wastewater samples provided by Eco Solution Services Sdn. Bhd. in Batu Pahat, Johor, Malaysia. The characteristics of the textile wastewater sample can be found in Table 4.2.4. Briefly, the COD reduction test was performed in accordance with the procedure outlined by HACH Company. 2 ml of treated samples were pipetted into COD vials and digested at 150℃ for 2 h using the HACH COD reactor (DRB200, United States). The vials were then cooled to room temperature before the COD measurement was performed with the HACH Spectrometer (DR3900, United States). The removal of COD was calculated using the following Eq. (28).

$$COD\ removal\ (\%) = \frac{D_i - D_o}{D_i} \times 100\% \quad (28)$$

Colour measurements were conducted according to the Platinum-Cobalt unit with HACH Spectrometer (DR3900, United States) at fixed wavelength of 465 nm. The unit conversion of ADMI to PtCo is at the conversion factor of 1 (KgaA, 2019).The colour removal percentage was calculated using the following Eq. (29).

$$Color\ removal\ (\%) = \left(\frac{P_o - P_t}{P_o}\right) \times 100\% \quad (29)$$

Where P_o is the value of Pt Co of raw wastewater and P_t is the value of Pt Co of treated wastewater.

Table 4.2.4: Characteristics of textile wastewater sample collected from the industry.

Parameter	Value
pH	6.6
BOD (mg/L)	97
COD (mg/L)	363
Colour (ADMI)	446
Total suspended solids (mg/L)	46
Oil & Grease (mg/L)	0.5
Ammonical nitrogen as N (mg/L)	2.52

4.2.4.7 Mechanical stability study

To comprehensively analyse the mechanical stability of the grafted-chitosan PEGDA monolith for each structural design, a degradation study based on weight loss measurement was performed before and after adsorption. The measurements were carried out in triplicate, and the resulting mean value ± standard error was recorded. The weight of the samples was determined utilizing the equation specified as shown in Eq.(30).

$$\text{We}ight\ \text{loss}\ (\%) = \left(\frac{\mathrm{W_o} - \mathrm{W_f}}{\mathrm{W_o}}\right) \times 100\% \quad (30)$$

Where W_o and W_f represent the initial and final weight of the sample in g after undergoing an adsorption process, respectively. The mean value of three samples was calculated and subsequently reported.

4.3 Results and discussion

4.3.1 Characterisation samples

4.3.1.1 FESEM and EDX analysis

FESEM analysis was used to investigate the surface morphology and structure of the grafted – chitosan PEGDA monolith of different structural topologies (i.e., Gyroid, Fischer, Kagome and Centred cubic) as depicted in Figure 4.3.1. Figure 4.3.1a(i) to d(i) demonstrated an overview of different structural topologies of monolithic structures with an enlarged segment from top view prior to surface grafting (Figure 4.3.1a(ii) to d(ii). From the top view, a homogeneous and smooth surface can be seen whereas from cross-section view (Figure 4.3.1a(iii) to d(iii), wrinkled layers of silane-grafted chitosan were exhibited on the printed monolith of all structural topologies. However, monolith with a centred cubic design has a more uniform coating compared to other designs. This is due to the design configuration, as the chitosan solution easily flow in each section of the monolith blocks during the coating procedure. The uniformity of the coating was further validated using FTIR which will be discussed in Section 4.3.1.2.

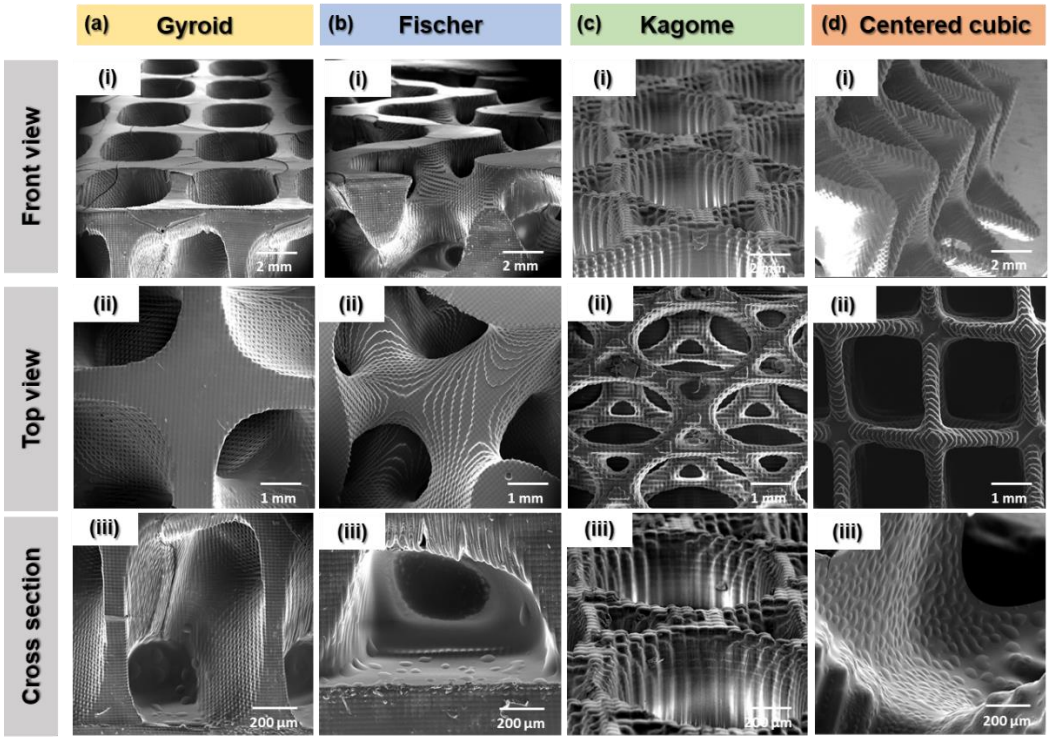


Figure 4.3.1: FESEM images of grafted – chitosan PEGDA monolith of different structural topologies of monolith from front, top and cross-section view at different magnifications. (a) Gyroid structure; (b) Fischer Koch S structure; (c) Flat Kagome structure; and (d) Body centred cubic structure.

The quantitative elemental composition of 3D-printed monolith and silane-crosslinked chitosan was studied using EDX analysis as shown in Table 4.3.1 The presence of C and O only can be seen in pure PEGDA monolith. In contrast, Si and N elements were detected on the surface of the monolith after grafting with silane cross-linked chitosan before the adsorption process. This observation confirmed that surface grafting has successfully induced the binding of Si ions and the protonation of chitosan on the surface of the monolith. The S element, a component of the chemical structure of MO dye, appeared in the EDX spectrum with 0.7wt% in the monolith after the adsorption study. This provides the evidence for the successful adsorption of MO dye. The N element was

reduced after the adsorption, showing that the element was used during the adsorption process. The possible mechanism of MO dye adsorption on the silane-grafted chitosan is attributed to electrostatic attractions between the dye ion pairs of the SO_3^- group and ion pair associations of the protonated chitosan layer. As a result, when the N element interacts electrostatically with the dye ions, the spectra intensity is reduced.

Table 4.3.1: EDX analysis of elemental weight composition of pure PEGDA monolith and silane-crosslinked chitosan samples before and after adsorption.

Sample	**Elemental weight %**				
	C	**N**	**O**	**Si**	**S**
Pure PEGDA monolith	59.2	0	40.8	0	0
Silane-crosslinked chitosan before adsorption	49.1	3.8	43.1	3.6	0
Silane-crosslinked chitosan after adsorption	54.1	1.6	41.3	2.3	0.7

4.3.1.2 FTIR analysis

The uniformity of the coating on the different monolithic designs as well as molecular structure of the 3D-printed silane grafted chitosan were analysed via FTIR as depicted in Figure 4.3.2a. It was observable that the FTIR spectra of 3D-printed PEGDA and silane grafted chitosan of structural design of Fischer, Gyroid and Kagome have similar spectrum. The absorption band at 1633 cm^{-1} can be attributed to a C=C aliphatic double bond, and the peak at 1724 cm^{-1} can be ascribed to a carbonyl group (C=O). The C–O stretching vibration is visible at 1098 cm^{-1} and 1240 cm^{-1} whereas C-H band stretching vibration is at 2860 to 2930 cm^{-1}, respectively with weak intensity. The detected spectrum was in good agreement with the previously published spectra of acrylate bond, in this case is PEGDA (Li *et al.*, 2016; Askari *et al.*, 2019; Thukral *et al.*, 2014).

There is no obvious peak that showed detection of any spectrum associated to chitosan bonding. On the other hand, the detection of FTIR spectra of centred cubic structural design is different compared to other designs. The characteristic band at 3423 cm^{-1} was represented by $-NH_2$ and -OH stretching vibration, whereas the peak at 1639 cm^{-1} showed the characteristic of the amide group. However, the stretching of vibration at this absorption band could be due to the overlapping of the C=O amide band with the Si-OH bond from GPTMS and APTMS. These spectra further confirmed the uniformity of the silane-grafted chitosan on the monolith, as chitosan peaks were portrayed in Figure 4.3.2 for body centred cubic design. The Si-O-C bond at a small band of 1074 cm^{-1} showed an increase in intensity, which further confirmed that the chitosan was successfully grafted on the 3D-printed monolith (Reyes-Peces *et al.*, 2020). Figure 4.3.2b showed the FTIR analysis after the adsorption of MO dye. It was found that there is a new and intense peak corresponding to the sulfonic acid group (SO_3^-) that appeared at 1370 cm^{-1}, implying possible electrostatic interactions between the negatively charged SO_3^- of MO dye and the positively charged chitosan. Based on previous studies, it was identified that sulfonate groups are the most crucial electrostatic-attraction force donor for MO adsorption (Liu *et al.*, 2020; Wong, Wong and Lim, 2021). The peak at 1115 cm^{-1} and 825 cm^{-1} represented the S=O bond and -CH bond in para-benzene respectively, showing that the chitosan had successfully adsorbed the MO dye. Another evidence that the chitosan adsorbed MO dye as there is new peak at 2860 cm^{-1} that is attributed to the possible amine salt reaction,

between -NH group of chitosan and Na^+ of MO dye. Furthermore, based on the adsorption mechanism of MO dye as illustrated in Figure 4.3.3, there is high possibility of n-π stacking interaction that involved in the adsorption. As shown in Figure 4.3.2b, a new peak at 1600 cm^{-1}, indicating the vibration of MO anion phenyl groups. This is because n-π interaction occurs when the lone pair electrons on an oxygen atom are delocalized into an aromatic ring of dye orbital. The appearance of the weak intensity and shifted of C=O and C-O peaks after adsorption may have been attributed by the n-π interaction. Moreover, Yoshida H-bonding and dipole-dipole hydrogen bonding interactions are two types of hydrogen bonding that can occur during the adsorption process. Based on Yoshida-H bonding mechanism, the attraction occur by the interaction between H bonds from OH group with the delocalized π electron cloud (Yoshida, Osawa and Oda, 1964). In this work, the peak intensity of OH bond in Figure 4.3.2b also decreased noticeably and shifted from 3423 to 3450 cm^{-1} after adsorption. This is because the -OH bond of chitosan may overlap with the aromatic rings of MO dye that has delocalised π^* orbital of an aromatic ring, implying that the Yoshida H-bonding may also be involved in the adsorption process (Tran *et al.*, 2017; Bahrudin *et al.*, 2020). The interaction of dipole-dipole hydrogen bonding can be detected at the peak of 1548 cm^{-1} which is attributed to N-H bonding between the N atom on the MO dye and H atom of the silane-crosslinked chitosan. Dipole-dipole H bonding interaction occur due to the attractive force between a hydrogen atom covalently bonded to a very electronegative atom such as an N, O, or F atom. Overall, it can

be concluded that the plausible mechanism of MO dye adsorption on the grafted – chitosan 3D-printed may be mainly attributed to electrostatic attractions, n–π stacking interactions, Yoshida H-bonding and dipole-dipole hydrogen bonding interactions as illustrated in Figure 4.3.3. The similar outcome of adsorption mechanism was also reported by Jawad *et al.* (2019b) who studied on the adsorption of chitosan-glyoxal film for different reactive and acid dyes.

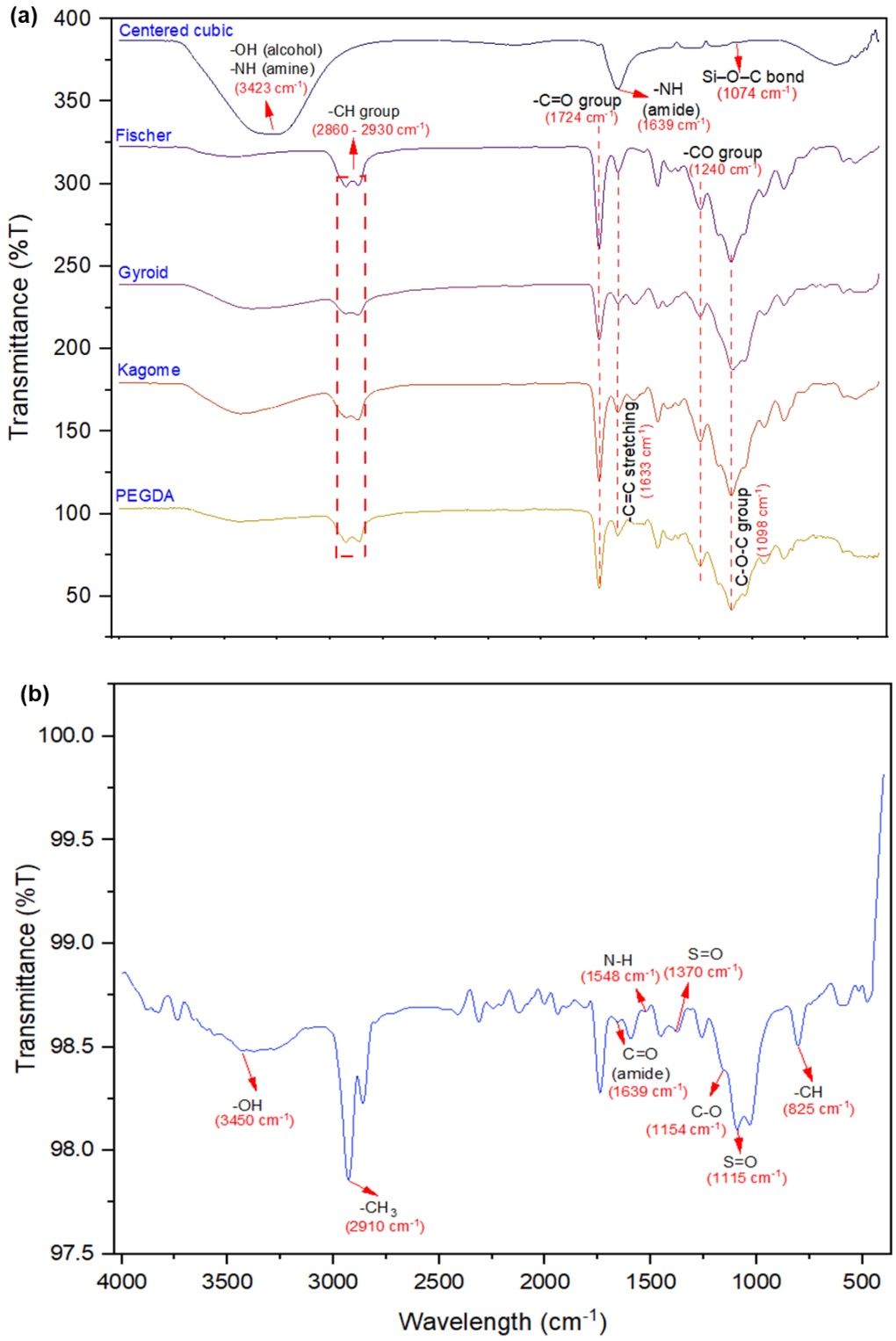


Figure 4.3.2: (a) FTIR spectra of pure 3D-printed PEGDA before grafting and grafted 3D-printed PEGDA of different monolithic structural designs before adsorption and (b) FTIR spectra of grafted 3D-printed PEGDA monolith after adsorption for body centred cubic design.

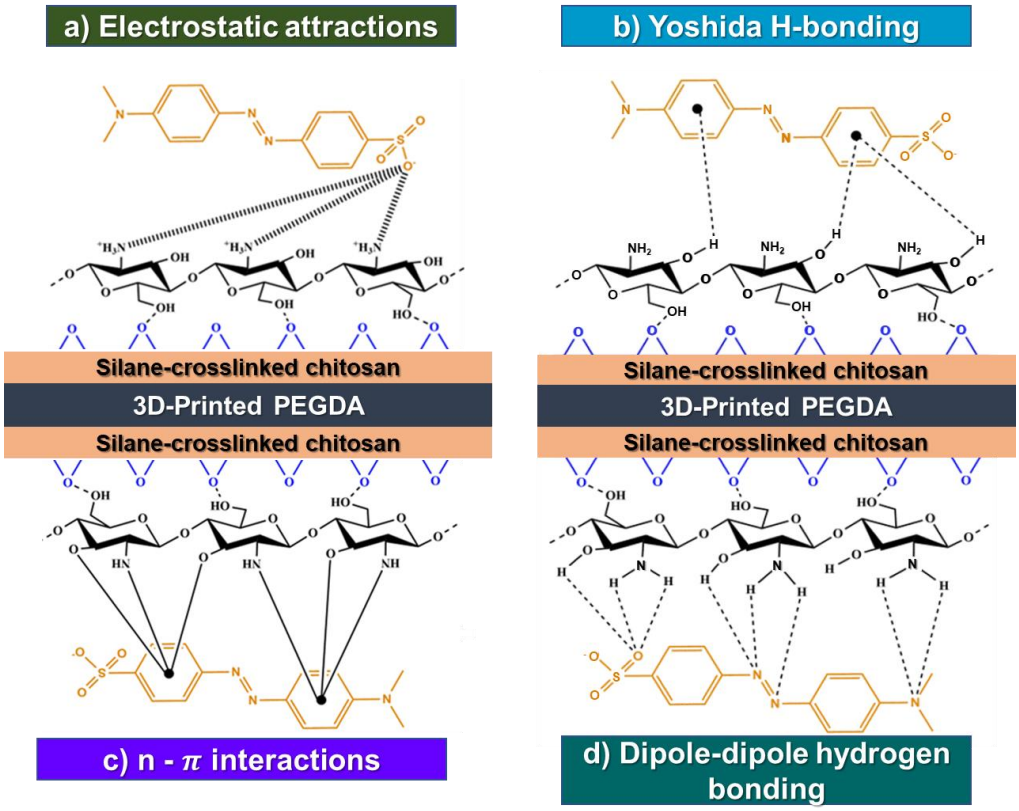


Figure 4.3.3: Schematic illustration of adsorption mechanism of MO dye with grafted 3D-printed PEGDA monolith. (a) Electrostatic attractions, (b) Yoshida H-bonding, (c) n-π interactions and (d) Dipole-dipole hydrogen bonding.

4.3.2 Mechanical properties

To demonstrate structure-property correlations more clearly, detailed data on yield strength and Young's modulus for the selected structural topologies were demonstrated in the Table 4.3.2. Fischer based design has the highest yield strength and Young's modulus, followed by Gyroid, Kagome and lastly body cubic centred design. The stress-strain responses curve also demonstrated the maximum stress is reached at different strains for different structural topologies. The maximum strength of Gyroid is at 26.8% strain and Fischer is at 32.04% strain. Kagome is at 36.24% strain and body centred cubic is at 63.06% strain. Cracking can begin before the maximum strength is reached; however, the impact

of these cracks on overall performance is minimal. Only after the maximum strength is reached do these cracking events accelerate, resulting in a noticeable decrease in mechanical properties.

Moreover, previous work has established that if the structures governed by a stretching-dominated deformation, it would have higher stiffness and strength per unit weight than structures governed by a bending-dominated deformation (Gibson, 2003). Structures with bending-dominated deformation behaviour, on the other hand, have higher energy absorption per unit volume, making them desirable for damage toleration and vibration-damping applications (Deshpande, Ashby and Fleck, 2001). The maximum strength and toughness of all currently analysed structural topologies exhibit an almost linear dependence except for body centred cubic design, which showed quadratic dependence. Linear dependence suggests stretching-dominated behaviour and is preferable for stronger composites; however, quadratic dependence (i.e., bending-dominated deformation) is also useful for damage-tolerant composites. Overall, all structural topologies can be considered for water application depending on the specific requirements of maximum loads and stress.

Table 4.3.2: Mechanical properties of 3D printed PEGDA monolithic structured with different structural topologies.

Mechanical properties	**Measurement (MPa)**			
	Gyroid	**Fischer**	**Kagome**	**Body centred cubic**
Yield strength (MPa)	2.30	2.58	1.82	1.51
Young's modulus	3.20	3.80	2.80	1.11

4.3.3 Removal efficiency of MO dye via adsorption

The removal efficiency of MO dye at optimum conditions were evaluated to study the influence of monolithic structural designs on adsorption efficiency. The experimental conditions has been optimised in our previous work (Husna *et al.*, 2022) at pH 6.3 and temperature = 60 ℃for reaction time of 2 h. Based on theoretical perspective, a high surface area will increase the number of active sites available for reaction, thereby increasing the adsorption performance (Proano-Pena, Carrano and Blersch, 2020). TPMS design has been reported to have high surface area compared to strut-based design. As illustrated in Figure 4.3.4, the body centred cubic structure (strut-based design) showed highest adsorption performance with removal efficiency of 90.4% and uptake capacity of 12.71 (mg/g), followed by fisher, Gyroid and lastly Kagome design. The main factor that contributed to this phenomenon is related to; (i) the specific surface area and (ii) the permeability of the structure which will be discussed in detail in Section 4.3.3.1.

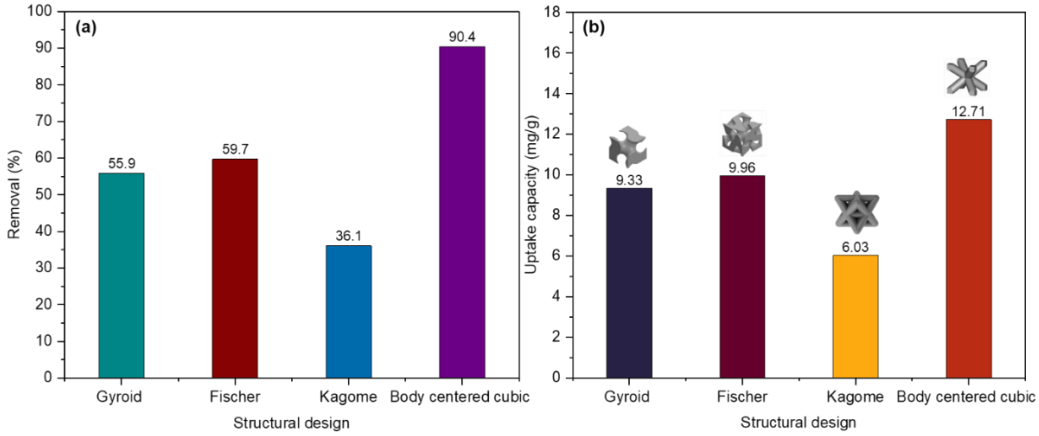


Figure 4.3.4: (a) Plot of removal efficiency of MO dye (%) and (b) Maximum uptake capacity of MO dye (mg/g) at optimum conditions (pH = 6.3, Temperature = 60℃) agitated for 2 h in incubator shaker at 150 rpm.

4.3.3.1 Specific surface area of monolithic structure

The surface area is the most important factor in the design of 3D printed adsorbent because it could lead to clogging problem when the surface area is extremely high. Zhang *et al.* (2019b) proposed that changing the structural design through topology optimisation can improve the efficiency and performance of commercially available adsorption media(Zhang *et al.*, 2019b). It is well known that a smaller size adsorption media is preferred as it provides greater surface area and interaction volume during the wastewater treatment process. As shown in the Table 4.2.2, body centred cubic design has highest surface area compared to other shapes which explains its highest percentage of removal as depicted in Figure 4.3.4. This outcome is consistent with the Adsorption Theory, where a higher surface area is advantageous because it has more active sites for the adsorption to occur, resulting in an improved wastewater treatment. There is an interesting observation from the adsorption performance trend as shown in Figure 4.3.4a and b. Although the surface area of Fischer is comparatively similar to the body centred cubic design with a slight deviation of 4.37%, the adsorption performance of Fischer is much lower at a removal efficiency of 59.7% as compared to the body centred design at 90.4%. For Fischer design, it is crucial to take into consideration of the pore size and other design constraints (e.g., overall size, manufacturability, etc.) as it is a type of microstructure design. The microstructure design tends to have clogging issues due to the small pore space configuration, hence reducing the effective surface area of the adsorbent. In this work, it has been demonstrated that efforts

to compare the surface area in a constant volume, and pore design and a similar infill density which may result in topologies prone to clogging especially for microstructures design (in this case Fischer and Gyroid). Clogging in the media can reduce the amount of mass transfer between the water and the coating material which lowers the system efficiency (Elliott *et al.*, 2017). Among two strut-based designs, Kagome has lower surface area than body centred design, with removal efficiency of 36.1% and uptake capacity of 6.03 mg/g. To further validate the influence of structural topologies on adsorption performance, the permeability study of each structural topology was discussed in detail in the following section.

4.3.3.2 Permeability of monolithic structure

Permeability is the primary correlation between the microstructure and macroscopic physical characteristics of the pores in lattice media. It was influenced not only by the topological structure but also by the geometry or shape of the pore design (Wu *et al.*, 2022). In this work, the porosity value, ∅ was set as 90% for all structural topologies as the correlation between permeability and porosity has been optimised by Asbai-Ghoudan, Ruiz de Galarreta and Rodriguez-Florez (2021). As depicted in Table 4.3.3, for strut-based design with more simple and straight porosity, body centred design has the highest permeability compared to other structural topologies, which allows the liquid to flow through easily. During the grafting procedure, it is easier to control and to graft a more uniform chitosan layer on the monolith as reflected in the SEM images in Section 4.2.4.1. A uniform coating improves the adsorption performance

as implied by the favourable outcome of body centred design as shown in Figure 4.3.4. For TPMS design, the Gyroid has a low permeability compared to Fischer due to the microstructures. This outcome is contradicting with previous study Asbai-Ghoudan, Ruiz de Galarreta and Rodriguez-Florez (2021) that the permeability increased with an increase in porosity from 50% to 90% for the TPMS design. However, the 50% porosity of Gyroid model has the highest permeability compared to other TPMS designs. This variation could be related to the pore distribution induced behaviour changes as the porosity increases from 50% to 90%. With 90% porosity, the pore of the Gyroid narrows, and the wall perpendicular to the flow thickens, causing more deviation and obstruction along the flow path. As a result, the pressure drop is greater, making the structure less permeable. This is justified by du Plessis *et al.* (2018) that the permeability does not always scale linearly with the pore size, instead it can vary significantly with the same pore size and total porosity of the structure. Therefore, it is necessary to take into the consideration of complex fluid flow in wastewater treatment application. The complexity of the flow path can be characterized by a parameter called tortuosity, which measures the duration a typical fluid flows through the medium in comparison to through a straight line. Higher tortuosity is thus expected to allow the wastewater to reach more lattice areas, improving the removal performance. In this case, Gyroid and Fischer has the lower tortuosity as the structure acts like open channels from top to bottom, but with no flow between them, hence it has negatively affected the adsorption performance, whereas strut-based

design (i.e., Kagome and body centred cubic) has good and reasonable tortuosity. This showed that even if the structure has a high surface area, it is not directly translated into a high permeability and tortuosity.

As a conclusion, a thorough analysis must be conducted on various cell sizes, porosities required and tortuosity to understand the behaviour of TPMS and strut-based architecture to achieve a uniform coating and further optimise the adsorption performance result. Based on the above discussion, all experiments in the following section were conducted using body centred cubic monolithic design as it has the highest surface area and permeability.

Table 4.3.3: Permeability measurement of different structural topologies

Permeability, k	Measurement (10^{-7} m^2)				
	Gyroid	Fischer	Kagome	Body centred cubic	
	1.05	1.30	0.87	2.57	

4.3.4 COD and colour removal efficiency using textile wastewater.

To further validate the adsorption mechanism of grafted chitosan of PEGDA monolith, experimental studies were carried out with textile wastewater to examine the adsorption performance in colour and COD removal. The experiment was run for 2 h at T = 60℃ and pH 6 to compare the removal rate with MO dye that was done previously. As shown in Figure 4.3.5, the colour reduction has achieved about 55% (446 to 203 PtCo) whereas for COD reduction is at 2.48% (from 363 to 354 mg/L) before a plateau was reached. Colour removal was higher than COD removal, which is most likely because the compounds such as organic

matters other than dyes had a lower affinity for the adsorbent and remained in the solution after the adsorption process, contributing to the effluent COD. This outcome is also in a good agreement with a study done by Brás *et al.* (2005). Brás *et al.* (2005) discovered that increasing the monoazo dye (Acid Orange 7) concentration from 60 mg/L to 300 mg/L will reduce COD efficiency from 92 to 67%. The authors concluded that the residual COD could be attributed to non-reduced dye, or its metabolites (aromatic amines), thus affected its removal efficiency. Common textile effluents contain a mixture of cationic or anionic reactive dyes that affect the adsorption rate which can be further enhanced by adjusting the pH of the system. According to the law of interactions between electric charges, pH value of the solutions has a significant impact on adsorption performance (Apul and Karanfil, 2015). On top of that, it has been discovered that the adsorption capacity of COD is impacted by dissolved salts during the dyeing process. These salts can change the hydrophobicity, ionic nature, size, and solubility of the adsorbent as well as its surface charge (Ip, Barford and McKay, 2009). Thus, it is crucial to understand the affinity and chemical interaction between the chitosan and the textile effluent to maximize the adsorption performance. In summary, this finding has demonstrated the viability of using a highly robust 3D-printed monolith with grafted chitosan to reduce the colour and COD in textile wastewater, subject to further optimisation in the future.

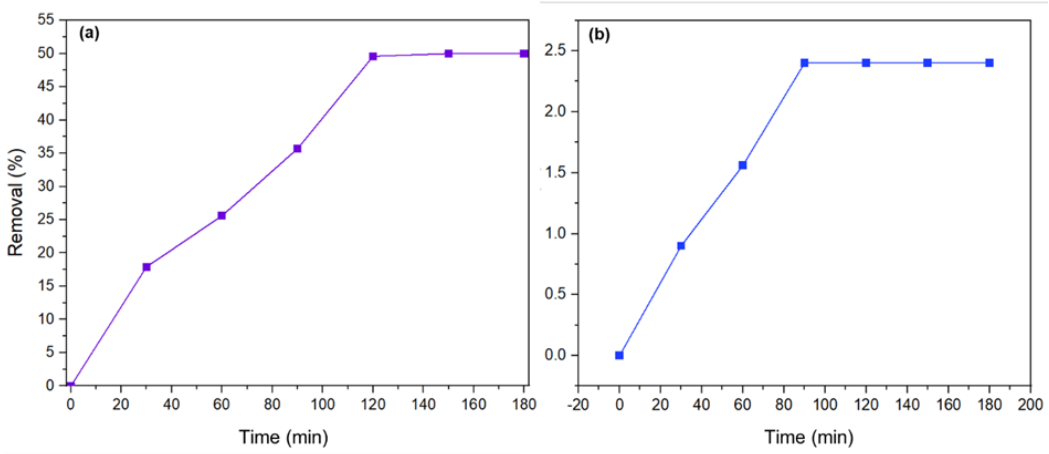


Figure 4.3.5: Percentage removal of (a) colour and (b) COD of real textile wastewater at optimum condition.

4.3.5 Mechanical stability

Table 4.3.4. demonstrates the mechanical stability of the grafted chitosan monolith of different structural designs by measuring the weight changes before and after adsorption. The tabular weight reduction for all structural designs were discovered to be approximately 1%. This shows that there is no leaching of grafted chitosan occur during the adsorption procedure. This observation is also in accordance with the characterisation analysis that verified the strong bonding of the silane – grafted chitosan to the 3D-printed monolith. Thus, it can be inferred that the silane - grafted chitosan of 3D - printed monolith remains stable after adsorption and suitable to be used as monolith.

Table 4.3.4: Weight of all structural design before and after MO dye adsorption.

Structure	Weight of the monolith (g)								Weight loss (%)
	Before adsorption				After adsorption				
	1	2	3	Avg.	1	2	3	Avg.	
Gyroid	0.445	0.451	0.428	0.441	0.441	0.449	0.423	0.438	0.756
Fischer Koch	0.323	0.341	0.329	0.331	0.319	0.338	0.326	0.328	1.01
Kagome	0.197	0.189	0.191	0.192	0.195	0.186	0.188	0.190	1.04
Body centred cubic	0.220	0.224	0.219	0.221	0.218	0.223	0.216	0.219	0.905

4.3.6 Comparison with other chitosan - based monolithic system

The assessment of the removal and uptake capacity of MO dye, colour and COD were executed in accordance with the data presented in Table 4.3.5. Without taking into consideration of optimisation studies, the outcomes acquired were found to be commensurate with other chitosan – based monolithic system. The table reveals that despite the monolith developed in this work taking a lower weight proportion in compared with other adsorbents, the 3D-printed monolith exhibits a comparable equilibrium adsorption capacity, demonstrating its high efficiency. It should be noted that the uptake capacity is lower due to the small-scale unit of monolith used in this work (2cm × 1 cm × 0.5cm) and the nature of the limitation of 3D printing resulting in a relatively smaller BET per weight. However, 3D printing does offer benefits in fabricating complex geometry and efficiency. Most importantly, incorporating the surface grafting method with 3D printing has the advantage of not requiring post-treatment, being easy to maintain, and more sustainable. This

exemplified the practicability and potentiality of the present methodology in synthesising silane – grafted chitosan of 3D-printed monolith as a green technology for water applications.

Table 4.3.5: Comparison of the adsorption properties for MO dye adsorption onto different chitosan-based monolithic system.

Adsorbent	Pollutant removal	Reaction time (min)	Solution pH	Temperature (℃)	Uptake capacity (mg/g)	Removal rate (%)	Ref.
Chitosan	Cu (II)	75	5.5	25	13.7	92.0	(Zhang *et al.*, 2019 b)
Poly (sulfonated polystyrene -co.- chitosan	Cu^{2+} ion	3600	5.5	75	45.2	~90.0	(Ai *et al.*, 2022)
	Co^{2+} ion		6.0		22.9		
Chitosan/UiO-66	Congo red	90	7.0	25	250	~90.0	(Wen *et al.*, 2020)
Chitosan	Cu (II)	60	5.5	25	92.1	96.1	(Hajili *et al.*, 2023)
Silane - grafted chitosan	Methyl orange	120	6.3	30	12.7	90.4	This work
	COD				-	2.46	
	Colour				-	55.0	

4.4 Conclusion

The purpose of this work is to study the influence of the structural topologies of 3D - printed monolith on the adsorption performance for wastewater treatment. By analysing and interpreting the data collected, current findings shows that each of the structural topology exhibits different specific surface area and permeability that affects the

adsorption performance. There is linear relationship between surface area and permeability with no obstacle on porosity. Among all four structural topologies, the centred cubic design presents the highest specific surface area (39.84 mm^2) and permeability (2.57×10^{-7} m^2), with the removal rate of MO dye at 90.4% and uptake capacity of 12.71 (mg/g) under optimal conditions. The colour and COD reduction was at 55% and 2.46% after 2 h using textile wastewater. Moreover, based on their mechanical behaviour of different topology structures, it was suggested all structural topologies can be considered for water application depending on the stretching-dominated behaviour or bending-dominated deformation to meet specific requirements. Hence, it can be concluded that it is vital to research a wide range of design parameters before selecting the best architecture for the intended application and meeting industry demand. In terms of its mechanical stability for practical application, there is no significant weight loss before and after adsorption. In summary, this work has demonstrated the feasibility of using comprehensive 3D-printed adsorption system that is greener and more sustainable for wastewater treatment. Nevertheless, extensive research can be conducted on the development of mathematical model designs based on the correlation between permeability, porosity, and surface area of a selected structural topology to further validate the experimental data. Furthermore, appropriately quantifying the stochasticity of tortuosity is required in deterministic permeability coefficients. Nevertheless, the findings from this work can serve as a

guideline to design monolithic structures and improve their ultimate performance for wastewater applications.

CHAPTER 5: COMPARISON OF DIFFERENT DRYING TECHNIQUES ON SILANE - GRAFTED CHITOSAN OF 3D-PRINTED PEGDA MONOLITHIC STRUCTURE AND ITS EFFECT ON ADSORPTION PERFORMANCE FOR ANIONIC DYE REMOVAL

This chapter covers the evaluation of different drying techniques and their effect on the surface morphology and adsorption performance for methyl orange dye removal. The final moisture content of each drying technique and energy consumption were further evaluated on its significance towards dye removal. This chapter consists of thesis-version of work submitted in the *Journal of Drying Technology*.

ABSTRACT

A robust approach of integrating 3D printing and surface grafting of chitosan is one of the emerging adsorbents for removing pollutants from wastewater, particularly dye pollutants. This study investigated and compared the effects of drying methods on silane-grafted chitosan of 3D-printed PEGDA monolith using convective hot air drying, vacuum drying and freeze-drying methods. It was found that convective hot air drying of chitosan (ODC) silane-grafted monolith was more desirable than vacuum drying chitosan (VDC) and freeze drying of chitosan (FDC). To test the efficacy of methyl orange (MO) dye removal, a batch adsorption performance was tested at 50 mg/L of MO dye at optimal conditions found using response surface methodology (RSM). It was found that the maximum dye removal efficiency of ODC silane-grafted monolith is 90% with an uptake capacity, K of 12.7 mg/g. The recycle ability of all three absorbents was verified by evaluating their adsorption for five cycles and retained its performance after the second cycle. The convective hot air-drying method is better than the vacuum drying and freeze-drying method as the silane-grafted chitosan of 3D-printed monolith obtained has excellent surface properties and adsorption capability for dye removal.

Keywords: 3D printing; Functional group; Drying Technology; Adsorption; Dye removal

5.1 Introduction

The issue of water pollution resulting from the activities of dye industries, which consisting of food, textile, plastic, cosmetics, paper production, printing, and dye synthesis, has garnered increasing concern (Fu *et al.*, 2015; Luo *et al.*, 2010). This is due to the fact that a majority of dyes are known to be detrimental to living organism, humans, and the environment (Jun *et al.*, 2019). Therefore, it is critical to treat these dye effluents before they are released into the environment. Most of the synthetic dyes are difficult to decolourize due to their existence of stable aromatic rings in dyes makes them non-biodegradable and toxic (Shah *et al.*, 2021). Numerous methodologies have been introduced to treat wastewater contaminated with dyes, such as physical, chemical, and biological approaches (Madrakian *et al.*, 2011). Nevertheless, these aforementioned methods are frequently associated with certain drawbacks, such as the generation of substantial quantities of toxic and carcinogenic by-products, exorbitant expenses and high energy requirements (Sajab *et al.*, 2013).

Yaseen and Scholz (2018) has critical reviewed on different methods treating textile wastewater Based on the review, the adsorption method has proved to be a successful technique for removing pollutants from textile wastewater, owing to its remarkable advantages such as high efficiency, cost-effectiveness, zero generation of by-product and ease of design (Haitham, Razak and Nawi, 2019; Shah *et al.*, 2021; Oloo *et al.*, 2020). Various adsorbents such as activated carbons (El maguana *et al.*, 2020), rice husk (Ahmad *et al.*, 2020), mineral sorbents (Tonge *et al.*,

2021), soy meal hull (Haji and Mahmoodi, 2012), chitosan (Shin *et al.*, 2022), and agrowaste (Amalina *et al.*, 2022) have been developed for the past decade for the removal of dyes.

Chitosan is a popular and the most abundant biopolymer after cellulose that has been extensively garnered interest among researchers to be developed for dye removal (Kyzas, Bikiaris and Mitropoulos, 2017; da Silva Alves *et al.*, 2021). Its synthesis involves deacetylating the acetoamide group of chitin using a concentrated alkaline solution (Novikov *et al.*, 2023). The chitosan was discovered to have exceptional adsorption properties toward various reactive dyes and heavy metal as a result from the high concentration of amino functionalities (Wang *et al.*, 2017). The deacetylation of amino groups of chitosan leads to the potential protonation of its amino groups. The resulting polycationic features are reported to significantly contribute to the charged interactions of the dye (Saha and Bhoumik, 2010). Nonetheless, using chitosan as a standalone adsorbent has limitations such as, lower adsorption capacity, low surface roughness, low surface area, and lack of reusability (Vakili *et al.*, 2019; Eltaweil *et al.*, 2021). As a result, in order to amplify the adsorption capacity of chitosan adsorbents, adsorbent with high specific surface area and porous was proposed. In order to achieve this, the operating state of the drying method to create a supercritical condition can be a relevant option via freeze-drying and vacuum drying method. The drying method is reported to have a substantial impact on the surface structures and functions of the chitosan (Dotto *et al.*, 2011). Therefore, it is crucial to select the best drying process without altering

the functionality of the chitosan for excellent adsorption performance for the dye removal. For example, Luk (2015) adopted freeze-drying method to produce chitosan beads for removal of reactive dye (Reactive blue 19) with complete decolourization of RB19 at a concentration of 0.15 mM within 2 h at a pH 3 and temperature of 37℃. Although it showed excellent performance to treat the water, it requires post-processing treatment, and the separation of the adsorbate after the treatment remains problematic and can cause clogging issue. To achieve the retrievability of adsorbents following dye adsorption, the integration of magnetic materials such as Fe_3O_4 nanoparticles into chitosan adsorbents has been introduced (Gul *et al.*, 2016; Kim, Jang and Park, 2016). However, complete retrieval has proven to be challenging, leading to undesired secondary pollution. In this context, using a monolithic adsorbent type is deemed preferable for dye adsorption, as it facilitates the recoverability of the adsorbent (Wang *et al.*, 2017). This is because monolithic adsorbents offer a better non-polluting approach, recyclability and avoiding the formation of by-product such as sludge generation that required secondary treatment as compared to conventional method (Yang *et al.*, 2023a; Yusoff *et al.*, 2023). In terms of the application, the monolithic adsorbent can be embedded in a packed bed column. In contrast, the 3D-printed monolith adsorbent will be used with a microchamber, which will be operated continuously (Usman and Khan, 2022). The adsorbent can be recovered using an osmotic backwashing approach with a specific solvent or water, a more sustainable means to ensure zero harmful chemical discharge.

The optimisation and influence of structural topology, surface area, and permeability on the adsorption performance for water and wastewater treatment has been reported previously in our work (Yusoff *et al.*, 2023). Based on the experimental results, the body-centred cubic (BCC) design had the highest adsorption capacity, as well as the maximum permeability and surface area. Chitosan chains can be conveniently linked to the surface of the monolith using various surface functionalisation techniques such as dip coating, plasma treatment and surface grafting, forming a vast 3D porous monolith structure for practical application (Wang *et al.*, 2017; Mohd Yusoff *et al.*, 2023). Based on the literature, surface grafting via silane functionalisation was preferred as a modifier and crosslinking agent as it can enhance the chemical bonding of the polymer surface (Husna *et al.*, 2022). Otalvaro, Avena and Brigante (2019) studied on the stability of the usage of 3-aminopropyltriethoxysilane (APTES) to functionalise mesoporous silica for removal of organic pollutants. The results showed that the addition of silane coupling agent reduced the adsorption capacity with the polar species such as antibiotics, however higher removal for anionic species such as methyl orange (MO) dye. It is postulated that the adsorption process is connected to the electrostatic attractions or hydrogen bonds between the functional groups in the pollutants and the amino groups of the modified silica. In the work conducted by Zeng *et al.* (2016), pioneering polyvinylidene fluoride (PVDF) nanofiltration membranes were synthesised through the incorporation of halloysite nanotubes (HNTs) at various concentrations to facilitate the efficient removal of

heavy metals and dye. The findings of this study demonstrated that by utilizing silane functionalised HNTs in conjunction with PVDF, the hydrophilicity of the membrane, selectivity for dye rejection, heavy metal rejection, and adsorption capacity were all measurably enhanced. Furthermore, based on the flux recovery ratio (FRR) of membranes the functionalised membrane still achieves 91.2%, compared to 81.3% for pure PVDF membrane. The outcomes presented above suggest that the A-HNTs@PVDF membrane demonstrated a commendable ability to treat the pollutants and possess the potential to be regenerated and reused in practical applications. Therefore, choosing a suitable silane coupling agent is very important to reduce and minimise the leaching effect as well as improving the surface adhesion, which is one of the crucial requirements for the adsorbent to be used in water application (Alaei Shahmirzadi and Kargari, 2020).

In our previous work, we have highlighted the feasibility of grafting the chitosan on the surface of the 3D-printed monolith structure via silanization and dried using hot air drying method (Husna *et al.*, 2022). Drying is necessary to remove the moisture content and should be carried out in such a way that it preserves the intrinsic characteristics of the chitosan and allow adequate moisture content for storage (Arantes *et al.*, 2015). This is because the storage duration of chitosan films leads to a noteworthy alteration in the optical, barrier, and mechanical characteristics, owing to the restructuring of polymer chains during the storage period (Li *et al.*, 2022a; Leceta *et al.*, 2015). To the best of our knowledge, in-depth studies on selecting the most appropriate drying

methods of silane-grafted chitosan of 3D-printed PEGDA monolith have yet to be reported in any study to obtain the desired adsorption performance results. Therefore, the present research aims to conduct a comparative investigation of the drying techniques for silane–grafted chitosan of 3D-printed PEGDA monolith through using hot air drying, freeze drying and vacuum drying methods. Additionally, an investigation to characterize the surface morphology and chemical compositions of the prepared samples was executed, followed by comparing the adsorption performance of all samples for methyl orange dye removal efficiency.

5.2 Materials and methods

5.2.1 Materials

Glycidyloxypropyl trimethoxysilane (GPTMS) (≥98 %, MW: 236.34 g/mol) and (3-aminopropyl) trimethoxysilane (APTMS) (97 %, MW: 179.29 g/mol, density: 1.027 g/ml at 25 °C) were purchased from Sigma-Aldrich, USA. Chitosan (CS) white powder (AR grade; degree of deacetylation of 99 %, MW: average of 890,000 g/mol) was purchased from Fulltime Asia Sdn. Bhd. Hydrochloric acid (HCl) (37 %, MW:36.46 g/mol), isopropyl alcohol (IPA) (≥90 %, MW: 60.1 g/mol), and sodium hydroxide (NaOH) (99 %, MW: 40 g/mol) were purchased from Giti Eco Sdn. Bhd., Malaysia. Poly (ethylene glycol) diacrylate (PEG200DA) (MW PEG Block= 200; n=4, viscosity: 25 cP at 25 ℃) was purchased from Ryoji, China. The acrylate Magma plant-based resin (≥ 99.9 %, MW: 308 g/mol, viscosity: 10 – 30 cP at 25 ℃) was purchased from 3D Gadgets Malaysia. Photoinitiator (Irgacure 819); Phenylbis(2,4,6-trimethylbenzoyl)

phosphine oxide (MW: 418.5 g/mol) and methyl orange dye (MO) ACS reagent (85 %, MW: 327.34 g/mol, pKa = 3.4) were purchased from Chemmart Asia Sdn. Bhd. All the chemicals are used without any further purification unless stated otherwise.

5.2.2 Sample preparation of silane-grafted chitosan of 3D-printed monolith

5.2.2.1 Preparation of resin formulations and 3D printer settings

A photocurable polymer resin formulation was formulated by mixing plant-based acrylate resin, 1wt.% of photoinitiator and poly (ethylene glycol) diacrylate (PEG200DA) in the ratio of 1:0.01:2. The formulation was agitated at 350 rpm using a magnetic stirrer (Thermo Fisher Scientific, United Kingdom) until a homogeneous mixture was achieved. The 3D-printed monolith support with dimensions of (0.3cm × 1cm × 2cm) was designed using computer-aided design (CAD) software and subsequently sliced in the slicing tool software (Chitubox). In this work, Digital Light Processing (DLP) printing technique was chosen due to its high precision, better printing accuracy, fast and energy saving (Quan *et al.*, 2020; Huang *et al.*, 2022b). The 3D-printed monolith was fabricated using a Phrozen Sonic Mini UV Photocuring LCD resin 3D printer. After printing, the monolith support was washed with 90% isopropyl alcohol (IPA) to remove residual resin and irradiated with UV light for 10 min to allow compete curing and sufficient polymerization (Sahrir *et al.*, 2023; Dwamena, 2023). During the printing process, there is photo-polymerisation reaction between photo curable resin with a cross-linker a seen in Figure 5.2.1a. The photoinitiator absorbed UV light throughout

the printing process, producing free radicals that interacted with the monomer molecules in PEG200DA via the opening of carbon-carbon bonds. The increasingly reactive monomers continue to join and assemble until two chains completely react and combined (Pagac *et al.*, 2021).

5.2.2.2 Surface functionalisation with silane-grafted chitosan on 3D-printed monolith via epoxide amine reaction and the use of different drying methods

In this work, a hybrid silane agent was selected for its capacity to enhance the thermal and mechanical properties of materials. Moreover, the development of 3D-printed monolith with hydrophobic behaviour, strong chemical resistance and mechanical stability is essential. This is because it impacts how the surface of the samples interact with its surroundings and determines the lifespan of the monolith. Hybrid silane agents can enhance the surface wetting characteristics of the substrate with good mechanical properties, thermodynamic properties of hydrogen bonds and interaction energy (Wang *et al.*, 2019). The enhancement is due to the content of the siloxane inorganic network and an organic function associated with the same silicon atom, which can either interact with or form an organic polymeric network. Specifically, a formulation of silane agent consisting of APTMS and GPTMS was mixed with IPA and DI water at a ratio of 1:3:6:1, following the method described by Zhang *et al.* (2019b) with some modification for 5 min in a beaker. To form silane-crosslinked chitosan, 1 ml of hybrid silane mixture was added into 10 ml of 2wt.% of chitosan (pH ~ 5 – 6) and continuously stirred until the

mixture became homogenous, as shown in Figure 5.2.1b. Then, the 3D-printed monolith was dipped in the solution for 45 min. The final samples were dried using convective hot air drying, vacuum drying and freeze drying methods. ODC silane-grafted monolith was dried in the convective hot air dryer (Memmert UN30plus, Germany) for 4 h at 60 ℃ (Husna *et al.*, 2022), whereas VDC silane-grafted monolith was dried in a vacuum dryer (Memmert VO 200, Germany) for 8 h at 50 mmHg and 50℃ (Amor *et al.*, 2023). On the other hand, FDC silane-grafted monolith was frozen for overnight at -18℃ in a freezer and subsequently freeze-dried in a freeze dryer (Alpha 1-2 LDplus Martin Christ Gefriertrocknungsanlagen GmbHChrist, Germany) at -40℃ and 100 Pa for 48 h (Ummas *et al.*, 2019). All the operating conditions were selected after the optimisation based on the literature. The prepared samples were kept in a desiccator until further analysis.

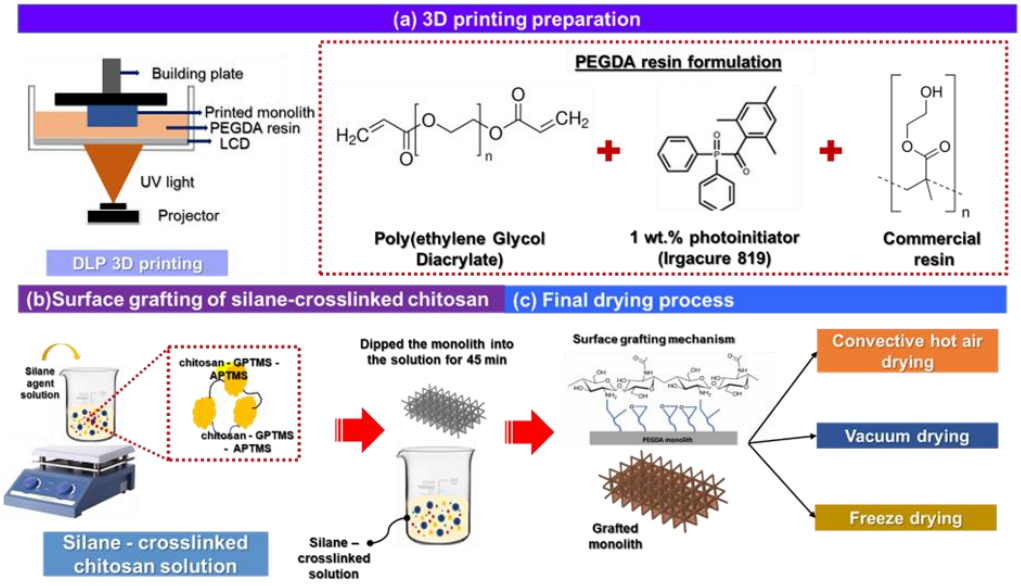


Figure 5.2.1: Schematic diagram of sample preparation of silane-grafted chitosan on 3D-printed monolith with different drying techniques.

5.2.3 Characterisation studies

5.2.3.1 Field emission scanning electron microscopy (FESEM) analysis

The microstructure and surface morphology and microstructure of the silane – grafted chitosan of 3D-printed monolith was examined before and after surface grafting procedure using field emission scanning electron microscopy (FESEM, FEI Quanta 400 F, USA). Due to its non-conductive nature, the pure PEGDA and silane – grafted chitosan of 3D-printed monolith was coated with gold in a rotary pumped coater (Quorum, 150 A S Plus, UK) at a deposition rate of 6 nm/min and a deposition current of 20mA. The gold-coated samples were placed inside the FESEM vacuum chamber and electron beams were sputtered onto the surface. The images were examined at different magnifications ranging from (90-1600x).

5.2.3.2 Fourier transform infrared (FTIR) spectroscopy.

Fourier transform infrared spectra (ATR-FTIR, Perkin Elmer Frontier FT Mid-IR/Far-IR, USA) were utilised to confirm the grafting of the silane-grafted chitosan on the surface of the monolith and to identify the functional groups involved in the adsorption. The spectrum analysis was carried out in triplicate at three separate points in the range 400 - 4000 cm^{-1}.

5.2.3.3 X-ray diffraction (XRD) analysis

The composition, stoichiometry, crystalline structure, and lattice parameter of the produced material were determined using a Panalytical powder diffractometer XRD equipment (X′Pert Pro, Netherlands). Cu K

X-rays are used to irradiate the XRD diffractometer. Diffraction patterns with a wavelength of 0.154 nm are acquired at 45 kV generator voltage and 40 mA currents. The scan was performed with two angles (2θ) ranging from 7° to 80°, each with a step of 0.2° and 0.5°respectively.

5.2.4 Energy consumption in all drying methods

The total amount of electric energy used by the dryer throughout the drying process is known as energy consumption (EC). A clamp meter (Kaise SK-7711, Japan) was used to measure the electrical current, and the electrical energy consumption. The electrical power of the dryer was calculated using the following equation (31).

$$P = \frac{A \times V \times P.F.}{1000} \quad (31)$$

The energy consumption was calculated using equation (32).

$$E_t = P \times t \quad (32)$$

Where E_t is the total energy consumption for each dryer (kW) and t is drying time (h).

Then, the specific energy consumption can be obtained the following equation (33).

$$E_s = \frac{E_t}{W_s} \quad (33)$$

Where E_s is the specific energy consumption (kJ/kg) and W_s is the initial weight of the samples (kg).

5.2.5 Moisture content analysis

A gravimetric approach was used to calculate the loss on drying of the 3D-printed samples for all types of drying in triplicates (Wai *et al.*, 2019; Wid and Alca, 2016). The sample was dried to a consistent mass for 24

h at 105℃ to find the final weight. Based on the weight of the sample before and after drying, the moisture content can be calculated using the following Equation (34).

$$Moisture\ content\ (\%) = \frac{M_w - M_d}{M_s} \times 100\% \quad (34)$$

Where M_w is the initial weight of wet sample (g), M_d is weight of dry sample (g) and M_s is weight sample (g).

5.2.6 Batch adsorption - desorption studies

A 100 mg/L methyl orange (MO) dye stock solution was prepared. After that, the stock solution was diluted to the desired concentrations. A fixed volume of 50 ml of 50 mg/L of MO dye solutions were prepared for batch adsorption studies. The MO dye solutions was adjusted to desired pH using 0.1M of NaOH or HCl. After that, a single unit of monolith was used to test the adsorption performance in an incubator shaker at 150 rpm (N) for 2 h at optimal operating condition of pH 6.3 and 60℃ as optimised in the previous work using response surface methodology (RSM) (Husna *et al.*, 2022). The optimised experimental results were obtained using a 3-level Box-Behnken design (BBD) that encompasses 4 continuous factors (34−1) with a total of 27 sets of experiments. The chitosan concentration, dipping time, pH, and process temperature are the influencing parameters in this investigation. The full details of RSM results can be found in Table 3.2.3. Then, the MO dye samples were collected at 20 min intervals for examination, and the residual concentration was evaluated with a UV-Vis spectrophotometer (Perkin Elmer Lambda 35, United States) at a fixed wavelength of 464 nm. The removal efficiency and uptake capacity of the MO dye was calculated

using equation (35) and(36).

$$MO \text{ dye removal efficiency } (\%) = \frac{C_o - C_t}{C_o} \times 100\% \quad (35)$$

$$Uptake \text{ capacity of MO dye, K } (mg/g) = \frac{(C_o - C_t)V}{m} \quad (36)$$

where C_0 and C_t is the initial and the concentration and time t respectively, V is dye solution volume (L) and m is the mass of the grafted monolith.

Batch desorption studies were carried out with a 0.01 M NaOH solution. The desorption eluent was mixed with the exhaust adsorbent material for several hours. Subsequently, once desorption equilibrium was attained, the concentration of NaOH solution containing the desorbed MO dye was examined. The adsorbent material was then rinsed with distilled water until reach pH7, dried at 60 ℃, and reused for further adsorption studies for 5 cycles to verify its recyclability. The desorption ratio, τ was calculated using equation (37).

$$\tau = \frac{C_2 V_2}{(C_0 - C_1)V} \quad (37)$$

where C_2 denotes as the concentration of MO dye in NaOH solution(mg/L), C_1 is the final concentration of MO dye (mg/L) and V_2 is the volume of NaOH solution (L).

5.3 Results and discussion

5.3.1 Characterisation study

FESEM analysis was performed to elucidate the microstructure and morphologies changes of the samples due to surface grafting and drying methods. Figure 5.3.1a showed the blank 3D-printed monolith with a

smooth surface. A wrinkled layer with swelling pockets can be seen on the surface of ODC silane grafted monolith as depicted in Figure 5.3.1 b, demonstrated that the monolith was successfully grafted with the chitosan layer. This is because chitosan has a unique properties of swelling behaviour, that play important role in the adsorption process (Hastuti, Masykur and Hadi, 2016). The relationship between the adsorption capacity and swelling behaviour of the chitosan is highly affected by the availability of the active sites. As the process of swelling enlarges the size of pores, it increases the ease with which adsorbate ions can infiltrate, resulting in an enhancement of the adsorption efficiency of the chitosan (Mahmoodi, Fattahi and Motevassel, 2021; da Silva Alves *et al.*, 2021). Moreover, the surface of the VDC silane grafted monolith appeared rough and ruptured the swelling pockets. This could be because of vacuum condition during the drying process. Using a vacuum might cause structural damage when the gas grows inside the pores. This occurrence has the potential to generate permanent consequences owing to mechanical stresses, resulting in structural rigidity loss caused by debonding and the breakdown of the sample wall connections (Soares *et al.*, 2018). A similar findings was also reported by Chen *et al.* (2015) where during the vacuum drying process, the top layer also produces bubbles that ultimately burst and forming a crater-like structure. On the FDC silane grafted monolith, silane-chitosan layer with pores was found, which is due to the collapse of surface pores during the freeze-drying process (Figure 5.3.1d). In the course of the freeze-drying process, there were two primary phases. The initial stage involved

the creation of ice crystals between the chitosan polymers through the process of freezing. The subsequent step was the sublimation of ice (Nowak and Jakubczyk, 2020). The velocity of freezing during the first stage significantly impacted the formation of ice crystals, which affected the size and distribution of the ice crystals in the samples (Quiévy *et al.*, 2010). During the slow freeze-drying process, the ice crystals gradually enlarged, leading to the progressive destruction of the skeletal structure (Li *et al.*, 2022a). The samples would then collapse upon the sublimation of ice as shown in Figure 5.3.1d (highlighted in the red circles). According to Zhao *et al.* (2017), the pores were formed as a result of the creation of ice crystals. Overall, it could be seen that different drying methods did change the surface properties of the silane-grafted chitosan on the 3D-printed monolith.

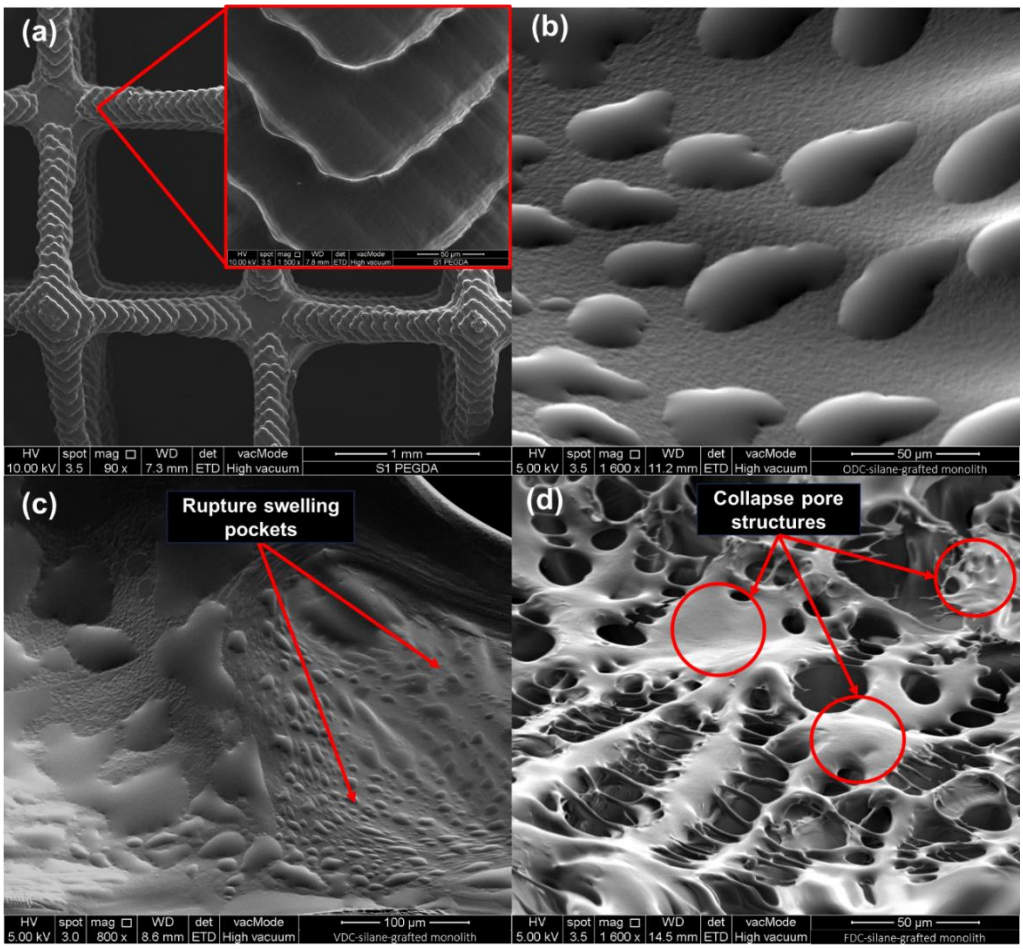


Figure 5.3.1: SEM images of (a) Blank PEGDA monolith with enlarged segment of monolith struts; (b) ODC silane-grafted monolith;(c) VDC silane-grafted monolith and (d) FDC silane-grafted monolith.

FTIR analysis were carried out to verify grafting of the silane-grafted chitosan on the surface of the monolith using different drying methods and to confirm the adsorption of the methyl orange dye. Comparing with ODC and VDC as shown in Figure 5.3.2a, the observed data of FDC exhibits a discernible reduction in the intensity of the wide-ranging peak of O-H stretching, which is situated in the (3558 to 3299 $cm^{-1)}$ range and is closely associated with the hydroxyl groups of chitosan. The broadening of this peak is attributed to the compound's intra- and intermolecular hydrogen bonds with water. Another obvious difference is

at the peak position of about 1414 cm^{-1} as the peak is less intense compared to ODC and VDC. The samples contain two distinct varieties of water, namely free water and water which is associated with the matrix via various forces. Liquid film, present on the surface of solid particles, is classified as unbound water and can be easily removed by evaporation, while bound moisture is confined within the microstructure of the solid material. In such circumstances, the moisture must traverse to the exterior surface to undergo evaporation and vaporization (Parikh, 2015). Hence, out of all these drying processes, freeze drying has the capability to remove bound water (Nowak and Jakubczyk, 2020). During the freeze-drying, the moisture turns into vapor when it reaches the set process temperature and pressure. The vapours gather outside the chamber on a condensing surface and condenses back into ice. The procedure is finally completed by gradually raising the temperature, which releases more vapours and removes any bound water from the samples. On the other hand, by using heat-applied drying methods, there is notably a slight reduction in intense peak of -OH for vacuum drying compared to hot-air drying. However, both drying methods are almost similar based on the final moisture content (%) which is about 6%. This is because vacuum drying is a method that is conceptually appropriate for materials that are sensitive to heat and oxygen, as it effectively reduces the risk of oxidation reactions (Mella *et al.*, 2022). Chitosan is a polycationic material and has a good oxygen barrier (Lazar *et al.*, 2019). Therefore, it can be concluded that both drying methods are possibly removing the unbound water and less effective is removing the bound water. The

removal of moisture content is could also be linked to the slight shift of -CH band (at peak 2900 cm^{-1} and 911 cm^{-1}) in the region as the -CH stretching band contributes more when the overlapped -OH vibration band is less intense. Moreover, as depicted in Figure 5.3.2b, the $-NH_2$ and -OH stretching vibrations were represented by the typical band at 3423 cm^{-1}, whilst the amide group was represented by the peak at 1639 cm^{-1}. The stretching of vibration at this absorption band, on the other hand, might be caused by the overlaying of the C=O amide band with the Si-OH bond from GPTMS and APTMS. These spectra corroborated the grafting of the silane-grafted chitosan on the 3D-printed monolith. Moreover, it was discovered that after the adsorption, there is a new and strong peak at 1370 cm^{-1} that corresponds to the sulfonic acid group (SO_3^-), signalling probable electrostatic interactions between the negatively charged SO_3^- of MO dye and the positively charged chitosan. The sulfonate groups have been identified as the most important electrostatic-attraction force donor for MO adsorption (Bahrudin *et al.*, 2020; Liu *et al.*, 2020; Wong, Wong and Lim, 2021). The peaks at 1115 cm^{-1} and 825 cm^{-1} corresponded to the S=O and -CH bonds in para-benzene, indicating that the chitosan had effectively adsorbed the MO dye. Another indication that chitosan absorbed MO dye is the presence of a new peak at 2860 cm^{-1}, which is ascribed to a potential amine salt. This finding is in good agreement with previously published studies (Husna *et al.*, 2022; Yusoff *et al.*, 2023; Bahrudin, Nawi and Sabar, 2019; Liu *et al.*, 2020).

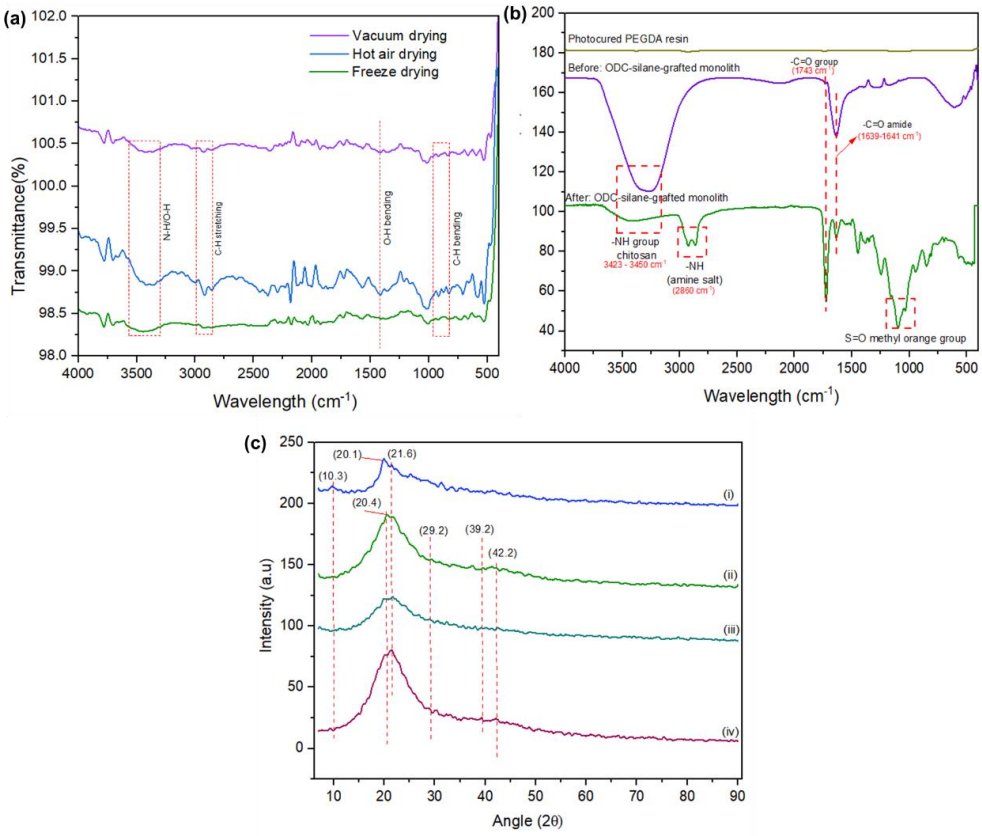


Figure 5.3.2: (a) FTIR spectra for different drying methods; (b) FTIR spectra of photocured PEGDA resin, ODC silane-grafted monolith before and after adsorption; and (c) XRD spectra of (i) pure chitosan; (ii) ODC silane-grafted monolith, (iii) VDC silane-grafted monolith and (iv) FDC silane-grafted monolith.

The crystalline structure of all samples was studied via XRD analysis as shown in Figure 5.3.2c. The XRD plot for all three adsorbents has a similar pattern. However, there is a minor shift was detected for the ODC silane-grafted, VDC silane-grafted, and FDC silane-grafted monolith, with 2θ = 10.3° and 20.4°, respectively when comparing with the pure chitosan alone. There are two large peaks can be detected for pure chitosan, one at 2θ = 10.3° (crystal forms I) and the other at 2θ = 20.1° (crystal forms II), as seen Figure 5.3.2c(i). This effect might be attributed to the surface grafting technique, in which the lengthy chain inhibited the development of inter- and intramolecular hydrogen bonds. In XRD

spectra for all three adsorbents, the characteristics of chitosan disappeared as there is potential of the peak was overshadowed by the PEGDA spectra. Moreover, a few minor peaks at 29.2°, 39.2° and 42.2° were detected. These peaks are attributed to the PEGDA monolith, whereas strong diffraction peak at 21° are caused by intermolecular hydrogen bonding between the -OH groups of the glycol (Bhattacharyya and Ray, 2015). All the findings stated here is in a good agreement with previous studies reported (Husna *et al.*, 2022; Piao *et al.*, 2022).

5.3.2 Energy consumption and moisture content analysis

The energy consumption to remove moisture content of the samples as well as the final moisture content of the 3D printed materials are presented in Table 5.3.1. As seen in the Table 5.3.1, the energy consumption and specific energy consumption of freeze drying is the highest compared to heat-applied drying methods. This is due to a strong correlation between energy consumption and drying time. During freeze drying process, a significant energy required for maintaining the vacuum, sublimation and circulation (Chen *et al.*, 2020a). As reported by Ratti (2001), the sublimation accounts for nearly half of the total energy expended during the process whereas other processes such as vacuum and condensation shared almost equal amount of energy consumed. Comparing to heat-applied drying method, the process is straight forward which only involve heating of air and its circulation (Lewicki, 2006). On the contrary, the moisture contents of 3D printed samples were determined to be 5.69%, 3.89 and 5.84% for the hot air-drying, freeze-drying, and vacuum drying methods respectively. Evidently, these

outcomes divulged that the process of freeze drying has the potential to enhance the efficacy of the dehydration process to remove the moisture content. Removal of moisture content for adsorbent is important to ensure consistent and enhanced the adsorption performance for water treatment. This is because the presence of moisture in chitosan has the potential to occupy pore spaces and active sites on the surface of the material, thereby decreasing the available surface area for adsorption. Moreover, the acceleration of polymer degradation through hydrolysis reactions is directly proportional to the increase in water content within the chitosan structure, hence appropriate moisture content is required to ensure its functionality for the adsorption process. The investigation conducted by Szymańska and Winnicka (2015) posited that the moisture content of chitosan must be kept in between 6-10%, in order to enhance its aptitude to establish hydrogen bonding. Therefore, based on the data calculated as depicted in Table 5.3.1, heat-applied drying methods, in this case ODC and VDC are preferable to remove the moisture content of the silane-grafted chitosan monolith.

Table 5.3.1: Energy consumption, and moisture content of silane-grafted chitosan monolith of different drying methods.

Drying method	Energy consumption for dryer (kWh)	Specific energy required to dry the sample (kWh/kg)	Final equilibrium moisture content (%)
ODC	4.31	13.3	5.84
FDC	132	406	3.89
VDC	11.6	35.7	5.69

5.3.3 Adsorption and desorption studies

The removal efficiency (%) and the uptake capacity, K (mg/g) of ODC silane-grafted, VDC silane-grafted, and FDC silane-grafted monolith

were analysed at the optimal conditions as depicted Figure 5.3.3. It was identified that the ODC silane-grafted monolith has the highest removal efficiency of 90.4% with an uptake capacity of 12.7mg/g. Chitosan possesses amino and hydroxyl groups in its molecules, which play important role for various potential adsorption mechanism between chitosan and the contaminants (Jin *et al.*, 2018; Liakos *et al.*, 2021). The vast number of unoccupied adsorption sites on the adsorbent surface contributed to the initial rapid dye adsorption (Jin *et al.*, 2018). As equilibrium states were reached after 120 min there were no significant variations in the adsorption rate up to 180 min. A similar trend can be observed with all three adsorbents. Moreover, the VDC silane-grafted monolith was identified to be the least efficient adsorbent, with a removal efficiency of 32% and an uptake capacity of 5.03 mg/g. This could be because the vacuum condition changed the physicochemical properties and caused depolymerization of the chitosan, as it affects the swelling behaviour of the chitosan. According to Arantes *et al.* (2015), the moisture and water removal rate was fast and higher in the first drying steps under vacuum conditions, with the temperature exerting a more potent effect, causing an increase in the thermal vibration of C-C bonds in the polymer main chain, resulting in depolymerisation. At a certain point, the polymer can further degrade and lose its amine functional groups that play an important role in adsorption. Therefore, this reaction affects the adsorption performance of the MO dye since the adsorption mechanism for most of the biopolymers is mainly related to the functional groups (Zhao *et al.*, 2017). On the other hand, the FDC silane-grafted

monolith has a lower adsorption removal compared to the ODC silane-grafted monolith. These findings contrast with the previous studies, as the freeze-drying method has the capability to create a tailorable mesoporous structure for better dye adsorption (Takeshita *et al.*, 2021; Mahmodi *et al.*, 2020; Chartier *et al.*, 2022). However, without optimising the operating conditions such as freezing time, temperature and rate for the freeze-drying method, it could reduce the pore volume and specific surface area of chitosan, which leads to a decrease in the removal rate of MO dye (Song *et al.*, 2021; Chartier *et al.*, 2022). Takeshita *et al.* (2021) revealed that the cooling protocols have indicated not only cooling rate but also the actual freezing rate, freezing temperature, degree of super-cooling, and cooling direction have complicated effects on the form and size of ice crystals. Rapid cooling often produces smaller ice crystals, which in turn produce smaller secondary pores whereas slow cooling rate produces larger pores. Moreover, according to Song *et al.* (2021), the freezing time can influence the pore size of the chitosan due to the formation and distribution of ice crystals. An increase in freezing time results in thinner and larger pore walls, higher porosities, and bigger specific surface areas of the microspheres, as well as more functional groups exposed on the surface and within the chitosan. This is because as the ice got larger, and "pore pressure" increased with the freezing time, causing chitosan to flow to the surface and create the pores. Therefore, it is necessary to further optimised the operating conditions of freezing drying method in order to get desired size of pores. In this work, the convective hot air-drying method is preferable for drying the chitosan

silane-grafted monolith without damaging the functional groups of the chitosan.

Furthermore, adsorption-desorption experiments were carried out to determine the reusability and durability of grafted-chitosan monoliths for industrial applications, as shown in Figure 5.3.3c. The sample was examined and reused under ideal conditions for five consecutive cycles. For each cycle, a new batch of the MO dye was replaced after 2 h of adsorption and absorbance measurements were performed at regular intervals. It was identified that even after five adsorption-desorption cycles, the adsorption rate retained after the second cycle and the best adsorption of the silane-grafted chitosan of 3D-printed monolith occurs during the first filtration for all three adsorbents, indicating they can be reused. It was noticeable that ODC has the highest decreasing rate for recyclability compared to other adsorbents. Theoretically, the performance of the adsorbents depending on the surface charge which normally required alteration of the pH of the aqueous system. Hence, during this process there is potential of secondary reaction to occur during desorption procedure in the alkaline solvent which leading to irreversible degradation of adsorbents (Dutta *et al.*, 2019). Furthermore, as the chitosan has the ability to swell, some of the bound moisture was trapped in the materials and hard to be removed in comparing with other drying methods. This causes less availability of the functional group to adsorb the pollutants for ODC. On the other hand, the decrement in adsorption rate for all three adsorbents is due to the saturation point of chitosan adsorption.

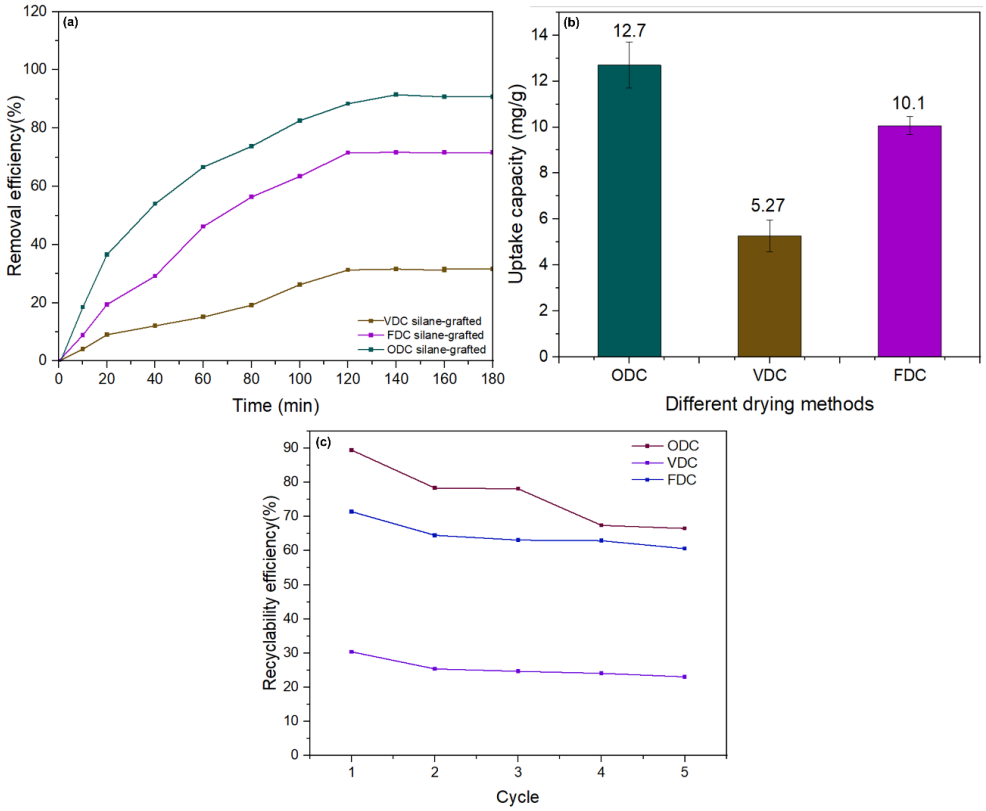


Figure 5.3.3: Plot of (a) Removal efficiency (%) and (b) Uptake capacity, K (mg/g) of different drying methods at optimal conditions (pH = 6.3, temperature = 60 ℃) agitated in incubator shaker at 150 rpm for 2 h and (c) Recyclability efficiency of different drying methods for 5 cycles.

The plausible adsorption mechanism of MO dye is illustrated in Figure 5.3.4. There is a significant likelihood of n- π stacking interaction in the adsorption. The O single bond H bonds or oxygen bonds on the surface of chitosan and aromatic ring in methyl orange are reflected by the n-π interaction**.** Referring to the Yoshida-H bonding mechanism, the attraction is caused by the interaction of H bonds from the OH group with the delocalized electron cloud. The -OH bond of chitosan may overlap with the aromatic rings of MO dye that has delocalized π* orbital of an aromatic ring, signalling that the Yoshida H-bonding may also be implicated in the adsorption process. Moreover, the hydrogen bonding

interaction is represented by the hydroxyl group on the surface of chitosan, as well as the nitrogen and oxygen in methyl orange, whereas MO dye contains SO_3^- ions and is electrostatically attracted to the positively charged -NH_2 in chitosan. Overall, it can be concluded that the plausible mechanism of MO dye adsorption on the grafted – chitosan 3D-printed mainly attributed to electrostatic attractions, n–π stacking interactions, Yoshida H-bonding, and hydrogen bonding interactions.

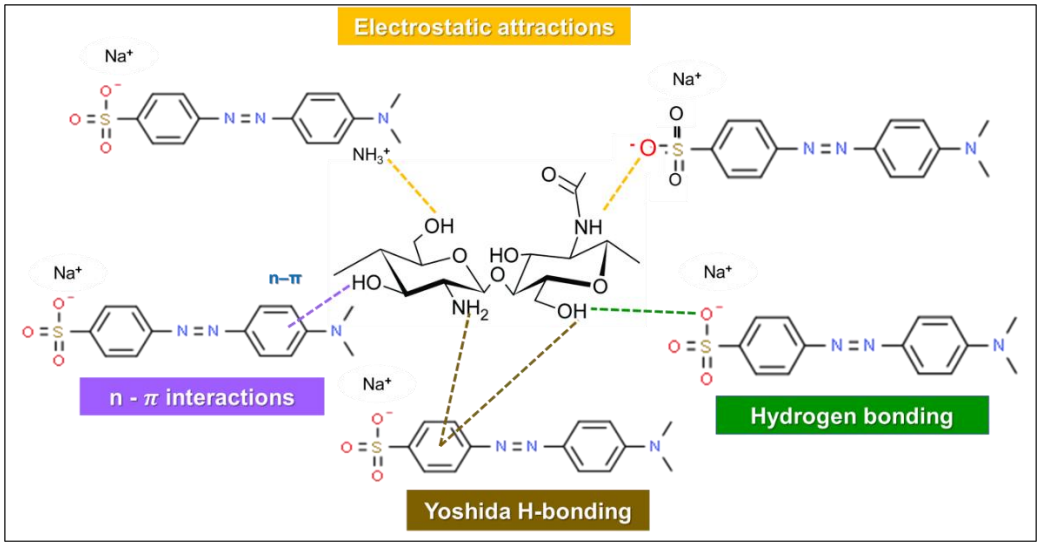


Figure 5.3.4: Possible adsorption mechanism between chitosan and methyl orange (MO) dye.

5.4 Conclusion

In conclusion, the convective hot air-drying method is preferable to the freeze drying and vacuum drying methods for drying silane-grafted chitosan monolith. ODC silane-grafted monolith has more desirable properties and less surface structural damage than VDC silane-grafted and FDC silane-grafted monolith. Up to 90.4% of the MO dye was eliminated at the best operating conditions. Furthermore, all three adsorbents retained nearly all their adsorption properties after at least

five adsorption cycles. The adsorption-desorption study was also carried out, and no post-treatments were required to accurately separate the adsorbate from the aqueous solution. The findings of this study are proof of concept for constructing monolithic design structures employing various drying processes that may alter surface characteristics and adsorption.

CHAPTER 6: ENHANCING MULTIFUNCTIONAL PROPERTIES OF A BIOCOMPATIBLE PEGDA-BASED 3D PRINTED MONOLITH STRUCTURE FOR WATER APPLICATIONS

This chapter covers synthesis of a novel resin formulation using biopolymer materials (PEGDA) to fabricate the 3D-printed monolith using Digital Light Processing (DLP) for water application. The addition of comonomer of BDDA and HDDA to enhance the mechanical and thermal properties was evaluated. The effect of surface grafting with 2 silane coupling agent system on the moisture absorption and creating hydrophobic surface was analysed.

ABSTRACT

In this work, novel acrylate-based photosensitive resins designed for Digital light processing (DLP) are prepared to fabricate 3D-printed monolith with poly (ethylene glycol) diacrylate (PEGDA), plant-based resin was prepared with addition of 2 different comonomers, 1,4-butanediol diacrylate (BDDA) and 1,6-hexanediol diacrylate (HDDA). The influence of comonomer concentration on the mechanical and thermal properties is systematically investigated. 3D-printed monolith was further grafted with silane coupling agent to enhance the moisture absorption and hydrophobicity behaviour to be applied for wastewater environment. The result showed that PEGDA with 3wt.% of HDDA has greatest Young's modulus, ultimate tensile strength and elongation at break. Surface grafting with single silane agent on the 3D-printed monolith was clarified to have a more balance effect than hybrid silane coupling agent for the lowering of moisture absorption and increase the hydrophobicity without causing any cracking in the inner truss. The synergistic effect of 3D-printed monolith with silane coupling agent was identified to have stable chemical and mechanical for practical application in water.

Keywords: Biopolymer; 3D printing; Silane coupling agent; Mechanical properties; Moisture absorption; Monolith

6.1 Introduction

Additive manufacturing (AM), or known as 3D printing, is an inverse of the subtractive manufacturing technique, which only uses needed material to produce a finished product. In recent years, the global market potential for additive manufacturing (AM) technologies has increased exponentially over the past few years. It is anticipated to reach about $20 billion by 2029 due to the rising development of new raw materials and technological advancements for 3D printing (Guit *et al.*, 2020). 3D printing has driven the demand in a wide range of industries and applications as a robust processing technique for designing prototypes. It can create customised products, reduce waste and cost, and significantly speed up design and development. 3D printing also can create complex geometries with high resolution and internal structures that are difficult or impossible to achieve with traditional manufacturing methods (Shaukat *et al.*, 2022; Zimmerling *et al.*, 2022).

Additive manufacturing can be classified into a few categories such as Vat Polymerization (VPP) (Huang *et al.*, 2022a), Material Jetting (MJT) (Segura *et al.*, 2023), Material Extrusion (MEX) (Cox, Kipling and Gibbons, 2023), Binder Jetting (BJT) (Kwon *et al.*, 2023), Powder Bed Fusion (PBF) (He, Ramani and Okwudire, 2023), Directed Energy Deposition (DED) (Su *et al.*, 2023) and Sheet Lamination (SHL) (Shimoda, Hikasa and Ali, 2023). All fabrication techniques enable the effective fabrication of 3D-printed objects from digital models through the layer-by-layer addition of materials. The most widely used printing technique is MEX, which is generally less expensive than other 3D

printers, making them accessible to a broader range of users (Nazir *et al.*, 2023). Even though MEX is the most popular rapid prototyping technique, it can only be printed with thermoplastic materials. MEX cannot be used to print other materials, for instance, metals, ceramic and biopolymer materials. MEX also cannot produce parts with the same smoothness or detail as some other 3D printing techniques due to its lack of accuracy and precision (Ngo *et al.*, 2018). As a result, the VPP technique is preferred because it is suitable for high-resolution prototyping and fabrication and can be used with customized photocurable resin (Shahzadi *et al.*, 2022; Shaukat *et al.*, 2022).

Photocurable resin for VPP requires the presence of functional groups to ensure network formation via crosslinking. Acrylate monomers typically go through photopolymerisation via radical system, which are typically consist of multifunctional monomers, oligomers (also known as macromonomers), a photoinitiator, and additives (i.e., optical absorbers, fillers and stabilizers) (Ligon-Auer *et al.*, 2016; Zawaski *et al.*, 2021). In addition, additives are added to improve the resin properties and printability of the end-product. The use of photocurable resin can offer a number of benefits, including energy efficiency due to reduced processing and fast curing times of a few min or sec, as well as ease of fabrication. Polymer-based materials have typically outperformed other 3D printing materials as they can eliminate the need for inert gases or vacuum conditions. Apart from that, polymerisation offers high resolution in the micrometer range for more complex structures of smaller prints (Bae *et al.*, 2021). Therefore, in recent years, polymer-based materials

have been used in many fields such as in aerospace, architectural, biomedical including environmental and water applications (Mohd Yusoff *et al.*, 2022). Specifically in water and wastewater treatment, the development of fabrication of various complex perforated feed spacers and membrane were established for water filtration, adsorbent (Husna *et al.*, 2022), oil/water separation(Yan *et al.*, 2019), and heavy metal removal (Liakos *et al.*, 2020) and desalination (Chowdhury Maqsud *et al.*, 2018).

Poly (ethylene glycol) diacrylate (PEGDA) is a low-cost, water-soluble, biodegradable and non-toxic synthetic polymer material that has been approved by the Food and Drug Administration (FDA) for the fabrication of a variety of medical devices and ecological applications. PEGDA is a typical hydrophilic polymer that contains double-bond acrylate groups at each end of the PEG chain, with terminal hydroxyl groups that have water affinity. This will limit the product durability as opposed to the carbonyl group, which affects the photostability of the material (Rekowska *et al.*, 2022; Sabatini *et al.*, 2019). Moreover, the surface wetting properties of PEGDA depend on the molecular weight. Nam *et al.* (2018) reported that PEGDA250 is insoluble in water and hydrocarbon oil, which exhibits both hydrophilic and hydrophobic properties. In contrast, PEGDA with higher molecular weight (400 – 2000), such as PEGDA575 and PEGDA700, are soluble in water which make it suitable to be used for hydrogel, microfluidic device, and encapsulation fabrication (Pullagura, Amarapalli and Gundabala, 2021; Zhang *et al.*, 2011a). However, to develop 3D-printed monolith, hydrophobic behavior is extremely crucial in making 3D

printed polymers with good chemical resistance and mechanical stability. This is because it affects how the surface of the printed device interacts with its environment and influences the lifespan of the monolith. Although PEGDA has good processability, stable polymer through a cross-linking reaction, and forming high-precision specimens, creating a superhydrophobic surface from pure PEGDA substrate remains a challenge.

Alternatively, surface functionalisation such as etching, coating, surface grafting, and macromolecule incorporation were effective methods of improving the surface hydrophobicity and overall mechanical properties (Jiang *et al.*, 2020; Mohd Yusoff *et al.*, 2022). One of the established surface functionalisation methods is surface grafting using organofunctional silanes or organosilane or known as silane coupling agent (Mostofi Sarkari *et al.*, 2020). Silane coupling agent is a bioactive functional derivative that can improve mechanical properties, interaction energy, and the thermodynamic properties of hydrogen bonds (Wang *et al.*, 2019). Depending on the thickness of the bonding material at the interface, the silane coupling agent or adhesion promoter can serve as a primer or size, a finish or surface modifier, or as an adhesive. When used as crosslinking agents, silane coupling agents can interact with polymers to graft trialkoxysilyl groups onto the polymer's backbone, forming crosslinks through siloxane links and producing a stable 3D structure.

3-Glycidoxypropyltrimethoxysilane (GLYMO), a trifunctional epoxy-terminated organosilane grafting approach, has recently generated considerable interest as an effective way to stack biopolymer materials

such as chitosan on the acrylate and ceramic substrates. GLYMO grafting has the ability to convert surface oxides from hydrophilic to hydrophobic character. Karim *et al.* (2018) used GLYMO as a grafting agent to prepare a reduced graphene oxide(rGO) composite membrane to ensure strong interfacial adhesion between the ceramic support and rGO membrane layer with improved surface wettability. Lou *et al.* (2014) also demonstrated a similar approach by silane-grafting the ceramic support membrane via the facile dip-coating method using GLYMO. Mostofi Sarkari *et al.* (2020) recently deposited and grafted GLYMO self-assembled layers on silane-crosslinked polyethylene (Si-XLPE) to modify the surface bonding properties. The result of GLYMO vapor-phase deposition has led to the formation of a hydrophobic surface. This showed that the silane grafted method using GLYMO could be a pathway to improve the surface wettability properties of the substrate and potentially be used in water applications.

Furthermore, it is essential to understand the hygrothermal aging behaviour of the 3D-printed polymer that reacts with its environment for water application. Although the polymer has superior mechanical, physical, and chemical resistance, one of the few disadvantages of the material is its proclivity to absorb moisture underwater (Rajaram, Gin Boay and Srikanth, 2020). The absorbed moisture affects the strength of the materials, stiffness, and thermomechanical behaviour (Tual *et al.*, 2015; Wu *et al.*, 2006). The lifespan of the printed polymer is also influenced by environmental factors such as temperature, humidity, and aging medium. Rajaram, Gin Boay and Srikanth (2020) studied the effect

of aging temperature and curing cycle on the moisture absorption behaviour of epoxy and its carbon fiber composite material. Jiang *et al.* (2014) reported on the fiber-reinforced polymer's moisture diffusion characteristics and mechanical behaviour. Mansouri *et al.* (2019) showed the effect of hygrothermal aging on the mechanical behaviour of short composite fiber/woven composite laminates in different media. Based on the latest literature, all the reported studies focus on epoxy resin and composite materials only as a coating material for concrete protection from corrosive environments. To the best of the authors' knowledge, the moisture behaviour of silane-graft onto PEGDA using GLYMO for water application has yet to be reported in any literature or experimental work.

Herein, a newly developed resin formulation was proposed to fabricate the monolithic structure using vat polymerization (VPP) 3D printing technology. Various resin formulations were proposed, mainly consisting of PEGDA, photoinitiator, 2 different diluent comonomers, and plant-based resin. Subsequently, the printed monolithic structure is grafted with 3-Glycidoxypropyltrimethoxysilane (GLYMO) to alter its surface properties and create a hydrophobic surface depending on the preparation conditions. For comparison, a hybrid silane coupling agent, 3-Glycidoxypropyltrimethoxysilane (GLYMO) and 3 - aminopropyltriethoxysilane (APMTS) was proposed. The mechanical properties, thermogravimetric profile, and surface wetting behaviour were characterized. Furthermore, the moisture absorption behaviour of the silane - grafted PEGDA was also evaluated. Section 6.2 of the paper will describe the materials and methods used in this experiment, followed

by the results and discussion section, and finally, the conclusion for the experimental work.

6.2 Materials and methods

6.2.1 Materials

Acrylate Magma plant-based resin (≥ 99.9 %, MW: 308 g/mol, viscosity: 10 – 30 cP at 25 ℃) was purchased from 3D Gadgets Malaysia. The photoinitiator (Irgacure 819); Phenylbis (2,4,6-trimethylbenzoyl) phosphine oxide (MW:418.5 g/mol) was purchased from Chemmart Asia Sdn Bhd. Glycidyloxypropyl trimethoxysilane (GPTMS) (≥98 %, MW:236.34 g/mol), (3-aminopropyl) trimethoxysilane (APTMS) (97 %, MW:179.29 g/mol, density:1.027 g/ml at 25 °C), 1,6-Hexanediol diacrylate (HDDA) (80 %, MW:226.27 g/mol, density:1.01 g/mL at 25 °C) and 1,4-Butanediol diacrylate (BDDA) (87 %, MW:198.22 gmol, density:1.051 g/mL at 25 °C) were purchased from Sigma-Aldrich, USA. Poly (ethylene glycol) diacrylate (PEG250DA) was purchased from Ryoji, China. Isopropyl alcohol (IPA) (≥90%, MW:60.1 g/mol), hydrochloric acid (HCl) (37%, MW:36.46 g/mol), and sodium hydroxide (NaOH) (99%, MW:40 g/mol) were purchased from Giti Eco Sdn. Bhd, Malaysia. All chemicals were used as received with no further modifications or purification.

6.2.2 Formulation and preparation of photocurable resin

For water applications, the selection of suitable polymeric material is crucial. The biocompatible PEGDA was chosen and used as the primary monomer source to formulate a new photosensitive resin for 3D printing in this study. A natural bio-based resin was used as secondary monomer

source because of its very low toxicity and does not emit volatile organic compounds. Two types of low viscosity diluents (HDDA and BDDA) with high photopolymerisation reactivity were added to achieve fast printing and high precision in the printed parts, while Irgacure 819 which undergoes homolytic cleavage and formed radicals that initiate radical polymerization when exposed to UV light was used as the free-radical photoinitiator (Yang *et al.*, 2015). The photocurable resins were prepared as follows: First, a premix was obtained by dissolving the bio-based resin into the PEGDA. Various BDDA concentrations were gradually added to the premix under magnetic stirring at 500 rpm to increase the photocuring intensity and thus the mechanical strength in the printed parts. After a thorough mixing for 30 min, 1wt.% of Irgacure 819 was added to the pre-polymer solution to prepare the photosensitive resin. A similar procedure was applied for HDDA at different concentrations. Table 6.2.1 listed the compositions of the chemicals used in the formulation and preparation of the resin with the PEGDA resin as the control sample, as shown in Figure 6.2.1a.

Table 6.2.1: Composition of the different chemicals used in the formulation of resins.

Resin formulation	**PEGDA (part)**	**Bio-based resin (part)**	**Irgacure 819 (wt%)**	**HDDA (wt%)**	**BDDA (wt%)**
PEGDA	2	1	1	-	-
PEGDA/HDDA1				1	-
PEGDA/HDDA2				2	-
PEGDA/HDDA3				3	-
PEGDA/BDDA1				-	1
PEGDA/BDDA2				-	2
PEGDA/BDDA3				-	3

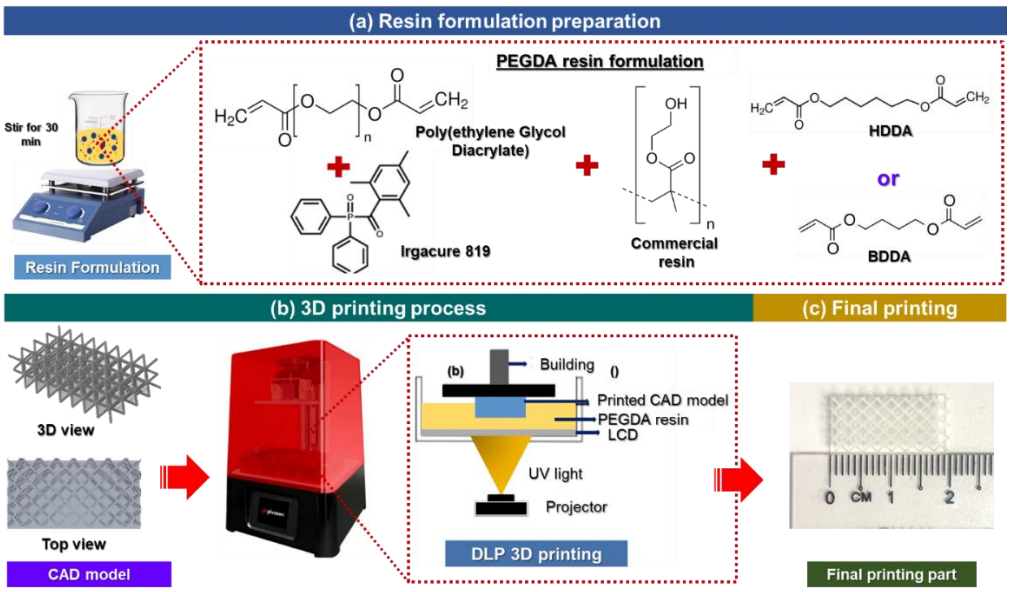


Figure 6.2.1: Schematic diagram of; (a) Preparation of resin formulations; (b) 3D printing process and (c) Final printing part of the 3D-printed monolith.

6.2.3 3D printing of monolith structure

In this study, the monolith fabrication was performed using Phrozen Sonic Mini UV Photocuring LCD resin 3D printer. The printer has a preset slicing thickness of 100 µm and lateral printing resolution of 50 µm. A monolith structure with dimension of 0.5 × 2 × 1 cm was designed using computer-aided design software (CAD) and imported as an STL file as illustrated in Figure 6.2.1b. The 3D model was divided into a series of 2D images based on the geometric features and predefined slicing thickness. Then, the sliced shapes were projected by the LED UV lighting system onto the resin vat to cross-link the formulated photosensitive resin. After the printing was completed, the samples were removed from the printing platform and cleaned with isopropanol. To ensure a complete cross-linking of the resin, post-curing treatment with UV light was performed for 10 min. Figure 6.2.1c showed the final printed part of the monolith which can be used for the subsequent surface functionalisation.

The printing parameters that were set to print the monolith can be found in Section 3.2.2.

6.2.4 Surface functionalisation via silane coupling agent.

The procedures for surface functionalisation of the 3D - printed monolith using different silanes are described as below:

6.2.4.1 Surface grafting with (3-Glycidyloxypropyl) trimethoxy silane

The first method followed the procedures reported previously in (Lou *et al.*, 2014), with some modifications, as shown in the schematic diagram in Figure 6.2.2a(i). The printed monolith was immersed in the GPTMS/ethanol solution for 30 min at a volume ratio of 1:1. The support was then oven dried for 4 h at 110 °C. This serves as benchmark for comparison with the proposed hybrid silanization strategy.

6.2.4.2 Surface grafting with hybrid silanization strategy

Hybrid silanization using a combination of coupling agents of GPTMS and APTMS was proposed, as it is expected to lead to an increase in both the mechanical and thermal stabilities (Lee *et al.*, 2018; Wang *et al.*, 2020). Briefly, isopropanol, APTMS, and deionized water were mixed in a ratio of 1:3:6 for 2 min. GPTMS was added to the mixture and mixed until they became homogenous. A thin layer of hybrid silane was deposited on the 3D-printed monolith structure by immersing the sample into the prepared solution for 3 min. The treated sample was then oven-dried for 20 min at 100 °C. Subsequently, ultrasonic cleaning was performed using IPA to remove any impurities from the surface. The samples were washed with DI water and air-dried in a fume hood. All the samples were stored in a desiccator at room temperature (25 °C) for

further analysis. The process of silanization is schematically depicted in Figure 6.2.2a(ii), whereas the coated samples with GPTMS/ethanol and hybrid silane were shown in Figure 6.2.2b(i) and b(ii), respectively.

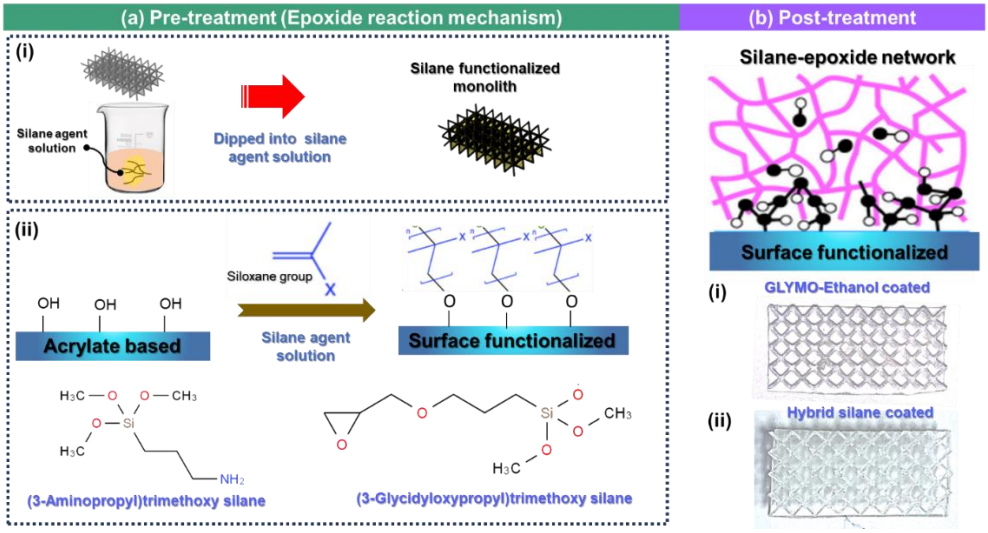


Figure 6.2.2: Schematic of the surface functionalisation process via surface-grafted silanization. The structures of the silane agent used are known.

6.2.5 Characterisation study

6.2.5.1 FESEM analysis

The surface morphology and elemental composition of the silane-functionalised monolith were studied using a field-emission scanning electron microscope (FESEM, FEI Quanta 400 F, USA) coupled with an energy-dispersive X-ray analyser (EDX). The sample was coated with gold in a rotary pumped coater (Quorum, 150 A S Plus, UK) at a deposition rate of 6 nm/min and a deposition current of 20 mA. The prepared samples were placed in a vacuum chamber and sputtered with an electron beam. The images were viewed at various magnifications (90-3000x) at a voltage of 10 kV.

6.2.5.2 X-ray photoelectron spectroscopy (XPS)

The chemical composition, binding energy of the compound, and type of bond on the pure 3D-printed PEGDA and silane-functionalised 3D-printed monolith were determined using X-ray photoelectron spectroscopy (XPS) (Kratos Axis Ultra DLD, United Kingdom). The samples were examined in ultra-high vacuum (UHV) conditions and exposed to monochromatic Al Kα (1486.6eV) x-rays, respectively.

6.2.5.3 X-ray diffraction analysis (XRD)

The composition, crystalline or amorphous structure, and lattice parameter of the 3D-printed monolith of different resin formulations and silane-functionalised monolith were determined using a Panalytical powder diffractometer XRD system (X′Pert Pro, Netherlands). Cu K X-rays are used to irradiate the XRD diffractometer. The scan is performed with two theta (2θ) ranging from 7° to 80°, each with a step of 0.2° and 0.5° per step. Diffraction patterns with a wavelength of 0.154 nm are collected at 45 kV generator voltage and 40 mA currents.

6.2.5.4 Thermogravimetric and differential scanning calorimetric analysis (TGA – DSC)

The thermal stability of the samples was determined by thermogravimetric analysis (TGA) and differential scanning calorimetry (DSC) (Perkin Elmer STA6000, USA). The analysis was carried out using approximately 6 – 9 mg of the samples in a temperature range of 0 – 400 ℃ at a cooling and heating rate of 10 ℃/min.

6.2.5.5 Texture Analyser

A tensile test was carried out using a texture analyser (TA. XT Plus, Stable Micro Systems, USA), following the American Standards for Testing Methods (ASTM) D1708, and subjected to a load cell of 50 $\pm$ N. Five specimens were tested for each case to ensure reliability of the test results. The tensile strength, Young's modulus, and elongation at break of each sample were measured using the generated graphs.

6.2.5.6 Dynamic Mechanical Thermal analysis (DMTA)

Dynamic Mechanical Thermal Analysis (DMTA) tests were conducted to determine the viscoelastic properties of the samples. The storage modulus (*G'*), tangent delta (tan δ) and glass transition temperature (T_g) using a PE-DMTA (USA) under a single cantilever mode with a frequency of 1 Hz. The temperature sweep range was between 20 and 80 ℃ at a heating rate of 10 ℃/min.

6.2.6 Moisture absorption analysis in distilled water and dried state

The 3D-printed monolithic structure before and after surface grafting with GLYMO and hybrid silane agent (GLYMO-APTMS) were rinsed with distilled water and then dried for 24 h in a vacuum oven at 60℃ (Krauklis, Gagani and Echtermeyer, 2018b). The amount of water absorbed by the resins was then calculated as a function of immersion time. At regular intervals, the samples were removed from the water, wiped down, and weighed on a weighing balance with an accuracy of 0.01mg. The samples should be weighed every 30 min until an equilibrium is achieved. The moisture content in the samples due to absorption of water, M_c can be calculated using Eq. (38).

$$M_c(\%) = \frac{(m\,(t) - m_{dried})}{m(t)} \times 100\% \quad (38)$$

Where $m(t)$ is the mass of the total mass of resin with moisture and m_{dried} is the mass of the resin after drying.

In the case of moisture release or desorption methods, the saturated samples were then dried in an air atmosphere with natural convection at 60℃ for a specified time before being moved back to the ambient condition. The sample mass was measured again over the course of 24 h using an analytical weight as per described by (Cichosz and Masek, 2020). The moisture release M_r at time "t" was calculated using Eq. (39).

$$M_r(\%) = \frac{(m_h - m_{dried})}{m_h} \times 100\% \quad (39)$$

where m_h is the mass of the humidified sample and m_{dried} is the mass of the sample after drying to a constant mass. All mass were taken in mg and the mean $\pm$ standard deviation data from three repeated experiments were taken to ensure reliability of the results.

The polymers' moisture absorption and release rates are expressed in exponential curve using regression equation of the rate of moisture absorption and release (Ahmad, Ansell and Smedley, 2011), as shown in Eq. (40). The graph of moisture absorption and release of the samples at interval time was plotted.

$$\frac{M_t}{M_s} = Kt^n \quad (40)$$

Where M_t is the moisture content at the t time and M_s is the moisture content at equilibrium. K is a constant that is determined by the polymer's

structural properties and its interaction with moisture. K can be determined based on the plot of $log\frac{M_t}{M_s}$ vs t.

Typically, the moisture absorption in polymers is studied in terms of Fickian diffusion, which plotting the results as weight gain (as a percentage of dry weight) versus squared root of time.

Diffusion coefficient, D, is another parameter to quantify the polymers' moisture absorption behavior by measuring the movement of the penetrant molecules within the segment of the polymer. The diffusion coefficient *D* was calculated using Eq. (41).

$$D = \pi\left(\frac{h\theta}{4M_{eq}}\right)^2 \quad (41)$$

Where M_{eq} is the moisture content of the samples at equilibrium, h is the initial thickness of the samples and θ is the initial slope of the linear portion of the water absorption curve.

6.2.7 Surface contact angle analysis

The contact angle (θ) of the 3D printed part surface coated with the silane agent is an essential indicator of wettability and is related to surface tension. Wettability is the ability of the material to form boundary surfaces and spread on a surface, indicating whether the surface is hydrophilic or hydrophobic. The experimental work was carried out based on the procedures described in (Buenaflor *et al.*, 2022; Xu *et al.*, 2015). Briefly, a 1 µL deionised water droplet was deposited on the surface of the samples at room temperature. The average value of contact angle was determined by taking at least three images and analysed using ImageJ

software with the Contact Angle Plug-in to obtain θ using the following Eq. (42).

$$Contact\ angle = 180° - \theta \quad (42)$$

Where θ is the contact angle obtained from ImageJ software based on either a circle (Theta *C*) or ellipsoid (Theta *E*) calculation.

6.2.8 Mechanical and chemical stability of the grafted surface

Excellent mechanical and chemical stability in harsh conditions is essential when selecting suitable materials for wastewater applications. The mechanical stability of the surface functionalised 3D-printed monolith was tested by exposing the samples to ultrasonication for 60 min. The change in water contact angle before and after the sonication at intervals of 10 min was taken to evaluate its mechanical stability. For chemical stability analysis, the samples were immersed in 3 different solvents (NaCl, NaOH and HCl) as described by (Jin *et al.*, 2021) for 24 h. After immersion, the change in water contact angle for each condition was calculated using ImageJ software.

6.3 Results and discussion

6.3.1 Photopolymerisation reaction in the formulated PEGDA-based resins

The crosslinking reaction in the formulated resin is based on the process of photopolymerisation. As shown in Figure 6.3.1a, free radicals were produced when Irgacure 819 is exposed to UV light, which combine and react with the PEGDA monomers (Figure 6.3.1b). The reaction consists of two significant steps: (1) exposing a photo-initiator (Irgacure 819) to UV irradiation and decomposing an initiator molecule into two radicals;

and (2) allowing the free radicals to react with the monomers (PEGDA and HDDA/BDDA), thereby initiating a PEGDA/HDDA or PEGDA/BDDA chain by opening their carbon-carbon double bonds. The co-polymer chains spread through reactions with the other available vinyl bonds on monomers or other polymer chains. As a result, two chains combine to form dead polymer chains, causing the growing polymer to terminate (Figure 6.3.1c).

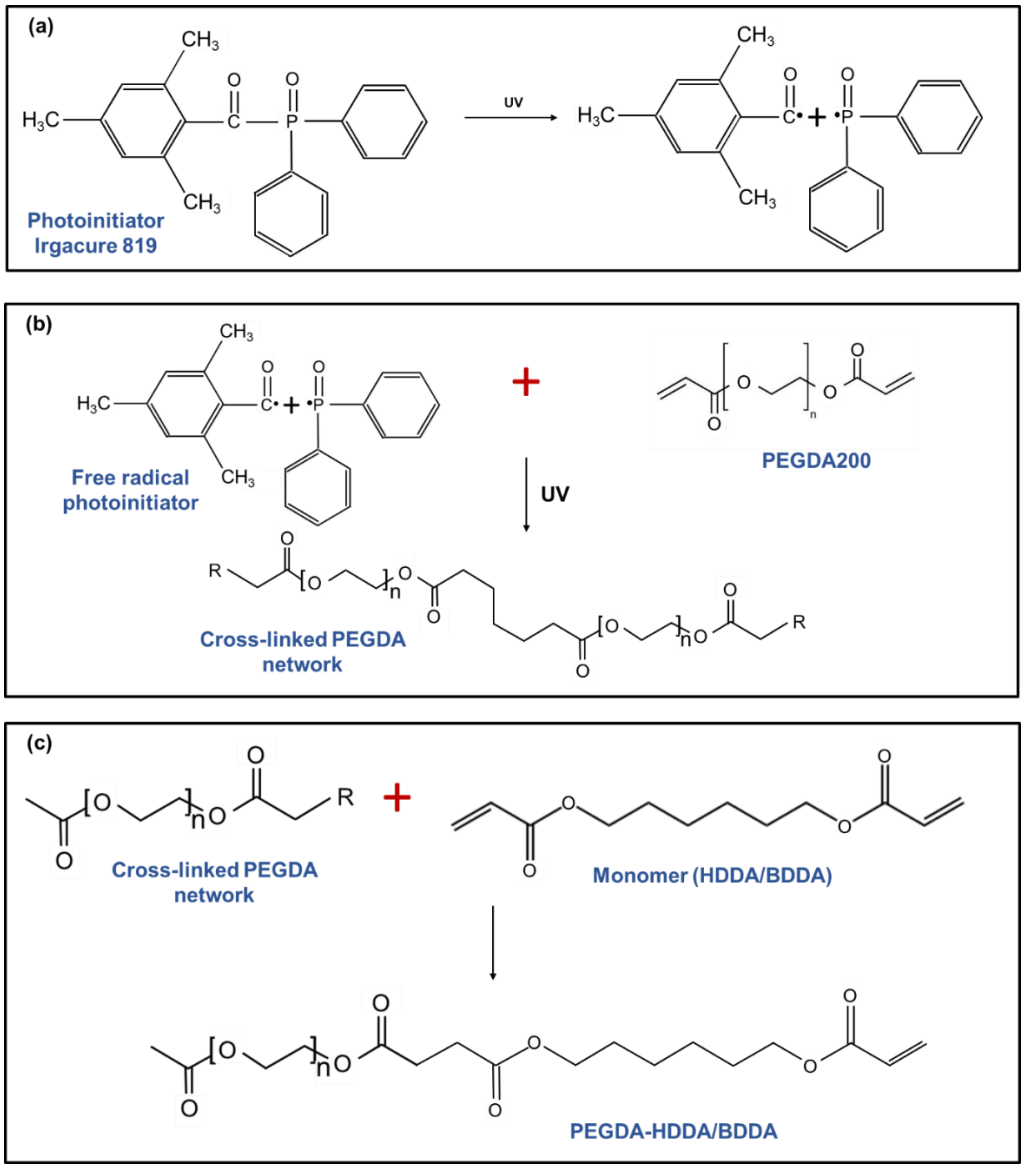


Figure 6.3.1: Illustration of photopolymerisation of PEGDA200 with Irgacure 819 and comonomer under UV exposure.

6.3.2 Surface functionalised 3D-printed monolith structure

The morphology of 3D-printed monolith before and after surface functionalisation with silane agent was observed by using scanning electron microscopy (SEM) and FTIR analysis as portrayed in Figure 6.3.2a.

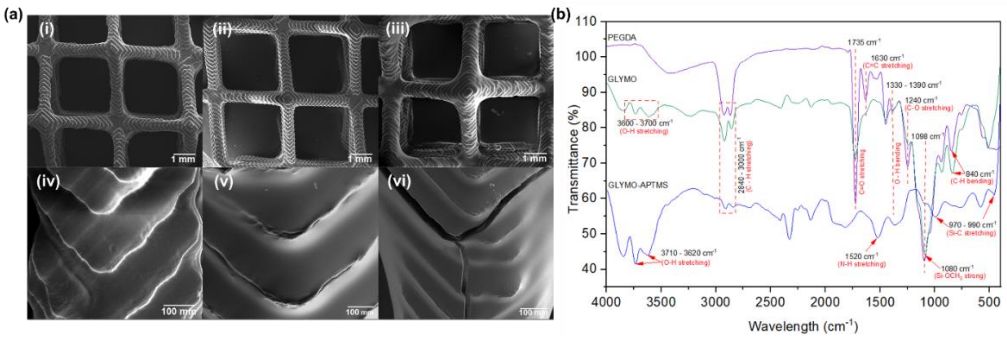


Figure 6.3.2**:** (a) FESEM images and (b) FTIR analysis of pure PEGDA and silane - grafted 3D-printed monolith.

Table 6.3.1**:** EDX analysis of pure PEGDA monolithic structure before and after silane grafted.

Sample ID	Sample name	Elemental weight %		
		C	O	Si
PG1	Pure PEGDA monolith	59.2	40.8	0
PG2	GLYMO	49.1	43.1	3.60
PG3	Hybrid silane	46.9	43.7	9.31

The surface of the monolithic structure printed with the formulated PEGDA-based resin was initially clear and smooth before the surface grafting (Figure 6.3.2a(i)). It was observed that the surface appears glassy after surface grafting with GLYMO (Figure 6.3.2a(ii)) and hybrid silane agent (Figure 6.3.2a(iii)). Silane coupling agents or organosilane agents are monomeric silicone-based chemicals consisting of silicon and carbon atom, which gives a crystalline look (Dawood, 2014). However, it is worth noting that surface grafting with excessive hybrid silane agent

causes the truss of the monolith to crack. The intense epoxide-amide reaction with the acrylate substrate has caused a severe expansion and deep crack in monolith structures (Zhang *et al.*, 2021a; Fiore *et al.*, 2020; Wang *et al.*, 2016). The fracture mechanism could be explained by polymer matrix debonding and crack pinning, in which the pinning of a crack by a particle acts as an obstacle on the polymer, resulting in secondary cracks and new fracture surfaces (Wang *et al.*, 2016). Apart from that, another possible cause of the cracking is the design of molecular structure of the silane agent as the organic component in the agent is typically composed of hydrophobic groups, which can result in a rigid and inflexible coating. Such rigidity then lead to stress buildup and, eventually cause cracking (Lung and Matinlinna, 2010). Therefore, it is suggested to use silane agent with a lower silica content to mitigate the fracture issue. From SEM analysis, it verified that both 3D-printed monolithic structure samples were successfully grafted with silane agents.

Furthermore, elemental composition of the 3D printed samples was investigated using energy dispersive X-rays (EDX). As shown in Table 6.3.1, and O elements were detected on all 3 different samples. In addition, Si element was detected on the monolith surface grafted with silane coupling agent. The composition of Si element of GLYMO grafted sample is 3.6 wt.%, whereas it is 9.31 wt.% for hybrid silane grafted sample. This result further confirmed that surface grafting has successfully induced the binding of silane coupling agent on the surface of the 3D-printed monolith.

Further analysis into the successful of surface functionalisation was carried out using FTIR, where the chemical composition and molecular structure of the 3D-printed monolithic structure before and after the grafting process were determined and depicted in Figure 6.3.2b. Referring to Figure 6.3.2b, FTIR spectra of all three components demonstrated a similar pattern at peak between 2840 – 3000 cm^{-1}. This peak corresponds to the stretching vibration of the C – H stretching bond, which refers to the asymmetric and symmetric CH_2 bonds of the PEGDA substrate (Li *et al.*, 2016). The spectrum at peak 1630cm^{-1} is associated to the stretching of double bond of C = C, whereas C = O stretching vibration at 1735 cm^{-1}. A strong intense band of C – H bending was observed at spectra 840 cm^{-1}, which corresponds to the substituted CH_3 group. Furthermore, the intense band between 3600 and 3700 cm^{-1} corresponds to O – H in the samples grafted with silane coupling agent, as well as associated with Si-OH from the hydrolysis reaction of GLYMO and the GLYMO-APTMS structure (Husna *et al.*, 2022). The FTIR spectra further revealed an intense broad absorption band at 1098 and 1080 cm^{-1} due to absorption from the Si – O - C bond (Azhary *et al.*, 2019). Another peak at 970 - 990 cm^{-1} featured the non-bridging oxygen of Si - OH bonds in the silica network (Connell *et al.*, 2014; Reyes-Peces *et al.*, 2020). The abovementioned peaks are indications that GLYMO and hybrid silanes were successfully grafted on the 3D-printed monolithic structure.

Further to this, the bonding and the elemental composition of the pure PEGDA before and after grafted with silane were conducted using XPS.

XPS studies were conducted to determine the elemental composition and bonding on the surface of the grafted - chitosan PEGDA monolith. The broad scan spectra of 3D-printed PEGDA monolith comprises C, O, whereas there is additional of Si element found after grafted with GLYMO, as illustrated in Figure 6.3.3a. The peaks corresponding to Si 2s, and Si 2d orbital energy levels arise following the reaction with a coupling agent containing GLYMO. High-resolution spectra of C1s, O1s and Si 2p give further information about the chemical binding state. It is clear that the spectrum produced by PEGDA acrylate-based substrate differs from GLYMO-modified spectrum. The spectrum can be divided into three parts; (i) a strong signal which attributed to C-C/C-H peaks at 284.6 eV; (ii) C-O peak at 286.5 eV and (iii) C=O peak at 288.0 eV. The major O 1s peak at 532.3 eV represents the oxygen of aliphatic bond of PEGDA as illustrated in Figure 6.3.3c. All these peaks correspond to PEGDA acrylate substrate. Furthermore, it is noteworthy that the Si 2p core level spectrum at peak 99.4 eV, depicted in Figure 6.3.3d, is representative of a Si element of silane-grafted monolith. The C1s core level, as illustrated in Figure 6.3.3d, exhibits a prominent peak at 281.39 eV, which is intrinsically linked with the GLYMO silicon carbide bond. Si and C atoms form highly strong tetrahedral covalent connections, which makes them the best candidate to use as a crosslinker (Cheng *et al.*, 2018; Li *et al.*, 2008). Overall, the results show that the silane was effectively grafted onto the surface of the 3D-printed monolith.

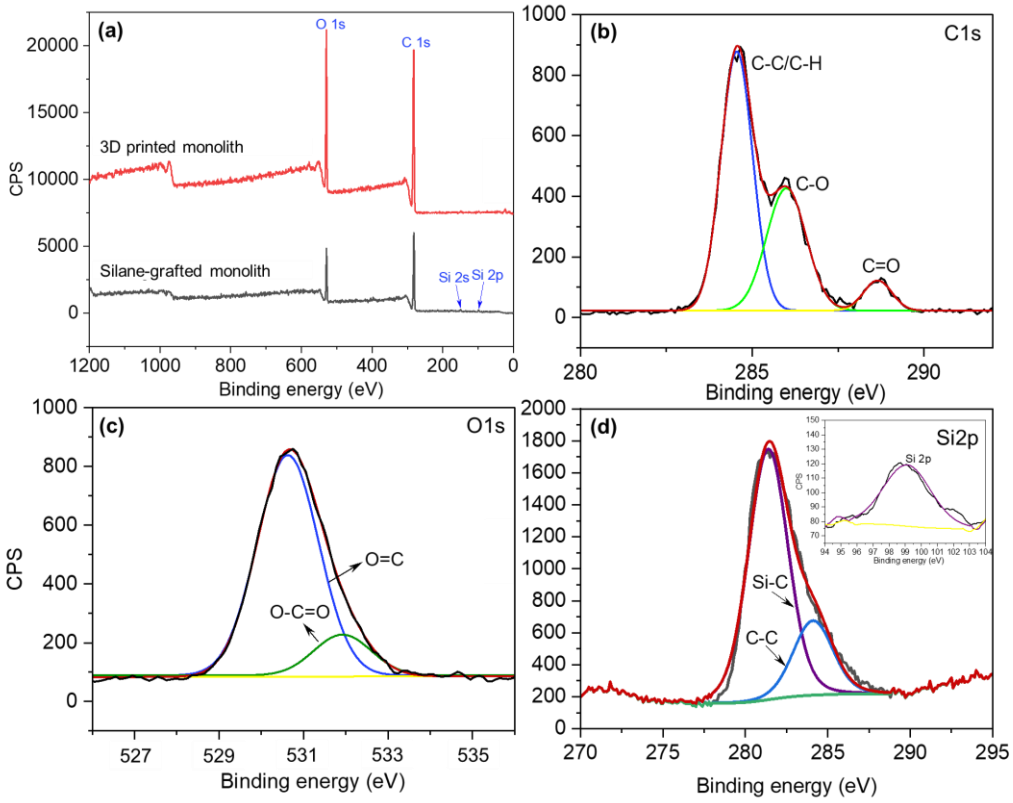


Figure 6.3.3: (a) XPS spectra wide scan of 3D-printed PEGDA monolith before and after silane grafting; High resolution spectra of;(b) C1s of 3D-printed PEGDA monolith; (c) O1s of 3D-printed PEGDA monolith; and (d) Si2p of silane grafted monolith.

Based on the XRD pattern, the crystalline and amorphous behaviour of the material was identified. Figure 6.3.4a depicted the XRD patterns for different resin formulations for 3D-printed monolith. The XRD plot for all resin formulations showed semicrystalline behaviour. This finding is in a good agreement with previous studies, where most of the polymers are amorphous with minimal crystallinity. On the other hand, in Figure 6.3.4b, both peaks before and after grafting with silane agent exhibit two strong XRD peaks at 20.5° and 22.1°, with some small peaks at 26.7°, 30.9°,40.7° and 71.9°. These peaks are attributed to the crystallinity that is induced by intermolecular hydrogen bonding between the -OH groups of glycols. Moreover, the introduction of silane agent with the polymer

matrix can minimise crystallinity of the polymer which can increase the mechanical properties such as tensile strength, moisture resistance, stretch strength. This is because intermolecular bonding is stronger in the crystalline phase (Ella *et al.*, 2021). The outcome of the XRD result is tally with the finding reported in mechanical properties section (Section 6.3.4).

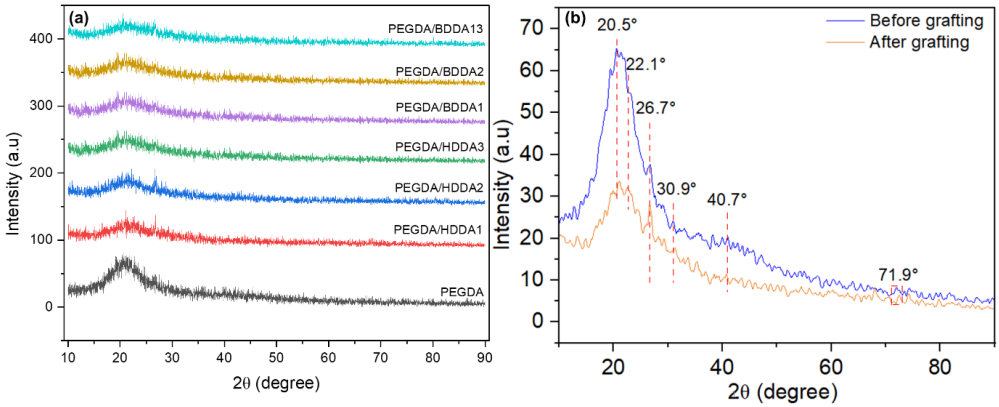


Figure 6.3.4: XRD pattern for (a) different resin formulation for 3D-printed monolith and (b) 3D-printed PEGDA monolith with and without grafted silane.

6.3.3 Improvement in thermo-mechanical properties

6.3.3.1 Thermal properties

TGA and DSC curves and their data of 3D-printed samples before and after the surface grafting with GLYMO and hybrid silane agent are shown in Figure 6.3.5 and Table 6.3.2.

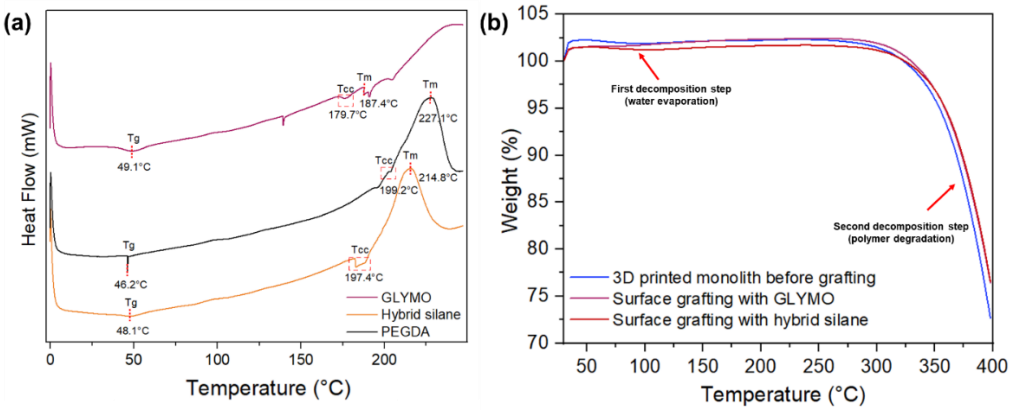


Figure 6.3.5**:** (a) DSC and (b) TGA results of pure 3D-printed PEGDA monolith, surface grafting with GLYMO and hybrid silane (GLYMO-APTMS).

Table 6.3.2**:** DSC and TGA data for pure 3D-printed PEGDA monolith, surface grafting with GLYMO and hybrid silane (GLYMO-APTMS).

Sample name	DSC			TGA			
	T_g	T_m	Enthalpy	Initial weight	Weight loss	Tonset	Residue at 400℃
	℃	℃	Jg^{-1}	mg	%	mg	℃
Pure PEGDA	46.2	227	31.4	5.99	31.1	363	4.12
PEGDA/HDDA1	47.8	181	9.35	6.16	24.1	360	4.68
PEGDA/HDDA2	48.3	185	11.4	9.06	23.0	359	6.97
PEGDA/HDDA3	48.8	191	6.50	7.03	23.4	359	5.39
PEGDA/BDDA1	48.7	161	19.4	6.42	25.4	362	4.79
PEGDA/BDDA2	48.1	223	23.5	7.28	26.0	357	5.38
PEGDA/BDDA3	48.6	213	32.7	6.04	29.1	356	4.28
After grafting							
GLYMO	48.1	187	0.297	8.10	27.5	350	5.88
Hybrid silane	49.1	215	19.7	8.25	26.4	355	6.07

From DSC analysis, the glass transition temperature as well as the melting temperature of all samples were determined and listed in Table 6.3.2 and Supplementary information – Section 7.3.2.1. The addition of comonomers or known as chain-extender such as HDDA and BDDA into the resin formulation has improved the thermal properties of the printed parts (Goswami, Umarji and Madras, 2013; Ma, Xie and Wang, 2019) as

their straight chain structure is beneficial for forming long chain linear block copolymers. DSC data has revealed that the change of glass transition temperature is not obvious, in a narrow range between 47℃ and 48℃, for all formulated resins. In contrast, the melting temperature has notably increased with the addition of comonomer, regardless of amount and concentration. This is mainly because the presence of the comonomer (HDDA or BDDA) has restricted the flexibility of the polymer chain, thus increases the melting point temperature.

For HDDA comonomer, the samples exhibited increasing trend in glass transition temperature with increasing comonomer concentration. The flexibility and mobility of the chain segments to rotate along the chain backbone affect the glass transition temperature of polymeric chains. As the mobility of the chains is restricted, the glassy state becomes more stable, and therefore more energy is required to break and free the chain at lower temperature. As a result, the glass transition temperature has been increased with the addition of the HDDA, which is consistent with previously reported works (Yu *et al.*, 2018; Thiessen and Abetz, 2021). A similar trend was observed when BDDA comonomer has been added to the formulation.

The samples grafted with hybrid silane agent has higher glass transition temperature and melting point temperature than grafted with GLYMO only, as compared in Table 6.3.2. This is due to microstructure variation caused by the cross-linked portion of the sample. The polymer chains tend to lose their rigidity when the silane coupling agent is associated

with them. These interactions caused partial crystallization to occur near 200℃ as shown in Figure 6.3.5a. It is also worth noting all the resin formulations before surface grafting are amorphous whereas after surface grafting procedure, it showed some crystallinity characteristics due to the presence of Si element (Miller and Berg, 2002) as previously discussed in Section 6.3.2. The thermal properties of all samples were further analysed using TGA analysis. The respective thermogravimetric profiles of all prepared resin formulations in this work can be found in Supplementary information – Section 7.3.2.1. Referring to Figure 6.3.5b and TGA plots in Supplementary information – Section 7.3.2.1, all the plotted graphs showed a single decomposition pattern. The figure indicates that even when different concentrations of HDDA or BDDA were used during the polymerization process, the thermal degradation temperatures of the formulated resin were almost similar, which is approximately 360℃. At this stage, random-chain scission, side-chain cleavage and end-chain scission can occur during thermal degradation. Chain scission reduces the molecular weight and changes the molecular weight distribution of the polymer, affecting viscosity and flow properties and the quality of the polymer processes. Commonly, the first thermal degradation occur with removal of the moisture of the samples and volatile matter release up to 150℃ (Cichosz and Masek, 2020) .Then, the degradation continues with related to the carbonate bonds. From these data, it can be concluded that the addition of any comonomer did not greatly affecting the polymer structure and its thermal properties.

Moreover, after surface grafted with the silane coupling agent, the thermal degradation of both samples are reduced to about 350℃. The silanols bond are coupled to each other to form cross-linking during the hydrolysis reaction. This cross-linked structure are more likely to degrade and lead to formation of char (Lu *et al.*, 2006). This is because at certain point, the amount of SiO_2 cannot form a rigid barrier to sustain at high temperature, which leads to the very fast weight loss rate as shown in Table 6.3.2, where the percentage of weight loss of grafted samples is slightly higher compared to different types of the resin formulations. From these results, it can be concluded that all the samples have good thermal stability and can be used for the water application as the monolith commonly operated at the range of 30 to 50℃.

6.3.4 Mechanical properties

The result of the mechanical properties of all resin formulations surface grafted with GLYMO and hybrid silane coupling agent GLYMO-APTMS were presented in Figure 6.3.6 and Table 6.3.3.

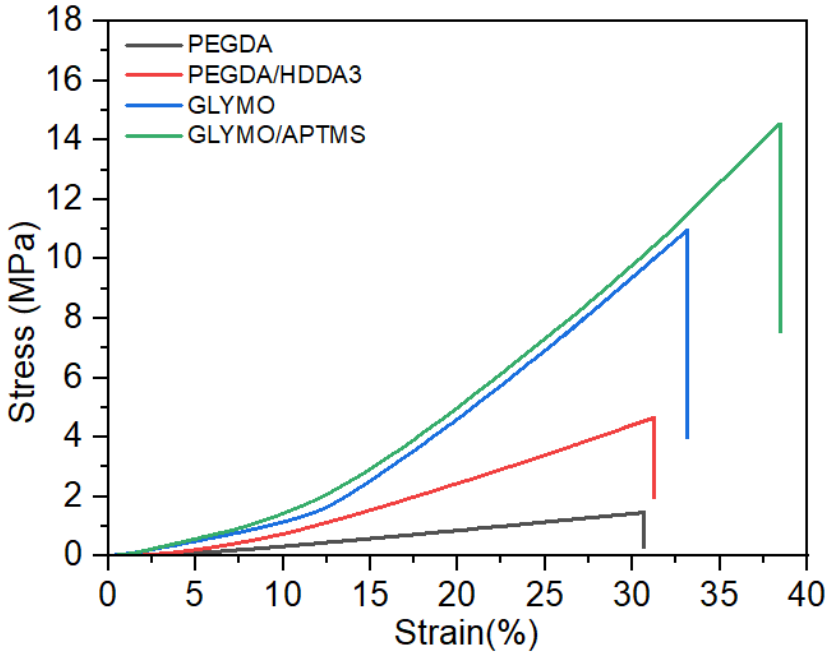


Figure 6.3.6**:** Stress-strain curve of PEGDA with and without silane grafted.

Table 6.3.3**:** Mechanical properties of different resin formulations and surface grafted with GLYMO and hybrid silane coupling agent GLYMO-APTMS for 3D-printed monolithic structure.

	Young's modulus (MPa)	Tensile Strength (MPa)	Elongation at break (%)
PEGDA	337.52	1.45	6.1 ± 2.9
PEGDA/HDDA1	515.24	2.59	7.9 ± 1.4
PEGDA/HDDA2	577.89	2.84	9.8 ± 0.6
PEGDA/HDDA3	595.77	3.08	11.2 ± 0.4
PEGDA/BDDA1	418.27	1.59	6.8 ± 0.7
PEGDA/BDDA2	452.24	1.74	7.5 ± 0.4
PEGDA/BDDA3	478.90	2.20	7.6 ± 0.7
After grafting			
Silane grafted with GLYMO	601.78	9.34	5.6 ± 0.6
Silane grafted with hybrid silane GLYMO-APTMS	667.89	15.41	4.7 ± 0.8

On the other hand, the addition of HDDA comonomer has increased the elongation at break as well. More bonds are introduced between chain

segments and lead to an increase in crosslinking density that reduces the polymer chain mobility, which is critical in highly elastic systems. In contrast, highly mobile polymers untangle their chain segments and unfold to release the energy generated by an external load. The difficulty of the chains sliding past one another determines the modulus for elastic polymers. When the polymers are fully stretched out, the limit of this mobility, or indirectly the strain at break, is reached. This limit is reached at lower strain for highly crosslinked polymers chain. As a result, the energy is primarily used to break crosslinking bonds at lower strains caused by the external load, resulting in plastic deformation.

From the experimental results, it can be concluded that the addition of 3wt.% of HDDA has enhanced the mechanical properties significantly as compared to other resin formulations. Thus, 3D-printed monolith using PEGDA/HDDA3 formulation was surface functionalised, and its mechanical properties was evaluated again. As shown in Table 6.3.3, the monoliths grafted with hybrid GLYMO-APTMS silane have a higher Young's modulus and tensile strength, whereas those grafted with GLYMO have a higher elongation at break. The further improvement in mechanical properties in the 3D-printed monolith is believed to be due to the strong interaction between the acrylate substrate and the silane coupling. The 3D-printed monolith's surface has ample of hydroxyl and carbonyl end groups, which interact with the epoxy group in GLYMO through a nucleophilic substitution reaction and primary amine structure in APTMS via hydrogen bonds, respectively. The formation of hydrogen

bonding and covalent bond has increased the interfacial strength, and therefore the thermomechanical properties (Wang *et al.*, 2016).

6.3.5 Viscoelastic analysis

The viscoelastic properties and morphologies of all samples can be obtained from the dynamic mechanical thermal analysis as presented in Table 6.3.4.

Table 6.3.4: Dynamic mechanical thermal analysis data of different resin formulations and surface grafted with GLYMO and hybrid silane coupling agent GLYMO-APTMS.

Samples	Storage modulus (MPa)	Loss Modulus (MPa)	Glass transition temperature (°C)	Tan δ
PEGDA	336	45.1	57.0	0.274
PEGDA/HDDA1	95.6	24.7	41.8	0.266
PEGDA/HDDA2	109.4	26.8	40.7	0.242
PEGDA/HDDA3	130	31.5	41.4	0.248
PEGDA/BDDA1	244	25.5	55.9	0.251
PEGDA/BDDA2	247	38.0	52.1	0.258
PEGDA/BDDA3	306	41.1	53.7	0.270
After surface grafting				
GLYMO	471	49.8	49.8	0.769
Hybrid silane	483	47.3	50.2	0.421

The storage modulus measures a sample's ability to store deformation energy elastically. This is proportional to the degree of cross-linking, where the greater the degree of cross-linking, the greater the storage modulus. Referring to data in Table 6.3.4, the addition of the cross-linking comonomer of HDDA and BDDA has significantly affected the storage modulus, G'. In both cases, storage modulus increased as the comonomer concentration increases. The presence of the comonomer reduces the spacing between the chain molecules and yield a high

degree of crosslinking. A similar trend was observed for loss modulus of samples, G", in which the comonomer molecules were well dispersed in the polymer backbone and enhanced the elastic properties and friction between the polymer matrices. It is noteworthy that the storage modulus for samples added with BDDA is higher compared to those added with HDDA, suggesting low molecular weight and short chain length of the comonomer has restricted the relative movement in the polymer matrix, and therefore the sample consumed more internal energy that led to an increase in the storage modulus loss factor (Zhao *et al.*, 2020).

The results imply that addition of BDDA has greater impact on the storage modulus of the 3D-printed monolith. Therefore, samples printed using PEGDA/BDDA3 formulation were surface functionalised for further dynamic mechanical thermal analysis and the obtained results were presented in Table 6.3.4. As expected, the grafting of silane agent (both GLYMO or GLYMO-APTMS) layer on the 3D-printed monolith has increased both storage and loss modulus since the silane agent is effect in reducing agglomeration and allowing the silicon particles to fully react with the epoxy resin matrix via hydrolysis reaction.

6.3.6 Enhancement in surface properties

6.3.6.1 Resistance to moisture absorption

The moisture equilibrium content of the 3D-printed monolithic structure before and after surface grafting with GLYMO and hybrid silane agent (GLYMO-APTMS) are presented in Figure 6.3.7a. The 'dry' samples already have a true moisture content of about 0.63%, indicating that they have some water present initially and are in equilibrium with water vapor

in the air (Krauklis, Gagani and Echtermeyer, 2018b; Krauklis, Gagani and Echtermeyer, 2018a). After an immersion time of 24 h, the water absorption became stagnant for all samples, therefore this was determined as the equilibrium water absorption. The bare 3D-printed monolith (without surface grafting) can absorb more water and achieved a moisture content as high as 4.40 wt.% due to the unique chemical properties of the PEGDA and commercial resin used (Rekowska *et al.*, 2019). The water absorption has decreased after surface grafting with GLYMO and hybrid silane (GLYMO-APTMS). The surface functionalisation process has effectively grafted a lining of hydrophobic layer on the surface, which reduces moisture absorption. It was noted that the hybrid silane coupling agent GLYMO-APTMS was very effective on reduction of moisture absorption, as evidenced by a mere increase of moisture content from 0.63 wt.% to 0.69 wt.%, while the GLYMO coated sample has seen the moisture content increased from 0.63 wt.% to 1.97 wt.%. This is because some of the hybrid silane coupling agents are able to physiosorbed on the 3D-printed monolith's surface, diffuse into and forming a longer chain polymer matrix that enhanced the water repellent capability of the surface (Nakamura *et al.*, 2020).

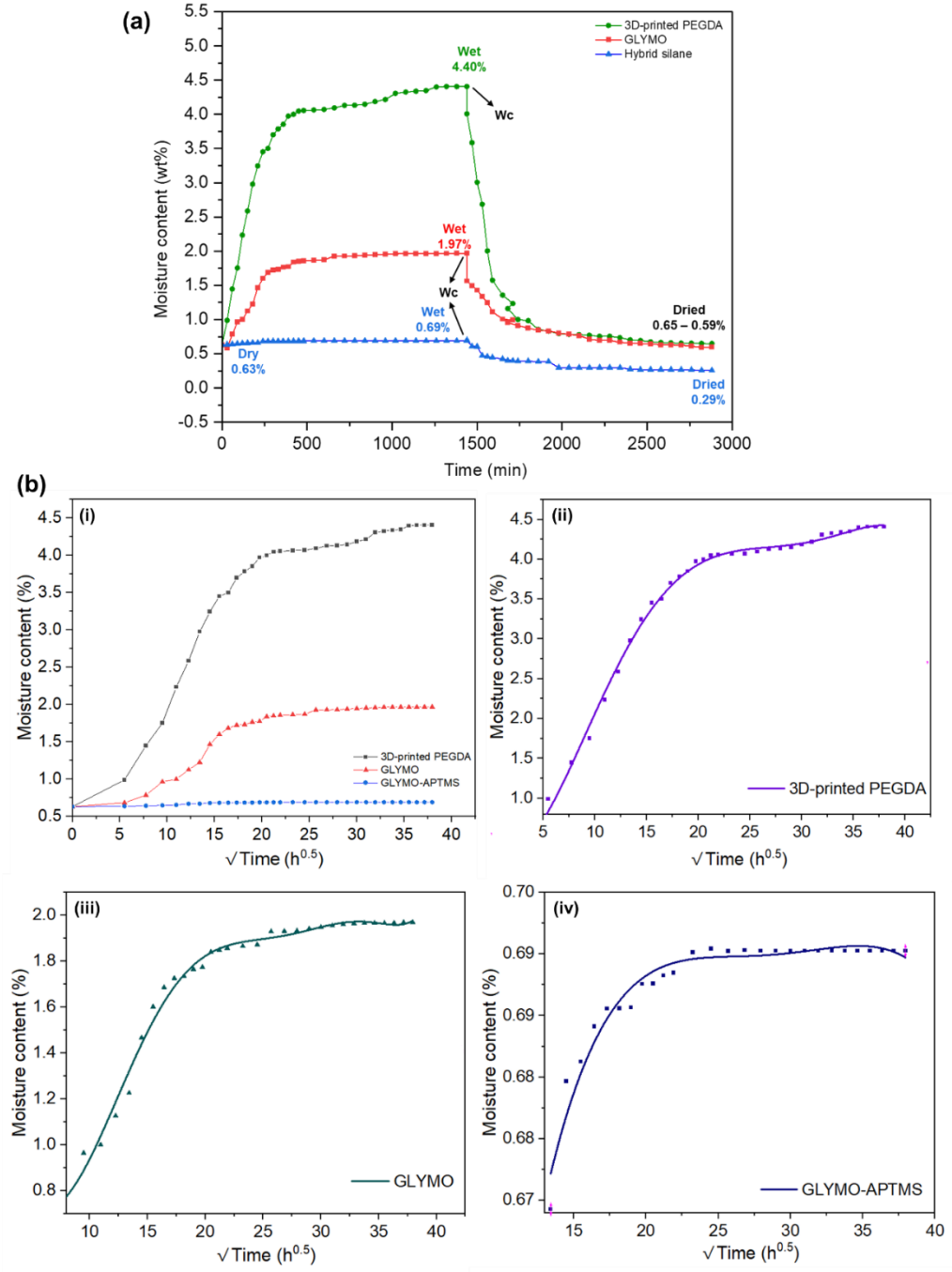


Figure 6.3.7**:** Experimental moisture absorption-desorption data of the samples before and after surface grafted with different silane coupling agents. Moisture absorption rate curve of all samples and fitted curve of moisture absorption rate curve of; (b) 3D-printed PEGDA, (c) Silane functionalised with GLYMO and (d) Silane functionalised with GLYMO-APTMS.

Based on the moisture absorption curve plotted, the initial absorption slope of all samples follows the linear behaviour with respect to squared root time, obeying Fick's second law. According to Fick's law, it was assumed that the amount of water absorbed in the material is proportional to the concentration gradient. The amount of water absorption gradually increases as the aging time increases until it reaches saturation point (Fan *et al.*, 2022). The trend of the fitted curve of all samples are in good agreement of Case I based on Fickian behaviour which can be categorised as:

Case I - Fickian diffusion: The diffusion rate of the penetrant is lower than the rate of relaxation processes, where based on Eq. (40), the constant n is 0.5.

Case II - Non- Fickian diffusion: The diffusant's diffusion rate is faster than its relaxation rate. A sharp advancing boundary can be used to describe the diffusion, n = 1.

Case III - Anomalous diffusion: The diffusion and relaxation rate are comparable, $0.5 < n < 1$.

The diffusion coefficient of all samples was tabulated in Table 6.3.5. The obtained values were also comparable with the graph illustrated Figure 6.3.7b. The separation between the lines in the graph indicates the effect of the surface functionalised with different silane agents. It was shown that the separation of the curve that has the largest deviation demonstrated the best performance for the surface treatment, in this case functionalising with hybrid silane agent. Moreover, as shown in the

table, the largest diffusion coefficient was found for 3D-printed PEGDA monolith without functionalising with any silane coupling agent. Higher diffusion coefficient indicates that the diffusion occurs at a faster rate, which is less favourable in this case as it cannot provide protection for the materials. The smallest diffusion coefficient was found for functionalising with hybrid silane. The hybrid silane treatment was more effective in forming the hydrophobic layer near the very front surface cover and highly demonstrated water repellent properties, resulting in a significant reduction of moisture absorption. The surface treatment provides a greater resistance against moisture, presumably arising from the pore-lining or water-proofing agent effect (Kim *et al.*, 2020b). Moreover, the reduction of the moisture absorption is greatly affecting the hydroxyl group of the polymer. When hydrolysed silane solutions are grafted on the surface, reactive silanol groups are attracted to each other, forming Si-O-Si bonds as well as hydrogen connections with the hydroxyl sites of the silanes with polymer substrates. Surya *et al.* (2022) discovered a similar result when they prepared biopolymeric packaging films using natural red seaweed and kenaf cellulose nanofiber, followed by film surface treatment with silane to create hydrophobic properties. In another work, Kim *et al.* (2020b) discovered surface treatment with silane can improve ionic transport resistance and achieve lower water absorption rate. Therefore, in this work, it can be concluded that the surface treatment with silane coupling agent can reduce moisture absorption, hence making it a potential material to be applied for water

applications. Further analysis on surface wetting was done based on the water contact angle analysis in Section 6.3.6.2.

Table 6.3.5: Values of initial slope of the water absorption curve and diffusion coefficient for each of the samples

Sample	**Gradient ($h^{-1/2}$)**	**Diffusion coefficient (m^2/s) x10^{-10}**	**R^2**
3D-printed PEGDA monolith	0.2460	16.025	0.996
Silane functionalised with GLYMO	0.0807	0.343	0.992
Silane functionalised with GLYMO -APTMS	0.00339	7.487 x 10^{-5}	0.944

6.3.6.2 Surface wettability and its stability

The change in surface wetting property of the grafted surface was studied based on water contact angle measurement. As shown in Figure 6.3.8a, the WCA of the 3D-printed PEGDA monolith was measured as 71.7°, which indicates a hydrophilicity behaviour before the surface grafting. A contact angle of 87.9° was obtained for 3D-printed PEGDA monolith that was grafted with GLYMO, indicating a hydrophobicity characteristic as the contact angle is nearly 90°. On the other hand, there is a significant increase in the contact angle from 87.9° to 149.3° for 3D-printed PEGDA monolith that was grafted with hybrid silane GLYMO-APTMS. Hybrid silane has higher proportion of hydrophobic organic functional groups, thus reduces the surface energy and provide stronger hydrophobic properties (Nambafu, Kim and Kim, 2022). The non-hydrolysable alkyl groups (-CH_3) that serve as end groups in alkoxysilane-functionalised PEGDA precursors has replaced the -H and the -OH on the substrate surface after the surface grafting process,

increases the surface hydrophobicity (Nambafu, Kim and Kim, 2022). Such results obtained are encouraging as a strong hydrophobic surface is desirable in water application.

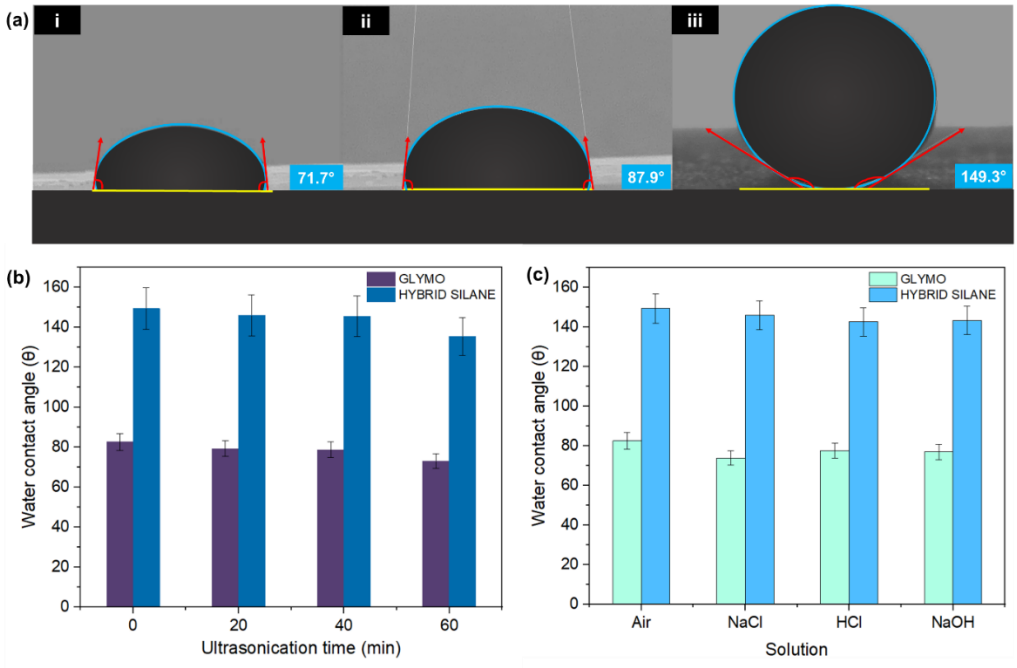


Figure 6.3.8: Water contact angle measurements; (a) 3D-printed PEGDA monolith before surface grafting; (b) Grafted with GLYMO and (c) Grafted with hybrid silane agent GLYMO – APTMS. Water contact angle (WCA) measurements of; (a) Ultrasonication time and (b) after 24 h immersion in three different solvents.

Mechanical and chemical stability of the surface grafting are the two important requirements for the 3D-printed PEGDA monolith to be used for wastewater application. Ultrasonic tests were carried out to assess the mechanical stability of the surface grafting. The difference in water contact angle before and after sonication testing is depicted in Figure 6.3.8b. There are no obvious changes in WCA after sonication of 60 min on both samples, with changes in WCA less than 2%, indicating that the samples exhibit good mechanical stability. To evaluate the chemical stability, both samples are immersed in different solutions. As shown in

Figure 6.3.8c, WCA for both samples decreases slightly after 24 h of immersion but remains above 80° for GLYMO grafted samples and 140° for hybrid silane GLYMO-APTMS grafted samples, suggesting that both samples have excellent chemical stability and can be used in harsh water environments.

6.3.7 Comparison with other studies

The comparison of the mechanical properties based on the materials for water application were made as shown in Table 6.3.6. The obtained results were comparable with other works without taking into consideration testing method and optimisation conditions. By comparing conventional methods and 3D printing, this technology has achieved excellent mechanical properties by looking at the tensile strength and Young's modulus. This is because by introducing chemically crosslinkable groups such as monomer, in this case, HDDA and BDDA into the chains of the precursor can improve their mechanical properties (Qiu, Hamilton and Temenoff, 2011). Moreover, this technology can be considered green as it uses biopolymer-based materials. Adding the monomers has greatly aided in improving the properties of biopolymers by fine-tuning them to be suitable for specific applications. Monomer materials have been critical in revolutionizing polymer technology to achieve a specific application. This demonstrated the feasibility and potential of the current synthesis approach for fabricating 3D-printed monolith for wastewater application with superior mechanical properties.

Table 6.3.6**:** Comparison of the mechanical properties of the materials for 3D printing and conventional method in water application.

Method	Printing method	Material	Mechanical properties (MPa)			Water application	Ref.
			Storage modulus	Tensile strength	Young's modulus		
Conventional	-	Poly (vinylidene fluoride	-	27.9	0.05 to 0.2	Membrane (Oil/Water separation)	(Ji *et al.*, 2021)
	-	Poly (vinylidene fluoride	-	50.0	-	Membrane (Oil/Water separation)	(Liang *et al.*, 2019)
	-	Polylactic acid/ carbon nanotube	-	4.75	-	Membrane (Oil/Water separation)	(Qin *et al.*, 2020)
	-	Chitosan/nanocellulose				Thin-film Membrane	(Mao *et al.*, 2019)
	MEX	Sodium alginate/ gelatin/ Cu-BTC nanoparticle	-	0.4	1.79 – 2.62	Adsorption	(Pei *et al.*, 2020)
3D printing	PBF	Polyamide-12	-	4.7	-	Membrane (Oil/Water separation	(Yuan *et al.*, 2020)
	PBF	Polysulfone	-	17.3	-	Membrane (Oil/Water separation)	(Yuan *et al.*, 2017)

	VPP	Clear resin (Formlabs)	-	101.1	-	Membrane (Oil/Water separation)	(Song *et al.*, 2020)
	VPP	PEGDA and plant-based commercial resin (Magma)	427.73	1.34	-	Monolith (Adsorption)	(Husna *et al.*, 2022)
	VPP	Silane functionalised with GLYMO PEGDA/HDDA	471.36	15.41	601.78	Monolith (Adsorption)	This study

6.4 Conclusion

In the present work, a novel biopolymer-based resin consisting of PEGDA mixed with plant-based commercial resin and the addition of a comonomer has been synthesised and printed by vat polymerization (VPP) technology to achieve 3D printing successfully, broadening the range of green materials that can be used in 3D printing for wastewater application. Apart from that, the materials were further enhanced by surface functionalisation via surface grafting using a silane coupling agent to improve the hydrophobicity of the printed parts. This work systematically investigated the viscoelastic properties, mechanical and thermal behaviour of VPP-printed parts with different HDDA and BDDA contents. Then, after surface grafting with different silane coupling agents, its moisture absorption behaviour, surface wetting, mechanical and chemical stability were further analysed for its practicality to be used

in water application. Adding comonomers such as BDDA and HDDA has greatly affected the mechanical properties of the 3D-printed monolith. Increasing HDDA content has effectively improved the Young's modulus, elongation at break, and tensile strength. In contrast, BDDA has increased the storage modulus more than HDDA. Both comonomers do not have a significant impact on the thermal properties. For the wastewater application, water technology requires a more stiff and tough material to increase its lifespan. Based on these results, PEGDA/HDDA3 resin formulation is the best candidate to be further explored in 3D-printed monolith. Moreover, the 3D-printed monolith was further treated by surface grafting with 2 different silane coupling agents: single grafting with GLYMO and hybrid GLYMO-APTMS. Silane grafted with GLYMO-APTMS has enhanced the hydrophobicity with a surface contact angle of 149.3° and reduced moisture absorption content. However, excessive grafting has caused the truss of the monolithic crack. On the other hand, silane grafted with GLYMO can achieve a hydrophobic surface and has the ability to reduce the moisture absorption without compromising the inner crack of the monolith. The 3D-printed monolith functionalised with silane grafted GLYMO also achieved Young's modulus and tensile strength (UTS) of 601.78MPa and 9.34×10^6 MPa respectively. This has shown that this material is the best candidate as a biopolymer to be developed as green water technology. Nevertheless, several aspects still require in-depth investigations to enhance the current results. This includes studying the grafting density to increase the surface wetting of the materials, the influence of the aging temperature on the moisture

absorption content, and its lifespan in the water environment. This research has demonstrated the potential of exploring a robust approach of synthesising biopolymer-based resin and incorporating it with surface grafting as a new method to develop green and sustainable technology for wastewater application.

CHAPTER 7: EFFECT OF ELECTRON BEAM IRRADIATION ON SILANE - GRAFTED NANOCHITOSAN OF 3D - PRINTED MONOLITH ADSORBENT FOR COLOUR REMOVAL IN TEXTILE WASTEWATER TREATMENT

This chapter covers the application of electron beam irradiation on silane – grafted nanochitosan of 3D-printed monolith to improve the adsorption performance and reduce the reaction time. Different electron beam dosages were applied and the effect on the surface morphology, mechanical properties and adsorption performance were further analysed.

ABSTRACT

The utilisation of 3D printing technology has brought about diverse advancements in various industries including in wastewater treatment. 3D printing has garnered considerable attention owing to its affordability, user-friendliness, and ability to manufacture complex structures rapidly with minimum wastage which supports sustainability mission. In this work, the influence of electron beam (be) irradiation treatment at different doses (50cGy, 100cGy and 200cGy) on the silane - grafted nanochitosan of 3D-printed monolith for the adsorption performance in a batch process was investigated. The highest removal efficiency of 96% with the adsorption capacity of 12.2 $\pm$ 0.7 mg/g were achieved within 80 min by utilising 200cGy. Several characterisation examinations were conducted to obtain a comprehensive understanding of the surface morphology and topology, chemical structure, and elemental compositions of the silane - grafted nanochitosan. The result of characterisation study revealed that, with the increase in electron beam irradiation, the roughness of the surface changed which enhanced the adsorption performance for wastewater treatment. This research endeavour has the potential to pique further investigation for the application of surface modification on surface functionalised 3D printing, particularly with regard to the achievement of sustainable water remediation.

Keywords: 3D printing; nanochitosan; electron beam; surface modification; textile wastewater treatment

7.1 Introduction

The textile industry generates large amounts of wastewater effluent due to its extensive utilisation of water in the various stages including in the dyeing bleaching and mercerizing process (Mondal, Baksi and Bose, 2016) . Wastewater from printing and dyeing units is frequently coloured, containing residues of dye colour pigments (i.e., synthetic, reactive dyes), and high levels of dissolved solids, metals and salts which are challenging to be treated (Al-Tohamy *et al.*, 2022). The presence of these pollutants in the effluent for extended periods of time causes major health concerns and affects the aquatic plant photosynthetic activity (Dutta and Bhattacharjee, 2022).

A combination of physical, chemical, and biological processes is commonly employed to treat the textile wastewater in meeting the standard discharge. The physical or physicochemical treatment with Adsorption has emerged as a viable option for the many treatments discussed in the literature, owing to its ease of use and high effectiveness. It has encouraged researchers to investigate new adsorbent materials that might be used to combat water pollution. Chitosan, a biopolymer, has received much interest as a substrate for adsorbent material synthesis due to its numerous hydroxyl (-OH) and primary amine ($-NH_2$) groups and these groups act as dynamic adsorption sites, making it as an efficient adsorbent (Wan Ngah, Teong and Hanafiah, 2011; da Silva Alves *et al.*, 2021).

Chitosan is a polysaccharide that has been deacetylated and is generated from chitin and found mostly in crustacean shells as well as

the cell walls of some insects and fungi (Limchoowong *et al.*, 2016). Chitosan has emerged as a viable material due to its extraordinary features, which include biodegradability, biocompatibility, and antibacterial activity (Liakos *et al.*, 2021). Furthermore, because it is cationic, it can interact with other molecules, increasing its adsorption capability. The presence of amino and hydroxyl groups in the structure of chitosan allows for chemical modification to increase its solubility and electric charge, making it a more viable material for a variety of applications such as in pharmaceutical, surgical, tissue engineering and wastewater treatment. Despite its numerous benefits, the chitosan has several intrinsic limits. It is known to have the issue of recovery and regeneration as commonly chitosan comes in the form of powder or flakes (Wani, Masoodi and Akhter, 2021).

Several ways have been investigated to overcome this limitation, including integrating chitosan with 3D printing approach. 3D-printed chitosan-based adsorbent is novel approach which have yielded excellent results in resolving the constraints of chitosan, opening the path for their broader application in wastewater treatment. For instance, Wang *et al.* (2023) developed 3D-printed filter for heavy metal removal where a mixed solution of chitosan and hydroxyapatite was injected into a 3D-printed polylactic acid (PLA) monolith, and subsequently freeze-dried. In a cyclic adsorption experiment, the monolithic PLA@CS/HAP filters displayed outstanding effectiveness in the removal of copper ions, with 90% of copper ions efficiently removed during within 2 h. In terms of its recyclability and reusability, the adsorption capacity reduced just

marginally from 98.9% to 97.17% over 5 adsorption-desorption cycles indicating it is stable to be used for practical applications. Further to this, we have developed a robust technique by integrating 3D printing and surface functionalisation method to graft chitosan using silane coupling agent onto the 3D-printed PEGDA monolith. The silane-grafted chitosan of 3D-printed monolith has shown a remarkable adsorption performance of 90.4% within 2 h for removal of methyl orange dye (Husna *et al.*, 2022). This robust technique can reduce by-product waste produced while maintaining wastewater treatment efficacy. In another study, we have optimised the design of the silane-grafted chitosan of 3D-printed monolith as the structural topology can influence the adsorption performance. The findings revealed that the body-centred cubic (BCC) configuration displayed the greatest capacity for adsorbing MO along with the highest level of permeability (2.57×10^{-7} m^2) and surface area (39.84 mm^2) (Yusoff *et al.*, 2023). However, both studies showed that the equilibrium adsorption was achieved after 2 h, which can be further reduced to meet the industrial requirements.

Increasing surface roughness and changing the size of particles to nano size are one of the many ways to enhance the adsorption performance (Niu *et al.*, 2016). This can be done through surface modification via electron beam irradiation treatment (Kurbanova *et al.*, 2023). The use of radiation treatment to improve the surface or near-surface properties has various benefits over traditional methods. Firstly, the reaction may be started at room temperature and may not require the presence of crosslinking agents in some circumstances. Second, the procedure is

quite simple and easy to control during the process. UV-induced surface photo-crosslinking is one such method for photochemically crosslinking biopolymers. Electron beam (EB) irradiation is another approach for catalytic surface functionalisation and polymer surface changes, resulting in a more robust matrix and a less permeable polymer. Because of its quick performance, the EB irradiation procedure is considered inexpensive. High-energy EB irradiation of a polymeric chain causes ionization and excitation, which leads to the generation of radicals through hydrogen and hydroxyl abstractions. EB irradiation causes the development of reactive species in a polymer, including radical, peroxide, and ionic species. Furthermore, the irradiation dose may be simply adjusted. It should be emphasised that the absorbed dosage influences the crosslinking density, which depends on the irradiation period for radiation-based procedures. The strength of the irradiation determines the final molecule size. Specifically, the polymer chains may undergo crosslinking, resulting in more giant molecules, or degradation, resulting in smaller fractions. Due to its high penetrating ability, ionising radiation holds the potential to instigate chemical reactions in either solid or liquid states (Crini *et al.*, 2019). For instance, electron beam irradiation has been used in the process of chitosan gel synthesis. Piatkowski *et al.* (2017) discovered a unique microwave-irradiated process for generating multifunctional chitosan hydrogels with no waste and no crosslinking agent. The hydrogels developed were biodegradable bifunctional polymers with both negative and positive surface charges. Furthermore, these hydrogels demonstrated exceptional water absorption and the

ability to remove various water pollutants, making them intriguing materials for environmental applications. The findings of the study open up a new avenue for the creation of multifunctional hydrogels with environmental advantages. In another study, Czechowska-Biskup *et al.* (2016) formulated chitosan-based gels by irradiating them using electron beams at lower doses (i.e., 25kGy) and to some extend as low as 200Gy. Despite the partial degradation of polymer chains during irradiation, the utilisation of ionising radiation has been deemed expedient by the authors in the synthesis of chitosan-based hydrogels, with potential uses not only in biomedicine but also in water and wastewater treatment.

Based on the previously published findings on the electron beam irradiation treatment, there has yet to be any examination of the effects of EB irradiation on the physicomechanical and structural aspects of nanochitosan. In the present investigation, we scrutinised the influence of electron beam (EB) on the efficacious properties of silane - grafted nanochitosan of the 3D-printed monolith at different irradiation doses. The primary aims of this study were to assess the impact of EB irradiation on the functional properties, including surface roughness, mechanical characteristics, and structural attributes in coherence with the crystalline pattern and morphological features of silane – grafted nanochitosan. Subsequently, this research investigated the influence of EB irradiation treatment on the silane – grafted nanochitosan of 3D-printed monolith on the adsorption performance with methyl orange (MO) dye in a batch process. The primary objective of this study is to incite innovative research methodology in the domain of wastewater treatment, with a

particular focus on the efficacy and practicability of 3D printing technology. Section 7.2 of this work will expound upon the materials and methods employed, subsequently followed by an elaborate discourse on the results and discussion section. Finally, the experimental work was concluded with a concise conclusion.

7.2 Experimental

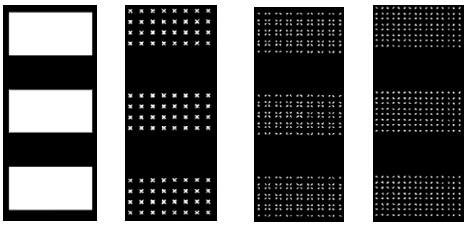
7.2.1 Materials

Chitosan (CS) white powder (AR grade; degree of deacetylation of 99 %, MW: average of 890,000 g/mol) was purchased from Fulltime Asia Sdn. Bhd. Hydrochloric acid (HCl) (37 %, MW:36.46 g/mol) and 2-propanol (IPA) (AR grade, MW: 60.1 g/mol) were purchased from R&M Chemicals. Sodium hydroxide (NaOH) (reagent grade, ≥98%, pellets (anhydrous)), Glycidyloxypropyl trimethoxysilane (GPTMS) (≥98 %, MW: 236.34 g/mol) and 1,6-Hexanediol diacrylate (HDDA) (80 %, MW:226.27 g/mol, density:1.01 g/mL at 25 °C) were purchased from Sigma-Aldrich, USA. Poly (ethylene glycol) diacrylate (PEG200DA) (MW PEG Block= 200; n=4, viscosity: 25 cP at 25 ℃) was purchased from Ryoji, China. Acrylate Magma plant-based resin (≥ 99.9 %, MW: 308 g/mol, viscosity: 10 – 30 cP at 25℃) was purchased from 3D Gadgets Malaysia. Phenylbis (2,4,6-trimethyl benzoyl) phosphine oxide; Irgacure 819(MW: 418.5 g/mol) and methyl orange dye (MO) ACS reagent (85 %, MW: 327.34 g/mol, pKa = 3.4) were purchased from Chemmart Asia Sdn. Bhd. All chemical substances were utilised in their initial state without any additional refinement unless it was explicitly stated otherwise.

7.2.2 3D-printed monolithic structure fabrication

3D-printed monolith was prepared as previously described in our previous work (Husna *et al.*, 2022). Figure 7.2.1a showed a custom photopolymerisable resin that was formulated using poly (ethylene glycol) diacrylate (MW PEG Block = 200) as the monomer, 1% (w/w) phenylbis(2,4,6-trimethylbenzoyl) phosphine oxide (Irgacure 819) as the photoinitiator, and a plant-based photopolymer resin. To accomplish fast printing and great accuracy in the printed parts, 3 wt.% of HDDA with strong photopolymerisation reactivity was added. The formulated liquid resin was well stirred for 30 minutes with a magnetic stirrer (Thermo Fisher Scientific, United States) and stored in a dark brown bottle to avoid light exposure because this formulation is sensitive to UV radiation. Phrozen Sonic Mini 3D printer with digital light processing (DLP) was chosen and utilised for additive manufacturing.

Table 7.2.1: 3D printing specifications for the monolithic structure design.

Parameters	**Values**	**Overall printed layers**
Layer thickness	0.05 mm	Total printing layers: 100
Normal exposure time	4 s	10 layers 25 layers 50 layers 75 layers 
Bottom exposure time	40 s	
Resting time	1 s	
Bottom layers	8	

7.2.3 Synthesis of nanochitosan

The nanochitosan solution by means of physical method with some modification was prepared as described by Chen (2010). Briefly, 2 wt.% of chitosan was dissolved in 2 wt.% of acetic acid and stirred for 24h

under vigorous conditions. The samples were then stored in the amber bottle for further use.

7.2.4 Surface functionalisation of silane - grafted nanochitosan and irradiation process

The surface grafting of silane coupling agent followed the modified the process as described by Lou *et al.* (2014), as indicated in the schematic design in Figure 7.2.1b. The printed monolith was submerged in a 1:1 volume ratio GPTMS/ethanol solution for 30 min. After that, the support was oven dried for 4 h at 110 ℃ . Then, the chitosan growth technique was then carried out by dipping the sample into the nanochitosan solution, as shown in Figure 7.2.1b and leaving it in the oven at 60℃ for 4 h. The steps were repeated for 3 layers of coating. After that, the sample was washed with deionised water to remove any remaining contaminants and polymer on the surface.

Following surface grafting, the batch of the samples are irradiated under the treatment field size of 20×20 cm^2 with the setting of 50MU(1cGy/MU) by using energy of 6 MeV electron beam with dose rate of 400MU/min as depicted in Figure 7.2.1c. Penetration depth of 6MeV electron is 1.2 cm with the surface samples. Untreated silane - grafted nanochitosan samples were repeatedly treated in the presence of air to achieve the appropriate cumulated dosages of 100 or 200 cGy. All the treated samples were kept in the desiccator for further analysis.

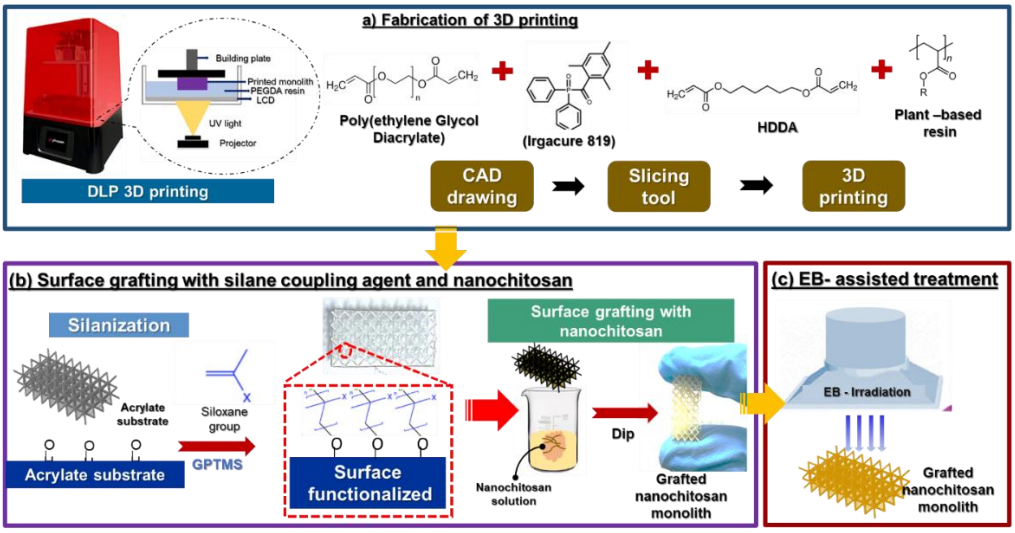


Figure 7.2.1: Schematic diagram preparation of electron beam assisted silane – grafted nanochitosan of 3D-printed monolith.

7.2.5 Characterisation analysis

The present study utilised a field-emission scanning electron microscope (FESEM, FEI Quanta 400 F, USA) to examine the surface morphology at different magnifications ranging from 90 to 3000x and voltage of 10 kV. Prior to imaging, the sample underwent gold coating via a rotary pumped coater (Quorum, 150 A S Plus, UK) at a deposition rate of 6 nm/min and current of 20 mA. The elemental composition of the grafted nanochitosan monolith using an energy-dispersive X-ray analyzer (EDX). Perkin Elmer Frontier (FT Mid-IR/Far-IR) spectrometer with a wavenumber range of 4000-400 cm^{-1} and a resolution of 1 cm^{-1}, was used to acquire Fourier transform infrared (FTIR) spectra before and after the grafting technique to assess the possible influence of the electron beam on the grafted nanochitosan at triplicates at five distinct places. FTIR analysis was carried out to determine the molecular changes in chitosan caused by e-beam irradiation and to compute the degree of deacetylation (DD%) by using the following Equation (43).

$$Degree\ of\ deacytelation\ (DD\%) = 100 - \frac{A_{1655}}{A_{2870}} \times \frac{100}{1.33} \quad (43)$$

Where A_{1655} is associated with the determination for the residual of -CO-NH- groups whereas A_{2870} is related to the reference band of -CH at 2880 cm^{-1}. The benefit of using this reference band is that the peak intensity is considerable, the band is not engaged in the hydrogen bond, and water does not cause any interference peaks (Kasaai, 2008).

Apart from that, X-ray photoelectron spectroscopy (XPS) (Kratos Axis Ultra DLD, United Kingdom) facilitated the determination of the binding energy, chemical composition and bonding type of the 3D-printed PEGDA monolith and silane - grafted nanochitosan at monochromatic Al Kα (1486.6eV) x-rays in ultra-high vacuum (UHV) conditions. Atomic Force Microscopy (AFM, Park Systems NX-10, Korea) was used to evaluate the surface roughness profile of electron beam treated of grafted nanochitosan at different dosage. The crystal structures of the nanochitosan were examined using high-resolution X-ray diffraction (XRD) on an Panalytical powder diffractometer XRD system (X′Pert Pro, Netherlands) under the operating parameters of Cu K α X-rays at 45 kV and 40 mA, with a scanning rate of 0.02°/s.

7.2.6 Batch adsorption studies

The batch adsorption experiments required a set volume of 50 mL for the MO dye solutions, which were constantly stirred in the incubator shaker for 2 h at 150 rpm (N). The efficacy of silane - grafted nanochitosan of 3D-printed monolith treated at different EB dosage was assessed until it reached equilibrium time. The concentration of all MO solution samples was analysed at 30 min intervals through UV-Vis spectrophotometer

(Perkin Elmer Lambda 35, United States) at a fixed wavelength of 564 nm, which is closely correlated with the absorbance (Nandini and Vishalakshi, 2012). The removal percentage ($R\%$) and the amount of MO dye adsorbed per unit mass of grafted nanochitosan at equilibrium (q_e, mg/g) were computed using a specific Eq. (44) and (45).

$$R\% = \frac{C_o - C_t}{C_o} \times 100\% \quad (44)$$

$$q_e = \frac{(C_0 - C_t)V}{m} \quad (45)$$

where C_o, C_t, V and m signify the initial MO dye concentration (ppm), the MO concentration at time t (ppm), the volume of the MO dye solution (L), and the mass of grafted nanochitosan (g) utilised.

7.2.7 Mechanical properties and stability

The mechanical characteristics of the grafted chitosan were determined using a texture analyser (TX-XT Plus Stable Micro Systems, USA), at a crosshead speed of 1 mm/min and a maximum load of 30 N load cell. The initial elastic slope of the stress-strain curve was used to calculate the Young's modulus whereas the peak of the curve was denoted as the ultimate tensile strength of the sample. Furthermore, the Perkin Elmer dynamic mechanical thermal analyzer (PE-DMTA, USA) was used to calculate the storage and loss modulus E′ of the monolith before and after grafted with nanochitosan with different electron beam dosage. The studies were conducted in single cantilever mode at temperature ranging from 20 to 150 ℃, with a heating rate of 10 ℃/min and a frequency of 1 Hz.

The mechanical stability of the 3D-printed monolith was further verified based on the degradation study, where mass before and after adsorption

was measured triplicates and the mean value error of the mean was calculated using Eq. (46).

$$M\% = \frac{M_o - M_f}{M_o} \times 100\% \quad (46)$$

Where M_o and M_f is the mass of grafted nanochitosan before and after adsorption in g.

7.3 Result and discussion

7.3.1 Characterisation

FESEM analysis was used to investigate the changes in surface morphology of silane - grafted nanochitosan onto 3D-printed PEGDA monolith before and after EB treatment with different dosages with magnification factors of x300 and x3000. As seen in Figure 7.3.1a(i) and enlarged segments of the monolith (Figure 7.3.1a(ii)), the initial surface of the PEGDA chitosan has wrinkled structures and big swelling pockets. On the other hand, it can be seen that the as the dose of the EB increases, the grafted surface becomes rougher and has a ragged look, indicating that the EB treatment has impacted the surface roughness on the grafted materials. It is worth noting that as depicted from Figure 7.3.1b(iii) to Figure 7.3.1d(iii), the EB treatment creates some pulling and folding effect at the monolith wall, which increase the surface area for better adsorption. The rough surface of the structures increases the contact point of dye molecules and facilitates their transfer to the depth of the network structure, resulting in increased adsorption capacity.

The EDX spectra were utilised to examine the quantitative elemental composition of 3D-printed PEGDA and silane – grafted nanochitosan monolith before and after adsorption. The findings from Table 7.3.1

indicates that the 3D-printed PEGDA monolith comprises elements C and O. In contrast, elements N and Si signify the practical application of the silane – grafted nanochitosan. It was observed that the composition of N was reduced from 42.9 to 2.57 wt.% after the adsorption, which indicates that N atom associated with chitosan is interacted with the adsorbate during the adsorption process. The electrostatic interaction between the positively charged amine groups ($-NH_3^+$) of chitosan and the negatively charged of MO dye is the key mechanism driving this adsorption process (Alyasi, Mackey and McKay, 2023). Further to this, the detection of the existence of the S element in the EDX spectrum, which is an intrinsic chemical composition of MO dye, further verified the successful adsorption of MO dye.

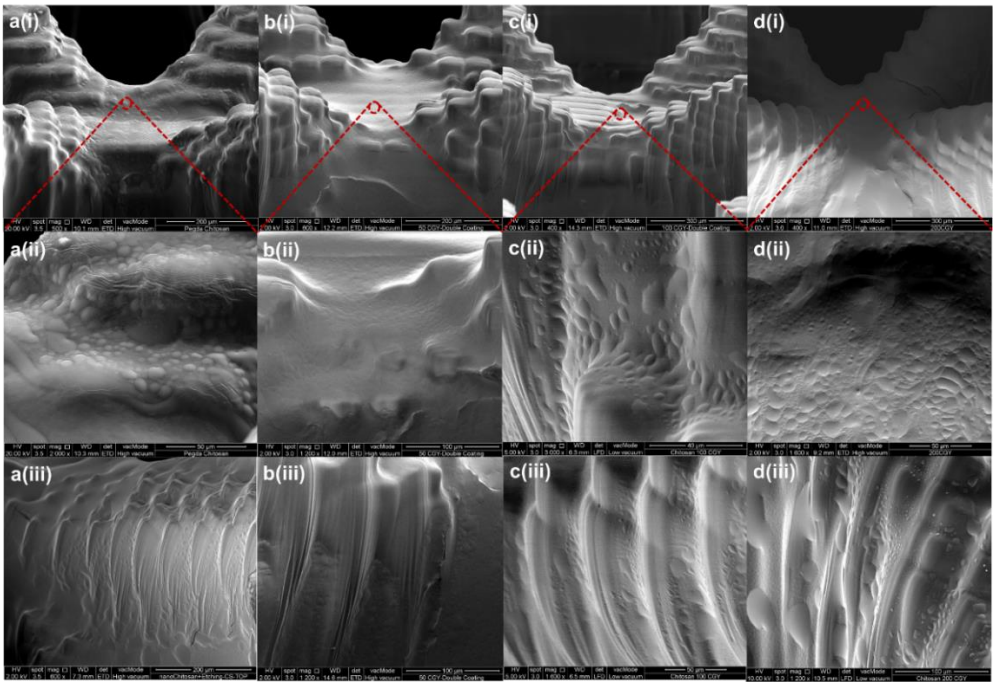


Figure 7.3.1: FESEM of the grafted-nanochitosan 3D-printed PEGDA monolith;(a) before EB treatment; after EB treatment at (b) 50cGy; (c) 100cGy and (d) 200cGy.

Table 7.3.1: Elemental weight composition of 3D-printed PEGDA monolith before and after adsorption from EDX analysis.

Sample	Elemental weight (%)				
	C	O	N	Si	S
3D-printed PEGDA monolith	56.8	41.3	0	1.92	0
Before adsorption	44.3	10.9	42.9	1.90	0
After adsorption	54.1	41.3	2.57	1.34	0.70

The AFM images depicted smooth and nanochitosan surfaces can be observed in Figure 7.3.2. It can be observed that the topographic profile of the silane-grafted nanochitosan of 3D-printed monolith before and after EB treatment covers a wider range of depth in comparison to that of the 3D-printed PEGDA monolith. Moreover, for better comparison, the root means squared roughness (Rq), which is a measure of deviations in the surface from the mean plane of the sample, and arithmetic roughness (Ra), were analysed based on the AFM results as shown in Table 7.3.2 . Rq serves as an indicator of variations in the surface compared to the average plane of the specimen, whereas Ra represents the overall average roughness relative to the reference length (Liu *et al.*, 2011; Kumru *et al.*, 2019). The value root mean squared roughness and arithmetic roughness of PEGDA photocured resin before grafting with nanochitosan are 0.112μm and 0.0814μm respectively. After grafting with nanochitosan, the value of root mean squared roughness and arithmetic roughness increased to 0.211 μm and 0.141 $\mu m.$ It is worth noting that after the samples of silane - grafted nanochitosan irradiated with electron beam at different doses, the value of root mean squared

roughness increases in between range of 0.377 to 0.847 whereas the value of arithmetic roughness increases from 0.178 to 0.424. This is because the influence of electron beam irradiation on the surface morphology of polymers and biomass materials is a common effect, with surface roughness rising monotonically as irradiation doses increase. This pattern is ascribed to the formation of cracks and free radicals on the surface as a result of the irradiation (Su *et al.*, 2020). Therefore, it can be inferred that the surface roughness increased after being bombarded with different dosages. The effect of electron beam treatment on the adsorption performance for dye removal was further investigated in Section 7.3.2.

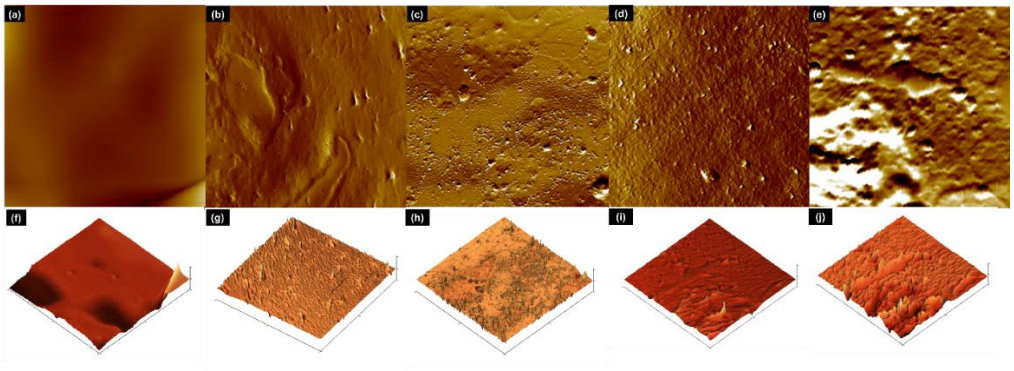


Figure 7.3.2: AFM images in 2D and 3D view of; (a,f) 3D-printed PEGDA, (b,g) silane-grafted nanochitosan before EB treatment, silane-grafted nanochitosan at (c,h) 50cGy, (d,i) 100 cGy and (e,j) 200 cGy.

Table 7.3.2: Root mean squared roughness and arithmetic roughness of 3D printed samples.

Sample	Rq	Ra
	μm	μm
3D-printed PEGDA monolith	0.112	0.0814
Nanochitosan	0.211	0.141
50 cGy	0.377	0.178
100 cGy	0.594	0.259
200 cGy	0.847	0.424

The results of the FTIR analysis on nanochitosan, as depicted in Figure 7.3.3a, were found to be consistent with previously published spectra of chitosan (Ayodele *et al.*, 2018; Luthfiyana *et al.*, 2022). The -NH and -OH groups were observed in the FTIR spectra of nanochitosan powder at a wavenumber of 3437 cm^{-1}, the -CH group at a wavenumber of 2950 cm^{-1}, the -CO functional group at a wavenumber of 1643 cm^{-1} and $-CH_2$ group at a wavenumber of 1388 cm^{-1}. Based on FTIR spectra of PEGDA, there is a sharp and broad peak at 1095 cm^{-1} attributed to -COC functional group, which disappeared when grafted with nanochitosan, indicating that the success of surface grafting onto the photocured PEGDA resin. The locations of the characteristic bands of chitosan are almost similar in the FTIR spectra of both non-irradiated and irradiated nanochitosan. Therefore, although some alterations might be seen, the development of new groups was not detected as a result of irradiation. Furthermore, the decline in glycosidic bond linkage, in between bands at 1150 and 900 cm^{-1}, indicated that there is molecular chain scission occurred in nanochitosan for all irradiation doses. Moreover, the formation of new peaks in at, 690 cm^{-1}, 930 cm^{-1} and 1030 cm^{-1} which corresponding to –CH stretching vibrations revealed the presence of benzene ring in the MO dye (Kalyani *et al.*, 2009). Additionally, a peak is observed at 817 cm^{-1}, indicative of –CH stretching vibrations in a di-substituted benzene ring. Moreover, the confirmation of sulfonic nature of the MO is verified by the peak observed at 1110 cm^{-1} that corresponds to the –S=O stretching vibrations. The -CN stretching produced a tiny

peak at 1180 cm^{-1}, further confirming the MO dye (Shen *et al.*, 2015). All the peaks confirmed that the MO dye was adsorbed onto the nanochitosan layer for all EB samples.

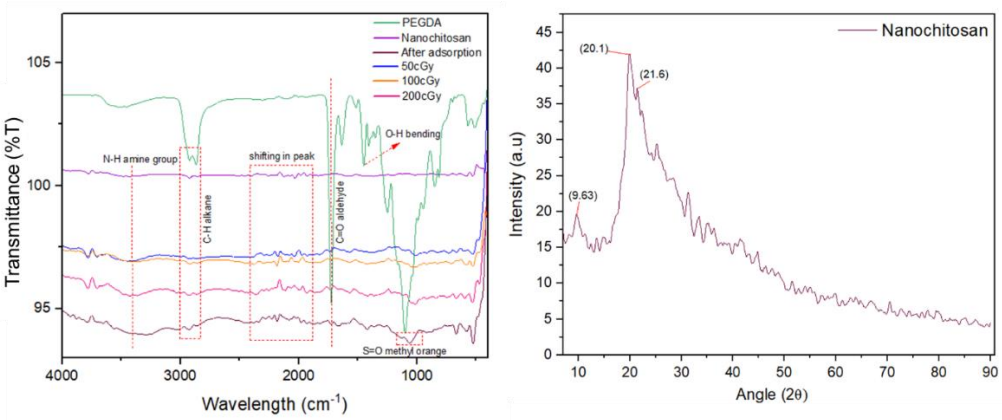


Figure 7.3.3: (a) FTIR spectra of photocured PEGDA resin, grafted-nanochitosan before and after EB treatment, and grafted-nanochitosan after adsorption. (b) XRD spectra of nanochitosan.

The XRD pattern acquired for nanochitosan are displayed in Figure 7.3.3b. The nanochitosan displayed a characteristic crystalline peak at 2θ = 20.1°, which was slightly shifted to a higher diffraction angle. Moreover, the peaks around 9.63° and 20.1° are associated with crystal-I and crystal-II in the structure of chitosan, and both of these peaks indicate that the produced chitosan has a high degree of crystallinity, revealing a typical identification for semi-crystalline chitosan (Dey *et al.*, 2016; Anand *et al.*, 2018).

The chemical bonding and elemental composition of grafted nanochitosan before and after surface grafting was explored further using XPS, as shown in Figure 7.3.4. The elemental spectra of the photocured PEGDA monolith revealed the presence of C and O, while the addition of Si and N was observed following grafting with

glycidyloxypropyltrimethoxysilane (GLYMO) and nanochitosan, as depicted in the result Figure 7.3.4. The chemical bonding state of a material is often studied through the energy levels of its orbitals. Furthermore, by analyzing C1s, O1s, and Si 2p spectra with high resolution, further information about the chemical binding state can be observed. As observed in Figure 7.3.4a and b, the spectrum of the PEGDA acrylate-based substrate can be detected at three parts: a strong signal attributed to C-C/C-H peaks at 284.6 eV, a C-O peak at 286.5 eV, and a C=O peak at 288.0 eV. All of these peaks correspond to the PEGDA acrylate substrate. It is worth noting that the Si 2p core level spectrum at peak 99.4 eV, shown in Figure 7.3.4c, represents a Si element of a silane-grafted monolith. The energy levels of Si 2p orbital can be observed as peaks after reacting with a coupling agent that contains GLYMO as depicted in Figure 7.3.4d. The proportion of silicon to oxygen is roughly 1:5, confirming the successful formation of epoxy groups on the outside of the 3D-printed structure. Moreover, the detection of chitosan may be determined through the O 1s spectrum, which has been visually illustrated in Figure 7.3.4e. It is important to note that the most pronounced peak observed at 532.3 eV is indicative of the C-O bond of the oxygen polysaccharide backbone. This finding suggests that the presence of nanochitosan can be attributed to the aforementioned bond. As presented in Figure 7.3.4f, another signal at 531.0 eV indicates the existence of an amide group in the acetylated function. The N 1s XPS spectrum has a primary component at 399.5 eV and an associated contribution near 401.5 eV, both of which imply the

presence of non-protonated amine and protonated amine, respectively. All the findings confirmed that the nanochitosan was successfully anchored on the PEGDA substrate.

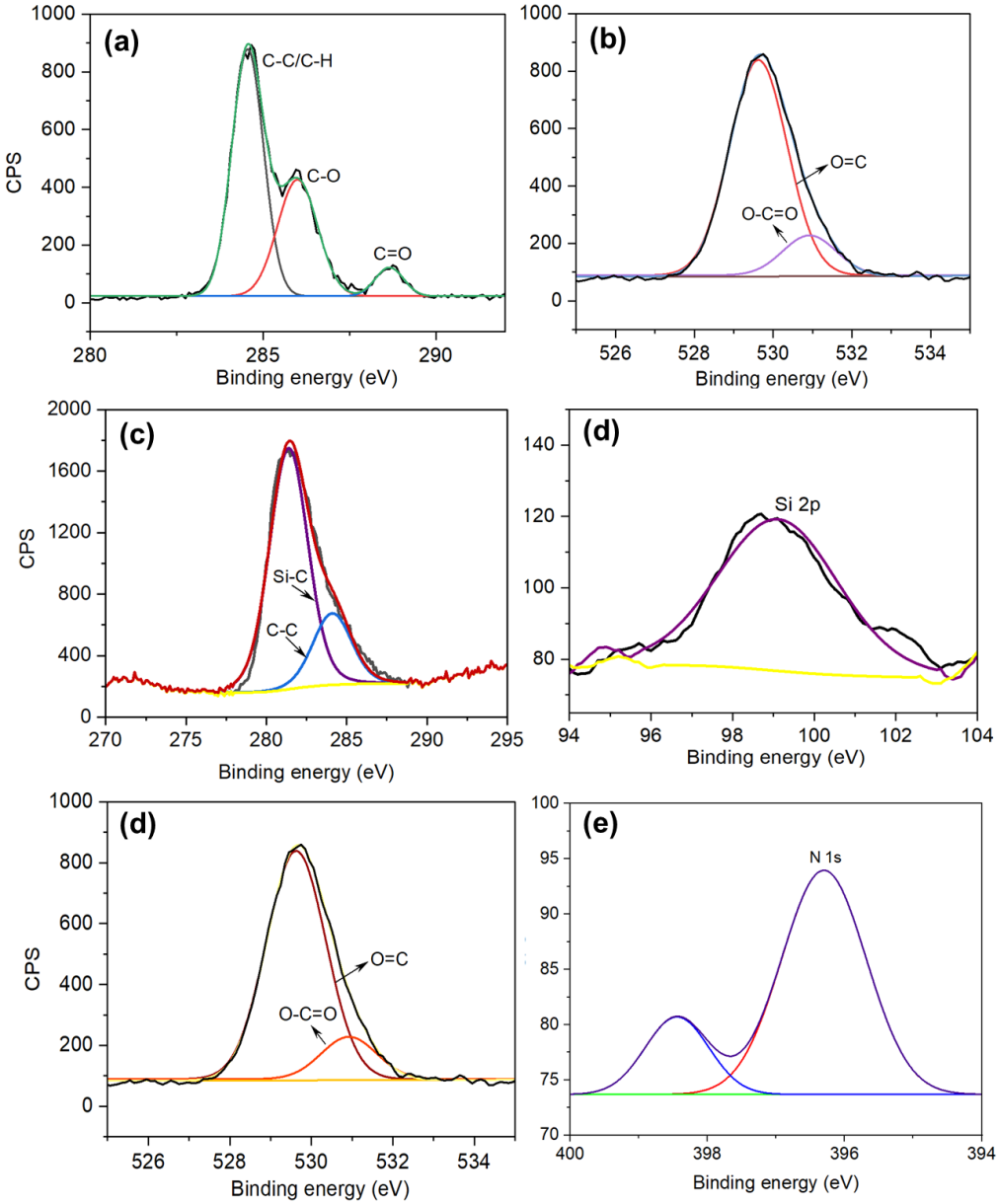


Figure 7.3.4: (a - b) High-resolution XPS spectra peak for C1s in PEGDA monolith, (c - d) Si-C and Si2p high-resolution spectra peaks for GLYMO after surface grafting and (d - e) High resolution spectra for O1s and N1s produced by nanochitosan coated substrate.

7.3.2 Adsorption studies

The effect of electron beam treatment of silane – grafted nanochitosan on the adsorption performance was studied in detail as shown in Figure 7.3.5. There was significant improvement in the removal efficiency when the silane-grafted nano chitosan was subjected to irradiation. The removal efficiency rises with increasing irradiation dosage. It is worth noting that the silane-grafted nanochitosan with 200cGy achieved equilibrium removal efficiency at a shorter time at 80 min as shown in Figure 7.3.5a. In contrast, the non-irradiated sample required 2 h to achieve equilibrium contact time. This finding is in good agreement with the AFM results, as electron beam treatment can increase the surface roughness of the materials. Increasing in the surface roughness might be ascribed to surface oxidation or the loss of organic substances such as gases during sample treatment (Gamboa *et al.*, 2022). The enhancement of surface roughness can lead to better adsorption due to the possibility in the increment of surface area and active sites. Therefore, more MO dye ions can be adsorbed onto the irradiated silane-grafted nanochitosan. From the experimental data, it can be deduced that the 200cGy silane-grafted nanochitosan has showed the highest removal rate, 96% with the adsorption capacity of 12.2 $\pm$ 0.7 mg/g (Figure 7.3.5b). As seen in Figure 7.3.5c, there is inverse trend for the adsorption rate and adsorption capacity of all irradiated samples. As the adsorption capacity increases, the adsorption rate decreases. From the plotted graph, 50 cGy has the lowest adsorption rate of 0.205 $mgg^{-1}s^{-1}$ with adsorption capacity of 4.10 mg/g, whereas the adsorption rate for

100 cGy is 0.239 $mgg^{-1}s^{-1}$ with adsorption capacity of 9.577 mg/g respectively. Further to this, the adsorption rate for 200 cGy is 0.302 $mgg^{-1}s^{-1}$ with adsorption capacity of 6.041 mg/g. The decline in the adsorption rate ($mgg^{-1}s^{-1}$) as the adsorbent capacity increases can be attributed to the division in the flow rate or the difference in concentration between the solute concentration in the solution and that on the surface of the adsorbent, resulting in a reduction in the adsorption rate. Further to this, by comparing all the irradiated - EB amples and non-irradiated sample, it can be concluded that silane-grafted nanochitosan treated with 200cGy has highest adsorption rate indicating that it has high mass transfer which greatly influenced the adsorption efficiency (Yang *et al.*, 2023b).

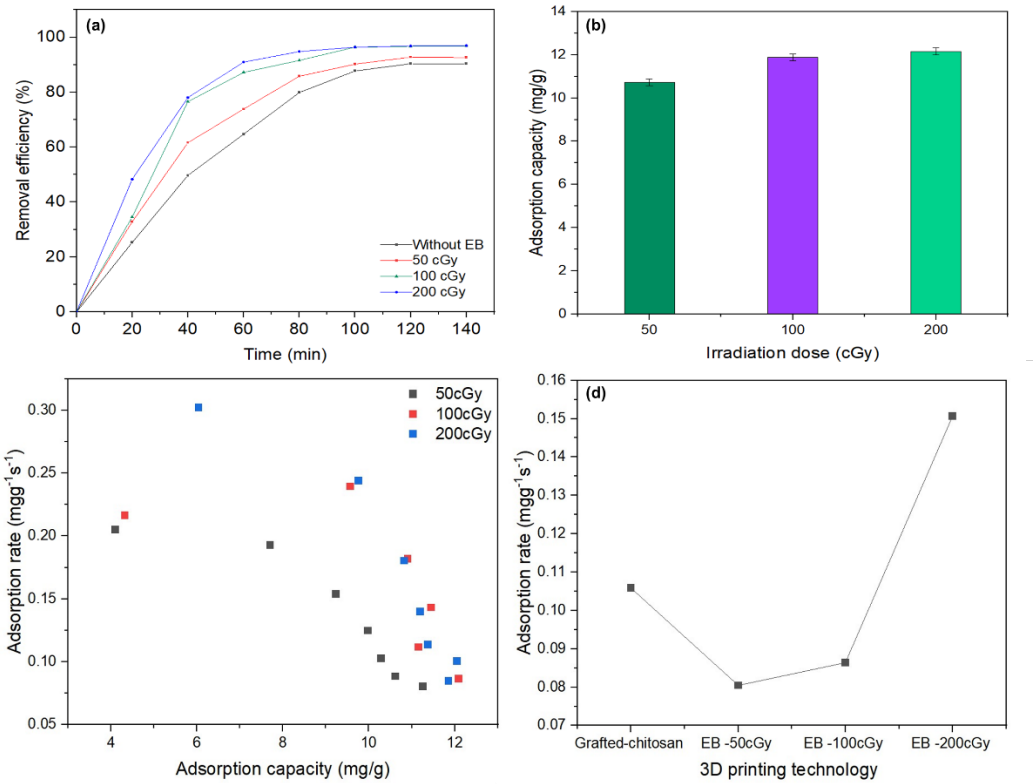


Figure 7.3.5: (a) Removal efficiency rate and (b) Adsorption capacity of silane - grafted nanochitosan for different dosage of electron beam treatment.

Moreover, as reported by Amor *et al.* (2023), the deacetylation degree of chitosan is significant because the adsorption capacity of chitosan increases as the value of deacetylation increases. The deacetylation degree is the metric that ascertains the molar percentage of monomeric glucosamine units present in chitosan, which play important roles in adsorption. As presented in Table 7.3.3, The values of deacetylation degree, which are derived from the area ratio between the amide band and the C–H band (43) as determined by FTIR measurements. These deacetylation degree values were found to be relatively consistent across varying levels of irradiation, with an average value of 85 ± 3 % when accounting for errors. However, it should be noted that a slight decrease in deacetylation degree value was observed as irradiation dose increased, as indicated in Table 7.3.3. This outcome is consistent with existing research on the scission depolymerisation of chitosan proton beam irradiation as well as through γ-irradiation in a solid state. Hence, the functional groups remained unaffected by the free radical attack in irradiated and non-irradiated samples, which were not distributed as the dominant effect on the adsorption performance.

Table 7.3.3: Degree of deacetylation of different dosages electron beam irradiation.

Dose (cGy)	Degree of deacetylation (DD%)
0	86 ± 0.3
50	85 ± 0.6
100	84 ± 0.8
200	84 ± 0.6

7.3.3 Mechanical strength and stability

The mechanical strength and the stability of the silane-grafted nanochitosan with and without irradiation were further examined as this is one of the important parameters for the water technology to be used in real application. As depicted in Table 7.3.4, it is evident that the surface grafting procedure utilsing silane coupling agent as the crosslinker has resulted in a notable enhancement of the mechanical properties of the silane – grafted chitosan of 3D-printed monolith. This is demonstrated by the significant increase in the storage modulus, Young's modulus and ultimate tensile strength values, which highlights a strengthening of the interaction between chitosan and the silane coupling solution. As a result, the grafted-chitosan of 3D-printed monolith exhibits greater stiffness. The fundamental mechanism of the GLYMO and PEGDA substrate can be explained in the following manner. Firstly, upon the modification of the surface of the PEGDA monolith by GLYMO, the alkoxy group in the molecule undergoes hydrolysis to generate silanol. Subsequently, the silanol molecules undergo dehydration and condensation with the hydroxyl group on the PEGDA substrate, forming a chemical bond through cross-linking. Another potential crosslinking reaction is through the epoxy functional group at the terminus of GLYMO, which reacts with the organic matrix via ring-opening reply, thereby stimulating an increase in the crosslink density of the organic phase. Consequently, GPTMS exerts a considerable improvement in the mechanical properties of the PEGDA monolith. However, after the samples were irradiated at different dosages, the mechanical properties of the samples were slightly

decreased with increases in EB dose. This could be caused by molecular chain degradation due to an increase in irradiation dosage, resulted in the formation of shorter polymer chains (Baroudi, García-Payo and Khayet, 2018). As reported by Mastalerz *et al.* (2021), the utilisation of high energy radiation for processing polymers has been documented to bring about alterations in the macromolecular structure through the process of competitive chain scission and cross-linking. However, it is important to note that the dominance of one reaction over the other is largely dependent on the radiation dose. Therefore, it can be inferred that the occurrence of either of these reactions is not only a function of the radiation exposure but also the extent of its effect on the material (Darwis *et al.*, 1998). Moreover, it should be emphasised that the magnitude of these effects may be less obvious, especially at lower radiation doses. Empirical findings have demonstrated that the irradiation process exerts an influence on the crystallinity and structure of the polymers, which could potentially impinge on the rate of biodegradation (Pantani and Sorrentino, 2013). Since the irradiation dose used in this work is particularly very low which is less than 1kGy as compared to other works, the effect on the mechanical properties is not significant.

Table 7.3.4: Mechanical properties of silane-grafted nanochitosan before and after EB treatment.

Mechanical properties	Measurement (MPa)				
	PEGDA monolith	Grafted nanochitosan PEGDA monolith			
		0 cGy	50 cGy	100 cGy	200 cGy
Storage modulus	130	229	225	221	217
Young modulus	0.596	1.13	1.10	1.05	1.03
Ultimate tensile strength	3.08	3.15	3.13	3.12	3.12

The determination of mechanical stability for the silane - grafted nanochitosan of 3D-printed monolith can be examined through the measurement of weight changes before and after adsorption (dried to a constant weight), as demonstrated in Table 7.3.5. The table indicates that the weight loss percentage varies from 0.6 to 0.9%, signifying the chitosan layer remains stable during the adsorption process in water. This aligns with the characterisation analysis, which confirms that the grafted nanochitosan is firmly anchored onto the monolith even after adsorption.

Table 7.3.5: The retention weight of grafted-nanochitosan monoliths before and after MO dye adsorption for different EB dose.

Dose (cGy)	Mass before adsorption (g)	Mass after adsorption (g)	Weight loss (%)
0	0.325 ± 0.04	0.322 ± 0.01	0.923
50	0.317 ± 0.07	0.315 ± 0.02	0.631
100	0.328 ± 0.02	0.325 ± 0.03	0.915
200	0.319 ± 0.08	0.316 ± 0.04	0.940

7.4 Conclusion

In this work, the effect of electron beam irradiation on structural and morphological characteristics of the silane – grafted nanochitosan of 3D-printed monolith was investigated. This innovative method for adsorption for colour removal has enhanced the contact time required to attain equilibrium uptake capacity, while simultaneously eliminating the need for additional post-treatment measures for sample recovery. Moreover, the successful of applying EB irradiation on the silane - grafted nanochitosan coating were validated through a series of characterisation analysis, including FESEM, FTIR, XRD, XPS and AFM. These examinations provided comprehensive insights into the surface morphology, elemental composition, and chemical structure of the silane - grafted nanochitosan grafted on the 3D-printed monolith. The mechanical properties and mechanical stability of the silane – grafted nanochitosan at different EB dosages were enhanced through the surface grafting technique. The results showed that the application EB irradiation did not significantly affect the mechanical properties of the silane – grafted nanochitosan of 3D-printed monolith as the EB dose applied is lower than 1 kGy. Further to this, 200cGy silane-grafted nanochitosan has showed the highest adsorption removal rate, 96% with the adsorption capacity of 12.2 ± 0.7 mg/g. It was found that the silane - grafted nanochitosan of 3D-printed monolith exhibits excellent mechanical stability as no significant mass loss, indicating nanochitosan is firmly anchored onto the monolith. Thus, it can be concluded that with the help of EB irradiation for surface modification, the modified silane -

grafted nanochitosan can improve the adsorption efficiency for the wastewater treatment application.

CHAPTER 8: IDENTIFICATION AND CLASSIFICATION OF COLOUR PREDICTIONS OF TEXTILE WASTEWATER USING CONVOLUTIONAL NEURAL NETWORK AND ALEXNET

This chapter covers the comparative study of different deep learning tools for image processing in classifying the colour prediction of textile wastewater treatment. The optimisation was carried out to increase the training accuracy of deep learning tools of convolutional neural network and AlexNet in identifying the colour prediction.

ABSTRACT

The water quality of the wastewater treatment plant is generally observed by carrying out the water quality testing and by visual observation by the wastewater engineer. However, to get the lab testing result is very time consuming and proper treatment cannot be implemented on time to treat the wastewater. To overcome this drawback, deep learning tools using convolutional neural network (CNN) and AlexNet were used with transfer learning to automatically detect, categorise, and quantify the permissible and unacceptable colour value of textile effluent. Both networks demonstrated excellent results in terms of its ability to accurately classify data, as well as its efficient training and testing time. For large data sets, CNN has the highest training accuracy with 94.2%, while AlexNet has better performance in handling small date sets with 89.8%. This work can open an avenue for the application of deep learning tools for image processing in the textile wastewater.

Keywords: Convolutional neutral network; AlexNet; Colour prediction; Water quality; wastewater treatment

8.1 Introduction

Water pollution has become a more significant concern due to the rapid industrialisation, posing a serious threat to water resources (Norsaliza and Ismail, 2010; Wang *et al.*, 2022a). Out of all other industries such as pulp and paper, food and pharmaceutical industries, textile industry have contributed to one of the world's most serious environmental pollution problems, releasing unwanted dye effluents (Yaseen and Scholz, 2018). The effluent generated by the textile industry consists of dyes mixed with various contaminants in various quantities, which are commonly measured in the unit of American Dye Manufacturers' Institute (ADMI). In most industrialised nations, the treated wastewater discharge must be tested and monitored to ensure discharge permits are satisfied in order to safeguard the environment and human health (Fu *et al.*, 2020). Traditionally in the industrial practice, the effluent was collected, and subsequent analysis was done in the laboratory setting which is both resource-intensive and time-consuming. In order to conforms the water quality permit limits, majority of the wastewater treatment plants will tend to apply the chemical dosing excessively. This excessive dosage not only results in inflated chemical expenses but also poses a hindrance to the reuse of treated wastewater due to the rise in dissolved contaminants. On the other hand, some of the wastewater treatment plants will not treat the water according to the standards in order to save the cost. Therefore, continuous observation of the true colour of the wastewater is vital for the prompt management of the decolorization process in wastewater treatment.

It is conceivable that, even in cases where multiple dischargers are present in streams, a reliable system could be employed to estimate the potential colour of the effluent. The implementation of such tools would have the effect of reducing the frequency of sampling and minimising the expenses associated with analysis (Chen *et al.*, 2020b).

Digital image analysis (DIA) is a cost-effective approach that lends itself well to the real-time monitoring of numerous industrial processes (Li *et al.*, 2020). Different DIA techniques have been applied in the monitoring and control the operation in water and wastewater treatment. It has the potential to significantly lower both the expenses related to laboratory testing and workforce (Amaral and Ferreira, 2005). DIA has proven beneficial in the continuous monitoring of the true colour of textile wastewater. Lei (2000) introduced a technique for monitoring the RGB values of wastewater by analysing digital images derived from a single true colour image. Based on author's finding, the American Dye Manufacturers' Institute 3 and 31 wavelength methods, when coupled with a spectrophotometer, offer an efficient means of measuring true colour and apparent colour in wastewater through a tristimulus filter. In another study, Yu, Cheng and Chu (2005) develop online monitoring of wastewater treatment based on true colour using DIA method and proposed a correlation of the colour measurement based on ADMI value. The DIA method exhibits a high level of precision and low minimum detection limits when assessing these specimens. Nevertheless, the linear associations between the AMDI 31 WL and 3 WL values, as well as AMDI 31 WL and DIA values, differed depending on the hues of the

samples. This suggests that it would be unsuitable to compare these colour values without considering the varying hues of the samples. To improve the aforementioned issues, digital image analysis and artificial intelligence has been incorporated to enhance its application. Yu *et al.* (2017) employed DIA to monitor particle variations and to record the MGV/R/G/B data of the images captured during chemical coagulation batch settling took place. Subsequently, these real-time DIA data were incorporated into regression and artificial neural network (ANN) models to forecast the suspended solid (SS) and colour removal efficiencies for real textile wastewater post chemical coagulation and sedimentation. The outcome of the research has shown that it can recalibrate using the same image information with high accuracy and prediction. This approach is similar to using deep learning techniques such as convolutional neural networks (CNN) to solve the aforementioned issues and shown their capability with excellent results in image processing analysis and classification. Specifically in water-related fields, including hydrology applications, CNN has been widely applied for image processing and object detection for underwater, online water monitoring systems, image-based water level estimation of the river and recently, it has garnered attention for extracting water bodies based on the images for lake water. CNN has been found to eliminate the need for pre-processing and the use of a specific feature extraction method. Therefore, it may reduce the workload associated with training and choosing the best feature extraction method for automated identification. Additionally, a better performance can be achieved if a suitable learning

process was implemented based on the knowledge obtained from the trained hidden layers, which would require understanding the underlying structure of the data.

Based on the literature, only digital image analysis has been proposed and less attention has been given to the characterisation of colour of textile wastewater by implementing image vision and deep learning tools. In order to address the shortcomings of earlier research endeavours, we posit a new research idea based on image-based processing technology and CNN as a deep learning tool in this study which facilitates expeditious, uncomplicated, and cost-efficient monitoring of textile wastewater quality. Therefore, the objective of the present study is to identify the quantitative relationship between image and the colour composition of the textile wastewater, which solves the subjective judgement problem of water quality prediction by vision. Hence, an extensive investigation was conducted on the progress of training, performance, and utilisation of the proposed network. The visualisation of each mechanism's features, information entropy of feature images, and the most potent activations of sample sub-images of each mechanism were examined. These findings not only broaden the horizons of deep learning applications but also provide valuable insights into water quality management through the lens of deep learning with computer vision.

8.2 Methodology

8.2.1 Fabrication of silane – grafted nanchitosan of 3D-printed monolith

Briefly, as depicted in Figure 8.2.1a the monolith structure was fabricated using Digital Light Processing method and subsequently grafted with silane coupling agent which was first mix with ethanol at a ratio of 1:1 volume ratio (ethanol/ (3-Glycidyloxypropyl) trimethoxysilane). Then, the silane – grafted samples were further grafted with chitosan and oven dried from 4 h at 60 ℃. Lastly, the silane – grafted nanochitosan of 3D - printed monolith was irradiated with electron beam at 200 cGy. The treated samples were kept in desiccator for further analysis.

8.2.2 Sample collection and treatment

The samples of textile wastewater were taken at a textile plant in Batu Pahat, Johor. The sample locations are the equalisation tank, the clarifier tank, and the ultimate discharge point after treatment. The colour of the water ranged from purple to red, and there was no discernible precipitation. The water samples were treated using silane – grafted nanochitosan of 3D-printed monolith in a batch process for 80 min as illustrated in Figure 8.2.1b. All the quantitative data of colour value and images were labelled properly before being utilised for future imaging analysis. The raw and treated textile wastewater samples were stored in 5L sterile polypropylene containers and kept in a 4 ℃ refrigerator.

8.2.3 Operating parameter analysis

The water quality indicator that was measured is the colour value of the textile wastewater before and after the treatment. According Sela *et al.* (2020), the textile effluent was filtered first to remove solid particles. The

pH of the effluent was then corrected to desired pH by adding 0.1 M of hydrochloric acid using pH meter (Mettler Toledo FP20, United States). For colour analysis, the measurements were taken at a fixed wavelength of 465nm using HACH Spectrometer (DR3900, USA) in the unit of Platinum-Cobalt (Pt Co). The ADMI is converted to Pt Co using a conversion factor of 1 as shown in the Eq. (47).

$$\mathrm{Colour(Pt\,Co)} = \mathrm{A_o} \tag{47}$$

Where A_o is the value of Pt Co of corrected wastewater after applying conversion factor.

8.2.4 Data acquisition

The images of the colour of the textile wastewater were taken using digital single-lens reflex camera Canon EOS 500D, Japan as depicted in Figure 8.2.1d. All the images were taken from a 3ml plastic cuvette with a fixed distance between the lens and the cuvette as depicted in Figure 8.2.1c. A total of 800 images were taken with one image per colour of the textile wastewater.

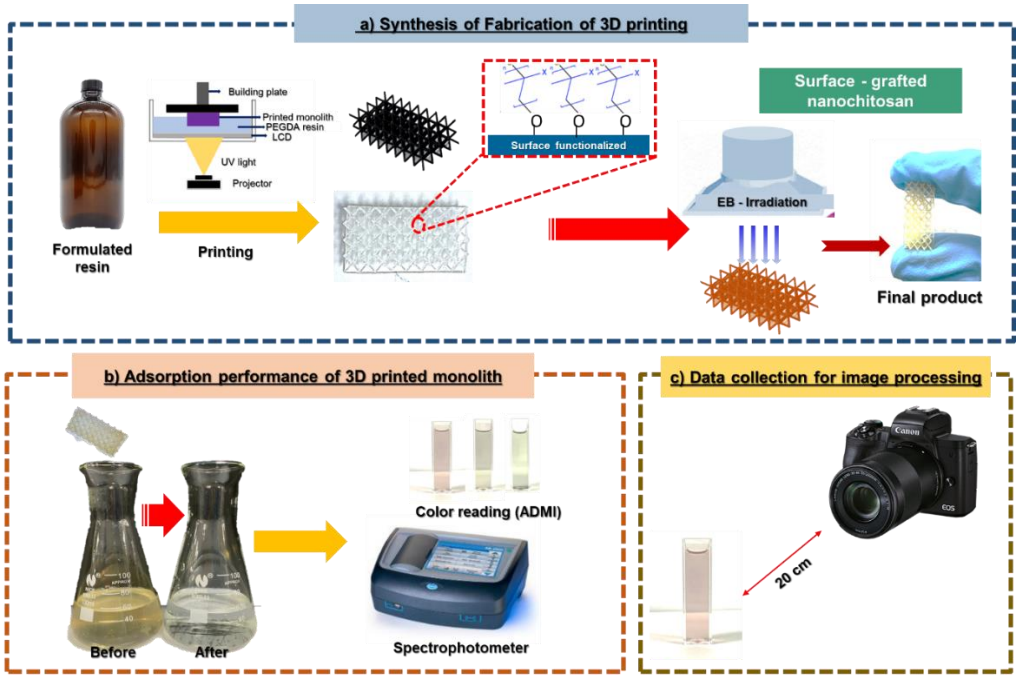


Figure 8.2.1: Schematic diagram of: (a) Synthesis of silane - grafted nanochitosan of 3D-printed monolith, (b) Adsorption performance of 3D printed monolith and (c) Data collection of water samples.

8.2.5 Image Normalisation

It is not possible to use the original images that have a variety of colours that were captured at different times without any further modifications for classification. The objective of image segmentation is to change how the image is presented in order to get a more thorough and straightforward analysis while also modifying the scale of the sub-image to fit CNN and AlexNet. Image segmentation has a significant impact the consistency of the colour of the textile wastewater contained inside each sub-image, allowing for more accurate classification and faster calculation of the percentage of each mechanism.

8.2.6 Image labelling

There are 2 classes of the images: A for acceptable and NA for non-acceptable. All the images including sub-images were labelled as ‘A’ and

‘NA’. If the value of the colour of the wastewater is below 200, it is considered acceptable, whereas above 200 is not acceptable. This is because the standard discharge for the wastewater for colour index is 200. All of the images for manual labelling were carefully selected and utilised as the basis for training and testing. To ensure the reliability and stability of the proposed technique, the training and testing datasets were fully split.

8.2.7 Network architecture

8.2.7.1 Convolutional Neural Network (CNN)

The inception of Convolutional Neural Network (CNN) dates back to the year 1980 when it was first introduced by Fukushima (1980). Its subsequent enhancement was accomplished by Lecun *et al.* (1998). CNN employs convolutional layers to recognize patterns and represent image features(Deng *et al.*, 2009). The neurons in CNN are linked to a smaller feature from the previous layer, enabling it to receive images or a multi-dimensional matrix. In this study, a Convolutional Neural Network (CNN) comprising of three convolutional layers, three pooling layers, a fully connected layer, and a Dropout layer has been developed to address the issue of over-fitting as overviewed in Figure 8.2.2 and Table 8.2.1.

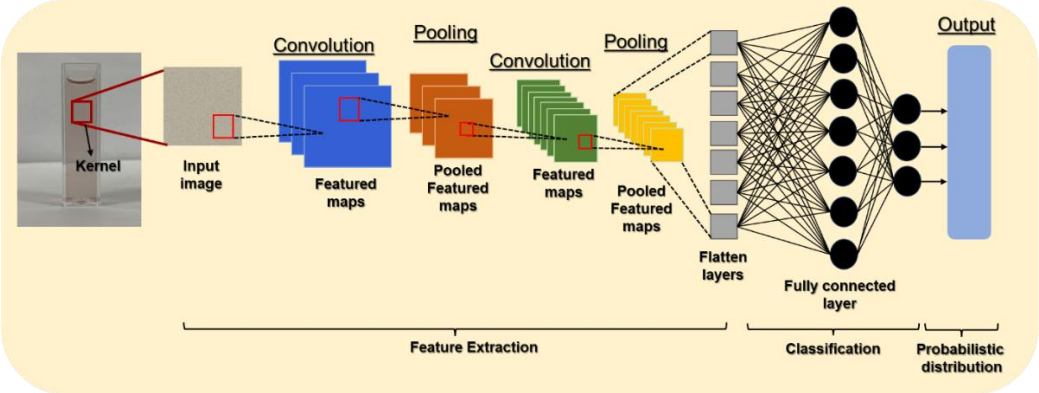


Figure 8.2.2: Schematic diagram of CNN architecture.

Table 8.2.1:The architecture of CNN.

Layers	Name	Layers	Name
0	Image input layer	7	Max pooling layer
1	Convolution layer	8	Convolution layer
2	Batch normalization layer	9	Batch normalization layer
3	ReLU layer	10	ReLU layer
4	Max pooling layer	11	Fully connected layer
5	Convolution layer	12	Softmax layer
6	Batch normalization layer	13	Classification output layer
7	ReLU layer		

For input layer, the determination of the number of nodes in a CNN input layer is contingent upon the dimension of the input vector. In the context of the present study, the binarized image dimension to be recognised is 28 × 28, necessitating an input layer node count of 784 based on Eq. (48).

$$\text{Param} = (k_w \times k_h \times Ch_s + 1) \times k_n \quad (48)$$

Where k_w is the width of convolution kernel, k_h is the height of convolution kernel, k_n is the number of convolution kernel and Ch_s is the number of input data of channels.

In general, the activation function of the convolutional layer must be able to transform a linear input into a non-linear signal. In this study, the

rectified linear unit (ReLU) was employed as the activation function. When compared to other activation functions, such as the tangent sigmoid function, this particular function has been proven to improve both the computing speed and accuracy (Nagi *et al.*, 2011). It is worth noting that the ReLU function overcomes the vanishing gradient problem by exponentially lowering the training gradient. For the convolution layer, the first convolution layer can be expressed as: Conv2D (16,3, padding = 'same', activation = 'ReLU') which can be calculated based on Eq. (49).

$$\text{Param} = (3 \times 3 \times 3 + 1) \times 16 = 448 \quad (49)$$

Then, the second layer is: Conv2D (3, 32, padding = 'same', activation = 'relu'). After the initial application of 16 convolutional kernels within the first convolutional layer, the input data's channel count in the second convolutional layer is augmented to 16 as shown in Eq.
(50).

$$\text{Param} = (3 \times 3 \times 16 + 1) \times 32 = 4640 \quad (50)$$

The third layer is: Conv2D (3, 64, padding = 'same', activation = 'relu'). After the second convolution layer has undergone 32 convolution kernels, the number of channels pertaining to the input data shall then be transformed to 32 in the second convolution layer as shown in Eq.(51).

$$\text{Param} = (3 \times 3 \times 32 + 1) \times 32 = 18496 \quad (51)$$

For the fourth layer of the network is the first maximum pooling layer. The specified parameters for the layer mentioned above include a pooling size of 2 and a fill technique of valid padding. The objective of applying

pooling is to minimise the data dimensions with the parameter set to 0. The applied pooling technique reduces the data's dimension by half of its original size, resulting in an output data dimension of (14, 14, 16) after traversal through the pooling layer.

The initial maximum pooling layer for the network is represented by the sixth layer, which by default has the following settings: valid padding of 2, pooling size 2, and a data output dimension of (7, 7, 32). Similarly, the eighth layer of the network serves as the principal maximum pooling layer, with the same default parameters of pooling size 2, valid padding, and data output dimension (3, 3, 64).

Next is the dropout layer which was developed to combat overfitting in deep learning. With this method, the network design is randomly altered, and during the forward propagation phase, some connections are specifically ignored(Garbin, Zhu and Marques, 2020). This causes certain neurons to temporarily become inactive, improving the network's capacity for generalization and reducing the danger of depending too heavily on local features.

In the CNN, the intervening flatten layer serves as a transformation layer between the convolution layer and the fully connected layer. The output of the convolution layer is a two-dimensional tensor, which after passing through produces several feature maps. These feature maps can only be joined to the fully connected layer by first being converted into a series of vectors.

The last layer in CNN is fully connected layer and output layer. The neural network consisting of a fully connected layer is composed of two distinct layers which can be determined based on the number of neuron weights within each respective layer. The calculation can be determined as using Eq. (52).

$$\text{Param} = \ (Ch_s + 1) \times k_n \tag{52}$$

For model training using deep learning models like CNN, it is necessary to select hyperparameters such as epoch number, batch size, and learning rate. The epoch number pertains to the number of iterations on the complete training dataset, while the batch size refers to the quantity of samples processed during each training cycle. The learnfunctions signifies the size of the step taken during each iteration for the purpose of minimising the loss function. For this study, the epoch number and mini batch were designated as 7 and 10, respectively, and a learning rate of 0.001 was implemented. Test datasets will be utilised to gauge the model accuracy and precision. After the system identifies the character, the program will convert into range of colour data of the textile wastewater based on the image.

8.2.7.2 AlexNet

For comparison of a different CNN architecture, AlexNet was selected which consisting of five convolutional layers, multiple max-pooling layers, three fully connected layers, and a 1000-way softmax as its final layer. AlexNet, which has five convolutional layers, numerous max-pooling layers, three fully connected layers, and a 1000-way softmax as its final layer, was chosen. AlexNet has become the most extensively used CNN

architecture due to its enhanced image classification performance. Its network topology is shown in Table 8.2.2.

Table 8.2.2: The architecture of AlexNet.

Layers	Name	Layers	Name
1	Image input layer	14	Grouped convolution layer
2	Convolution layer	15	ReLU layer
3	ReLU layer	16	Max pooling layer
4	Cross channel normalization layer	17	Fully connected layer
5	Max pooling layer	18	ReLU layer
6	Grouped convolution layer	19	Dropout layer
7	ReLU layer	20	Fully connected layer
8	Cross channel normalization layer	21	ReLU layer
9	Max pooling layer	22	Dropout layer
10	Convolution layer	23	Fully connected layer
11	ReLU layer	24	Softmax layer
12	Grouped convolution layer	25	Classification output layer
13	ReLU layer		

The final three layers of the AlexNet design were replaced with transfer learning in order to reduce the problem of overfitting in the network, as seen in Figure 8.2.3. The pre-trained network and the transferred network were divided up into the whole structure of the proposed network. The pre-trained network's parameters may be modified for feature extraction on the microscope image dataset because they had already been trained on the ImageNet dataset. Additionally, the pre-trained network's features that were extracted made it easier for the training process to converge a relatively small training dataset can also fit the requirements of transfer learning since the parameters in the transferred network only make up a tiny fraction of the whole network.

For this work, MATLAB version R2023a was used for the data analysis and image processing activities. The network was created on a personal desktop with an Intel(R) Core (TM) i5-1135G7 processor and NVIDIA® GeForce. The Adaptive Moment Estimation (ADAM) algorithm was used to train the transferred portion of AlexNet. In this particular network, the learning rate drop factor and period were given values of 0.1 and 10, respectively, and the starting learning rate was set at 0.0001. The maximum epoch was set at 6, and the minibatch size was established as 10.

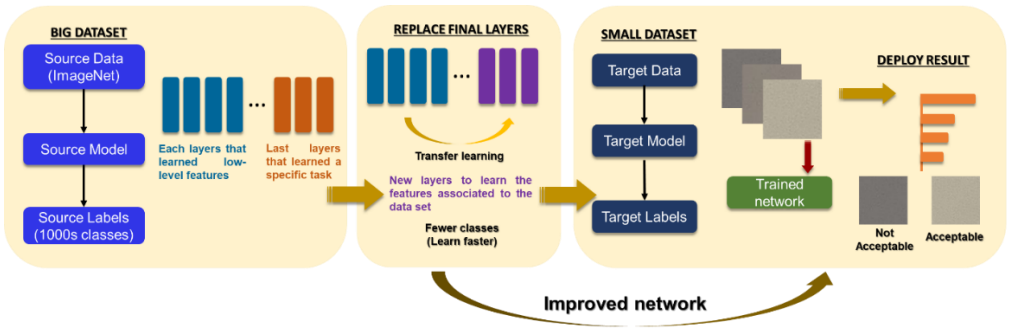


Figure 8.2.3: Transfer learning architecture of AlexNet.

8.3 Result and Discussion

8.3.1 Performance of the trained network

The progression of CNN and AlexNet network's training were carried out based on several case studies as listed below:

Case I: Comparison of acceptable value (colour range of 0 to 190) vs not acceptable value (200 and above)

Case II: Comparison of colour range (0 to 50) vs (90-100)

Case III: Comparison of colour range (0 to 50) vs (200 -300)

Case IV: Comparison of colour range (0 to 50) vs (300 -600)

Figure 8.3.1 shows the plot graph of training progress for Case I. The validation accuracy at 7th epoch for CNN network was 94.23%, while the validation loss was 0.5, the lowest cross-entropy loss experienced during training was 0. As for AlexNet network, the validation accuracy at 6th epoch 89.77% with the validation loss of 0.3 and the lowest cross-entropy loss experienced during training was 0.1. Since the result is consistent for both networks, the epoch number set for CNN and AlexNet are 7 and 6 respectively. The same parameters were also applied to other cases and their validation accuracy were tabulated in Table 8.3.1. Based on the results as portrayed in Table 8.3.1, CNN network gives better classification accuracy compared to AlexNet network when handling big data sets. Although CNN has better classification accuracy, CNN has higher means error compared to AlexNet network. Moreover, when comparing small data sets involving range of colour of textile wastewater images, Alextnet network offered better training accuracy than CNN. This is because AlexNet architecture is better suited for the analysis of smaller-scale data images as it is effectively extracting feature information from various scales, while simultaneously facilitating the fusion of these features with higher-level feature information. Moreover, this fusion is accomplished through the transfer of multiple lower-level feature information in a downward manner. Consequently, this process allows for a more comprehensive and precise representation of the image information, ultimately leading to the construction of a more accurate classifier (Zhang and Li, 2020; Zhao and Chen, 2022). Moreover, as reported by Sultan and Bekeneva (2022), the accuracy of

the designed CNN exhibits an increase proportionate to the number of images utilised in the training, thereby corroborating the network's underwhelming performance when confronted with a limited training dataset. It is also worth noting that the accuracy achieved by AlexNet surpasses that of the designed CNN, owing to its prior exposure to an extensive array of millions of images during its training phase. In order to validate the application for water quality production, AlexNet was chosen as the network to test small data sets which will be discussed in Section 8.3.2.

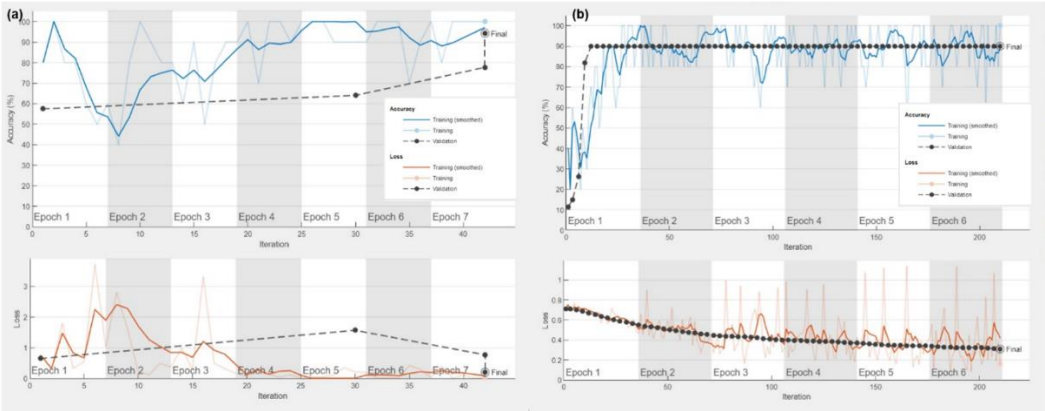


Figure 8.3.1: Training and validation accuracy plots of Case I for (a) CNN and (b) AlexNet.

Table 8.3.1: Classification accuracy and cross-entropy loss for each epoch of training and validation for all cases.

Case	Training network					
	CNN			AlexNet		
	Validation accuracy	Validation loss	Cross-entropy loss	Validation accuracy	Validation loss	Cross-entropy loss
I	94.2	0.53	0.5	89.8	0.32	0.1
II	81.5	1.02	0.1	86.6	0.15	0
III	87.7	0.34	0	93.4	0.22	0.05
IV	90.2	0.55	0	95.7	0.10	0

8.3.2 Application of trained network

There are total of 9 water images that were chosen to serve as examples to demonstrate the behaviour of the proposed network in terms of its application for water quality prediction. The original images of these images were depicted in Figure 8.3.2. The utilisation of the trained network as a benchmark was necessary in order to identify and quantify the proportions of the two distinct classifications present in each colour range. Subsequently, the results of this analysis were consolidated and exhibited in Table 8.3.2. It is apparent that the combination of qualitative indicators (i.e., the categorisation of each category) and quantitative indicators (i.e., the percentage of accuracy and range of colours) permits a clear representation of the predominant physical colour of the wastewater from textiles and their corresponding proportions within a given image. This approach effectively avoids the non-scientific approach commonly employed by the conventional method, where two images are typically positioned side by side and subjectively evaluated through visual examination to ascertain the level of consensus or disagreement. Furthermore, the proposed network exhibited a high level of efficiency as it can generate results promptly. Specifically, it required only 19 seconds for AlexNet and 30 seconds for CNN to identify and calculate all the 9 images. Additionally, this method boasts the advantages of being time efficient and enhancing the informational content and utility of images for predicting water quality for textile wastewater.

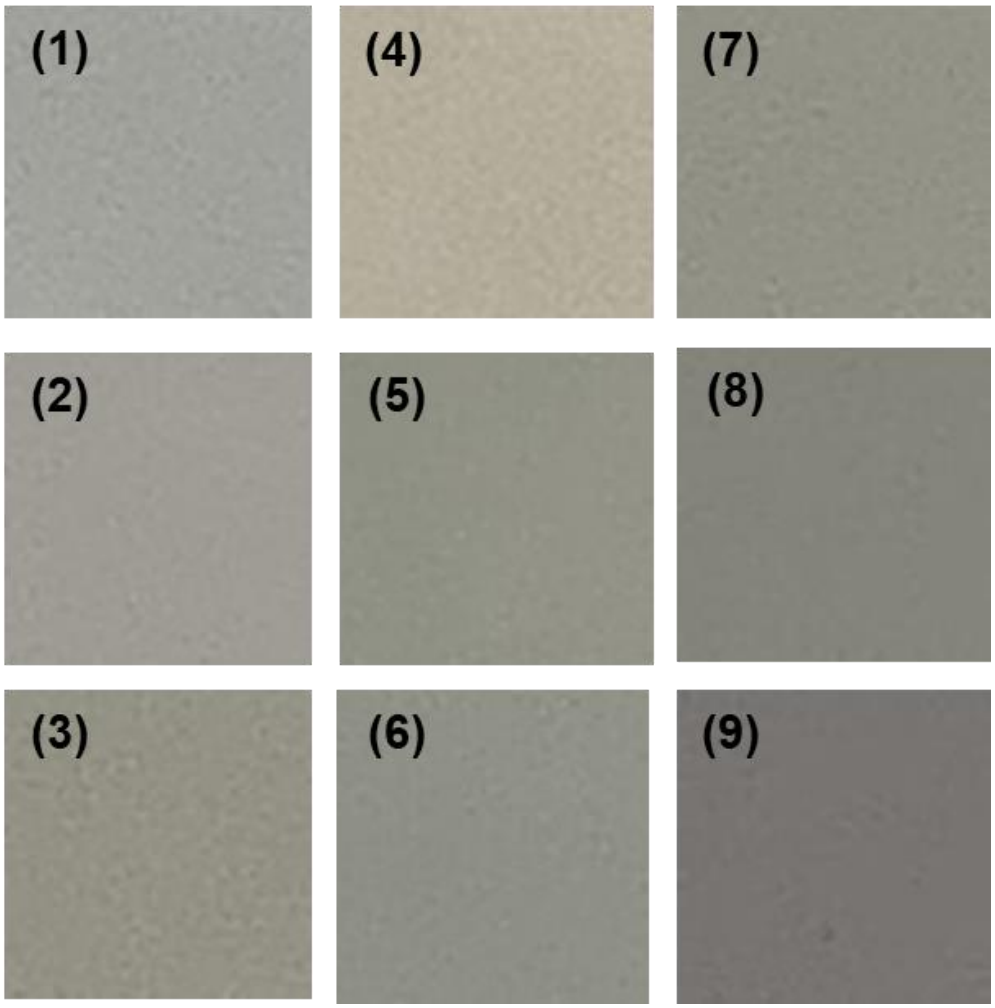


Figure 8.3.2: Original images of textile wastewater.

Table 8.3.2: Percentage of classification accuracy for each image.

Image ID	Classification	Value of the colour range	Percentage of accuracy (%)
1	Acceptable	0 - 10	97%
2	Acceptable	50 - 60	94.9%
3	Acceptable	100 - 110	96.2%
4	Acceptable	190 – 200	95.5%
5	Not acceptable	150 - 160	94.3%
6	Not acceptable	200 - 300	95.2%
7	Not acceptable	300 - 400	98.1%
8	Not acceptable	500 - 600	98.8%
9	Not acceptable	>600	99.7%

8.4 Conclusion

A comparative analysis of different CNN architecture is conducted in this paper, examining the classification of colour parameter of the textile wastewater using the CNN and AlexNet architectures. The results indicate that the CNN architecture displays superior precision and recall compared to the AlexNet architecture for large datasets. For smaller data sets, AlexNet has better training accuracy than CNN network. The high scores obtained by both architectures suggest that the classifier yields accurate results. However, it should be noted that the AlexNet architecture necessitates a longer training period due to its greater number of layers in comparison to the CNN architecture. Furthermore, the AlexNet architecture demonstrates enhanced performance in classifying the range of colour of textile wastewater. This technological advancement will prove highly beneficial to wastewater engineer in monitoring the water quality of the wastewater treatment plant especially in textile wastewater as it is both effective and time-efficient, particularly for larger fields. Additionally, this study has also revealed the ability of deep learning architectures to distinguish between significant and insignificant features within a set of images.

CHAPTER 9: CONCLUSION AND FUTURE WORK

This thesis project established the experimental work and modelling approach. In terms of experimental work, the fabrication of silane-grafted chitosan of 3D-printed monolith for colour removal in textile wastewater treatment was synthesised. The application of deep learning for colour prediction of textile wastewater based on real-time image was shown in this work. The key research findings throughout this study were presented in this chapter. This section also showcases the recommended work to be explored in the future.

9.1 Conclusion

In this research, a novel and robust approach for designing silane-grafted chitosan of 3D-printed monolith for wastewater treatment was proposed as illustrated in Figure 9.1.1. The summary for designing this 3D-printed enhanced adsorbent can be categorised into 4 stages which are consisting of; (i) fabrication of 3D-printed monolith, (ii) surface functionalisation step via surface grafting method, (iii) enhancement strategy to improve adsorption performance and (iv) surface modification with electron beam treatment. The combination of 4 stages strategy will be able to design 3D-printed enhanced adsorbent with excellent adsorption performance, mechanical and chemical stability as well as good reaction time to treat the wastewater in meeting industrial needs.

In the fabrication stage, Digital Light Processing (DLP) technique was chosen to fabricate 3D-printed monolith which has high precision, surface quality and detail accuracy compared to other printing methods. A photocurable resin was formulated by mixing PEGDA, photoinitiator

and plant-based commercial resin. If the formulated resin does not meet the desired requirement of mechanical properties, comonomer can be added to enhance the mechanical strength of the 3D-printed enhanced adsorbent. In this work, monolithic structure which can be designed in CAD drawing was chosen as optimal design due to its high surface area, controllable pore, good mechanical strength and can be mass produced. A good 3D-printed monolith was successfully fabricated using the correct printing parameters which were set in the slicing tools settings. Optimisation of printing parameters such as setting normal exposure time, bottom exposure time, retract speed and lifting distance is required to ensure a successful printing. The indicators to have a good printing for the 3D-printed monolith are the sample is printed based on the size set during the design process and has complete structure with good mechanical strength.

Next, in the surface functionalisation stage, surface grafting approach using silane coupling agent was proposed and subsequently grafting the chitosan onto the silane-grafted 3D-printed monolith. The mechanical strength, chemical and mechanical stability as well as surface wetting behaviour of the silane-grafted 3D-printed monolith has also been evaluated. Then, a correct technique and operating condition were identified to obtain success silane-grafted chitosan of 3D-printed monolith without causing any rupture, blocking or cracking structure and leaching of chitosan in the wastewater during the adsorption process. At this stage, the process of surface grafting was conducted by utilising either a single or hybrid silane coupling agent in conjunction with an

epoxide amide reaction. In order to prevent any potential shortcomings in the surface grafting procedure, it is strongly advised to manipulate the silane coupling agent in an inert environment, as its stability is compromised in ambient conditions. Additionally, it is crucial to verify the absence of any obstructions during the grafting operation. The structural integrity may be compromised by excessive grafting, leading to ruptures due to the vigorous chemical reaction. Surface grafting procedure carried out with the aim of enhancing both the hydrophobic properties and mechanical robustness of the 3D-printed monolith. This step is very important to prolong the lifespan of the 3D-printed monolith in the aqueous environment. Then, a layer for chitosan was grafted onto the samples to develop 3D-printed enhanced adsorbent.

Thirdly, the evaluation of 3D-printed enhanced adsorbent on adsorption performance were conducted. The optimum condition to achieve equilibrium adsorption capacity and removal were identified using Box-Behnken design in RSM. The reusability and recyclability of the 3D-printed enhanced adsorbent was also evaluated in this stage to verify its practicality to be used in real application. At this stage, the optimum experimental conditions have been determined before moving to the enhancement stage to further improve the performance of the 3D-printed enhanced adsorbent.

Further to this, the enhancement strategy was carried out to further improve the adsorption performance by; (i) comparing different structural topology of monolithic structure; (ii) application of different drying method

and (iii) surface modification using electron beam technique. It was identified body-centred cubic (BCC) has the highest permeability and surface area with excellent adsorption performance compared to other structural. Moreover, the convective hot air drying is preferable as it has the ability to remove desired moisture content without causing any damage on the structural properties that will affect the adsorption performance.

In the last stage, surface modification method was proposed using electron beam irradiation treatment to further enhance the adsorption performance with excellent contact time to meet the industrial requirement. Different dosage of electron beam irradiation was evaluated. 200cGy was chosen as desired dose as it has the capability to increase the surface roughness and adsorption performance within 1h. Through the integration of various enhancement strategy, a high-quality 3D-printed enhanced adsorbent with good adsorption capabilities, reduced reaction time, and outstanding mechanical and chemical properties has been effectively developed.

Lastly, a modelling approach of using deep learning tool to predict the colour of the textile wastewater based on real-time image were proposed by comparing CNN and AlexNet model. The combination of deep learning and experimental data is to verify and predict the colour value of the textile wastewater before and after the treatment.

Although this research works has achieved remarkable milestones, this work still has some limitations. The limitation and recommendation of work to overcome such failures were listed as follow:

i) Variation of 3D-printed polymeric materials

The primary concern pertains to the 3D-printed materials. Despite a well-defined strategy outlined in this thesis, there remains a significant need for substantial efforts to broaden the range of polymer materials used, akin to those in traditional manufacturing. It is essential to expand the variety of polymers utilised, including polylactic acid (PLA), polycaprolactone (PCL), and polyhydroxyalkanoate-type polymer (PHBV), for the purpose of developing the environmentally friendly resin. This shift is driven by the prevailing emphasis on sustainability and the adoption of circular economy frameworks. Further investigation is required to tackle these constraints and delve into the possibilities of this emerging technology.

ii) Extended the application of surface grafting technique using silane coupling agent with other adsorbent materials.

This study has limitation in terms of material used as the adsorbent. Particularly in this work, chitosan was used as bio-adsorbent which has been successfully grafted on the 3D-printed monolith at specific pH (i.e., pH 5 to 6) and temperature (i.e., 100 to 110 ℃). Substituting the adsorbent material has the potential to induce leaching concerns when utilised under same grafting procedures, consequently impacting the efficiency of adsorption in the treatment of textile wastewater. Therefore,

additional modifications and optimisation are imperative for the implementation of surface grafting techniques employing a silane coupling agent for diverse adsorbents. Additionally, a comprehensive grasp of the adsorption mechanism, isotherm, and kinetic models of individual adsorbent materials is crucial. This necessity arises from the significant role these variables play in elucidating the adsorption process, which is contingent upon a multitude of factors such as the structural composition of the adsorbent and the inherent physical and chemical properties of the solute.

iii) Robust optimisation approach with uncertainties of different effluent of wastewater for colour prediction

The current work only focusing on its application for the colour prediction for textile wastewater and the range of colour index tested in CNN and AlexNet are in between 10 to 600. Although the range of colour has taken the consideration of water quality of different production and during shut-down time, it is only validated for the specific range of colour index for one industry. Hence, it will limit its robust applicability to be used in different industries such as for palm oil mill effluent (POME) and any industries that uses dye in the process. To overcome this, it is important to increase the number of samples and range of data to improve the consistency of the training accuracy.

In summary, the synergistic approach of combining surface functionalisation and 3D printing is more sustainable and supports Sustainable development goals (SDGs) as the 3D-printed enhanced

adsorbent takes a different approach from the conventional method that uses chemical dosing, which produces secondary waste. It is more cost-effective solution as the cost of spending on chemicals and maintenance can be reduced. This work is aligned with the current water innovation roadmap to satisfy the community's water needs whilst minimising the adverse environmental and social impacts at the lowest rate.

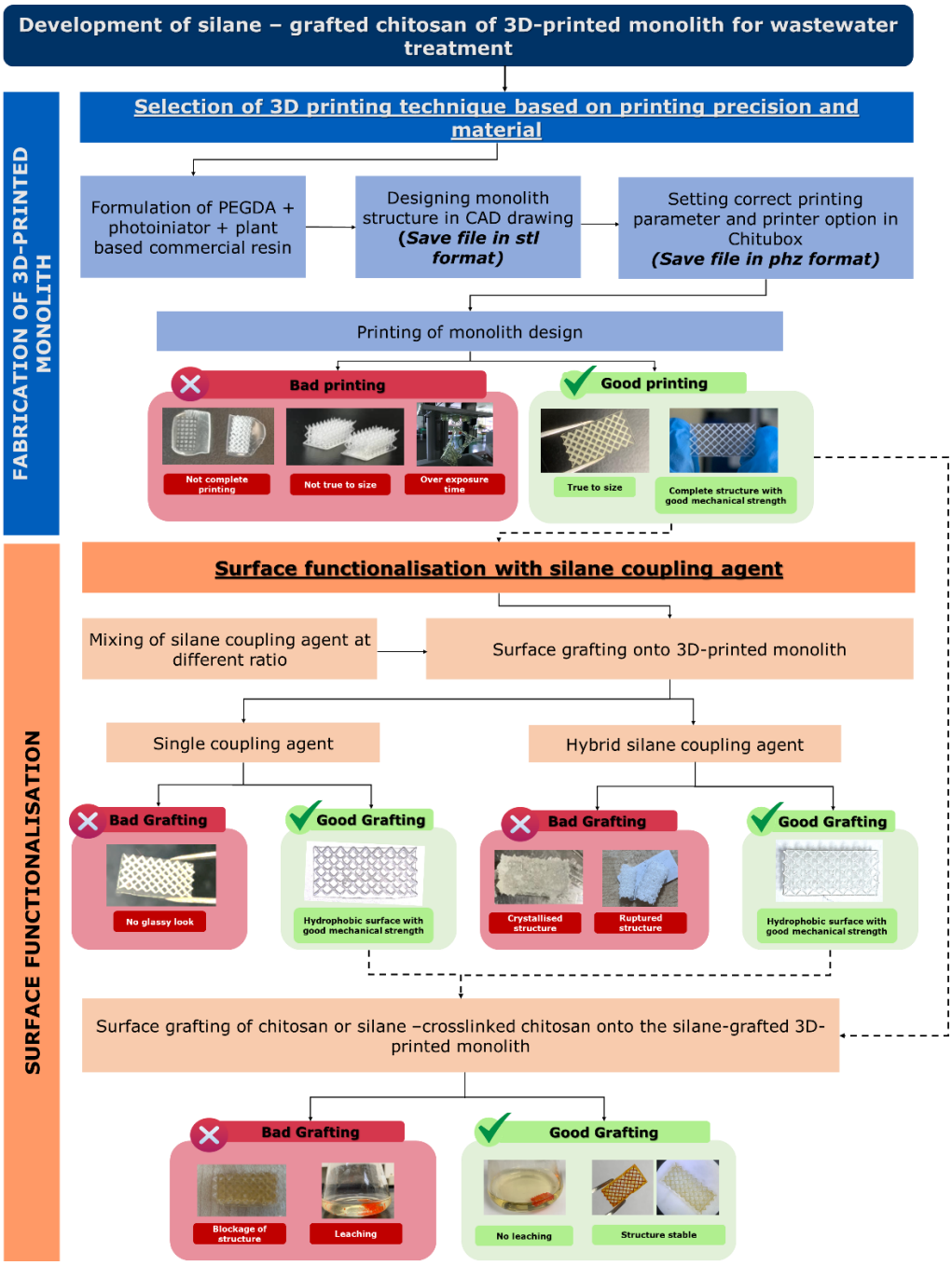


Figure 9.1.1:Summary of the design of silane -grafted chitosan of 3D-printed monolith.

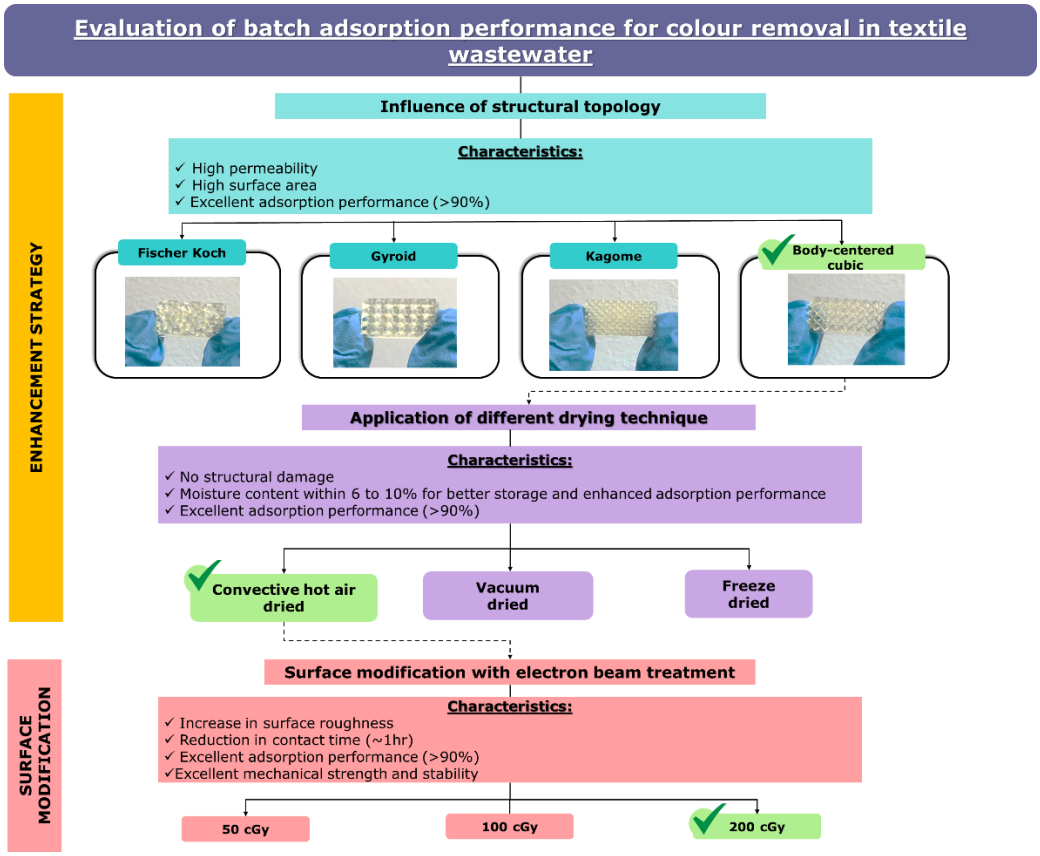


Figure 9.1.1:(Continued).

9.2 Future work

The goal of this work is to establish the working strategy functionalised 3D-printed enhanced adsorbent. The establishment of the framework for the development of functionalised 3D-printed enhanced adsorbent has been accomplished and addressing the research gaps identified in this work. Although a variety of specifics pertaining to the mechanisms has been addressed, however the underlying scientific principles that enable this process remained to be ascertained. The synergistic approach of combining surface functionalisation and 3D printing technology has opened the avenue for wastewater treatment, it required mature experimental skills and expensive equipment to ensure the success in the it is imperative to possess a high level of experimental skills and known optimal parameter of surface functionalisation to achieve desired results. One of the potential domains for exploration lies in the realm of initiator-integrated 3D printing material for the purpose of wastewater application. This new generation of material, known as initiator-integrated 3D printing material (i3DP), can be manufactured by integrating a functional initiator into a photocurable resin to create functional structural materials with tuneable surface properties. The integration of 3D printing in structural design and surface modification aided before printing process can be a cost-efficient and simple approach to substantially augment the capability of functional 3D printing. Consequently, this method has the ability to bestow the 3D printing technology with a broader range of practical applications.

Secondly, it is recommended to examine the feasibility of the product design of functionalised 3D-printed enhanced adsorbent for wastewater treatment application by taking economic and sustainability considerations into account. This approach can be done by using graphical graph theoretic framework, known as P-graph. The P-graph approach facilitates the methodical development of processes with economic and sustainability consideration. This framework is built on axioms and algorithms, as well as a bipartite graphical representation of process units. Combinatorial approaches of possible process or design can be used to solve design challenges using this graphical form. Based on the proposed algorithms, P-graph framework can suggest the feasible pathway to fabricate the product based on the cost and sustainability index input. Currently, this framework has been utilised in various domains to carry out process network synthesis but in product design synthesis is remain unexplored. Therefore, P-graph framework can be a design tool to show the conceptual design of product synthesis and the feasibility of the functionalised 3D-printed enhanced adsorbent to be employed for practical applications.

REFERENCES

Adeyi, A. A., Jamil, S. N. A. M., Abdullah, L. C. and Choong, T. S. Y. (2019) 'Adsorption of Malachite Green Dye from Liquid Phase Using Hydrophilic Thiourea-Modified Poly(acrylonitrile-co-acrylic acid): Kinetic and Isotherm Studies', *Journal of Chemistry,* 2019, pp. 4321475.

Ahmad, A., Khan, N., Giri, B. S., Chowdhary, P. and Chaturvedi, P. (2020) 'Removal of methylene blue dye using rice husk, cow dung and sludge biochar: Characterization, application, and kinetic studies', *Bioresource Technology,* 306, pp. 123202.

Ahmad, Z., Ansell, M. P. and Smedley, D. (2011) 'Moisture Absorption Characteristics of Epoxy Based Adhesive Reinforced with CTBN and Ceramic Particles for Bonded-in Timber Connection: Fickian or Non-Fickian Behaviour', *IOP Conference Series: Materials Science and Engineering,* 17(1), pp. 012011.

Ahn, D., Kweon, J.-H., Choi, J. and Lee, S. (2012) 'Quantification of surface roughness of parts processed by laminated object manufacturing', *Journal of Materials Processing Technology,* 212(2), pp. 339-346.

Ai, H., Lei, D., Wu, M., Li, S. and Du, K. (2022) 'Magnetically derived fabrication of aligned porous poly(sulfonated polystyrene-co.-chitosan) monolith as a high efficient adsorbent for metal ions separation', *Journal of Cleaner Production,* 380, pp. 135170.

Al-Tohamy, R., Ali, S. S., Li, F., Okasha, K. M., Mahmoud, Y. A. G., Elsamahy, T., Jiao, H., Fu, Y. and Sun, J. (2022) 'A critical review on the treatment of dye-containing wastewater: Ecotoxicological and health

concerns of textile dyes and possible remediation approaches for environmental safety', *Ecotoxicology and Environmental Safety,* 231, pp. 113160.

Alaei Shahmirzadi, M. A. and Kargari, A. (2020) 'Chapter 5 - Application of functional single-element and double-element oxide nanoparticles for the development of nanocomposite membranes', in Sadrzadeh, M. and Mohammadi, T. (eds.) *Nanocomposite Membranes for Water and Gas Separation*: Elsevier, pp. 113-144.

Aljbour, N. D., Beg, M. D. H. and Gimbun, J. (2019) 'Acid Hydrolysis of Chitosan to Oligomers Using Hydrochloric Acid', *Chemical Engineering & Technology,* 42(9), pp. 1741-1746.

Alyasi, H., Mackey, H. and McKay, G. (2023) 'Adsorption of Methyl Orange from Water Using Chitosan Bead-like Materials', *Molecules*, 28(18). DOI: 10.3390/molecules28186561.

Amalina, F., Razak, A. S. A., Krishnan, S., Zularisam, A. W. and Nasrullah, M. (2022) 'Dyes removal from textile wastewater by agricultural waste as an absorbent – A review', *Cleaner Waste Systems,* 3, pp. 100051.

Amaral, A. L. and Ferreira, E. C. (2005) 'Activated sludge monitoring of a wastewater treatment plant using image analysis and partial least squares regression', *Analytica Chimica Acta,* 544(1), pp. 246-253.

Amor, I. B., Hemmami, H., Laouini, S. E., Abdelaziz, A. G. and Barhoum, A. (2023) 'Influence of chitosan source and degree of deacetylation on antibacterial activity and adsorption of AZO dye from water', *Biomass Conversion and Biorefinery*.

Anand, M., Sathyapriya, P., Maruthupandy, M. and Hameedha Beevi, A. (2018) 'Synthesis of chitosan nanoparticles by TPP and their potential mosquito larvicidal application', *Frontiers in Laboratory Medicine,* 2(2), pp. 72-78.

Andrade, C. A., Zambrano-Intriago, L. A., Oliveira, N. S., Vieira, J. S., Quiroz-Fernández, L. S. and Rodríguez-Díaz, J. M. (2020) 'Adsorption Behavior and Mechanism of Oxytetracycline on Rice Husk Ash: Kinetics, Equilibrium, and Thermodynamics of the Process', *Water, Air, & Soil Pollution,* 231(3), pp. 103.

Anusha, A. and Jayatunga, A. (2017) 'CORRELATION BETWEEN BIOCHEMICAL OXYGEN DEMAND (BOD) AND CHEMICAL OXYGEN DEMAND (COD) FOR DIFFERENT INDUSTRIAL WASTE WATERS', *Journal of the National Science Foundation of Sri Lanka,* 21.

Apul, O. G. and Karanfil, T. (2015) 'Adsorption of synthetic organic contaminants by carbon nanotubes: A critical review', *Water Research,* 68, pp. 34-55.

Arantes, M. K., Kugelmeier, C. L., Cardozo-Filho, L., Monteiro, M. R., Oliveira, C. R. and Alves, H. J. (2015) 'Influence of the drying route on the depolymerization and properties of chitosan', *Polymer Engineering & Science,* 55(9), pp. 1969-1976.

Arslan, C. and Dogan, M. (2018) 'The effects of silane coupling agents on the mechanical properties of basalt fiber reinforced poly(butylene terephthalate) composites', *Composites Part B: Engineering,* 146, pp. 145-154.

Asbai-Ghoudan, R., Ruiz de Galarreta, S. and Rodriguez-Florez, N. (2021) 'Analytical model for the prediction of permeability of triply periodic minimal surfaces', *Journal of the Mechanical Behavior of Biomedical Materials,* 124, pp. 104804.

Askari, F., Zandi, M., Shokrolahi, P., Tabatabaei, M. H. and Hajirasoliha, E. (2019) 'Reduction in protein absorption on ophthalmic lenses by PEGDA bulk modification of silicone acrylate-based formulation', *Progress in Biomaterials,* 8(3), pp. 169-183.

Ayawei, N., Ebelegi, A. N. and Wankasi, D. (2017) 'Modelling and Interpretation of Adsorption Isotherms', *Journal of Chemistry,* 2017, pp. 3039817.

Ayodele, O., Okoronkwo, A., Olugbenga, O. and Taiwo, A. (2018) 'Utilization of blue crab shells for the synthesis of chitosan nanoparticles and their characterization', *Songklanakarin Journal of Science and Technology,* 40, pp. 1039-1042.

Azhary, S. Y., Purnama, D., Florena, F. F., Vanitha, M., Muchtaridi, Panatarani, C. and Joni, I. M. (2019) 'Synthesis and characterization of chitosan:SiO2 nanocomposite by ultrasonic spray drying', *IOP Conference Series: Materials Science and Engineering,* 550(1), pp. 012037.

Aziz, T., Ullah, A., Fan, H., Jamil, M. I., Khan, F. U., Ullah, R., Iqbal, M., Ali, A. and Ullah, B. (2021) 'Recent Progress in Silane Coupling Agent with Its Emerging Applications', *Journal of Polymers and the Environment,* 29(11), pp. 3427-3443.

Badalov, S., Oren, Y. and Arnusch, C. J. (2015) 'Ink-jet printing assisted fabrication of patterned thin film composite membranes', *Journal of Membrane Science,* 493, pp. 508-514.

Bae, J.-H., Won, J. C., Lim, W. B., Lee, J. H., Min, J. G., Kim, S. W., Kim, J.-H. and Huh, P. (2021) 'Highly Flexible and Photo-Activating Acryl-Polyurethane for 3D Steric Architectures', *Polymers*, 13(6). DOI: 10.3390/polym13060844.

Bahrudin, N. N., Nawi, M. A., Jawad, A. H. and Sabar, S. (2020) 'Adsorption Characteristics and Mechanistic Study of Immobilized Chitosan-Montmorillonite Composite for Methyl Orange removal', *Journal of Polymers and the Environment,* 28(7), pp. 1901-1913.

Bahrudin, N. N., Nawi, M. A. and Sabar, S. (2019) 'Immobilized chitosan-montmorillonite composite adsorbent and its photocatalytic regeneration for the removal of methyl orange', *Reaction Kinetics, Mechanisms and Catalysis,* 126(2), pp. 1135-1153.

Bakshi, P. S., Selvakumar, D., Kadirvelu, K. and Kumar, N. S. (2020) 'Chitosan as an environment friendly biomaterial – a review on recent modifications and applications', *International Journal of Biological Macromolecules,* 150, pp. 1072-1083.

Balogun, H. A., Sulaiman, R., Marzouk, S. S., Giwa, A. and Hasan, S. W. (2019) '3D printing and surface imprinting technologies for water treatment: A review', *Journal of Water Process Engineering,* 31, pp. 100786.

Baroudi, A., García-Payo, C. and Khayet, M. (2018) 'Structural, Mechanical, and Transport Properties of Electron Beam-Irradiated

Chitosan Membranes at Different Doses', *Polymers*, 10(2). DOI: 10.3390/polym10020117.

Berber, M. R. (2020) 'Current Advances of Polymer Composites for Water Treatment and Desalination', *Journal of Chemistry,* 2020, pp. 7608423.

Bernasconi, R., Carrara, E., Hoop, M., Mushtaq, F., Chen, X., Nelson, B. J., Pané, S., Credi, C., Levi, M. and Magagnin, L. (2019) 'Magnetically navigable 3D printed multifunctional microdevices for environmental applications', *Additive Manufacturing,* 28, pp. 127-135.

Berradi, M., Hsissou, R., Khudhair, M., Assouag, M., Cherkaoui, O., El Bachiri, A. and El Harfi, A. (2019) 'Textile finishing dyes and their impact on aquatic environs', *Heliyon,* 5(11), pp. e02711.

Bhattacharyya, R. and Ray, S. K. (2015) 'Removal of congo red and methyl violet from water using nano clay filled composite hydrogels of poly acrylic acid and polyethylene glycol', *Chemical Engineering Journal,* 260, pp. 269-283.

Bilińska, L. and Gmurek, M. (2021) 'Novel trends in AOPs for textile wastewater treatment. Enhanced dye by-products removal by catalytic and synergistic actions', *Water Resources and Industry,* 26, pp. 100160.

Blackburn, R. S. (2004) 'Natural Polysaccharides and Their Interactions with Dye Molecules: Applications in Effluent Treatment', *Environmental Science & Technology,* 38(18), pp. 4905-4909.

Blanquer, S. B. G., Werner, M., Hannula, M., Sharifi, S., Lajoinie, G. P. R., Eglin, D., Hyttinen, J., Poot, A. A. and Grijpma, D. W. (2017) 'Surface curvature in triply-periodic minimal surface architectures as a distinct

design parameter in preparing advanced tissue engineering scaffolds', *Biofabrication,* 9(2), pp. 025001.

Bohner, M., Loosli, Y., Baroud, G. and Lacroix, D. (2011) 'Commentary: Deciphering the link between architecture and biological response of a bone graft substitute', *Acta Biomaterialia,* 7(2), pp. 478-484.

Bolan, M., Dean, M. and Bardelcik, A. (2023) 'The Energy Absorption Behavior of 3D-Printed Polymeric Octet-Truss Lattice Structures of Varying Strut Length and Radius', *Polymers*, 15(3). DOI: 10.3390/polym15030713.

Boretti, A. and Rosa, L. (2019) 'Reassessing the projections of the World Water Development Report', *npj Clean Water,* 2(1), pp. 15.

Bough, W. A., Shewfelt, A. L. and Salter, W. L. (1975) 'Use of Chitosan for the Reduction and Recovery of Solids in Poultry Processing Waste Effluents', *Poultry Science,* 54(4), pp. 992-1000.

Brás, R., Gomes, A., Ferra, M. I. A., Pinheiro, H. M. and Gonçalves, I. C. (2005) 'Monoazo and diazo dye decolourisation studies in a methanogenic UASB reactor', *Journal of Biotechnology,* 115(1), pp. 57-66.

Bristow, J. and Inc, A. I. (2012) *Chitosan manufacturing process*. [Online]. Available at: https://patents.google.com/patent/US8318913B2/en?scholar.

Browne, M. P., Plutnar, J., Pourrahimi, A. M., Sofer, Z. and Pumera, M. (2019) 'Atomic Layer Deposition as a General Method Turns any 3D-Printed Electrode into a Desired Catalyst: Case Study in Photoelectrochemisty', *Advanced Energy Materials,* 9(26), pp. 1900994.

Budianto, E., Muthoharoh, S. and Nizardo, N. M. (2015) 'Effect of Crosslinking Agents, pH and Temperature on Swelling Behavior of Cross-linked Chitosan Hydrogel', *Asian Journal of Applied Sciences,* 03, pp. 581-588.

Buenaflor, J. P., Lydon, C. K., Zimmerman, A., DeSutter, O. L. and Wissinger, J. E. (2022) 'Student explorations of calcium alginate bead formation by varying pH and concentration of acidic beverage juices', 4(2), pp. 155-164.

Cai, P., Guo, L., Wang, H., Li, J., Li, J., Qiu, Y., Zhang, Q. and Lue, Q. (2020) 'Effects of slurry mixing methods and solid loading on 3D printed silica glass parts based on DLP stereolithography', *Ceramics International,* 46(10, Part B), pp. 16833-16841.

Cao, Y., Zhao, M., Ma, X., Song, Y., Zuo, S., Li, H. and Deng, W. (2021) 'A critical review on the interactions of microplastics with heavy metals: Mechanism and their combined effect on organisms and humans', *Science of The Total Environment,* 788, pp. 147620.

Casini, M. (2022) 'Chapter 8 - Advanced building construction methods', in Casini, M. (ed.) *Construction 4.0*: Woodhead Publishing, pp. 405-470.

Chandanshive, V., Kadam, S., Rane, N., Jeon, B.-H., Jadhav, J. and Govindwar, S. (2020) 'In situ textile wastewater treatment in high rate transpiration system furrows planted with aquatic macrophytes and floating phytobeds', *Chemosphere,* 252, pp. 126513.

Chartier, C., Buwalda, S., van den Berghe, H., Nottelet, B. and Budtova, T. (2022) 'Tuning the properties of porous chitosan: Aerogels and

cryogels', *International Journal of Biological Macromolecules,* 202, pp. 215-223.

Chen, F., Gällstedt, M., Olsson, R. T., Gedde, U. W. and Hedenqvist, M. S. (2015) 'A novel chitosan/wheat gluten biofoam fabricated by spontaneous mixing and vacuum-drying', *RSC Advances,* 5(114), pp. 94191-94200.

Chen, H., Zhou, Y., Wang, J., Lu, J. and Zhou, Y. (2020a) 'Polydopamine modified cyclodextrin polymer as efficient adsorbent for removing cationic dyes and Cu2+', *Journal of Hazardous Materials,* 389, pp. 121897.

Chen, J., Zhang, D., Yang, S. and Nanehkaran, Y. A. (2020b) 'Intelligent monitoring method of water quality based on image processing and RVFL-GMDH model', *IET Image Processing,* 14(17), pp. 4646-4656.

Chen, k.-m. L. K. L. Y.-L. C. H. R. C. M.-H. C. M. C. H.-Y. C. Q. (2010) *Method for preparing chitosan nanoparticle in water phase*. [Online]. Available at: https://patents.google.com/patent/JP2010031218A/en.

Chen, W., Tang, X., Chu, X., Yang, Y., Xu, W., Fu, D., Li, X. and Zhou, W. (2024) 'Impact of catalyst carrier with TPMS structures on hydrogen production by methanol reforming', *International Journal of Hydrogen Energy,* 58, pp. 1177-1189.

Cheng, H., Li, Y., Wang, B., Mao, Z., Xu, H., Zhang, L., Zhong, Y. and Sui, X. (2018) 'Chemical crosslinking reinforced flexible cellulose nanofiber-supported cryogel', *Cellulose,* 25(1), pp. 573-582.

Cho, D.-W., Jeon, B.-H., Chon, C.-M., Schwartz, F. W., Jeong, Y. and Song, H. (2015) 'Magnetic chitosan composite for adsorption of cationic

and anionic dyes in aqueous solution', *Journal of Industrial and Engineering Chemistry,* 28, pp. 60-66.

Chowdhury Maqsud, R., Steffes, J., Huey Bryan, D. and McCutcheon Jeffrey, R. (2018) '3D printed polyamide membranes for desalination', *Science,* 361(6403), pp. 682-686.

Cichosz, S. and Masek, A. (2020) 'Drying of the Natural Fibers as A Solvent-Free Way to Improve the Cellulose-Filled Polymer Composite Performance', *Polymers*, 12(2). DOI: 10.3390/polym12020484.

Connell, L. S., Romer, F., Suárez, M., Valliant, E. M., Zhang, Z., Lee, P. D., Smith, M. E., Hanna, J. V. and Jones, J. R. (2014) 'Chemical characterisation and fabrication of chitosan–silica hybrid scaffolds with 3-glycidoxypropyl trimethoxysilane', *Journal of Materials Chemistry B,* 2(6), pp. 668-680.

Cox, J. R., Kipling, I. and Gibbons, G. J. (2023) 'Ensuring supply chain integrity for material extrusion 3D printed polymer parts', *Additive Manufacturing,* 62, pp. 103403.

Crini, G. and Badot, P.-M. (2008) 'Application of chitosan, a natural aminopolysaccharide, for dye removal from aqueous solutions by adsorption processes using batch studies: A review of recent literature', *Progress in Polymer Science,* 33(4), pp. 399-447.

Crini, G., Torri, G., Lichtfouse, E., Kyzas, G. Z., Wilson, L. D. and Morin-Crini, N. (2019) 'Dye removal by biosorption using cross-linked chitosan-based hydrogels', *Environmental Chemistry Letters,* 17(4), pp. 1645-1666.

Czechowska-Biskup, R., Wach, R., Stojek, P., Kamińska, M., Rosiak, J. and Ulański, P. (2016) 'Synthesis of chitosan and carboxymethyl chitosan hydrogels by electron beam irradiation', *Progress on Chemistry and Application of Chitin and its Derivatives,* XXI, pp. 27.

da Silva Alves, D. C., Healy, B., Pinto, L. A. d. A., Cadaval, T. R. S. A. and Breslin, C. B. (2021) 'Recent Developments in Chitosan-Based Adsorbents for the Removal of Pollutants from Aqueous Environments', *Molecules,* 26(3).

Darwis, D., Mitomo, H., Enjoji, T., Yoshii, F. and Makuuchi, K. (1998) 'Heat resistance of radiation crosslinked poly(ε-caprolactone)', *Journal of Applied Polymer Science,* 68(4), pp. 581-588.

Das, P. and Debnath, A. (2021) 'Reactive orange 12 dye adsorption onto magnetically separable CaFe2O4 nanoparticles synthesized by simple chemical route: kinetic, isotherm and neural network modeling', *Water Practice and Technology,* 16(4), pp. 1141-1158.

Davis, R. F. (2017) 'Silicon Carbide', *Reference Module in Materials Science and Materials Engineering*: Elsevier.

Dawood, M. (2014) '4 - Durability of steel components strengthened with fiber-reinforced polymer (FRP) composites', in Karbhari, V.M. (ed.) *Rehabilitation of Metallic Civil Infrastructure Using Fiber Reinforced Polymer (FRP) Composites*: Woodhead Publishing, pp. 96-114.

del Rio, M., Villar, M., Quesada, S., Turnes Palomino, G., Ferrer, L. and Palomino Cabello, C. (2021) 'Silver-functionalized UiO-66 metal-organic framework-coated 3D printed device for the removal of radioactive iodine from wastewaters', *Applied Materials Today,* 24, pp. 101130.

Deng, J., Dong, W., Socher, R., Li, L. J., Kai, L. and Li, F.-F. 'ImageNet: A large-scale hierarchical image database'. *2009 IEEE Conference on Computer Vision and Pattern Recognition*, 20-25 June 2009, 248-255.

Deshpande, V. S., Ashby, M. F. and Fleck, N. A. (2001) 'Foam topology: bending versus stretching dominated architectures', *Acta Materialia,* 49(6), pp. 1035-1040.

Dey, S., Al-Amin, M., Rashid, T., Sultan, Z., Ashaduzzaman, M., Sarker, M. and Shamsuddin, S. (2016) 'PREPARATION, CHARACTERIZATION AND PERFORMANCE EVALUATION OF CHITOSAN AS AN ADSORBENT FOR REMAZOL RED', *International Journal of Latest Research in Engineering and Technology,* 2, pp. 52-62.

Diao, K., Zhang, L. and Zhao, Y. (2017) 'Measurement of tortuosity of porous Cu using a diffusion diaphragm cell', *Measurement,* 110, pp. 335-338.

Dong, Z. and Zhao, X. (2021) 'Application of TPMS structure in bone regeneration', *Engineered Regeneration,* 2, pp. 154-162.

Dotto, G., Souza, V., Moura, J., Moura, C. and Pinto, L. (2011) 'Influence of Drying Techniques on the Characteristics of Chitosan and the Quality of Biopolymer Films', *Drying Technology,* 29, pp. 1784-1791.

du Plessis, A., Yadroitsava, I., Yadroitsev, I., le Roux, S. G. and Blaine, D. C. (2018) 'Numerical comparison of lattice unit cell designs for medical implants by additive manufacturing', *Virtual and Physical Prototyping,* 13(4), pp. 266-281.

Dutta, S. and Bhattacharjee, J. (2022) 'Chapter 1 - A comparative study between physicochemical and biological methods for effective removal

of textile dye from wastewater', in Shah, M.P., Rodriguez-Couto, S. and Kapoor, R.T. (eds.) *Development in Wastewater Treatment Research and Processes*: Elsevier, pp. 1-21.

Dutta, S., Gupta, B., Srivastava, S. K. and Gupta, A. K. (2021) 'Recent advances on the removal of dyes from wastewater using various adsorbents: a critical review', *Materials Advances,* 2(14), pp. 4497-4531.

Dutta, S., Shreyash, N., Satapathy, B. K. and Saha, S. (2022) 'Advances in design of polymer brush functionalized inorganic nanomaterials and their applications in biomedical arena', *WIREs Nanomedicine and Nanobiotechnology,* n/a(n/a), pp. e1861.

Dutta, T., Kim, T., Vellingiri, K., Tsang, D. C. W., Shon, J. R., Kim, K.-H. and Kumar, S. (2019) 'Recycling and regeneration of carbonaceous and porous materials through thermal or solvent treatment', *Chemical Engineering Journal,* 364, pp. 514-529.

Dwamena, M. (2023) *How Long Does It Take to Cure Resin 3D Prints? â 3D Printerly*. Available at: https://3dprinterly.com/how-long-does-it-take-to-cure-resin-3d-prints/ (Accessed: 24 July 2023).

Egan, P. F. (2023) 'Design for Additive Manufacturing: Recent Innovations and Future Directions', *Designs*, 7(4). DOI: 10.3390/designs7040083.

El maguana, Y., Elhadiri, N., Benchanaa, M. and Chikri, R. (2020) 'Activated Carbon for Dyes Removal: Modeling and Understanding the Adsorption Process', *Journal of Chemistry,* 2020, pp. 2096834.

Ella, K., Fadila, M., Mahatmanti, F. W., Jumaeri, Lukman, A. and Nurul, W. (2021) 'Characterization of Chitosan Membrane Modified with Silane-

Coupled Nanosilica for Polymer Electrolyte', in Mohammed, B. (ed.) *Chitin and Chitosan*. Rijeka: IntechOpen, pp. Ch. 9.

Elliott, O., Gray, S., McClay, M., Nassief, B., Nunnelley, A., Vogt, E., Ekong, J., Kardel, K., Khoshkhoo, A., Proaño, G., Blersch, D. M. and Carrano, A. L. (2017) 'Design and Manufacturing of High Surface Area 3D-Printed Media for Moving Bed Bioreactors for Wastewater Treatment', *Journal of Contemporary Water Research & Education,* 160(1), pp. 144-156.

Elmorsi, T. (2011) 'Equilibrium Isotherms and Kinetic Studies of Removal of Methylene Blue Dye by Adsorption onto Miswak Leaves as a Natural Adsorbent', *Journal of Environmental Protection,* 02.

Elmoubarki, R., Taoufik, M., Moufti, A., Tounsadi, H., Mahjoubi, F., Bouabi, Y., Qourzal, S., Abdennouri, M. and Barka, N. 'Box-Behnken experimental design for the optimization of methylene blue adsorption onto Aleppo pine cones'.

Eltaweil, A. S., Omer, A. M., El-Aqapa, H. G., Gaber, N. M., Attia, N. F., El-Subruiti, G. M., Mohy-Eldin, M. S. and Abd El-Monaem, E. M. (2021) 'Chitosan based adsorbents for the removal of phosphate and nitrate: A critical review', *Carbohydrate Polymers,* 274, pp. 118671.

Fan, Y., Liu, Z., Zhao, G., Liu, J., Liu, Y. and Shangguan, L. (2022) 'Influence of Hydrothermal Aging under Two Typical Adhesives on the Failure of BFRP Single Lap Joint', *Polymers*, 14(9). DOI: 10.3390/polym14091721.

Fang, J., Zhang, Y., Yan, S., Liu, Z., He, S., Cui, L. and Yin, J. (2014) 'Poly(l-glutamic acid)/chitosan polyelectrolyte complex porous

microspheres as cell microcarriers for cartilage regeneration', *Acta Biomaterialia,* 10(1), pp. 276-288.

Ferreira, R. T. L., Amatte, I. C., Dutra, T. A. and Bürger, D. (2017) 'Experimental characterization and micrography of 3D printed PLA and PLA reinforced with short carbon fibers', *Composites Part B: Engineering,* 124, pp. 88-100.

Figuerola, A., Rodríguez, F., Palomino Cabello, C. and Turnes Palomino, G. (2022) 'Carbon@ceramic 3D printed devices for bisphenol A and other organic contaminants extraction', *Separation and Purification Technology,* 299, pp. 121749.

Fiore, V., Orlando, V., Sanfilippo, C., Badagliacco, D. and Valenza, A. (2020) 'Effect of Silane Coupling Treatment on the Adhesion between Polyamide and Epoxy Based Composites Reinforced with Carbon Fibers', *Fibers,* 8(8).

Fu, J., Chen, Z., Wang, M., Liu, S., Zhang, J., Zhang, J., Han, R. and Xu, Q. (2015) 'Adsorption of methylene blue by a high-efficiency adsorbent (polydopamine microspheres): Kinetics, isotherm, thermodynamics and mechanism analysis', *Chemical Engineering Journal,* 259, pp. 53-61.

Fu, Z., Cheng, J., Yang, M., Batista, J. and Jiang, Y. (2020) 'Wastewater discharge quality prediction using stratified sampling and wavelet de-noising ANFIS model', *Computers & Electrical Engineering,* 85, pp. 106701.

Fukushima, K. (1980) 'Neocognitron: A self-organizing neural network model for a mechanism of pattern recognition unaffected by shift in position', *Biological Cybernetics,* 36(4), pp. 193-202.

Fuxiang, S., Na, W., Qiangqiang, Z., Jie, W. and Bin, L. (2022) '3D printing calcium alginate adsorbents for highly efficient recovery of U(VI) in acidic conditions', *Journal of Hazardous Materials,* 440, pp. 129774.

Gadekar, M. R. and Ahammed, M. M. (2020) 'Use of water treatment residuals for colour removal from real textile dye wastewater', *Applied Water Science,* 10(7), pp. 160.

Gamage, A., Jayasinghe, N., Thiviya, P., Wasana, M. L. D., Merah, O., Madhujith, T. and Koduru, J. R. (2023) 'Recent Application Prospects of Chitosan Based Composites for the Metal Contaminated Wastewater Treatment', *Polymers*, 15(6). DOI: 10.3390/polym15061453.

Gamboa, V. S., Benvenutti, E. V., Kinast, É. J., Pires, M., Gasparin, F. P. and Ries, L. A. d. S. (2022) 'Efficient removal of chromium(VI) from dilute aqueous solutions using agro-industrial residue based on parboiled-rice husk ash', *Chemical Engineering Communications,* 209(8), pp. 1096-1110.

Gao, S., Sun, J., Liu, P., Zhang, F., Zhang, W., Yuan, S., Li, J. and Jin, J. (2016) 'A Robust Polyionized Hydrogel with an Unprecedented Underwater Anti-Crude-Oil-Adhesion Property', *Advanced Materials,* 28(26), pp. 5307-5314.

Garbin, C., Zhu, X. and Marques, O. (2020) 'Dropout vs. batch normalization: an empirical study of their impact to deep learning', *Multimedia Tools and Applications,* 79(19), pp. 12777-12815.

Ghannadpour, S. A. M., Mahmoudi, M. and Hossein Nedjad, K. (2022) 'Structural behavior of 3D-printed sandwich beams with strut-based

lattice core: Experimental and numerical study', *Composite Structures,* 281, pp. 115113.

Ghorbani, F. and Kamari, S. (2016) 'Application of response surface methodology for optimization of methyl orange adsorption by Fe-grafting sugar beet bagasse', *Adsorption Science & Technology,* 35(3-4), pp. 317-338.

Ghosal, P., Gupta, B., Ambekar, R. S., Rahman, M. M., Ajayan, P. M., Aich, N., Gupta, A. K. and Tiwary, C. S. (2021) '3D Printed Materials in Water Treatment Applications', *Advanced Sustainable Systems,* n/a(n/a), pp. 2100282.

Gibson, L. J. (2003) 'Cellular Solids', *MRS Bulletin,* 28(4), pp. 270-274.

Goswami, A., Umarji, A. and Madras, G. (2013) 'Study of Thermal Relaxation of Poly (HDDA-co-MMA) by Temperature Modulated DSC and Dielectric Spectroscopy', *Polymer-Plastics Technology and Engineering,* 52.

Grillo, F., Moulijn, J. A., Kreutzer, M. T. and van Ommen, J. R. (2018) 'Nanoparticle sintering in atomic layer deposition of supported catalysts: Kinetic modeling of the size distribution', *Catalysis Today,* 316, pp. 51-61.

Guit, J., Tavares, M. B. L., Hul, J., Ye, C., Loos, K., Jager, J., Folkersma, R. and Voet, V. S. D. (2020) 'Photopolymer Resins with Biobased Methacrylates Based on Soybean Oil for Stereolithography', *ACS Applied Polymer Materials,* 2(2), pp. 949-957.

Gul, K., Sohni, S., Waqar, M., Ahmad, F., Norulaini, N. A. N. and A. K, M. O. (2016) 'Functionalization of magnetic chitosan with graphene oxide

for removal of cationic and anionic dyes from aqueous solution', *Carbohydrate Polymers,* 152, pp. 520-531.

Habiba, U., Siddique, T. A., Li Lee, J. J., Joo, T. C., Ang, B. C. and Afifi, A. M. (2018) 'Adsorption study of methyl orange by chitosan/polyvinyl alcohol/zeolite electrospun composite nanofibrous membrane', *Carbohydrate Polymers,* 191, pp. 79-85.

Haitham, K., Razak, S. and Nawi, M. A. (2019) 'Kinetics and isotherm studies of methyl orange adsorption by a highly recyclable immobilized polyaniline on a glass plate', *Arabian Journal of Chemistry,* 12(7), pp. 1595-1606.

Haji, A. and Mahmoodi, N. M. (2012) 'Soy meal hull activated carbon: Preparation, characterization and dye adsorption properties', *Desalination and water treatment,* 44, pp. 237-244.

Hajili, E., Sugawara, A., Asoh, T.-A. and Uyama, H. (2023) 'Fabrication of 3D Hierarchically Porous Chitosan Monoliths by Thermally Induced Phase Separation of Chemically Modified Chitin', *ACS Sustainable Chemistry & Engineering,* 11(14), pp. 5473-5484.

Hammond, K. D. and Conner, W. C. (2013) 'Chapter One - Analysis of Catalyst Surface Structure by Physical Sorption', in Gates, B.C. and Jentoft, F.C. (eds.) *Advances in Catalysis*: Academic Press, pp. 1-101.

Hamzah, S., Ali, N. a., Mohammad, A. W., Ariffin, M. M. and Ali, A. (2012) 'Design of chitosan/PSf self-assembly membrane to mitigate fouling and enhance performance in trypsin separation', *Journal of Chemical Technology & Biotechnology,* 87(8), pp. 1157-1166.

Hastuti, B., Masykur, A. and Hadi, S. (2016) 'Modification of chitosan by swelling and crosslinking using epichlorohydrin as heavy metal Cr (VI) adsorbent in batik industry wastes', *IOP Conference Series: Materials Science and Engineering,* 107(1), pp. 012020.

He, C., Ramani, K. S. and Okwudire, C. E. (2023) 'An intelligent scanning strategy (SmartScan) for improved part quality in multi-laser PBF additive manufacturing', *Additive Manufacturing,* 64, pp. 103427.

Hehr, A., Wenning, J., Norfolk, M., Sheridan, J., Newman, J. A. and Domack, M. (2019) 'Selective Reinforcement of Aerospace Structures Using Ultrasonic Additive Manufacturing', *Journal of Materials Engineering and Performance,* 28(2), pp. 633-640.

Heydari Orojlou, S., Rastegarzadeh, S. and Zargar, B. (2022) 'Experimental and modeling analyses of COD removal from industrial wastewater using the TiO2–chitosan nanocomposites', *Scientific Reports,* 12(1), pp. 11088.

Ho, Y. S. and McKay, G. (1999) 'Pseudo-second order model for sorption processes', *Process Biochemistry,* 34(5), pp. 451-465.

Hopkinson, N., Hague, R. and Dickens, P. (2006) *Rapid Manufacturing: An Industrial Revolution for the Digital Age.*

Hu, Y., Ning, F., Wang, H., Cong, W. and Zhao, B. (2018) 'Laser engineered net shaping of quasi-continuous network microstructural TiB reinforced titanium matrix bulk composites: Microstructure and wear performance', *Optics & Laser Technology,* 99, pp. 174-183.

Huang, H., Chu, X., Su, H., Zhang, H., Xie, Y., Deng, W., Chen, N., Liu, F., Zhang, H., Gu, B., Deng, W. and Yang, W. (2019) 'Massively

manufactured paper-based all-solid-state flexible micro-supercapacitors with sprayable MXene conductive inks', *Journal of Power Sources,* 415, pp. 1-7.

Huang, J., Chen, Z., Wen, C., Ling, T. and Chen, Z. (2022a) 'Thermally assisted 3D printing of bio-polymer with high solute loading with improved mechanical properties', *Additive Manufacturing,* 59, pp. 103088.

Huang, J., Zhang, B., Xiao, J. and Zhang, Q. (2022b) 'An Approach to Improve the Resolution of DLP 3D Printing by Parallel Mechanism', *Applied Sciences*, 12(24). DOI: 10.3390/app122412905.

Huang, R., Liu, Q., Huo, J. and Yang, B. (2017) 'Adsorption of methyl orange onto protonated cross-linked chitosan', *Arabian Journal of Chemistry,* 10(1), pp. 24-32.

Hubs, D. (2022) *Selecting the right 3D printing process | Hubs*. Available at: https://www.hubs.com/knowledge-base/selecting-right-3d-printing-process/ (Accessed: 22 January 2022).

Husna, M. Y. N., Chong, C. H., Wong, V.-L., Cheah, K.-H. and Wan, Y. K. (2022) '3D-Printed PEGDA Monolith with Robust Silane-Grafted Chitosan for Enhanced Textile Wastewater Treatment', *Journal of Environmental Chemical Engineering*, pp. 108581.

Ip, A. W. M., Barford, J. P. and McKay, G. (2009) 'Reactive Black dye adsorption/desorption onto different adsorbents: Effect of salt, surface chemistry, pore size and surface area', *Journal of Colloid and Interface Science,* 337(1), pp. 32-38.

Iqbal, J., Wattoo, F. H., Wattoo, M. H. S., Malik, R., Tirmizi, S. A., Imran, M. and Ghangro, A. B. (2011) 'Adsorption of acid yellow dye on flakes of chitosan prepared from fishery wastes', *Arabian Journal of Chemistry,* 4(4), pp. 389-395.

Isaac, C. W. and Duddeck, F. (2022) 'Current trends in additively manufactured (3D printed) energy absorbing structures for crashworthiness application – a review', *Virtual and Physical Prototyping,* 17(4), pp. 1058-1101.

Iwuozor, K. (2019) 'Prospects and Challenges of Using Coagulation-Flocculation Method in the Treatment of Effluents', *Advanced Journal of Chemistry-Section A,* 2, pp. 105-127.

Javeed Ganaie, R., Rafiq, S. and Sharma, A. (2023) 'Recent Advances in Physico-chemical Methods for Removal of Dye from Wastewater', *IOP Conference Series: Earth and Environmental Science,* 1110(1), pp. 012040.

Jawad, A. H., Mamat, N. F. H., Hameed, B. H. and Ismail, K. (2019a) 'Biofilm of cross-linked Chitosan-Ethylene Glycol Diglycidyl Ether for removal of Reactive Red 120 and Methyl Orange: Adsorption and mechanism studies', *Journal of Environmental Chemical Engineering,* 7(2), pp. 102965.

Jawad, A. H., Norrahma, S. S. A., Hameed, B. H. and Ismail, K. (2019b) 'Chitosan-glyoxal film as a superior adsorbent for two structurally different reactive and acid dyes: Adsorption and mechanism study', *International Journal of Biological Macromolecules,* 135, pp. 569-581.

Ji, D., Xiao, C., Chen, K., Zhou, F., Gao, Y., Zhang, T. and Ling, H. (2021) 'Solvent-free green fabrication of PVDF hollow fiber MF membranes with controlled pore structure via melt-spinning and stretching', *Journal of Membrane Science,* 621, pp. 118953.

Ji, Y., Ma, Y., Ma, Y., Asenbauer, J., Passerini, S. and Streb, C. (2018) 'Water decontamination by polyoxometalate-functionalized 3D-printed hierarchical porous devices', *Chemical Communications,* 54(24), pp. 3018-3021.

Jiang, P., Ji, Z., Wang, X. and Zhou, F. (2020) 'Surface functionalization – a new functional dimension added to 3D printing', *Journal of Materials Chemistry C,* 8(36), pp. 12380-12411.

Jiang, X., Kolstein, H., Bijlaard, F. and Qiang, X. (2014) 'Effects of hygrothermal aging on glass-fibre reinforced polymer laminates and adhesive of FRP composite bridge: Moisture diffusion characteristics', *Composites Part A: Applied Science and Manufacturing,* 57, pp. 49-58.

Jin, Q., Li, Y., Yang, D. and Cui, J. (2018) 'Chitosan-derived three-dimensional porous carbon for fast removal of methylene blue from wastewater', *RSC Advances,* 8(3), pp. 1255-1264.

Jin, Z., Mei, H., Yan, Y., Pan, L., Liu, H., Xiao, S. and Cheng, L. (2021) '3D-printed controllable gradient pore superwetting structures for high temperature efficient oil-water separation', *Journal of Materiomics,* 7(1), pp. 8-18.

Jun, L. Y., Yon, L. S., Mubarak, N. M., Yeo, K. S., Khalid, M. and Bing, C. H. (2019) 'Comparison of Drying Method on Acid-functionalized Multi-walled Carbon Nanotube and their Application for Dye Removal', *IOP*

Conference Series: Materials Science and Engineering, 495(1), pp. 012057.

Kalam, S., Abu-Khamsin, S. A., Kamal, M. S. and Patil, S. (2021) 'Surfactant Adsorption Isotherms: A Review', *ACS Omega,* 6(48), pp. 32342-32348.

Kalyani, D. C., Telke, A. A., Govindwar, S. P. and Jadhav, J. P. (2009) 'Biodegradation and Detoxification of Reactive Textile Dye by Isolated Pseudomonas sp. SUK1', *Water Environment Research,* 81(3), pp. 298-307.

Kao, C. M., Chou, M. S., Fang, W. L., Liu, B. W. and Huang, B. R. (2001) 'Regulating colored textile wastewater by 3/31 wavelength admi methods in Taiwan', *Chemosphere,* 44(5), pp. 1055-1063.

Karim, A., Achiou, B., Bouazizi, A., Aaddane, A., Ouammou, M., Bouziane, M., Bennazha, J. and Alami Younssi, S. (2018) 'Development of reduced graphene oxide membrane on flat Moroccan ceramic pozzolan support. Application for soluble dyes removal', *Journal of Environmental Chemical Engineering,* 6(1), pp. 1475-1485.

Kasaai, M. R. (2008) 'A review of several reported procedures to determine the degree of N-acetylation for chitin and chitosan using infrared spectroscopy', *Carbohydrate Polymers,* 71(4), pp. 497-508.

Kasiri, M. B. (2019) '14 - Application of chitosan derivatives as promising adsorbents for treatment of textile wastewater', in Shahid ul, I. and Butola, B.S. (eds.) *The Impact and Prospects of Green Chemistry for Textile Technology*: Woodhead Publishing, pp. 417-469.

Author (2019)*: Manual Methods for Color Measurements*. Germany.

Khandaker, M., Orock, A., Tarantini, S., White, J. and Yasar, O. (2016) 'Biomechanical Performances of Networked Polyethylene Glycol Diacrylate: Effect of Photoinitiator Concentration, Temperature, and Incubation Time', *International Journal of Biomaterials,* 2016, pp. 3208312.

Khatri, J., Nidheesh, P. V., Anantha Singh, T. S. and Suresh Kumar, M. (2018) 'Advanced oxidation processes based on zero-valent aluminium for treating textile wastewater', *Chemical Engineering Journal,* 348, pp. 67-73.

Kim, H.-R., Jang, J.-W. and Park, J.-W. (2016) 'Carboxymethyl chitosan-modified magnetic-cored dendrimer as an amphoteric adsorbent', *Journal of Hazardous Materials,* 317, pp. 608-616.

Kim, K., Ratri, M. C., Choe, G., Nam, M., Cho, D. and Shin, K. (2020a) 'Three-dimensional, printed water-filtration system for economical, on-site arsenic removal', *PLOS ONE,* 15(4), pp. e0231475.

Kim, K. H., Kim, M. J., Kim, H. and Ann, K.-Y. (2020b) 'Effect of Hydrophobic Surface Treatment in Lowering Ionic Transport into Concrete', *Advances in Materials Science and Engineering,* 2020, pp. 4810259.

Kitsakis, K., Moza, Z., Iakovakis, V., Mastorakis, N. and Kechagias, J. (2015) *An investigation of dimensional accuracy of Multi-Jet Modeling parts.*

Ko, T.-J., Cho, S., Kim, S. J., Lee, Y. A., Kim, D. H., Jo, W., Kim, H.-Y., Yang, S., Oh, K. H. and Moon, M.-W. (2021) 'Direct recovery of spilled

oil using hierarchically porous oil scoop with capillary-induced anti-oil-fouling', *Journal of Hazardous Materials,* 410, pp. 124549.

Krauklis, A. E., Gagani, A. I. and Echtermeyer, A. T. (2018a) 'Hygrothermal Aging of Amine Epoxy: Reversible Static and Fatigue Properties', 8(1), pp. 447-454.

Krauklis, A. E., Gagani, A. I. and Echtermeyer, A. T. (2018b) 'Near-Infrared Spectroscopic Method for Monitoring Water Content in Epoxy Resins and Fiber-Reinforced Composites', *Materials*, 11(4). DOI: 10.3390/ma11040586.

Kumar, S., Bhushan, P. and Bhattacharya, S. (2018) 'Fabrication of Nanostructures with Bottom-up Approach and Their Utility in Diagnostics, Therapeutics, and Others', in Bhattacharya, S., Agarwal, A.K., Chanda, N., Pandey, A. and Sen, A.K. (eds.) *Environmental, Chemical and Medical Sensors*. Singapore: Springer Singapore, pp. 167-198.

Kumara, N. T. R. N., Hamdan, N., Petra, M. I., Tennakoon, K. U. and Ekanayake, P. (2014) 'Equilibrium Isotherm Studies of Adsorption of Pigments Extracted from Kuduk-kuduk (Melastoma malabathricum L.) Pulp onto TiO₂ Nanoparticles', *Journal of Chemistry,* 2014, pp. 468975.

Kumbhakar, P., Ambekar, R. S., Mahapatra, P. L. and Sekhar Tiwary, C. (2021) 'Quantifying instant water cleaning efficiency using zinc oxide decorated complex 3D printed porous architectures', *Journal of Hazardous Materials,* 418, pp. 126383.

Kumru, B., Barrio, J., Zhang, J., Antonietti, M., Shalom, M. and Schmidt, B. V. K. J. (2019) 'Robust Carbon Nitride-Based Thermoset Coatings for

Surface Modification and Photochemistry', *ACS Applied Materials & Interfaces,* 11(9), pp. 9462-9469.

Kurbanova, B., Aimaganbetov, K., Ospanov, K., Abdrakhmanov, K., Zhakiyev, N., Rakhadilov, B., Sagdoldina, Z. and Almas, N. (2023) 'Effects of Electron Beam Irradiation on Mechanical and Tribological Properties of PEEK', *Polymers*, 15(6). DOI: 10.3390/polym15061340.

Kwon, M., Choi, J.-H., Kim, J.-H., Choi, J.-H., Kim, U.-S., Hwang, K.-T., Kang, Y.-M. and Han, K.-S. (2023) 'Optimization of inorganic powder properties for manufacturing ceramic filter using binder jetting process', *Additive Manufacturing,* 70, pp. 103564.

Kyzas, G. Z., Bikiaris, D. N. and Mitropoulos, A. C. (2017) 'Chitosan adsorbents for dye removal: a review', *Polymer International,* 66(12), pp. 1800-1811.

Lasindrang, M., Suwarno, H., Tandjung, S. D. and Kamiso, H. N. (2015) 'Adsorption Pollution Leather Tanning Industry Wastewater by Chitosan Coated Coconut Shell Active Charcoal', *Agriculture and Agricultural Science Procedia,* 3, pp. 241-247.

Lazar, S., Garcia-Valdez, O., Kennedy, E., Champagne, P., Cunningham, M. and Grunlan, J. (2019) 'Crosslinkable-Chitosan-Enabled Moisture-Resistant Multilayer Gas Barrier Thin Film', *Macromolecular Rapid Communications,* 40(6), pp. 1800853.

Lebogang, K., Ntuli, F., Lekgoba, T., Kandjou, V. and Tsie, M. (2023) 'Characterization and utilization of water treatment sludge for coagulation of raw water', *Water Science and Technology,* 87(7), pp. 1587-1599.

Leceta, I., Peñalba, M., Arana, P., Guerrero, P. and de la Caba, K. (2015) 'Ageing of chitosan films: Effect of storage time on structure and optical, barrier and mechanical properties', *European Polymer Journal,* 66, pp. 170-179.

Lecun, Y., Bottou, L., Bengio, Y. and Haffner, P. (1998) 'Gradient-based learning applied to document recognition', *Proceedings of the IEEE,* 86(11), pp. 2278-2324.

Lee, J., Kim, J.-H., Choi, K., Kim, H.-G., Park, J.-A., Cho, S.-H., Hong, S. W., Lee, J.-H., Lee, J. H., Lee, S., Lee, S. Y. and Choi, J.-W. (2018) 'Investigation of the mechanism of chromium removal in (3-aminopropyl)trimethoxysilane functionalized mesoporous silica', *Scientific Reports,* 8(1), pp. 12078.

Lei, E. (2000) *The study of application the digital image technique for true color monitoring in wastewater.* masters thesis of Institute of Environmental Engineering, National Central ….

Lewicki, P. P. (2006) 'Design of hot air drying for better foods', *Trends in Food Science & Technology,* 17(4), pp. 153-163.

Li, C.-g., Dang, Q., Yang, Q., Chen, D., Zhu, H., Chen, J., Liu, R. and Wang, X. (2022a) 'Study of the microstructure of chitosan aerogel beads prepared by supercritical CO2 drying and the effect of long-term storage', *RSC Advances,* 12(33), pp. 21041-21049.

Li, D., Wang, J., Chang, Z. and Zhang, Z. (2008) 'The surface modification of silica with GPTMS', *Progress in Chemistry,* 20, pp. 1115-1121.

Li, J., Liu, Y., Campos, L. C. and Coppens, M.-O. (2021) 'Increased E. coli bio-adsorption resistance of microfiltration membranes, using a bio-inspired approach', *Science of The Total Environment,* 751, pp. 141777.

Li, J., Tong, J., Li, X., Yang, Z., Zhang, Y. and Diao, G. (2016) 'Facile microfluidic synthesis of copolymer hydrogel beads for the removal of heavy metal ions', *Journal of Materials Science,* 51(23), pp. 10375-10385.

Li, Q., Yang, D., Ma, G., Xu, Q., Chen, X., Lu, F. and Nie, J. (2009) 'Synthesis and characterization of chitosan-based hydrogels', *International Journal of Biological Macromolecules,* 44(2), pp. 121-127.

Li, Y., Peng, S., Li, K., Qin, D., Weng, Z., Li, J., Zheng, L., Wu, L. and Yu, C.-P. (2022b) 'Material extrusion-based 3D printing for the fabrication of bacteria into functional biomaterials: The case study of ammonia removal application', *Additive Manufacturing,* 60, pp. 103268.

Li, Y., Wang, X., Zhao, Z., Han, S. and Liu, Z. (2020) 'Lagoon water quality monitoring based on digital image analysis and machine learning estimators', *Water Research,* 172, pp. 115471.

Li, Y., Yu, J., Hu, S., Chen, Z., Sacchetti, M., Sun, C. C. and Yu, L. (2019) 'Polymer Nanocoating of Amorphous Drugs for Improving Stability, Dissolution, Powder Flow, and Tabletability: The Case of Chitosan-Coated Indomethacin', *Molecular Pharmaceutics,* 16(3), pp. 1305-1311.

Liakos, E. V., Lazaridou, M., Michailidou, G., Koumentakou, I., Lambropoulou, D. A., Bikiaris, D. N. and Kyzas, G. Z. (2021) 'Chitosan Adsorbent Derivatives for Pharmaceuticals Removal from Effluents: A Review', *Macromol*, 1(2), pp. 130-154. DOI: 10.3390/macromol1020011.

Liakos, I. L., Mondini, A., Dottore, E. D., Filippeschi, C., Pignatelli, F. and Mazzolai, B. (2020) '3D printed composites from heat extruded polycaprolactone/sodium alginate filaments and their heavy metal adsorption properties', *Materials Chemistry Frontiers,* 4(8), pp. 2472-2483.

Liang, J.-W., Prasad, G., Wang, S.-C., Wu, J.-L. and Lu, S.-G. (2019) 'Enhancement of the Oil Absorption Capacity of Poly(Lactic Acid) Nano Porous Fibrous Membranes Derived via a Facile Electrospinning Method', *Applied Sciences*, 9(5). DOI: 10.3390/app9051014.

Ligaray, M., Futalan, C. M., de Luna, M. D. and Wan, M.-W. (2018) 'Removal of chemical oxygen demand from thin-film transistor liquid-crystal display wastewater using chitosan-coated bentonite: Isotherm, kinetics and optimization studies', *Journal of Cleaner Production,* 175, pp. 145-154.

Ligon-Auer, S. C., Schwentenwein, M., Gorsche, C., Stampfl, J. and Liska, R. (2016) 'Toughening of photo-curable polymer networks: a review', *Polymer Chemistry,* 7(2), pp. 257-286.

Lim, H. R., Choo, C. M., Chong, C. H. and Wong, V.-L. (2021) 'Optimization studies for water defluoridation with two-stage coagulation processes using new industrial-based chemical coagulants', *Journal of Water Process Engineering,* 42, pp. 102179.

Limchoowong, N., Sricharoen, P., Techawongstien, S. and Chanthai, S. (2016) 'An iodine supplementation of tomato fruits coated with an edible film of the iodide-doped chitosan', *Food Chemistry,* 200, pp. 223-229.

Liu, D.-M., Dong, C., Zhong, J., Ren, S., Chen, Y. and Qiu, T. (2020) 'Facile preparation of chitosan modified magnetic kaolin by one-pot coprecipitation method for efficient removal of methyl orange', *Carbohydrate Polymers,* 245, pp. 116572.

Liu, L., Deng, Q.-F., Ma, T.-Y., Lin, X.-Z., Hou, X.-X., Liu, Y.-P. and Yuan, Z.-Y. (2011) 'Ordered mesoporous carbons: citric acid-catalyzed synthesis, nitrogen doping and CO2 capture', *Journal of Materials Chemistry,* 21(40), pp. 16001-16009.

Liu, S., Lo, C. K. Y. and Kan, C.-w. (2022) 'Application of artificial intelligence techniques in textile wastewater decolorisation fields: A systematic and citation network analysis review', *Coloration Technology,* 138(2), pp. 117-136.

Liu, W., Song, H. and Huang, C. (2020) 'Maximizing mechanical properties and minimizing support material of PolyJet fabricated 3D lattice structures', *Additive Manufacturing,* 35, pp. 101257.

Lollivier, G., Gressier, M., Ansart, F., Aufray, M. and Menu, M.-J. (2021) 'Influence of Hybrid Sol-Gel Crosslinker on Self-Healing Properties for Multifunctional Coatings', *Materials*, 14(18). DOI: 10.3390/ma14185382.

Lou, Y., Liu, G., Liu, S., Shen, J. and Jin, W. (2014) 'A facile way to prepare ceramic-supported graphene oxide composite membrane via silane-graft modification', *Applied Surface Science,* 307, pp. 631-637.

Lu, H., Hu, Y., Li, M., Chen, Z. and Fan, W. (2006) 'Structure characteristics and thermal properties of silane-grafted-polyethylene/clay nanocomposite prepared by reactive extrusion', *Composites Science and Technology,* 66(15), pp. 3035-3039.

Lu, Y., Cheng, L., Yang, Z., Li, J. and Zhu, H. (2020) 'Relationship between the morphological, mechanical and permeability properties of porous bone scaffolds and the underlying microstructure', *PLOS ONE,* 15(9), pp. e0238471.

Luk, C. (2015) 'Study of Freeze-dried Chitosan Beads Encapsulating Live Lactic Acid Bacteria for Removal of Reactive Dyes', *Journal of Fiber Bioengineering and Informatics,* 8.

Lung, C. Y. K. and Matinlinna, J. P. (2010) 'Resin Bonding to Silicatized Zirconia with Two Isocyanatosilanes and a Cross-linking Silane. Part II: Mechanistic Approach', *Silicon,* 2(3), pp. 163-169.

Luo, P., Zhao, Y., Zhang, B., Liu, J., Yang, Y. and Liu, J. (2010) 'Study on the adsorption of Neutral Red from aqueous solution onto halloysite nanotubes', *Water Research,* 44(5), pp. 1489-1497.

Luthfiyana, N., Bija, S., Anwar, E., Laksmitawati, D. R., Nugraeni, C. D., Nusaibah and Mutmaina (2022) 'Characteristics of Nanochitosan from Soft Shell Crab Culture Waste in TarakanUsing The Ionic Gelation Method', *IOP Conference Series: Earth and Environmental Science,* 1083(1), pp. 012078.

Lv, J., Jin, W., Liu, W., Qin, X., Feng, Y., Bai, J., Wu, Z. and Li, J. (2022) 'Selective Laser Melting Fabrication of Porous Ti6Al4V Scaffolds With Triply Periodic Minimal Surface Architectures: Structural Features, Cytocompatibility, and Osteogenesis', *Frontiers in Bioengineering and Biotechnology,* 10.

Lyu, Z., Ng, T. C. A., Tran-Duc, T., Lim, G. J. H., Gu, Q., Zhang, L., Zhang, Z., Ding, J., Phan-Thien, N., Wang, J. and Ng, H. Y. (2020) '3D-

printed surface-patterned ceramic membrane with enhanced performance in crossflow filtration', *Journal of Membrane Science,* 606, pp. 118138.

Ma, S. and Liu, H. (2022) 'Effects of 3D-printed bulking agent on microbial community succession and carbohydrate-active enzymes genes during swine manure composting', *Chemosphere,* 306, pp. 135513.

Ma, S., Liu, W., Wei, Z. and Li, H. (2010) 'Mechanical and Thermal Properties and Morphology of Epoxy Resins Modified by a Silicon Compound', *Journal of Macromolecular Science, Part A,* 47, pp. 1084-1090.

Ma, Y., Xie, Q. and Wang, X. (2019) 'Investigations on thermal properties of microencapsulated phase-change materials with different acrylate-based copolymer shells as thermal insulation materials', *Journal of Applied Polymer Science,* 136(31), pp. 47777.

Madihally, S. V. and Matthew, H. W. T. (1999) 'Porous chitosan scaffolds for tissue engineering', *Biomaterials,* 20(12), pp. 1133-1142.

Madrakian, T., Afkhami, A., Ahmadi, M. and Bagheri, H. (2011) 'Removal of some cationic dyes from aqueous solutions using magnetic-modified multi-walled carbon nanotubes', *Journal of Hazardous Materials,* 196, pp. 109-114.

Mahmodi, G., Zarrintaj, P., Taghizadeh, A., Taghizadeh, M., Manouchehri, S., Dangwal, S., Ronte, A., Ganjali, M. R., Ramsey, J. D., Kim, S.-J. and Saeb, M. R. (2020) 'From microporous to mesoporous

mineral frameworks: An alliance between zeolite and chitosan', *Carbohydrate Research,* 489, pp. 107930.

Mahmoodi, H., Fattahi, M. and Motevassel, M. (2021) 'Graphene oxide–chitosan hydrogel for adsorptive removal of diclofenac from aqueous solution: preparation, characterization, kinetic and thermodynamic modelling', *RSC Advances,* 11(57), pp. 36289-36304.

Mansouri, L., Djebbar, A., Khatir, S. and Abdel Wahab, M. (2019) 'Effect of hygrothermal aging in distilled and saline water on the mechanical behaviour of mixed short fibre/woven composites', *Composite Structures,* 207, pp. 816-825.

Mao, H., Wei, C., Gong, Y., Wang, S. and Ding, W. (2019) 'Mechanical and Water-Resistant Properties of Eco-Friendly Chitosan Membrane Reinforced with Cellulose Nanocrystals', *Polymers*, 11(1). DOI: 10.3390/polym11010166.

Marrone, M. (2020) *Temperature Control of Wastewater During Water Treatment Process | Cold Shot*. Available at: https://waterchillers.com/blog/post/temperature-control-of-wastewater-process (Accessed: 22 March 2022).

Mastalerz, C., Vroman, I., Coqueret, X. and Alix, S. (2021) 'Effects of Electron Beam Irradiation on 3D-Printed Biopolymers for Bone Tissue Engineering', *Journal of Composites Science*, 5(7). DOI: 10.3390/jcs5070182.

Mella, C., Vega-Gálvez, A., Uribe, E., Pasten, A., Mejias, N. and Quispe-Fuentes, I. (2022) 'Impact of vacuum drying on drying characteristics and

functional properties of beetroot (Beta vulgaris)', *Applied Food Research,* 2(1), pp. 100120.

Miller, A. C. and Berg, J. C. (2002) 'Predicting adhesion between a crystalline polymer and silane-treated glass surfaces in filled composites', *Journal of Adhesion Science and Technology,* 16(14), pp. 1949-1956.

Milosavljević, N. B., Ristić, M. Đ., Perić-Grujić, A. A., Filipović, J. M., Štrbac, S. B., Rakočević, Z. L. and Krušić, M. T. K. (2011) 'Removal of Cu2+ ions using hydrogels of chitosan, itaconic and methacrylic acid: FTIR, SEM/EDX, AFM, kinetic and equilibrium study', *Colloids and Surfaces A: Physicochemical and Engineering Aspects,* 388(1), pp. 59-69.

Mirzaie, M., Rashidi, A., Tayebi, H.-A. and Yazdanshenas, M. E. (2017) 'Removal of Anionic Dye from Aqueous Media by Adsorption onto SBA-15/Polyamidoamine Dendrimer Hybrid: Adsorption Equilibrium and Kinetics', *Journal of Chemical & Engineering Data,* 62(4), pp. 1365-1376.

Mishima, K., Deng, Y., Feng, S., Abe, M., Miyamoto, N. and Kano, N. (2019) 'Combined Experimental and Quantum Chemistry Studies on the pH Dependence of the Adsorption Efficiency of Uranium(VI): Lewis Theory of Acid–Base Reactions in Adsorption Processes', *The Journal of Physical Chemistry C,* 123(2), pp. 1032-1040.

Mohammad, A.-T., Abdulhameed, A. S. and Jawad, A. H. (2019) 'Box-Behnken design to optimize the synthesis of new crosslinked chitosan-glyoxal/TiO2 nanocomposite: Methyl orange adsorption and mechanism

studies', *International Journal of Biological Macromolecules,* 129, pp. 98-109.

Mohd Yusoff, N. H., Chong, C. H., Wan, Y. K., Cheah, K. H. and Wong, V. L. (2023) 'Optimization strategies and emerging application of functionalized 3D-printed materials in water treatment: A review', *Journal of Water Process Engineering,* 51, pp. 103410.

Mohd Yusoff, N. H., Irene Teo, L.-R., Phang, S. J., Wong, V.-L., Cheah, K. H. and Lim, S.-S. (2022) 'Recent Advances in Polymer-based 3D Printing for Wastewater Treatment Application: An Overview', *Chemical Engineering Journal,* 429, pp. 132311.

Mondal, P., Baksi, S. and Bose, D. (2016) 'Study of environmental issues in textile industries and recent wastewater treatment technology', *The Scientific World Journal,* 61, pp. 98.

Montazerian, H., Mohamed, M. G. A., Montazeri, M. M., Kheiri, S., Milani, A. S., Kim, K. and Hoorfar, M. (2019) 'Permeability and mechanical properties of gradient porous PDMS scaffolds fabricated by 3D-printed sacrificial templates designed with minimal surfaces', *Acta Biomaterialia,* 96, pp. 149-160.

Moosavi, S., Lai, C. W., Gan, S., Zamiri, G., Akbarzadeh Pivehzhani, O. and Johan, M. R. (2020) 'Application of Efficient Magnetic Particles and Activated Carbon for Dye Removal from Wastewater', *ACS Omega,* 5(33), pp. 20684-20697.

Morsi, R. and Elsalamony, R. (2019) 'Effect of cationic, anionic and non-ionic polymeric surfactants on the stability, photo-catalytic and

antimicrobial activities of yttrium oxide nanofluids', *Journal of Molecular Liquids,* 297, pp. 111848.

Mostafaei, A., Elliott, A. M., Barnes, J. E., Li, F., Tan, W., Cramer, C. L., Nandwana, P. and Chmielus, M. (2021) 'Binder jet 3D printing—Process parameters, materials, properties, modeling, and challenges', *Progress in Materials Science,* 119, pp. 100707.

Mostofi Sarkari, N., Doğan, Ö., Bat, E., Mohseni, M. and Ebrahimi, M. (2020) 'Tethering vapor-phase deposited GLYMO coupling molecules to silane-crosslinked polyethylene surface via plasma grafting approaches', *Applied Surface Science,* 513, pp. 145846.

Nagi, J., Ducatelle, F., Caro, G. A. D., Cireşan, D., Meier, U., Giusti, A., Nagi, F., Schmidhuber, J. and Gambardella, L. M. 'Max-pooling convolutional neural networks for vision-based hand gesture recognition'. *2011 IEEE International Conference on Signal and Image Processing Applications (ICSIPA)*, 16-18 Nov. 2011, 342-347.

Nakamura, T., Tabuchi, H., Hirai, T., Fujii, S. and Nakamura, Y. (2020) 'Effects of silane coupling agent hydrophobicity and loading method on water absorption and mechanical strength of silica particle-filled epoxy resin', *Journal of Applied Polymer Science,* 137(17), pp. 48615.

Nam, C., Yoon, J., Ryu, S. A., Choi, C.-H. and Lee, H. (2018) 'Water and Oil Insoluble PEGDA-Based Microcapsule: Biocompatible and Multicomponent Encapsulation', *ACS Applied Materials & Interfaces,* 10(47), pp. 40366-40371.

Nambafu, G. S., Kim, N. and Kim, J. (2022) 'Hydrophobic coatings prepared using various dipodal silane-functionalized polymer precursors', *Applied Surface Science Advances,* 7, pp. 100207.

Nandini, R. and Vishalakshi, B. (2012) 'A Study of Interaction of Methyl Orange with Some Polycations', *E-Journal of Chemistry,* 9, pp. 343928.

Nazir, A., Gokcekaya, O., Md Masum Billah, K., Ertugrul, O., Jiang, J., Sun, J. and Hussain, S. (2023) 'Multi-material additive manufacturing: A systematic review of design, properties, applications, challenges, and 3D printing of materials and cellular metamaterials', *Materials & Design,* 226, pp. 111661.

Ngo, T. D., Kashani, A., Imbalzano, G., Nguyen, K. T. Q. and Hui, D. (2018) 'Additive manufacturing (3D printing): A review of materials, methods, applications and challenges', *Composites Part B: Engineering,* 143, pp. 172-196.

Niu, Y., Yu, M., Meka, A., Liu, Y., Zhang, J., Yang, Y. and Yu, C. (2016) 'Understanding the contribution of surface roughness and hydrophobic modification of silica nanoparticles to enhanced therapeutic protein delivery', *Journal of Materials Chemistry B,* 4(2), pp. 212-219.

Norsaliza, U. and Ismail, M. H. (2010) 'Use of Remote Sensing and GIS in Monitoring Water Quality', *Journal of Sustainable Development,* 3.

Novikov, V. Y., Derkach, S. R., Konovalova, I. N., Dolgopyatova, N. V. and Kuchina, Y. A. (2023) 'Mechanism of Heterogeneous Alkaline Deacetylation of Chitin: A Review', *Polymers*, 15(7). DOI: 10.3390/polym15071729.

Nowak, D. and Jakubczyk, E. (2020) 'The Freeze-Drying of Foods—The Characteristic of the Process Course and the Effect of Its Parameters on the Physical Properties of Food Materials', *Foods*, 9(10). DOI: 10.3390/foods9101488.

Okey-Onyesolu, C. F., Chukwuma, E. C., Okoye, C. C. and Onukwuli, O. D. (2020) 'Response Surface Methodology optimization of chito-protein synthesized from crab shell in treatment of abattoir wastewater', *Heliyon,* 6(10), pp. e05186-e05186.

Oloo, C. M., Onyari, J. M., Wanyonyi, W. C., Wabomba, J. N. and Muinde, V. M. (2020) 'Adsorptive removal of hazardous crystal violet dye form aqueous solution using Rhizophora mucronata stem-barks: Equilibrium and kinetics studies', *Environmental Chemistry and Ecotoxicology,* 2, pp. 64-72.

Otalvaro, J. O., Avena, M. and Brigante, M. (2019) 'Adsorption of organic pollutants by amine functionalized mesoporous silica in aqueous solution. Effects of pH, ionic strength and some consequences of APTES stability', *Journal of Environmental Chemical Engineering,* 7(5), pp. 103325.

Pagac, M., Hajnys, J., Ma, Q.-P., Jancar, L., Jansa, J., Stefek, P. and Mesicek, J. (2021) 'A Review of Vat Photopolymerization Technology: Materials, Applications, Challenges, and Future Trends of 3D Printing', *Polymers,* 13(4).

Pang, Y. L. and Abdullah, A. Z. (2013) 'Current Status of Textile Industry Wastewater Management and Research Progress in Malaysia: A Review', *CLEAN – Soil, Air, Water,* 41(8), pp. 751-764.

Pantani, R. and Sorrentino, A. (2013) 'Influence of crystallinity on the biodegradation rate of injection-moulded poly(lactic acid) samples in controlled composting conditions', *Polymer Degradation and Stability,* 98(5), pp. 1089-1096.

Parikh, D. (2015) 'Vacuum Drying: Basics and Application', *Chemical Engineering,* 122.

Pei, R., Fan, L., Zhao, F., Xiao, J., Yang, Y., Lai, A., Zhou, S.-F. and Zhan, G. (2020) '3D-Printed metal-organic frameworks within biocompatible polymers as excellent adsorbents for organic dyes removal', *Journal of Hazardous Materials,* 384, pp. 121418.

Phang, S. J., Wong, V.-L., Cheah, K. H. and Tan, L.-L. (2021) '3D-printed photoreactor with robust g-C3N4 homojunction based thermoset coating as a new and sustainable approach for photocatalytic wastewater treatment', *Journal of Environmental Chemical Engineering,* 9(6), pp. 106437.

Piao, M., Du, H., Sun, Y. and Teng, H. (2022) 'Self-regeneration hybrid hydrogel for bisphenol a adsorption in water', *Environmental Science and Pollution Research*.

Piatkowski, M., Janus, Ł., Radwan-Pragłowska, J. and Raclavsky, K. (2017) 'Microwave-enhanced synthesis of biodegradable multifunctional chitosan hydrogels for wastewater treatment', *Express Polymer Letters,* 11, pp. 809-819.

Pimraksa, K., Setthaya, N., Thala, M., Chindaprasirt, P. and Murayama, M. (2020) 'Geopolymer/Zeolite composite materials with adsorptive and

photocatalytic properties for dye removal', *PLOS ONE,* 15(10), pp. e0241603.

Pitakpoolsil, W. and Hunsom, M. (2014) 'Treatment of biodiesel wastewater by adsorption with commercial chitosan flakes: Parameter optimization and process kinetics', *Journal of Environmental Management,* 133, pp. 284-292.

Pollard, S. J. T., Fowler, G. D., Sollars, C. J. and Perry, R. (1992) 'Low-cost adsorbents for waste and wastewater treatment: a review', *Science of The Total Environment,* 116(1), pp. 31-52.

Potgieter, J. H., Pardesi, C. and Pearson, S. (2021) 'A kinetic and thermodynamic investigation into the removal of methyl orange from wastewater utilizing fly ash in different process configurations', *Environmental Geochemistry and Health,* 43(7), pp. 2539-2550.

Prakoso, A. T., Basri, H., Adanta, D., Yani, I., Ammarullah, M. I., Akbar, I., Ghazali, F. A., Syahrom, A. and Kamarul, T. (2023) 'The Effect of Tortuosity on Permeability of Porous Scaffold', *Biomedicines*, 11(2). DOI: 10.3390/biomedicines11020427.

Prevot, V. and Tokudome, Y. (2017) '3D hierarchical and porous layered double hydroxide structures: an overview of synthesis methods and applications', *Journal of Materials Science,* 52(19), pp. 11229-11250.

Proano-Pena, G., Carrano, A. L. and Blersch, D. M. (2020) 'Analysis of very-high surface area 3D-printed media in a moving bed biofilm reactor for wastewater treatment', *PLOS ONE,* 15(8), pp. e0238386.

Pullagura, B. K., Amarapalli, S. and Gundabala, V. (2021) 'Coupling electrohydrodynamics with photopolymerization for microfluidics-based

generation of polyethylene glycol diacrylate (PEGDA) microparticles and hydrogels', *Colloids and Surfaces A: Physicochemical and Engineering Aspects,* 608, pp. 125586.

Qamar, S. A., Ashiq, M., Jahangeer, M., Riasat, A. and Bilal, M. (2020) 'Chitosan-based hybrid materials as adsorbents for textile dyes–A review', *Case Studies in Chemical and Environmental Engineering,* 2, pp. 100021.

Qin, Y., Shen, H., Han, L., Zhu, Z., Pan, F., Yang, S. and Yin, X. (2020) 'Mechanically Robust Janus Poly(lactic acid) Hybrid Fibrous Membranes toward Highly Efficient Switchable Separation of Surfactant-Stabilized Oil/Water Emulsions', *ACS Applied Materials & Interfaces,* 12(45), pp. 50879-50888.

Qiu, Y., Hamilton, S. K. and Temenoff, J. (2011) '4 - Improving mechanical properties of injectable polymers and composites', in Vernon, B. (ed.) *Injectable Biomaterials*: Woodhead Publishing, pp. 61-91.

Quan, H., Zhang, T., Xu, H., Luo, S., Nie, J. and Zhu, X. (2020) 'Photo-curing 3D printing technique and its challenges', *Bioactive Materials,* 5(1), pp. 110-115.

Quero, R. F., Domingos da Silveira, G., Fracassi da Silva, J. A. and Jesus, D. P. d. (2021) 'Understanding and improving FDM 3D printing to fabricate high-resolution and optically transparent microfluidic devices', *Lab on a Chip,* 21(19), pp. 3715-3729.

Quiévy, N., Jacquet, N., Sclavons, M., Deroanne, C., Paquot, M. and Devaux, J. (2010) 'Influence of homogenization and drying on the thermal

stability of microfibrillated cellulose', *Polymer Degradation and Stability,* 95(3), pp. 306-314.

Raheem, A. (2018) 'Characteristics of the Effluent Wastewater in Sewage Treatment Plants of Malaysian Urban Areas', *Chemical Engineering Transactions,* 63.

Rajaram, A. N., Gin Boay, C. and Srikanth, N. (2020) 'Effect of curing on the hygrothermal behaviour of epoxy and its carbon composite material', *Composites Communications,* 22, pp. 100507.

Ramakrishna, D. and Bala Murali, G. (2022) 'Bio-inspired 3D-printed lattice structures for energy absorption applications: A review', *Proceedings of the Institution of Mechanical Engineers, Part L: Journal of Materials: Design and Applications,* 237(3), pp. 503-542.

Ratti, C. (2001) 'Hot air and freeze-drying of high-value foods: a review', *Journal of Food Engineering,* 49(4), pp. 311-319.

Rekowska, N., Arbeiter, D., Brietzke, A., Konasch, J., Riess, A., Mau, R., Eickner, T., Seitz, H., Grabow, N. and Teske, M. 'Biocompatibility and thermodynamic properties of PEGDA and two of its copolymer'. *2019 41st Annual International Conference of the IEEE Engineering in Medicine and Biology Society (EMBC)*, 23-27 July 2019, 1093-1096.

Rekowska, N., Huling, J., Brietzke, A., Arbeiter, D., Eickner, T., Konasch, J., Riess, A., Mau, R., Seitz, H., Grabow, N. and Teske, M. (2022) 'Thermal, Mechanical and Biocompatibility Analyses of Photochemically Polymerized PEGDA250 for Photopolymerization-Based Manufacturing Processes', *Pharmaceutics*, 14(3). DOI: 10.3390/pharmaceutics14030628.

Ren, L., Xu, J., Zhang, Y., Zhou, J., Chen, D. and Chang, Z. (2019) 'Preparation and characterization of porous chitosan microspheres and adsorption performance for hexavalent chromium', *International Journal of Biological Macromolecules,* 135, pp. 898-906.

Reyes-Peces, M. V., Pérez-Moreno, A., de-los-Santos, D. M., Mesa-Díaz, M. D., Pinaglia-Tobaruela, G., Vilches-Pérez, J. I., Fernández-Montesinos, R., Salido, M., de la Rosa-Fox, N. and Piñero, M. (2020) 'Chitosan-GPTMS-Silica Hybrid Mesoporous Aerogels for Bone Tissue Engineering', *Polymers,* 12(11).

Riveiro, A., Maçon, A. L. B., del Val, J., Comesaña, R. and Pou, J. (2018) 'Laser Surface Texturing of Polymers for Biomedical Applications', *Frontiers in Physics,* 6, pp. 16.

Rosso, M., van Steijn, V., de Smet, L. C. P. M., Sudhölter, E. J. R., Kleijn, C. R. and Kreutzer, M. T. (2011) 'Reaction-diffusion analysis for one-step plasma etching and bonding of microfluidic devices', *Applied Physics Letters,* 98(17), pp. 174102.

Rouf, S., Malik, A., Singh, N., Raina, A., Naveed, N., Siddiqui, M. I. H. and Haq, M. I. U. (2022) 'Additive manufacturing technologies: Industrial and medical applications', *Sustainable Operations and Computers,* 3, pp. 258-274.

Sabatini, V., Pargoletti, E., Longoni, M., Farina, H., Ortenzi, M. A. and Cappelletti, G. (2019) 'Stearyl methacrylate co-polymers: Towards new polymer coatings for mortars protection', *Applied Surface Science,* 488, pp. 213-220.

Sadeghi-Kiakhani, M., Arami, M. and Gharanjig, K. (2013) 'Dye removal from colored-textile wastewater using chitosan-PPI dendrimer hybrid as a biopolymer: Optimization, kinetic, and isotherm studies', *Journal of Applied Polymer Science,* 127(4), pp. 2607-2619.

Saha, B., Debnath, A. and Saha, B. (2022) 'Fabrication of PANI@Fe–Mn–Zr hybrid material and assessments in sono-assisted adsorption of methyl red dye: Uptake performance and response surface optimization', *Journal of the Indian Chemical Society,* 99(9), pp. 100635.

Saha, P. and Chowdhury, S. (2011) 'Insight Into Adsorption Thermodynamics', *Thermodynamics*.

Saha, T. and Bhoumik, N. (2010) 'Adsorption of Methyl Orange onto Chitosan from Aqueous Solution', *J. Water Resource and Protection,* 2, pp. 898-906.

Sahrir, C. D., Ruslin, M., Lee, S.-Y. and Lin, W.-C. (2023) 'Effect of various post-curing light intensities, times, and energy levels on the color of 3D-printed resin crowns', *Journal of Dental Sciences*.

Saidulu, D., Srivastava, A. and Gupta, A. K. (2022) 'Enhancement of wastewater treatment performance using 3D printed structures: A major focus on material composition, performance, challenges, and sustainable assessment', *Journal of Environmental Management,* 306, pp. 114461.

Sajab, M. S., Chia, C. H., Zakaria, S. and Khiew, P. S. (2013) 'Cationic and anionic modifications of oil palm empty fruit bunch fibers for the removal of dyes from aqueous solutions', *Bioresource Technology,* 128, pp. 571-577.

Samuels, R. J. (1981) 'Solid state characterization of the structure of chitosan films', *Journal of Polymer Science: Polymer Physics Edition,* 19(7), pp. 1081-1105.

Segura, L. J., Li, Z., Zhou, C. and Sun, H. (2023) 'Droplet evolution prediction in material jetting via tensor time series analysis', *Additive Manufacturing,* 66, pp. 103461.

Sela, S. K., Hossain, A. K. M. N.-U., Hussain, S. Z. and Hasan, N. (2020) 'Utilization of prawn to reduce the value of BOD and COD of textile wastewater', *Cleaner Engineering and Technology,* 1, pp. 100021.

Shah, S. S., Sharma, T., Dar, B. A. and Bamezai, R. K. (2021) 'Adsorptive removal of methyl orange dye from aqueous solution using populous leaves: Insights from kinetics, thermodynamics and computational studies', *Environmental Chemistry and Ecotoxicology,* 3, pp. 172-181.

Shahbazi, M., Jäger, H., Ahmadi, S. J. and Lacroix, M. (2020) 'Electron beam crosslinking of alginate/nanoclay ink to improve functional properties of 3D printed hydrogel for removing heavy metal ions', *Carbohydrate Polymers,* 240, pp. 116211.

Shahzadi, L., Maya, F., Breadmore, M. C. and Thickett, S. C. (2022) 'Functional Materials for DLP-SLA 3D Printing Using Thiol–Acrylate Chemistry: Resin Design and Postprint Applications', *ACS Applied Polymer Materials,* 4(5), pp. 3896-3907.

Sharma, P. and Kaur, H. (2011) 'Sugarcane bagasse for the removal of erythrosin B and methylene blue from aqueous waste', *Applied Water Science,* 1.

Shaukat, U., Sölle, B., Rossegger, E., Rana, S. and Schlögl, S. (2022) 'Vat Photopolymerization 3D-Printing of Dynamic Thiol-Acrylate Photopolymers Using Bio-Derived Building Blocks', *Polymers*, 14(24). DOI: 10.3390/polym14245377.

Shen, T., Jiang, C., Wang, C., Sun, J., Wang, X. and Li, X. (2015) 'A TiO2 modified abiotic–biotic process for the degradation of the azo dye methyl orange', *RSC Advances,* 5(72), pp. 58704-58712.

Shi, Z., Xu, C., Chen, F., Wang, Y., Li, L., Meng, Q. and Zhang, R. (2017) 'Renewable metal–organic-frameworks-coated 3D printing film for removal of malachite green', *RSC Advances,* 7(79), pp. 49947-49952.

Shimoda, M., Hikasa, M. and Ali, M. A. (2023) 'Micropore shape optimization of porous laminated shell structures', *Additive Manufacturing,* 69, pp. 103530.

Shin, C. S. and Chang, Y. C. (2021) 'Fabrication and Compressive Behavior of a Micro-Lattice Composite by High Resolution DLP Stereolithography', *Polymers*, 13(5). DOI: 10.3390/polym13050785.

Shin, J.-H., Yang, J. E., Park, J. E., Jeong, S.-W., Choi, S.-J., Choi, Y. J. and Jeon, J. (2022) 'Rapid and Efficient Removal of Anionic Dye in Water Using a Chitosan-Coated Iron Oxide-Immobilized Polyvinylidene Fluoride Membrane', *ACS Omega,* 7(10), pp. 8759-8766.

Shirosaki, Y., Okabayashi, T. and Yasutomi, S. (2020) 'Silane Coupling Agent Modifies the Mechanical Properties of a Chitosan Microfiber', *Molecules,* 25(22).

Shukla, N. B., Rattan, S. and Madras, G. (2012) 'Swelling and Dye-Adsorption Characteristics of an Amphoteric Superabsorbent Polymer', *Industrial & Engineering Chemistry Research,* 51(46), pp. 14941-14948.

Simonin, J.-P. (2016) 'On the comparison of pseudo-first order and pseudo-second order rate laws in the modeling of adsorption kinetics', *Chemical Engineering Journal,* 300, pp. 254-263.

Singh, R., Souillard, G., Chassat, L., Gao, Y., Mulet, X. and Doherty, C. M. (2020) 'Fabricating Bioactive 3D Metal–Organic Framework Devices', *Advanced Sustainable Systems,* 4(12), pp. 2000059.

Soares, A. d. S., Ramos, A. M., Vieira, É. N. R., Vanzela, E. S. L., de Oliveira, P. M. and Paula, D. d. A. (2018) 'Vacuum impregnation of chitosan-based edible coating in minimally processed pumpkin', *International Journal of Food Science & Technology,* 53(9), pp. 2229-2238.

Sokollu, B., Gulcan, O. and Konukseven, E. I. (2022) 'Mechanical properties comparison of strut-based and triply periodic minimal surface lattice structures produced by electron beam melting', *Additive Manufacturing,* 60, pp. 103199.

Song, H., Xie, J., Yin, P., Fu, H., Zhang, Y. and Yan, C. (2024) 'The investigation of the particle shape effect on the permeability of porous media through lattice Boltzmann simulation and experimental study', *International Journal of Thermal Sciences,* 201, pp. 108983.

Song, W., Xu, J., Gao, L., Zhang, Q., Tong, J. and Ren, L. (2021) 'Preparation of Freeze-Dried Porous Chitosan Microspheres for the

Removal of Hexavalent Chromium', *Applied Sciences*, 11(9). DOI: 10.3390/app11094217.

Song, Y., Wang, B., Altemose, P., Kowall, C. and Li, L. (2020) '3D-Printed Membranes with a Zwitterionic Hydrogel Coating for More Robust Oil–Water Separation', *Industrial & Engineering Chemistry Research,* 59(48), pp. 21058-21065.

Srinivasan, R., Suresh Babu, B., Udhaya Rani, V., Suganthi, M. and Dheenasagar, R. (2020) 'Comparision of tribological behaviour for parts fabricated through fused deposition modelling (FDM) process on abs and 20% carbon fibre PLA', *Materials Today: Proceedings,* 27, pp. 1780-1786.

Srivastava, V. and Choubey, A. K. (2021) 'Investigation of adsorption of organic dyes present in wastewater using chitosan beads immobilized with biofabricated CuO nanoparticles', *Journal of Molecular Structure,* 1242, pp. 130749.

Srivatsav, P., Bhargav, B., Shanmugasundaram, V., Jayaseelan, A., Kannappan Panchamoorthy, G. and Bhatnagar, A. (2020) 'Biochar as an Eco-Friendly and Economical Adsorbent for the Removal of Colorants (Dyes) from Aqueous Environment: A Review', *Water,* 12, pp. 3561.

Stefanakis, A. (2015) 'Modern water reuse technologies', pp. 371-382.

Stwora, A. and Skrabalak, G. (2013) 'Influence of selected parameters of selective laser sintering process on properties of sintered materials', *Journal of Achievements in Materials and Manufacturing Engineering,* 61(2), pp. 375-380.

Su, H., Liu, H., Jiang, H., Shen, Z., Chen, Q., Yu, M., Zhao, D., Li, X., Dong, D. and Zhang, Z. (2023) 'One-step preparation of melt-grown Al2O3/GdAlO3/ZrO2 eutectic ceramics with large size and irregular shape by directed energy deposition', *Additive Manufacturing,* 70, pp. 103563.

Su, X.-J., Zhang, C.-Y., Li, W.-J., Wang, F., Wang, K.-Q., Liu, Y. and Li, Q.-M. (2020) 'Radiation-Induced Structural Changes of Miscanthus Biomass', *Applied Sciences*, 10(3). DOI: 10.3390/app10031130.

Sultan, S. and Bekeneva, Y. (2022) 'A Comparative Analysis of a Designed CNN and AlexNet for Image Classification on Small Datasets', pp. 441-446.

Surya, I., Hazwan, C. M., Abdul Khalil, H. P. S., Yahya, E. B., Suriani, A. B., Danish, M. and Mohamed, A. (2022) 'Hydrophobicity and Biodegradability of Silane-Treated Nanocellulose in Biopolymer for High-Grade Packaging Applications', *Polymers*, 14(19). DOI: 10.3390/polym14194147.

Suwanboriboon, J., Meesiri, W. and Wongkokua, W. (2018) 'An application of spectrophotometer for ADMI color measurement', *Journal of Physics: Conference Series,* 1144(1), pp. 012064.

Szyguła, A., Guibal, E., Ruiz, M. and Sastre, A. M. (2008) 'The removal of sulphonated azo-dyes by coagulation with chitosan', *Colloids and Surfaces A: Physicochemical and Engineering Aspects,* 330(2), pp. 219-226.

Szygula, A., Ruiz, M., Guibal, E. and Sastre, A. (2008) *Removal of an Anionic Reactive Dye by Chitosan and its Regeneration.*

Szymańska, E. and Winnicka, K. (2015) 'Stability of Chitosan—A Challenge for Pharmaceutical and Biomedical Applications', *Marine Drugs*, 13(4), pp. 1819-1846. DOI: 10.3390/md13041819.

Tahari, N., de Hoyos-Martinez, P. L., Izaguirre, N., Houwaida, N., Abderrabba, M., Ayadi, S. and Labidi, J. (2022) 'Preparation of chitosan/tannin and montmorillonite films as adsorbents for Methyl Orange dye removal', *International Journal of Biological Macromolecules,* 210, pp. 94-106.

Takeshita, S., Zhao, S., Malfait, W. J. and Koebel, M. M. (2021) 'Chemistry of Chitosan Aerogels: Three-Dimensional Pore Control for Tailored Applications', *Angewandte Chemie International Edition,* 60(18), pp. 9828-9851.

Tan, G., Ouyang, K., Wang, H., Zhou, L., Wang, X., Liu, Y., Zhang, L. and Ning, C. (2016a) 'Effect of Amino-, Methyl- and Epoxy-Silane Coupling as a Molecular Bridge for Formatting a Biomimetic Hydroxyapatite Coating on Titanium by Electrochemical Deposition', *Journal of Materials Science & Technology,* 32(9), pp. 956-965.

Tan, L. J., Zhu, W. and Zhou, K. (2020) 'Recent Progress on Polymer Materials for Additive Manufacturing', *Advanced Functional Materials,* 30(43), pp. 2003062.

Tan, W. S., Chua, C. K., Chong, T. H., Fane, A. G. and Jia, A. (2016b) '3D printing by selective laser sintering of polypropylene feed channel spacers for spiral wound membrane modules for the water industry', *Virtual and Physical Prototyping,* 11(3), pp. 151-158.

Tang, B., Zhao, Y., Bin, L., Huang, S. and Fu, F. (2017) 'Variation of the characteristics of biofilm on the semi-suspended bio-carrier produced by a 3D printing technique: Investigation of a whole growing cycle', *Bioresource Technology,* 244, pp. 40-47.

Teh, C. Y., Budiman, P. M., Shak, K. P. Y. and Wu, T. Y. (2016) 'Recent Advancement of Coagulation–Flocculation and Its Application in Wastewater Treatment', *Industrial & Engineering Chemistry Research,* 55(16), pp. 4363-4389.

Theivarasu, C. and Mylsamy, S. (2011) 'Removal of Malachite Green from Aqueous Solution by Activated Carbon Developed from Cocoa (Theobroma Cacao) Shell - A Kinetic and Equilibrium Studies', *E-Journal of Chemistry,* 8, pp. 714808.

Thiessen, M. and Abetz, V. (2021) 'Influence of the Glass Transition Temperature and the Density of Crosslinking Groups on the Reversibility of Diels-Alder Polymer Networks', *Polymers*, 13(8). DOI: 10.3390/polym13081189.

Thukral, D. K., Dumoga, S., Arora, S., Chuttani, K. and Mishra, A. K. (2014) 'Potential carriers of chemotherapeutic drugs: matrix based nanoparticulate polymeric systems', *Cancer Nanotechnology,* 5(1), pp. 3.

Tonge, A. S., Harbottle, D., Casarin, S., Zervaki, M., Careme, C. and Hunter, T. N. (2021) 'Coagulated Mineral Adsorbents for Dye Removal, and Their Process Intensification Using an Agitated Tubular Reactor (ATR)', *ChemEngineering*, 5(3). DOI: 10.3390/chemengineering5030035.

Tran, H. N., You, S.-J., Nguyen, T. V. and Chao, H.-P. (2017) 'Insight into the adsorption mechanism of cationic dye onto biosorbents derived from agricultural wastes', *Chemical Engineering Communications,* 204(9), pp. 1020-1036.

Tual, N., Carrere, N., Davies, P., Bonnemains, T. and Lolive, E. (2015) 'Characterization of sea water ageing effects on mechanical properties of carbon/epoxy composites for tidal turbine blades', *Composites Part A: Applied Science and Manufacturing,* 78, pp. 380-389.

Ummas, H., Pratiwi, D., Eka Putri, S. and Alimin (2019) 'Adsorption Study for Removal of Acid Orange Dye using Modified Nano Chitosan', *Journal of Physics: Conference Series,* 1244, pp. 012034.

Usman, M. A. and Khan, A. Y. (2022) 'Selective adsorption of anionic dye from wastewater using polyethyleneimine based macroporous sponge: Batch and continuous studies', *Journal of Hazardous Materials,* 428, pp. 128238.

Vakili, M., Deng, S., Cagnetta, G., Wang, W., Meng, P., Liu, D. and Yu, G. (2019) 'Regeneration of chitosan-based adsorbents used in heavy metal adsorption: A review', *Separation and Purification Technology,* 224.

Vijay Anand, M., Sohitha, C., Saraswathi, G. N. and Lavanya, G. V. (2023) 'Water quality prediction using CNN', *Journal of Physics: Conference Series,* 2484(1), pp. 012051.

W. Jo, M.-W. M., H. J. Lee (2014) '3D Printed and Plasma Treated Superhydrophobic Mesh Filters for Oil-Water Separation', *TechConnect Briefs,* 1, pp. 237 - 240.

Waheed, S., Rodas, M., Kaur, H., Kilah, N. L., Paull, B. and Maya, F. (2021) 'In-situ growth of metal-organic frameworks in a reactive 3D printable material', *Applied Materials Today,* 22, pp. 100930.

Wai, C., Yee Bond, T., Nyam, K. and Pui, L. P. (2019) 'MALAYSIAN JOURNAL OF ANALYTICAL SCIENCES ANTIBACTERIAL PROPERTIES OF CHITOSAN EDIBLE FILMS INCORPORATED WITH MUSK LIME EXTRACTS FOR THE PRESERVATION OF SQUIDS'.

Wan Ngah, W. S., Teong, L. C. and Hanafiah, M. A. K. M. (2011) 'Adsorption of dyes and heavy metal ions by chitosan composites: A review', *Carbohydrate Polymers,* 83(4), pp. 1446-1456.

Wang, D., Chen, D. and Chen, Z. (2020) 'Recent Progress in 3D Printing of Bioinspired Structures', *Frontiers in Materials,* 7.

Wang, H., Sun, T., Peng, C. and Wu, Z. (2016) 'Effect of different silane coupling agents on cryogenic properties of silica-reinforced epoxy composites', *High Performance Polymers,* 30(1), pp. 24-37.

Wang, J., Zhai, Z., Zhu, Y., Zhang, L. and Fang, X. (2022a) 'Identification for water quality based on color characteristics', *IOP Conference Series: Earth and Environmental Science,* 983(1), pp. 012075.

Wang, L., Tang, C., Wang, X. and Zheng, W. (2019) 'Molecular dynamics simulation on the thermodynamic properties of insulating paper cellulose modified by silane coupling agent grafted nano-SiO2', *AIP Advances,* 9(12), pp. 125134.

Wang, M., Ma, Y., Sun, Y., Hong, S. Y., Lee, S. K., Yoon, B., Chen, L., Ci, L., Nam, J.-D., Chen, X. and Suhr, J. (2017) 'Hierarchical Porous

Chitosan Sponges as Robust and Recyclable Adsorbents for Anionic Dye Adsorption', *Scientific Reports,* 7(1), pp. 18054.

Wang, X., Shi, J., Zhuang, J., Chen, C., Ouyang, K., Xu, M. and Xu, Z. (2022b) 'Characterization and evaluation of the adsorption potential of chitosan-impregnated cellulose nanofiber multi-walled carbon nanotube aerogel for copper ions', *New Journal of Chemistry,* 46(7), pp. 3156-3167.

Wang, Y., Naleway, S. E. and Wang, B. (2020) 'Biological and bioinspired materials: Structure leading to functional and mechanical performance', *Bioactive Materials,* 5(4), pp. 745-757.

Wang, Y., Wang, Y., Qiu, S., Wang, C., Zhang, H., Guo, J., Wang, S. and Ma, H. (2023) '3D-Printed Filters for Efficient Heavy Metal Removal from Water Using PLA@CS/HAP Composites', *Polymers*, 15(20). DOI: 10.3390/polym15204144.

Wang, Y., Zou, M., Gao, K., Guo, W., Wang, G. and Tang, Q. (2020) 'Effects of surface modification on the physical, mechanical, and thermal properties of bamboo-polypropylene composites', *BioResources,* 15, pp. 6230-6243.

Wang, Z., Wang, J., Li, M., Sun, K. and Liu, C.-j. (2014) 'Three-dimensional Printed Acrylonitrile Butadiene Styrene Framework Coated with Cu-BTC Metal-organic Frameworks for the Removal of Methylene Blue', *Scientific Reports,* 4(1), pp. 5939.

Wani, T. A., Masoodi, F. A. and Akhter, R. (2021) 'Preparation and characterization of chitosan flake and chitosan nanopowder gels: A

comparative study of rheological, thermal and morphological perspectives', *LWT,* 148, pp. 111771.

Wawrzkiewicz, M. (2015) 'Anion Exchange Resins as Effective Sorbents for Removal of Acid, Reactive, and Direct Dyes from Textile Wastewaters', pp. 37-72.

Web of Science (2022) *Publication by topic: 3D printing and water treatment, refined by categories: Surface Functionalization*. Available at: https://www.webofscience.com/wos/woscc/summary/9a03234f-45e1-48d5-8037-947979096342-29974f20/relevance/1 (Accessed: 14 October 2021).

Wei, J., Wang, J., Su, S., Wang, S. and Qiu, J. (2015) 'Tough and fully recoverable hydrogels', *Journal of Materials Chemistry B,* 3(26), pp. 5284-5290.

Wen, L., Chen, X., Chen, C., Yang, R., Gong, M., Zhang, Y. and Fu, Q. (2020) 'Ice-templated porous polymer/UiO-66 monolith for Congo Red adsorptive removal', *Arabian Journal of Chemistry,* 13(6), pp. 5669-5678.

Westbeek, S., Remmers, J. J. C., van Dommelen, J. A. W. and Geers, M. G. D. (2020) 'Multi-scale process simulation for additive manufacturing through particle filled vat photopolymerization', *Computational Materials Science,* 180, pp. 109647.

Wid, N. and Alca, I. (2016) 'Extraction and Characterization of Chitosan from Shrimp Shell Waste in Sabah', *transactions on science and technology,* 3, pp. 227-237.

Wong, K. T., Wong, V. L. and Lim, S. S. (2021) 'Bio-sorptive Removal of Methyl Orange by Micro-Grooved Chitosan (GCS) Beads: Optimization

of Process Variables Using Taguchi L9 Orthogonal Array', *Journal of Polymers and the Environment,* 29(1), pp. 271-290.

Wong, Y. C., Szeto, Y. S., Cheung, W. H. and McKay, G. (2008) 'Effect of temperature, particle size and percentage deacetylation on the adsorption of acid dyes on chitosan', *Adsorption,* 14(1), pp. 11-20.

Wu, J., Xing, M., Yin, S., Zhang, C., Chen, X., Yi, S., Lian, H. and Xie, D. (2022) 'Analysis of Microstructure and Low Permeability with 3D Digital Rock Modeling', *Geofluids,* 2022, pp. 2462652.

Wu, L., Hoa, S. V., Minh, T. and Ton, T. (2006) 'Effects of composition of hardener on the curing and aging for an epoxy resin system', *Journal of Applied Polymer Science,* 99(2), pp. 580-588.

Xing, R., Huang, R., Qi, W., Su, R. and He, Z. (2018) 'Three-dimensionally printed bioinspired superhydrophobic PLA membrane for oil-water separation', *AIChE Journal,* 64(10), pp. 3700-3708.

Xu, D. and Lin, M. (2023) 'Design controllable TPMS structures for solar thermal applications: A pore-scale vs. volume-averaged modeling approach', *International Journal of Heat and Mass Transfer,* 201, pp. 123625.

Xu, W.-T., Zhao, Z.-P., Liu, M. and Chen, K.-C. (2015) 'Morphological and hydrophobic modifications of PVDF flat membrane with silane coupling agent grafting via plasma flow for VMD of ethanol–water mixture', *Journal of Membrane Science,* 491, pp. 110-120.

Yan, C., Ji, Z., Ma, S., Wang, X. and Zhou, F. (2016) '3D Printing as Feasible Platform for On-Site Building Oil-Skimmer for Oil Collection from Spills', *Advanced Materials Interfaces,* 3(13), pp. 1600015.

Yan, C., Jiang, P., Jia, X. and Wang, X. (2020) '3D printing of bioinspired textured surfaces with superamphiphobicity', *Nanoscale,* 12(5), pp. 2924-2938.

Yan, C., Ma, S., Ji, Z., Guo, Y., Liu, Z., Zhang, X. and Wang, X. (2019) '3D Printing of an Oil/Water Mixture Separator with In Situ Demulsification and Separation', *Polymers,* 11(5), pp. 774.

Yan, X., Bethers, B., Chen, H., Xiao, S., Lin, S., Tran, B., Jiang, L. and Yang, Y. (2021) 'Recent Advancements in Biomimetic 3D Printing Materials With Enhanced Mechanical Properties', *Frontiers in Materials,* 8, pp. 518886.

Yang, S., Cheng, Q., Hu, L., Gu, Y., Wang, Y. and Liu, Z. (2023a) 'Study on the Adsorption Properties of Oxalic Acid-Modified Cordierite Honeycomb Ceramics for Neutral Red Dyes', *ACS Omega,* 8(12), pp. 11457-11466.

Yang, W., Yu, H., Liang, W., Wang, Y. and Liu, L. (2015) 'Rapid Fabrication of Hydrogel Microstructures Using UV-Induced Projection Printing', *Micromachines,* 6(12), pp. 1903-1913.

Yang, X., Zhong, H., Zhang, W., Liu, Y., Sun, N., Kuang, R., Wang, C., Zhan, A., Zhang, J., Tang, Q. and Li, Z. (2023b) 'Progress in Adsorptive Removal of Volatile Organic Compounds by Zeolites', *Aerosol and Air Quality Research,* 23(5), pp. 220442.

Yaseen, D. and Scholz, M. (2018) 'Textile dye wastewater characteristics and constituents of synthetic effluents: a critical review', *International Journal of Environmental Science and Technology,* 16.

Yaseen, D. A. and Scholz, M. (2019) 'Textile dye wastewater characteristics and constituents of synthetic effluents: a critical review', *International Journal of Environmental Science and Technology,* 16, pp. 1193–1226.

Yasir AlJaberi, F. and Mohammed, W. (2018) *The Most Practical Treatment Methods for Wastewaters: A Systematic Review.*

Yeranee, K. and Rao, Y. (2022) 'A Review of Recent Investigations on Flow and Heat Transfer Enhancement in Cooling Channels Embedded with Triply Periodic Minimal Surfaces (TPMS)', *Energies*, 15(23). DOI: 10.3390/en15238994.

Yoshida, Z.-i., Osawa, E. and Oda, R. (1964) 'Intermolecular Hydrogen Bond Involving a π-Base as the Proton Acceptor. I. Detection by the Refractive Index Method', *The Journal of Physical Chemistry,* 68(10), pp. 2895-2898.

Yu, R.-F., Chen, H.-W., Cheng, W.-P. and Chu, M.-L. (2006) 'Measurements of Wastewater True Color by 4/6 Wavelength Methods and Artificial Neural Network', *Environmental Monitoring and Assessment,* 118(1), pp. 195-209.

Yu, R.-F., Cheng, W.-P. and Chu, M.-L. (2005) 'On-line Monitoring of Wastewater True Color Using Digital Image Analysis and Artificial Neural Network', *Journal of Environmental Engineering,* 131(1), pp. 71-79.

Yu, R. F., Chen, H.-W., Cheng, W. P. and Huang, H. D. (2017) 'Applying Online Image Analysis to Simultaneously Evaluate the Removals of Suspended Solids and Color from Textile Wastewater in Chemical

Flocculated Sedimentation', *Journal of Environmental Informatics,* 29, pp. 29-38.

Yu, X., Jia, J., Xu, S., Lao, K. U., Sanford, M. J., Ramakrishnan, R. K., Nazarenko, S. I., Hoye, T. R., Coates, G. W. and DiStasio, R. A. (2018) 'Unraveling substituent effects on the glass transition temperatures of biorenewable polyesters', *Nature Communications,* 9(1), pp. 2880.

Yuan, S., Strobbe, D., Kruth, J.-P., Van Puyvelde, P. and Van der Bruggen, B. (2017) 'Super-hydrophobic 3D printed polysulfone membranes with a switchable wettability by self-assembled candle soot for efficient gravity-driven oil/water separation', *Journal of Materials Chemistry A,* 5(48), pp. 25401-25409.

Yuan, S., Strobbe, D., Li, X., Kruth, J.-P., Van Puyvelde, P. and Van der Bruggen, B. (2020) '3D printed chemically and mechanically robust membrane by selective laser sintering for separation of oil/water and immiscible organic mixtures', *Chemical Engineering Journal,* 385, pp. 123816.

Yusoff, N. H. M., Chong, C. H., Wong, V. L., Cheah, K. H. and Wan, Y. K. (2023) 'The influence of structural topology of additively manufactured PEGDA monolith on adsorption performance for textile wastewater treatment', *Asia-Pacific Journal of Chemical Engineering,* n/a(n/a), pp. e2952.

Zawaski, C. E., Chatham, C. A., Wilts, E. M., Long, T. E. and Williams, C. B. (2021) 'Using fillers to tune material properties of an ion-containing semi-crystalline poly(ethylene glycol) for fused filament fabrication additive manufacturing', *Additive Manufacturing,* 39, pp. 101844.

Zeng, G., He, Y., Zhan, Y., Zhang, L., Pan, Y., Zhang, C. and Yu, Z. (2016) 'Novel polyvinylidene fluoride nanofiltration membrane blended with functionalized halloysite nanotubes for dye and heavy metal ions removal', *Journal of Hazardous Materials,* 317, pp. 60-72.

Zhang, C., Wang, X., Hu, Z., Wu, Q., Zhu, H. and Lu, J. (2021a) 'Long-term performance of silane coupling agent/metakaolin based geopolymer', *Journal of Building Engineering,* 36, pp. 102091.

Zhang, D., Xiao, J., Guo, Q. and Yang, J. (2019a) '3D-printed highly porous and reusable chitosan monoliths for Cu (II) removal', *Journal Material Science,* (54), pp. 6728–6741.

Zhang, D., Xiao, J., Guo, Q. and Yang, J. (2019b) '3D-printed highly porous and reusable chitosan monoliths for Cu(II) removal', *Journal of Materials Science,* 54(8), pp. 6728-6741.

Zhang, H., Wang, L., Song, L., Niu, G., Cao, H., Wang, G., Yang, H. and Zhu, S. (2011a) 'Controllable properties and microstructure of hydrogels based on crosslinked poly(ethylene glycol) diacrylates with different molecular weights', *Journal of Applied Polymer Science,* 121(1), pp. 531-540.

Zhang, J., Allardyce, B. J., Rajkhowa, R., Wang, X. and Liu, X. (2021b) '3D printing of silk powder by Binder Jetting technique', *Additive Manufacturing,* 38, pp. 101820.

Zhang, J., Hu, Q., Wang, S., Tao, J. and Gou, M. (2019c) 'Digital Light Processing Based Three-dimensional Printing for Medical Applications', *International journal of bioprinting,* 6(1), pp. 242-242.

Zhang, N., Qiu, H., Si, Y., Wang, W. and Gao, J. (2011b) 'Fabrication of highly porous biodegradable monoliths strengthened by graphene oxide and their adsorption of metal ions', *Carbon,* 49(3), pp. 827-837.

Zhang, X., Yang, D. and Nie, J. (2008) 'Chitosan/polyethylene glycol diacrylate films as potential wound dressing material', *International Journal of Biological Macromolecules,* 43(5), pp. 456-462.

Zhang, Y.-Z., Wang, Y., Jiang, Q., El-Demellawi, J. K., Kim, H. and Alshareef, H. N. (2020) 'MXene Printing and Patterned Coating for Device Applications', *Advanced Materials,* 32(21), pp. 1908486.

Zhang, Z. and Li, M. 'Research on Facial Expression Recognition Based on Neural Network'. *2020 International Conference on Computer Network, Electronic and Automation (ICCNEA)*, 25-27 Sept. 2020, 78-81.

Zhao, F., Repo, E., Yin, D., Chen, L., Kalliola, S., Tang, J., Iakovleva, E., Tam, K. C. and Sillanpää, M. (2017) 'One-pot synthesis of trifunctional chitosan-EDTA-β-cyclodextrin polymer for simultaneous removal of metals and organic micropollutants', *Scientific Reports,* 7(1), pp. 15811.

Zhao, J., Jiang, N., Zhang, D., He, B. and Chen, X. (2020) 'Study on Optimization of Damping Performance and Damping Temperature Range of Silicone Rubber by Polyborosiloxane Gel', *Polymers*, 12(5). DOI: 10.3390/polym12051196.

Zhao, Y. and Chen, D. (2022) 'Expression Recognition Using Improved AlexNet Network in Robot Intelligent Interactive System', *Journal of Robotics,* 2022.

Zhou, H. Y., Chen, X. G., Kong, M., Liu, C. S., Cha, D. S. and Kennedy, J. F. (2008) 'Effect of molecular weight and degree of chitosan

deacetylation on the preparation and characteristics of chitosan thermosensitive hydrogel as a delivery system', *Carbohydrate Polymers,* 73(2), pp. 265-273.

Zhou, Y., Lu, J., Zhou, Y. and Liu, Y. (2019) 'Recent advances for dyes removal using novel adsorbents: A review', *Environmental Pollution,* 252, pp. 352-365.

Zhou, Z., Lin, S., Yue, T. and Lee, T.-C. (2014) 'Adsorption of food dyes from aqueous solution by glutaraldehyde cross-linked magnetic chitosan nanoparticles', *Journal of Food Engineering,* 126, pp. 133-141.

Zhu, H. Y., Jiang, R., Fu, Y. Q., Jiang, J. H., Xiao, L. and Zeng, G. M. (2011) 'Preparation, characterization and dye adsorption properties of γ-Fe2O3/SiO2/chitosan composite', *Applied Surface Science,* 258(4), pp. 1337-1344.

Zhu, W., Groen, J. C., van Miltenburg, A., Kapteijn, F. and Moulijn, J. A. (2007) 'Kureha activated carbon characterized by the adsorption of light hydrocarbons', in Llewellyn, P.L., Rodriquez-Reinoso, F., Rouqerol, J. and Seaton, N. (eds.) *Studies in Surface Science and Catalysis*: Elsevier, pp. 287-294.

Zimmerling, C., Poppe, C., Stein, O. and Kärger, L. (2022) 'Optimisation of manufacturing process parameters for variable component geometries using reinforcement learning', *Materials & Design,* 214, pp. 110423.

APPENDICES

Supplementary information- Section 3.2.8 RSM DOE Approach

Table A1: Model summary of regression equation for removal efficiency (R%) generated from Minitab 19.

Removal (%) = -	256.2 + 76.2 A + 4.85 B + 25.22 C + 1.78 D - 8.58 A*A - 0.0604 B*B - 1.364 C*C + 0.0079 D*D + 0.097 A*B - 1.333 A*C - 0.488 A*D + 0.0316 B*C + 0.0113 B*D - 0.2005 C*D		
S	R-sq.	R-sq.(adj)	R-sq.(pred)
11.0575	82.74%	78.42%	72.18%

Footnote: A - Concentration, B - Dipping time, C - pH and D -Temperature

Table A2: Model summary of regression equation for uptake capacity, K (mg/g) generated from Minitab 19.

K = -	42.24 + 11.72 A + 0.755 B + 3.286 C + 0.472 D - 1.149 A*A - 0.00846 B*B - 0.1875 C*C - 0.00182 D*D - 0.0236 A*B - 0.178 A*C - 0.0616 A*D + 0.00592 B*C + 0.00128 B*D - 0.02494 C*D		
S	R-sq.	R-sq.(adj)	R-sq.(pred)
1.53930	80.91%	76.13%	68.59%

Footnote: A - Concentration, B - Dipping time, C - pH and D -Temperature

Supplementary Information – Section 3.3.1.1 FESEM and EDX Analysis

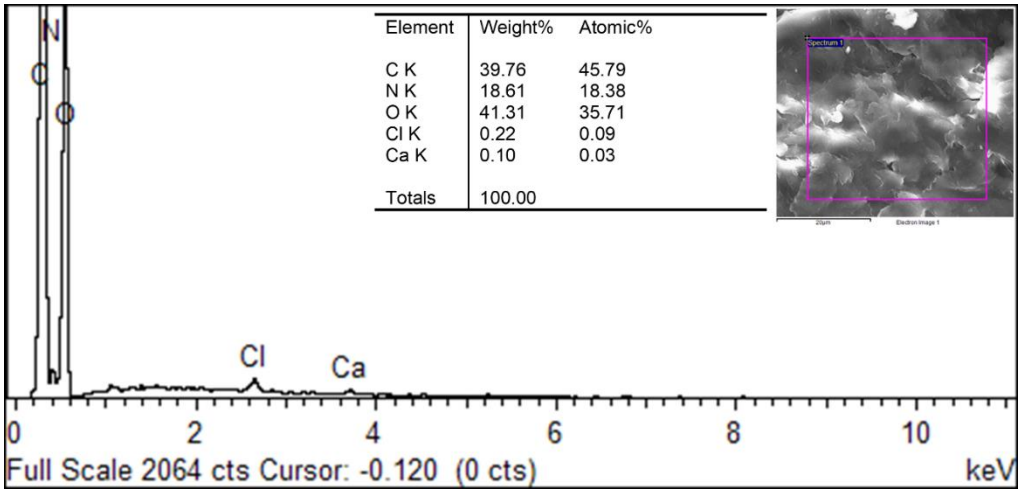


Figure A1: SEM - EDX Analysis of pure chitosan.

Supplementary Information – Section 3.3.3 Response Optimiser Plots for removal efficiency (R%) and uptake capacity, K (mg/g)

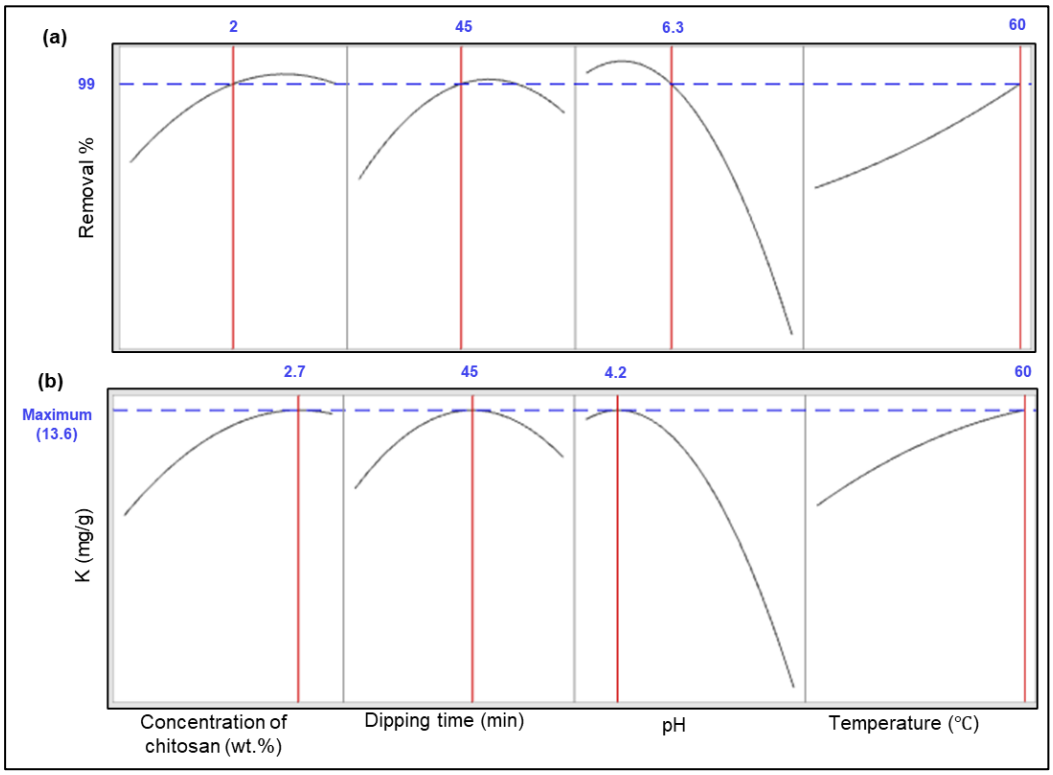


Figure A2: Optimisation plot of; (a) Removal efficiency (R%) and (b) Uptake capacity, K (mg/g).

Supplementary Information – Section 3.3.4 ANOVA Results

Table A0.1: Results of ANOVA for removal efficiency (R%).

Source	DF	Adj SS	Contribution	F-Value	P-Value	Status
Regression	16	37500	82.7%	19.2	0.000	
Concentration	1	5240	11.6%	42.9	0.000	
Dipping time	1	1260	2.8%	10.3	0.00200	
pH	1	15000	33.2%	123.0	0.000	Significant
Temperature	1	1370	3.02%	11.2	0.00100	
Concentration^2	1	1170	2.58%	9.56	0.00300	
Dipping time^2	1	2950	6.50%	24.1	0.000	
pH^2	1	7550	16.7%	61.8	0.000	
Temperature^2	1	37.7	0.0832%	0.310	0.580	Not significant
Concentration*Dipping time	1	25.6	0.0565%	0.210	0.649	Not significant
Concentration*pH	1	341.0	0.752%	2.79	0.100	Not significant
Concentration*Temperature	1	714.0	1.58%	5.84	0.0190	
Dipping time*pH	1	43.1	0.0951%	0.350	0.555	Not significant
Dipping time*Temperature	1	82.9	0.183%	0.680	0.413	Not significant
pH*Temperature	1	1670	3.69%	13.7	0.000	
Error	64	7820				
Lack of fit	**10**	**2398.2**		**2.50**	**0.075**	
Total	80	45300				

Table A0.2: Results of ANOVA for uptake capacity, K (mg/g).

Source	DF	Adj SS	Contribution	F-Value	P-Value	Comment
Regression	16	643	80.9%	17.0	0.000	
Concentration	1	101	12.7%	42.6	0.000	
Dipping time	1	21.3	2.68%	8.99	0.00400	
pH	1	260	32.7%	110	0.000	
Temperature	1	7.01	0.883%	2.96	0.0900	Not significant
Concentration^2	1	21.0	2.64%	8.85	0.00400	
Dipping time^2	1	57.9	7.28%	24.4	0.000	

pH^2	1	143	18.0%	60.3	0.000	
$Temperature^2$	1	2.01	0.253%	0.850	0.361	Not significant
Concentration*Dipping time	1	1.51	0.189%	0.640	0.428	Not significant
Concentration*pH	1	6.08	0.765%	2.57	0.114	Not significant
Concentration*Temperature	1	11.4	1.43%	4.81	0.032	
Dipping time*pH	1	1.51	0.191%	0.640	0.427	Not significant
Dipping time*Temperature	1	1.08	0.135%	0.450	0.503	Not significant
pH*Temperature	1	25.9	3.26%	10.9	0.00200	
Lack of fit	**10**	**133.3**		**2.47**	**0.159**	
Error	64	152				
Total	80	794				

Supplementary Information – Section 3.3.5 Confirmation of experiment

Table A0.1: Experimental setup with different conditions.

Set	Factors			
	C_0 of chitosan(wt.%)	Dipping time (min)	pH	Temperature
1	2	45	6.3	30
2	2	45	6.3	40
3	2	45	6.3	50
4	2	45	6.3	60

Supplementary Information – Section 3.3.10 Thermodynamic parameters for MO dye removal at different temperatures

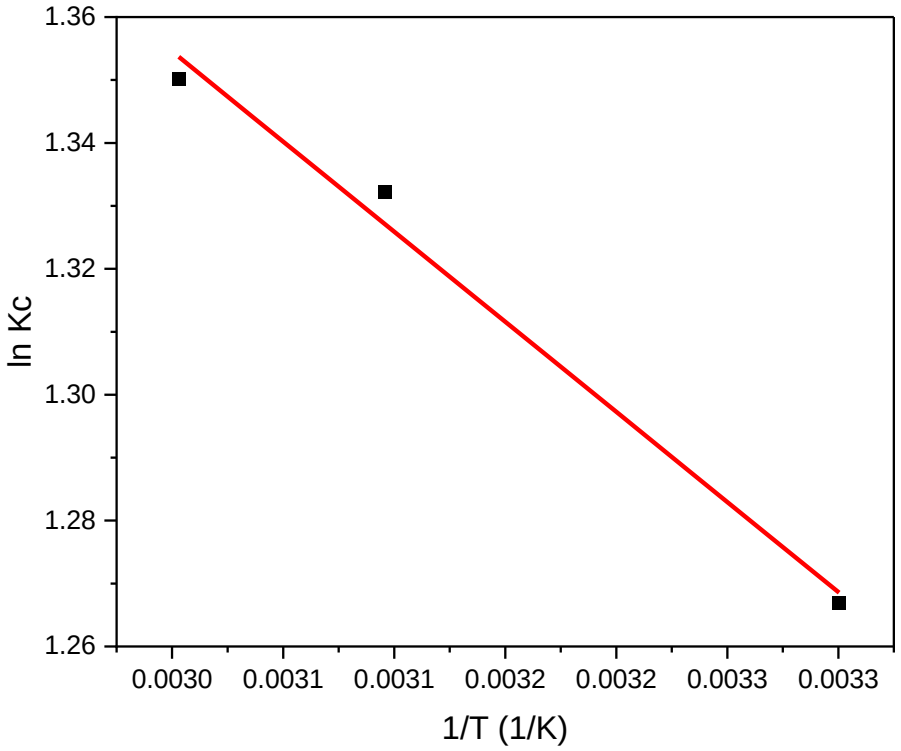


Figure A3: Plot of Activation energy of adsorption of MO dye on 3D-printed chitosan-grafted monolith.

Supplementary information- Section 6.3.2.1 DSC Analysis

Table A3: DSC data of different resin formulations.

Materials	Glass transition temperature	Melting temperature	Enthalpy
	℃	℃	Jg^{-1}
PEGDA/HDDA1	47.8	180.8	9.35
PEGDA/HDDA2	48.3	184.8	11.40
PEGDA/HDDA3	48.8	190.6	6.50
PEGDA/BDDA1	48.7	160.5	**1**9.42
PEGDA/BDDA2	4**8**.1	222.8	23.53
PEGDA/BDDA3	**48.6**	**212.9**	**32.69**

Supplementary information- Section 6.3.2.2 TGA Analysis

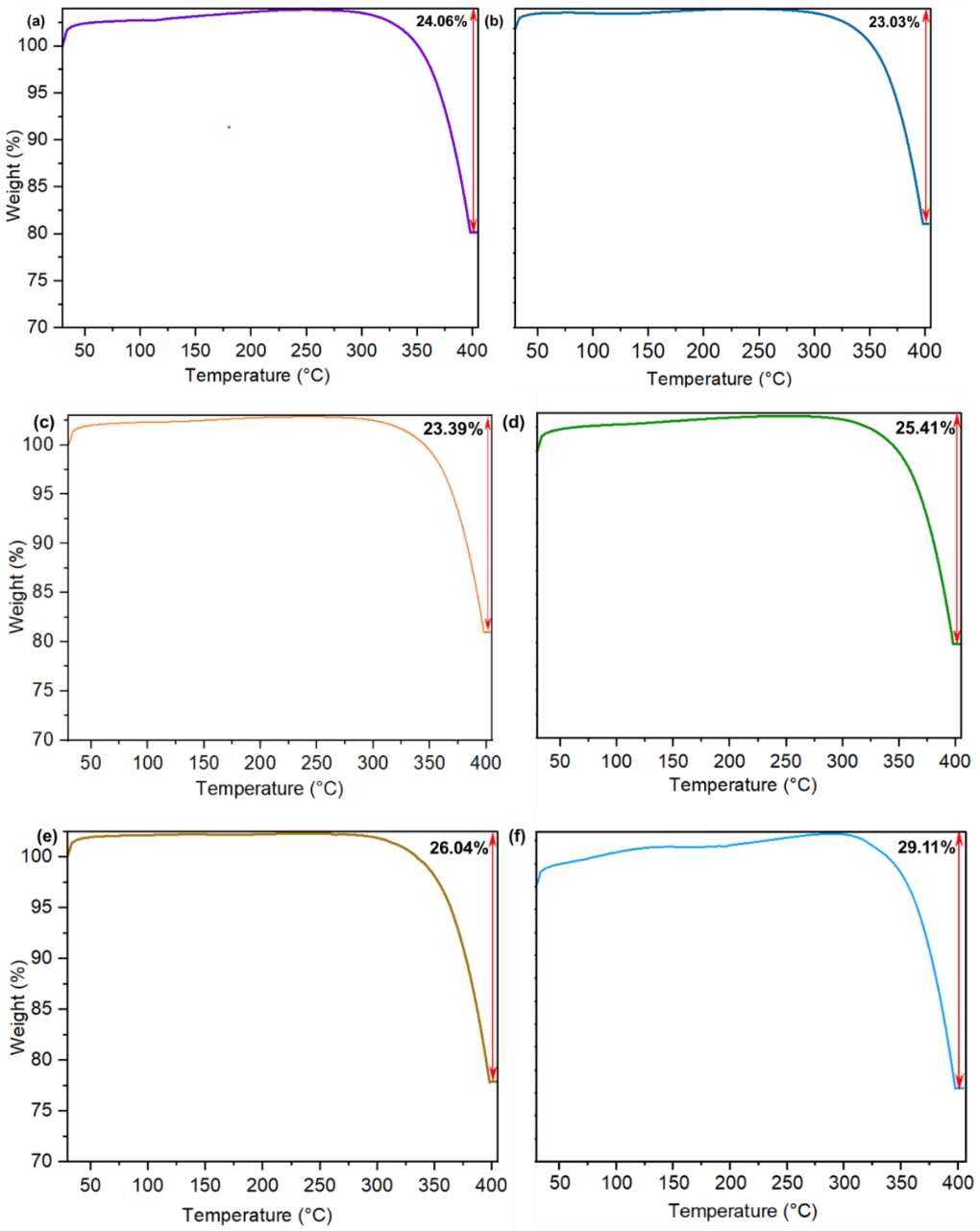


Figure A4: TGA results of; (a)PEGDA/HDDA1, (b) PEGDA/HDDA2, (c) PEGDA/HDDA3, (d) PEGDA/BDDA1, (e) PEGDA/BDDA2 and (f) PEGDA/BDDA3.

Table A4: TGA data of all different resin formulations.

Sample	Initial weight	Decomposition		Residue at 400℃
	mg	Weight loss%	T_{onset}	mg
PEGDA/HDDA1	6.16	24.06	360.1	4.68
PEGDA/HDDA2	9.06	23.03	358.8	6.97
PEGDA/HDDA3	7.03	23.39	358.5	5.39
PEGDA/BDDA1	6.42	25.41	362.3	4.79
PEGDA/BDDA2	7.28	26.04	356.5	5.38
PEGDA/BDDA3	6.04	29.11	355.9	4.28